Mg 2021

Magnesium 2021

Proceedings of the
12th International Conference on
Magnesium Alloys and
their Applications

EDITED BY

Alan Luo • Mihriban Pekguleryuz
Sean Agnew • John Allison
Karl Kainer • Eric Nyberg
Warren Poole • Kumar Sadayappan
Bruce Williams • Steve Yue

TMS

🛡 Springer

The Minerals, Metals & Materials Series

Alan Luo · Mihriban Pekguleryuz · Sean Agnew ·
John Allison · Karl Kainer · Eric Nyberg ·
Warren Poole · Kumar Sadayappan ·
Bruce Williams · Steve Yue
Editors

Magnesium 2021

Proceedings of the 12th International
Conference on Magnesium Alloys and their
Applications

TMS

Springer

Editors
Alan Luo
The Ohio State University
Columbus, OH, USA

Sean Agnew
University of Virginia
Charlottesville, VA, USA

Karl Kainer
Wrocław University of Science
and Technology
Wrocław, Poland

Warren Poole
University of British Columbia
Vancouver, BC, Canada

Bruce Williams
CanmetMATERIALS
Hamilton, ON, Canada

Mihriban Pekguleryuz
McGill University
Montreal, QC, Canada

John Allison
University of Michigan
Ann Arbor, MI, USA

Eric Nyberg
Tungsten Parts Wyoming
Laramie, WY, USA

Kumar Sadayappan
CanmetMATERIALS
Hamilton, ON, Canada

Steve Yue
McGill University
Montreal, QC, Canada

Preface

The 12th International Conference on Magnesium Alloys and their Applications (Mg 2021) was planned to be held in beautiful Montreal, Quebec, Canada on June 15–18, 2021. However, due to the limits of the COVID-19 pandemic on travel and in-person gatherings, the meeting is virtual for the first time in the 35-year history of this series of international conferences. Held every 3 years since 1986 in Europe, Asia, and North America, this event is considered the premier technical forum for the global magnesium community. We are excited to virtually host Mg 2021 on the same dates planned and with no physical boundaries.

As the lightest structural metal, magnesium has significant growth potential in a variety of applications from transportation and energy storage to electronics and consumer products. Advancements in magnesium have accelerated since the meeting last convened at Mg 2018. We are also seeing a change in the direction of alloy development activities that the conference will present. Notably, magnesium uses have expanded from traditional die casting alloys and aluminum alloying use to groundbreaking new biomedical and energy applications. Biodegradable and biocompatible implant applications are targeting both new alloys and new structures (e.g., scaffolds, foams). In the automotive industry, with the emergence of new automotive engine and alternate fuel technologies, magnesium powertrain casting-alloy research will take a step back while automotive structural and body alloys will step forward, with a focus on wrought and casting alloys with higher ductility/formability, and magnesium-based solid fuels. New understanding in fundamental aspects of magnesium alloys has been made with advanced characterization techniques and modeling methods. These techniques allow researchers to discover new microstructure-property relationships, such as long-period stacking ordered (LPSO) structures. First-principles calculations and machine learning are starting to revolutionize alloy development routes.

Discussions are arranged to explore developments in primary and manufacturing processes, including additive manufacturing, and the progress in advanced joining technologies of linear friction welding and friction stir welding. With the encouraging news that the restrictions on the in-cabin use of magnesium in aircrafts can be lifted, ignition-proof magnesium alloy research has found new impetus. In corrosion

science, steps are being taken toward stainless magnesium. These topics and more promise to illuminate and invigorate the minds gathering virtually at Mg 2021.

We are very pleased with the great response to the Call for Abstracts of Mg 2021 from around the world. We received over 180 abstracts, and 26 papers are included in this Proceedings. The conference program features 12 plenary lectures, 155 oral presentations (27 of which are invited), and 17 poster presentations. We are also planning to publish a set of papers presented at the conference in *Metallurgical and Materials Transactions A* in the near future.

We appreciate all the authors and reviewers for their contributions to the Proceedings and their effort to ensure the deadlines were met. We also thank the members of the International Committee for promoting Mg 2021 in the international community and the members of the Organizing Committee for their support to the conference organization. Special thanks go to the TMS staff members who are supporting all of the activities, particularly Kelcy Marini for her tireless efforts in keeping everything in order and Matt Baker for publishing the Proceedings.

<div align="right">

Alan Luo
Mihriban Pekguleryuz

</div>

Alan Luo is a Professor of Materials Science and Engineering and Integrated Systems Engineering at The Ohio State University (OSU). He leads the OSU Lightweight Materials and Manufacturing Research Laboratory (LMMRL) and is on the steering board of the OSU Center for Simulation Innovation and Modeling (SIMCenter). He is an elected Fellow of ASM International and SAE International. He is presently a Director of the board of the International Magnesium Association and a past Chair of the TMS Light Metals Division and SAE Materials Engineering Division. Prior to joining OSU in July 2013, he was a GM Technical Fellow at General Motors Global Research and Development Center with 20 years of industrial experience. He received his Ph.D. in Engineering Materials from the University of Windsor in 1993.

Professor Luo's research areas include: (1) lightweight materials (aluminum, magnesium, titanium and high-entropy alloys, bio-metals, super-wood, and

nanocomposites); (2) advanced manufacturing processes (casting, forming, additive manufacturing, and multi-material manufacturing); and (3) lightweight design and integrated computational materials engineering (ICME).

Mihriban Pekguleryuz is a Professor of Materials Engineering at McGill University and a Fellow of the Canadian Academy of Engineering (CAE). She has 30 years of combined industrial and academic research experience in light metals, specifically in magnesium-based materials some of which have been commercialized by automotive companies and metal producers globally. Her industrial experience ranges from IBM Canada to Noranda Technology (now Glencore) where she worked as Group Leader of Materials Engineering. In academia, she was awarded two industrial Research Chair positions, one with GM of Canada and the other with Alcan (now Rio Tinto). She was a founding member and a past Chair of the TMS Magnesium Committee. She is an Executive Member of the Canadian Institute of Mining, Metallurgy and Petroleum (CIM) and the Metallurgy and Materials Society (MetSoc) and is the Light Metals Section Editor and Editor-in-Chief/Engineering for *Experimental Results*. She received her B.Sc. and M.Sc. degrees in Materials Science and Engineering from the University of Florida, Gainesville (USA) and her Ph.D. in Metallurgical Engineering from McGill University (Canada) in 1987. She is currently leading the Light Metals Research Laboratory at McGill in research activities focused on lightweighting in transport applications (automotive body, ignition-proof Mg for aerospace, Mg materials for fast train and rail); biodegradable and biocompatible Mg implants; aluminum diesel engine alloys; lead-free electronic interconnect materials; corrosion-resistant Mg alloys; and the use of machine learning in light alloy development.

Contents

Par IX Recycling and Environmental Issues

Part I
Primary Production

A New Hydrometallurgical Process Combined With an Electrolytic Process for Magnesium Primary Production from Serpentine

Joel Fournier

Abstract The FOURNIER PROCESS owned by Alliance Magnesium Inc (AMI) is a hydrometallurgical process combined with an electrolytic process for primary magnesium production. It constitutes an improvement over the former Noranda Magnola Process and uses a combination of best in class technology to produce a high-quality magnesium for use in many applications, including the most demanding, namely, the automotive market. It also introduces a radical breakthrough in technological change by the production of some valuable by-products. AMI made the acquisition of Magnola company and assets in 2017 and is under construction of a commercial demonstration plant to restart the production of primary magnesium in Canada.

Keywords Primary magnesium production · Hydrometallurgy · Electrolysis

J. Fournier (✉)
Alliance Magnesium Inc, Danville, Canada
e-mail: jfournier@alliancemagnesium.com

3

Picture of AMI's site

Picture of the plant under construction

Introduction

The FOURNIER PROCESS, as well as the former Magnola Process, is used to recover magnesium from serpentine rock coming from mine tailing resulting from Asbestos production. Asbestos is a set of six naturally occurring silicate minerals

used commercially for their desirable physical properties. They all have in common their eponymous, asbestiform habit: long and thin fibrous crystals. Asbestos became increasingly popular among manufacturers and builders in the late nineteenth century because of its sound absorption; average tensile strength; its resistance to fire, heat, electrical and chemical damage; and affordability. It was used in such applications as electrical insulation for the nineteenth century. For a long time, the world's largest asbestos mine was the Jeffrey Mine in the town of Val-Des-Sources, Quebec. Asbestos production and sale are now banned in most of the countries around the world including Canada for health concern.

The discarded serpentine tailings from asbestos mining constitute the raw material and will be mined themselves by AMI for magnesium production. The tailings contain 24% magnesium, 38% silicate oxide, and minor elements like iron and nickel. It compares advantageously to other sources of mineral magnesium used for metal production.

Magnesium is a commercially important metal with many uses. It is only two-thirds as dense as aluminum. It is easily machined, cast, forged, and welded. It is used extensively in alloys, with aluminum and zinc, and with manganese. The magnesium is an essential ingredient for the lightweighting of transportation industry.

Taking out the magnesium metal from unrefined materials is a force exhaustive procedure requiring nicely tuned technologies. There is thus still a need for improved processes for extracting magnesium from magnesium-bearing ores such as asbestos.

Picture of former asbestos production residues (AMIS's raw material)

The Former Magnola Process

Magnola's magnesium production was based on a hydrometallurgical process followed by an electrolysis process. The production of 58,000 tons of magnesium required about 270,000 tons of serpentine rock (mine tailings) as raw material. Other inputs included magnesium oxide added to the brine neutralization and purification steps; hydrochloric acid to make up for quantities consumed by the process; caustic soda used for cleaning emissions; and sulfuric acid used to dry hydrogen chloride (Fig. 1).

The Magnola magnesium production facility was built and achieved 42% of its nominal capacity in a steady production mode. Certain technological challenges and weaknesses in the process were identified during the development and implementation of the leaching, neutralization, electrolysis, and other ancillary processes, the main ones being:

1. The residual iron, nickel, and silica were extracted from the brine by precipitation. The brine went through agitated neutralization reactors operating at about 110 °C, with a pH close to 4. The addition of anhydrous magnesia or Mg (OH) precipitated iron, calcium, nickel, and chromium. Following this hydrometallurgical step, the non-leached portion was filtered out and sent to the silica-iron
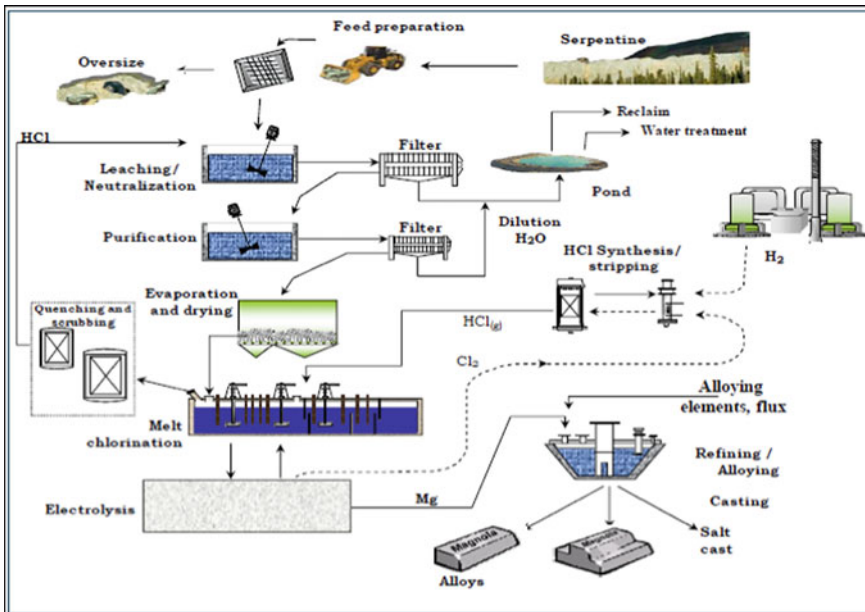
Fig. 1 The diagram depicts the main process stages of material preparation, magnesium extraction, leaching and neutralization, purification and drying, electrolysis and casting, and HCl synthesis and emission treatment. (Color figure online)

storage area. The cake obtained from the filter contained about 50–70% of the original solids. Water was added to bring the solid concentration to about 50%. This residue, called silica-iron residue, has created a large volume of residue in the pound after only 3 years of activities and required a costly operation system to maintain the level of liquid and prevent overflow.

2. The drying of $MgCl_2$ prills was done on a final step using a super chlorinator. This innovative technology at the time was based on the injection of HCl gas into a molten salt electrolysis to dry the $MgCl_2$ before being fed to the electrolysis cells. Generation of magnesium oxide was observed and was detrimental to electrolysis.

The FOURNIER PROCESS

The process described herein allows processing and extracting magnesium from tailings, such as asbestos mine tailings, obtained after processing of magnesium-bearing ores (Fig. 2).

Preparation and Classification

Tailings, and particularly asbestos tailings, can be finely crushed in order to assist the following leaching steps. The tailings have to be crushed sufficiently to shorten the reaction time by few hours (about 2 to 3 h). Screen classifiers can be used to select oversized pieces that can be re-crushed if necessary. After the initial mineral separation, the crushed tailings undergo a magnetic separation to selectively recover magnetite. This step provides an efficient way to reduce hydrochloric acid consumption. The yield of iron removal can reach over 90%. This magnetite is disposed of and will not be submitted to the further leaching step.

Acid Leaching

The crushed classified tailings then undergo acid leaching. Acid leaching comprises reacting the crushed classified tailings with a hydrochloric acid solution during a given period of time which allows dissolving the magnesium and other elements like iron and nickel. The silica remains totally undissolved after leaching. It is interesting to note that the hydrochloric acid leaching destroys 100% of the residual asbestos fibers contained in the serpentine.

The tailings residue is leached at a temperature of about 60° to about 125 °C. These conditions are possible due to the high salt content in the reaction mixture
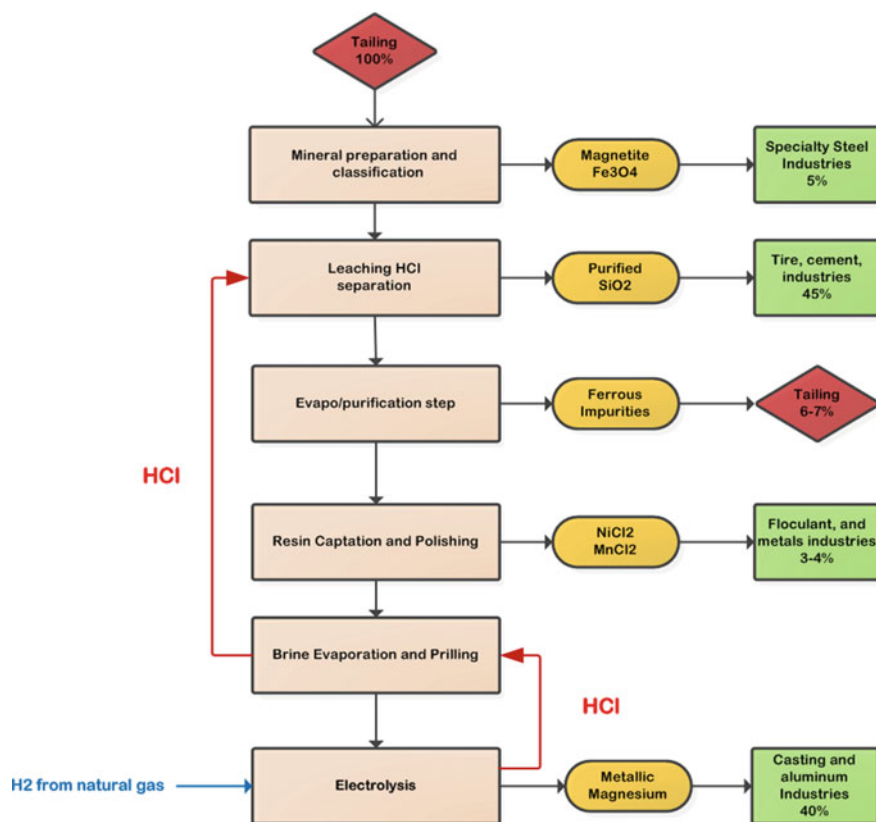
Fig. 2 FOURNIER PROCESS. (Color figure online)

preventing the aqueous solution from boiling. Particularly, the tailings/acid ratio can be about 1:10 (weight/volume), the HCl concentration can be about 25% to about 45 %, and the reaction time can be about 1 to about 7 hours. The leaching reaction converts most magnesium, iron, potassium, calcium, nickel, and manganese into water-soluble chloride compounds. A significant portion of the alumina and all the silica are inert to HCl digestion and remain solid in the reaction mixture.

Liquid/Solid Separation and Washing

Once the extraction is terminated, the solid can be separated from the liquid by filtration, after which it is washed. The corresponding residue can thereafter be washed many times with water so as to decrease acidity and to lower the quantities of sodium hydroxide (NaOH) that are required during this step. The process allows separating

the solid from the leachate and washing the solid so as to obtain silica having a purity of at least 85%. The amorphous silica obtained in that step has demonstrated a good potential to be used as a concrete additive.

Resin Captation and Impurity Removal

The spent acid (leachate) containing the metal chloride in solution obtained can then be passed on to a set of ion exchange resin beds comprising a chelating resin system to catch specifically the nickel chloride ($NiCl_2$). For example, the DOWEX^{TM} M4195 chelating resin can be used for recovering nickel from very acidic process streams. Removal of nickel from water and organic solvents is fairly common using strong acid cation resins. Methods of recovering nickel from high magnesium-containing Ni–Fe–Mg lateritic ores are also described in U.S. patent no. 5,571,308. Furthermore, pure nickel (Ni) can be obtained by electrolysis once the nickel chloride has been extracted. Nickel can also be precipitated at this stage as a hydroxide, filtered in a filter press and sold for a value. Iron and other impurity can be precipitated by a change in pH by MgO addition to obtain a very pure $MgCl_2$ brine.

Dehydration

The pure magnesium chloride solution then undergoes multiple dehydration steps, consisting of evaporation, prilling/crystallization, and dehydration.

First, the pure magnesium chloride hexahydrate undergoes a prilling step by using a fluidized bed dryer to essentially obtain a partially hydrated $MgCl_2$ in form of "prills" ($MgCl_2 \cdot 2H_2O$). To remove the water molecules, the prills are sent a second two-step fluidized bed to essentially obtain an anhydrous magnesium chloride with a drying gas containing hydrochloric acid, thereby separating anhydrous magnesium chloride from the remaining water. The drying process is realized by heating gas to about 150°–180 °C and the solution is fed to a concentrator to bring the magnesium chloride concentration up. The magnesium chloride gas-drying is carried out in two stages, targeting two molecules of hydration-water removal in each stage, so that the drying temperatures can be selected to optimize drying and minimize oxidation.

In the fluid bed dryer, dry hydrogen chloride gas heated up to about 450 °C allows fluidization of the particles, producing magnesium chloride granules. The reason for this is to avoid three negative characteristics of the magnesium hydrolysis reaction:

1. It creates magnesium oxide, which will later be concentrated as sludge in the electrolysis cells and will react with the graphite anodes and negatively affect the energy efficiency of the process.
2. Magnesium chloride is lost during the process.

3.   The acid gases produced during the reaction must be handled.

The use of gaseous HCl reduces the hydrolysis reactions, thus reducing the concentration of magnesium oxide in the product. In addition, opposite reactions to hydrolysis take place with HCl, which also reduce the magnesium oxide.

$$MgO + HCl\,(g) \rightarrow MgOHCl \qquad (1)$$

$$MgOHCl + HCl\,(g) \rightarrow MgCl_2(s) + H_2O\,(g) \qquad (2)$$
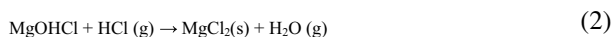
The HCl from the drying process is transferred to the raw material extraction and preparation process by passing through equipment used for the scrubbing of gaseous emissions. The resulting fluidizing gas contains hydrochloric acid which can be regenerated and brought back to the leaching step.

Electrolysis

Magnesium metal is then obtained by further electrolysis of the magnesium chloride. The magnesium chloride is fed to monopolarelectrolysis cells. The electrolyte composition allows the magnesium metal produced to form a light phase floating on top of the electrolysis bath. The anode can be a high surface area anode, such as, for example, a porous anode in which case hydrogen gas permeates the pores of the anode, such as by diffusion, or molten electrolyte containing the magnesium chloride permeates the pores of the anode, to provide the contact between the hydrogen gas and the chloride ions. This novel design of the electrolytic anode allows the injection of hydrogen in the bath to have an in situ HCl regeneration.

Environmental Benefits

AMI'S technology is a clean technology. It is the most environmental efficient process on the planet measured by the following aspects:

– Mining site remediation.
– Lowest Mg CO_2 emissions.
– Lowest Mg waste/slag generation.
– Lowest Mg energy consumption.

Based on the entire life cycle, each ton of magnesium produced by AMI permits the saving of 20 tons of CO_2 emission, compared with the current average Pidgeon process operated in China.

For each ton of magnesium produced by AMI, only 2.5 tons of CO_2 are emitted compared to traditional Pidgeon plants which produce 21.8 tons of GHS. Also, with AMI over 90% of the residue are converted into valuable product for an equivalent of 0.4 ton/ton of magnesium. (16 tons in Pidgeon plant.)

AMI's plant and the FOURNIER PROCESS are powered by at least 90% renewable hydroelectricity.

Picture of magnesium ingots

Effect of Pre-sintering in Silicothermic Reduction of MgO and Reduction Using Ca$_2$SiO$_4$ Instead of CaO

Takeru Saimura, Taiki Morishige, and Toshihide Takenaka

Abstract It was shown in our previous study that the contact condition between MgO, CaO, and Si strongly affected Mg metal production by silicothermic reduction of magnesium oxide derived from salt evaporation ponds. In this study, the influence of the contact condition of MgO, CaO, and Si in the reduction was studied; the dependence of the reduction rate on the preparation procedure of MgO–CaO mixture and pre-sintering before the reduction was examined. A short-term sintering improved the reduction rate, but a longer sintering worsened the rate. Sintering seems effective in the improvement of contact condition, but causes the surface oxidation on Si. In this study, Si reduction with Ca$_2$SiO$_4$ instead of CaO was also attempted to reduce CaO consumption, but it was shown that MgO was lost by CaMgSiO$_4$ formation.

Keywords Silicothermic reduction · Calcium silicate · Effect of pre-sintering

Introduction

The reduction in energy consumption and CO$_2$ generation in the production of Mg primary metal is necessary to wider use of Mg materials. Our laboratory has been researching the Mg material production using bittern-derived materials; the energy and CO$_2$ generation in Mg production can be reduced compared with the current Mg production using dolomite, and the bittern can be supplied from sea water in Japan, too.

In our previous studies, it is shown that the silicothermic reduction of MgO derived from bittern was possible, and that CaO addition was necessary [1]. The reduction rate was slightly lower than that of dolomite-derived material, even when enough CaO was added to MgO. The difference between the mixtures derived from bittern and

---

T. Saimura (✉)
Graduate School of Science and Engineering, Kansai University Suita, Osaka 564-8680, Japan
e-mail: k975313@kansai-u.ac.jp

T. Morishige · T. Takenaka
Department of Chemistry and Material Engineering, Kansai University Suita, Osaka 564-8680, Japan

dolomite can explain their mixed state; MgO and CaO were mixed at the molecular level in dolomite-derived material, while they were not in bittern-derived material. These results suggest that the preparation procedure of the MgO–CaO–Si mixture could affect the reduction rate because CaO is rarely contained in MgO derived from bittern. The minimum amount of CaO–MgO for efficient reduction must be clarified to reduce the added amount of CaO.

In this study, the mixture of MgO and CaO was prepared with two procedures; one is dry and involves calcination of $Mg(OH)_2$ and $Ca(OH)_2$ solution, and the other is dry mixing of MgO and CaO in a mortar. The influence of the procedures was evaluated by the change in the reduction rate. The effect of pre-sintering of the MgO–CaO–Si mixture was also studied. In addition, the reduction of the MgO–Ca_2SiO_4–Si mixture instead of the MgO–CaO–Si mixture was investigated to clarify the minimum amount of added CaO in this study.

Experimental

A MgO–CaO mixture was prepared with two procedures; in the wet procedure, $Mg(OH)_2$ and $Ca(OH)_2$ were dissolved in water, and then dried. The dried mixture was calcinated at 1073 K for 3 h to decompose into MgO and CaO. In the dry procedure, MgO and CaO were carefully mixed in a mortar. The prepared MgO–CaO mixture was compacted with Si and pre-sintered at 1073 K for hours. The molar ratio of MgO:CaO:Si was 2:2:1. In this study, a mixture of MgO–Ca_2SiO_4–Si (2:1:1 in molar) was also prepared by dry procedure without pre-sintering. These samples were set on a boron nitride (BN) boat, and heat reduced under vacuum at 1423 K for 3 h with the apparatus shown in Fig. 1.

After the reduction, the product condensed on the inner surface of vessel outside the furnace and the residual material on the BN boat was recovered. The product and residual material were observed and analyzed with SEM-EDX and XRD.
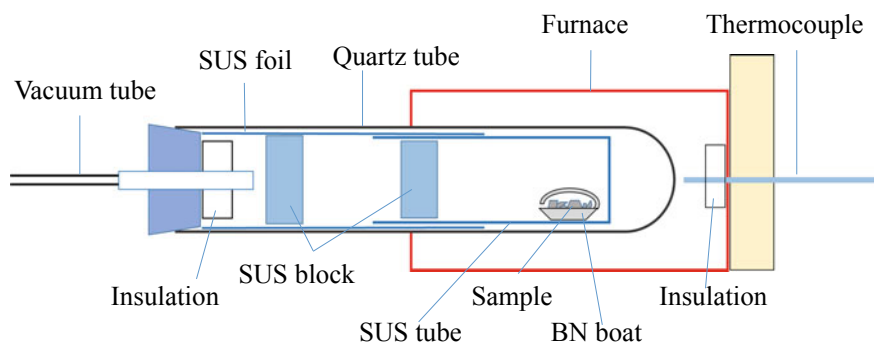
Fig. 1 Experimental apparatus. (Color figure online)

Results and Discussion

Effect of Preparation Procedure of MgO–CaO and Pre-sintering of MgO–CaO–Si

Fine particles mainly consisting of MgO were condensed on the inner surface of vessel outside the furnace regardless of the preparation procedure and pre-sintering. Since the amount of condensed material was very little, XRD analysis and weight measurement could not be performed. It is considered that Mg vapor was formed in the furnace, condensed in the low temperature part, and then oxidized when it was collected after experiment.

The weight of the residual material on the BN boat was always lower than that of the original mixture, and Ca_2SiO_4 was always detected in it. Considering the condensed and the residual materials, it is considered that the silicothermic reduction of Mg shown below occurred, and that Mg vapor and Ca_2SiO_4 were generated.

$$2MgO(s) + 2CaO(s) + Si(s) = 2Mg(g) + Ca_2SiO_4(s) \qquad (1)$$
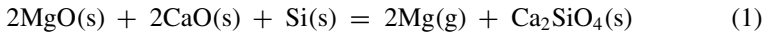
From the reaction (1), the weight change from the original sample to the residual material is thought to be the amount of Mg vapor, and the reduction rate can be calculated as follows:

$$\text{Reduction rate}(\%) = \frac{\Delta m}{m} \times 100 \qquad (2)$$

where m is the Mg content in the original specimen and Δm is the weight change.

Figure 2 shows the dependence of the reduction rate on the pre-sintering time for the sample prepared with wet and dry procedures. The reduction rate of the wet-prepared mixture tended to be higher than that of the dry-prepared mixture. This

Fig. 2 Effect of sintering time on reduction rate
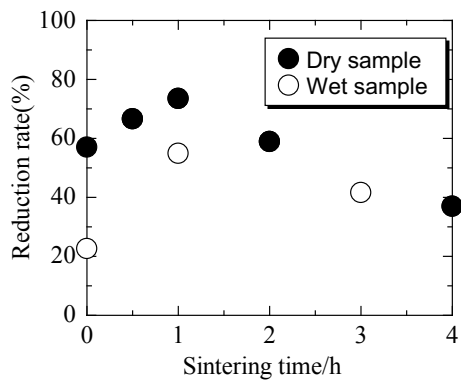
Fig. 3 X-ray diffraction
pattern after reduction of
MgO-Ca_2SiO_4-Si
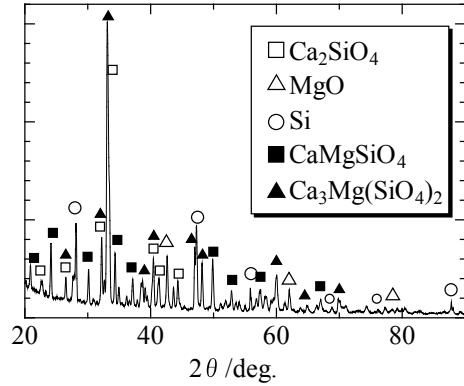
result suggests that the mixing procedure strongly influences the reduction efficiency, and that CaO should be added in bittern solution.

The reduction rate tends to increase with the short-term pre-sintering, but decrease with the long-term pre-sintering. It is considered that the contact state of MgO–CaO–Si is improved by the short-term pre-sintering, and that the surface of Si is oxidized by the long-term pre-sintering. The short-term pre-sintering should be effective for efficient silicothermic reduction of MgO derived from bittern.

Reduction Using Ca₂SiO₄ Instead of CaO

Figure 3 shows the XRD results of the residual material on a BN boat after the reduction of MgO–Ca₂SiO₄–Si mixture. Since CaMgSiO₄ and Ca₃Mg(SiO₄)₂ were detected, it is thought that the reactions occurred as follows:

$$4MgO(s) + Ca_2SiO_4(s) + Si(s) = 2Mg(g) + 2CaMgSiO_4(s) \qquad (3)$$

$$4MgO(s) + 3Ca_2SiO_4(s) + Si(s) = 2Mg(g) + 2Ca_3Mg(SiO_4)_2(s) \qquad (4)$$
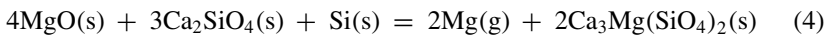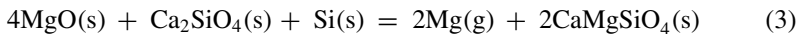
The reduction rate calculated by the formula (2) was about 30%. This value was a half of that using MgO–CaO–Si mixture, and consistent with the reaction (3).

By the reactions (3) and (4), the added amount of CaO can be reduced. However, MgO is unfortunately lost due to the formation of CaMgSiO₄ and Ca₃Mg(SiO₄)₂. The most desirable reaction for the least CaO addition as follows seems to be rarely achieved.

$$2MgO(s) + Ca_2SiO_4(s) + 2Si(s) = 2Mg(g) + 2CaSiO_3(s) \qquad (5)$$
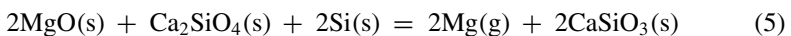
In the reduction of the MgO–CaO–Si mixture, only Ca2SiO4 was formed, and $CaMgSiO_4$ and $Ca_3Mg(SiO_4)_2$ seem not to be synthesized. From the reaction of Gibbs energy of production, γ-Ca_2SiO_4 is stable, and that the reactions (3) and (4) are more likely to occur in β-Ca_2SiO_4. In the reduction of the MgO–CaO–Si mixture under our experimental conditions, γ-Ca_2SiO_4 is thought to be synthesized. The structure of the mineral merwinite $Ca_3Mg(SiO_4)_2$ that seems to be mainly produced is similar to the β-Ca_2SiO_4 [2].

Ca_2SiO_4 used in this experiment was prepared by compaction sintering CaO and SiO_2 at 1673 K, and it is stable in the form of β-Ca_2SiO_4. However, the Ca_2SiO_4 produced by reaction (1) was γ-Ca_2SiO_4 and took the form of olivine. Since the change to β-Ca_2SiO_4 occurs under high pressure [3], it is considered to be γ-type under experimental conditions.

Conclusions

In this study, the dependence of the reduction rate on the preparation procedure of the MgO–CaO mixture and pre-sintering before the reduction was examined. The reduction rate of the wet-prepared mixture tends to be better than that on the dry-prepared mixture, which is thought due to the mixing state of MgO and CaO. The short-term pre-sintering is effective for efficient reduction because of the improvement of the contact condition. Conversely, the long-term pre-sintering worsened the reduction rate because of the surface oxidation of Si.

By the reduction using Ca_2SiO_4 instead of CaO, $CaMgSiO_4$ and $Ca_3Mg(SiO_4)_2$ were generated, which leads to the decrease in the added amount of CaO but the loss of MgO.

References

1. Ura J (2018) Kansai University, Faculty of Chemistry and Biotechnology, Department of Chemical and Material Engineering, Graduation Research
2. Moore PB, Araki T (1973) Atomic arrangement of merwinite, $Ca_3Mg[SiO^+]_2$, an unusual dense-packed structure of geophysical interest. Am Mineral 57:1355
3. Katsura T, ito E (1989) The system Mg_2SiO_4–Fe_2SiO_4 at high pressures and temperatures: Precise determination of stabilities of olivine, modified spinel, and spinel. J Geophys Res 94(B11):15663–15670

Oxide Films Formed on MoSi$_2$ Anode in Molten MgCl$_2$–NaCl–CaCl$_2$ and Molten LiCl–KCl

Takamasa Miyoshi, Taiki Morishige, and Toshihide Takenaka

Abstract The anodic formation of an oxide film on MoSi$_2$ in molten MgCl$_2$–NaCl–CaCl$_2$ containing oxide ions has been investigated based on our former study, and the compatibility as an inert anode in the melt is discussed in contradistinction in molten LiCl–KCl. A small anodic current flew continuously during potentio-static electrolysis, and gas bubble generation was seen. The weight of MoSi$_2$ was changed by the electrolysis, and an oxide film consisting of SiO$_2$ and MgSiO$_3$ was formed by the electrolysis above 1.9 V (vs. Mg/Mg^{2+}). The current contributions estimated from the weight change and the film thickness indicate that the reaction other than the Mo dissolution and the oxide film formation enlarged with the increase in the electrolysis duration and the raise in the electrolysis potential. The current contribution other than the Mo dissolution and the oxide film formation became above 90%, which suggests MoSi$_2$ is promising as an inert anode. A SiO$_2$ film was formed on MoSi$_2$ in molten LiCl–KCl containing oxide ions, but most of the current was consumed for the Mo dissolution and the oxide film formation. It is considered that the formation of MgSiO$_3$ influences the anodic behavior of MoSi$_2$.

Keywords Mg electrolysis · MoSi$_2$ anode · Oxide film

Introduction

Mg is produced by an electrolytic method using a molten chloride salt. The IG method and its improved method are the main methods for electrolyzing Mg. The electrolysis method has the advantages of being easy to scale up, being able to be made into a continuous manufacturing process, and being able to use MgO as a raw material with the generated Cl$_2$. Li is also produced by electrolysis like Mg. The production process of Mg and Li has been studied in order to be more efficient [1–3]. One of them is related to the anodic reaction.

Carbon-based materials are used for the anode in the molten chloride of Mg and Li. Carbon-based material has advantages in chemical stability in the bath.

T. Miyoshi · T. Morishige · T. Takenaka (✉)
Takatsuki, Japan
e-mail: ttakenak@kansai-u.ac.jp

However, since chloride salt has a high hygroscopic property, carbon-based material is consumed by electrochemical reaction with dissolved O^{2-}, for example, reaction (1).

$$C + xO^{2-} \rightarrow CO_x + 2xe \tag{1}$$
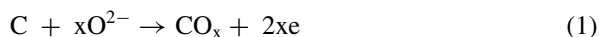
An inert anode is desired for the continuous formation of Mg, and it has been reported that glassy carbon [4] and boron-doped diamond [5] behaved as an inert anode in molten LiCl–KCl at 700 K. However, an inert anode which can be used at higher current density and at higher temperature has not been studied well. The authors proposed an inert anode by forming a stable passivation film on the electrode. A SiO_2 film was formed in molten LiCl–KCl containing oxide ions, but the anodic protection was insufficient [6, 7]. An oxide film consisting of SiO_2 and $MgSiO_3$ was formed in molten $MgCl_2$–NaCl–$CaCl_2$ containing oxide ions, and the anodic oxidation seemed to be inhabited.

In this paper, the anodic behaviors of $MoSi_2$ in molten $MgCl_2$–NaCl–$CaCl_2$ were compared with that in molten LiCl–KCl, and the protection property and the effect of $MgSiO_3$ were discussed.

Experimental

The experimental apparatus is illustrated in Fig. 1. In a glove box filled with Ar, about 50 g of $MgCl_2$–NaCl–$CaCl_2$ (about 20: 50: 30 in weight) was put in a transparent quartz glass crucible, and the saturation amount of MgO (99.9%, anhydrous) was added. The mixture was placed in an electric furnace with observation ports.

Fig. 1 Apparatus for electrochemical measurement and electrolysis. (Color figure online)

a. working electrode
b. reference electrode
c. Ar inlet
d. thermocouple
e. counter electrode
f. electrolysis device
g. electrolytic bath
h. observation window
i. Ar outlet
j. core tube
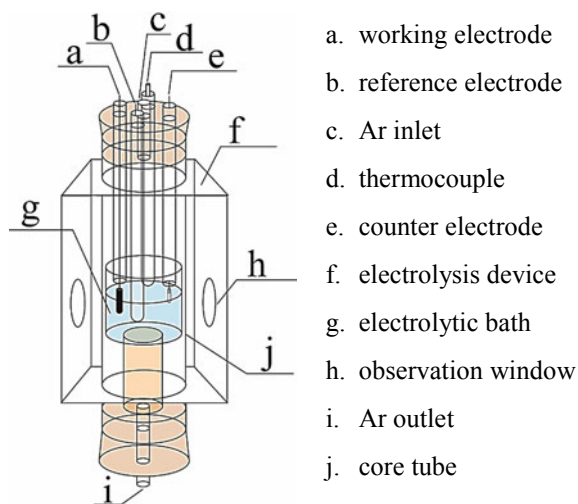
The furnace was heated about 973 K, and electrolysis was carried out under Ar atmosphere. Polished MoSi$_2$ rod (ϕ3.0 mm) was used as the working electrode. The counterelectrode was a Cu plate with a large surface area. A couple of Ag/AgCl in the same melt in a ceramic membrane was used as the reference electrode. Since the electrode potential of the Ag/AgCl reference electrode changes easily with the concentration of AgCl, its potential was calibrated via the Mg deposition potential.

The anodic behavior of MoSi$_2$ was investigated by cyclic voltammetry and potentio-static electrolysis. The appearance around the MoSi$_2$ electrode during electrolysis was simultaneously observed with a CCD camera, and recorded by a video system. The electrochemical response was synchronized and superimposed to the recorded view. The change in the MoSi$_2$ surface by electrolysis was analyzed by XRD (RINT 2500V) and SEM(JCM-6000)-EDX(Ex-5441). The protective property was discussed by the current contributions which were estimated from the weight change, the thickness of the formed film after the potentio-static electrolysis, and the quantity of electricity during electrolysis.

The experiment in molten LiCl–KCl is almost the same above; 44.4 g of LiCl–KCl having a eutectic composition was used, and about 0.2 g of Li$_2$O (99.9%) was added. The working and reference electrode are the same, while counterelectrode was an Al plate with a large surface area. All the experiments were carried out at 700 K.

Results and Discussion

Formation of Oxide Film on MoSi$_2$

Anodic passivation occurred both in molten MgCl$_2$–NaCl–CaCl$_2$ and molten LiCl–KCl containing oxide ions; a sharp anodic current peak was seen around 1.8 V (vs. Mg/Mg^{2+}) in cyclic voltammogram in molten MgCl$_2$–NaCl–CaCl$_2$, and around 3.4 V (vs. Li/Li$^+$) in that in molten LiCl–KCl.

By potentio-static electrolysis above the passivation potentials mentioned above, an oxide film was formed on MoSi$_2$ both in molten MgCl$_2$–NaCl–CaCl$_2$ and molten LiCl–KCl. Figure 2 shows a cross-sectional SEM image of the MoSi$_2$ electrode after potentio-static for 4 h in molten MgCl$_2$–NaCl–CaCl$_2$ at 4.7 V (vs. Mg/Mg^{2+}) and molten LiCl–KCl at 4.2 V (vs. Li/Li$^+$). The film formed in molten MgCl$_2$–NaCl–CaCl$_2$ is much thinner than the film formed in molten LiCl–KCl; the thickness of the film is about 3 μm in the former, while that is 125 μm in the latter. The growth of the oxide film in molten LiCl–KCl seems much higher than that in molten MgCl$_2$–NaCl–CaCl$_2$.

Figure 3 shows X-ray diffraction pattern of the MoSi$_2$ electrodes after potentio-static electrolysis for 4 h in molten MgCl$_2$–NaCl–CaCl$_2$ at 4.7 V (vs. Mg/Mg^{2+}) and molten LiCl–KCl at 4.2 V (vs. Li/Li$^+$). SiO$_2$ and Mo$_5$Si$_3$ were detected in both baths, so the following reactions were thought to take place on the surface of the anode electrode.
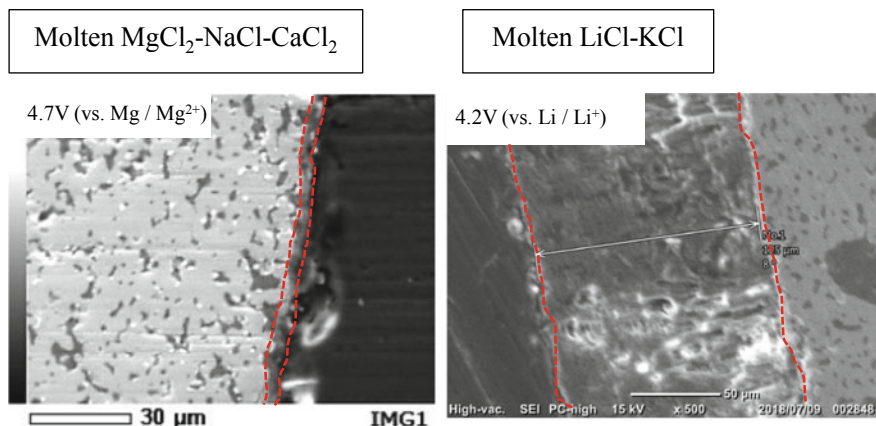
Fig. 2 Cross-sectional SEM image of the $MoSi_2$ electrode after potentio-static electrolysis for 4 h with molten $MgCl_2$–$NaCl$–$CaCl_2$ and molten $LiCl$–KCl. (Color figure online)
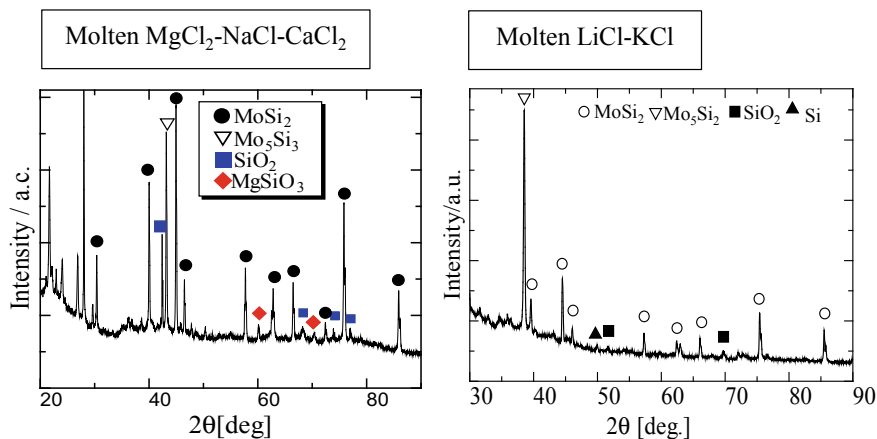
Fig. 3 X-ray diffraction pattern of electrode after potentio-static electrolysis for 4 h. (Color figure online)

$$MoSi_2 + 4O^{2-} \rightarrow Mo^{3+} + 2SiO_2 + 11e \tag{2}$$

$$5MoSi_2 + 14O^{2-} \rightarrow Mo_5Si_3 + 7SiO_2 + 28e^- \tag{3}$$
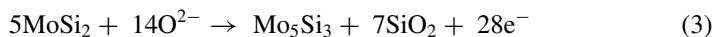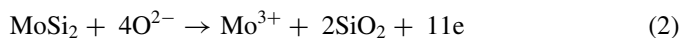
$MgSiO_3$ was detected only in molten $MgCl_2$–$NaCl$–$CaCl_2$, so reactions (4) and (5) were thought to take place on the surface of the anode electrode

$$SiO_2 + MgO \rightarrow MgSiO_3 \tag{4}$$

$$2Mg^{2+} + 6O^{2-} + MoSi_2 \rightarrow Mo^{3+} + 2MgSiO_3 + 11e \tag{5}$$
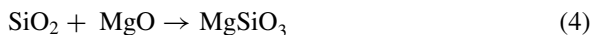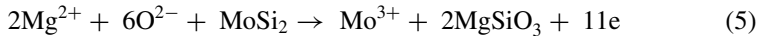
in molten $MgCl_2$–$NaCl$–$CaCl_2$ and molten $LiCl$–KCl.

Current Contribution to Anodic Reactions

A small current continuously flew during constant potential electrolysis in molten $MgCl_2$–$NaCl$–$CaCl_2$ and molten $LiCl$–KCl. The weight of $MoSi_2$ changed by electrolysis, and the formed oxide film grew with electrolysis duration.

$$n_{\text{oxide}} = \frac{V_{\text{layer}} \rho_{\text{oxide}}}{M_{\text{oxide}}} \tag{6}$$

The current contribution was calculated from the weight change of the $MoSi_2$ and thickness of the oxide layer referring to our previous study [8]; reactions (2) and (4) were considered in the calculation. It was also assumed that only an $MgSiO_3$ film was formed in molten $MgCl_2$–$NaCl$–$CaCl_2$, while only an SiO_2 was in molten $LiCl$–KCl. The current contribution of the oxide film formation P_{oxide} is given as (7) using the amounts of the formed oxide film layer, n_{oxide} (mol) as (6)

$$P_{\text{oxide}} = \frac{4 n_{\text{oxide}} F}{Q} \times 100 \tag{7}$$

where M_{oxide}, V_{oxide}, and ρ_{oxide} are the atomic weight of $MgSiO_3$ or SiO_2 (kg/mol), the film volume (cm³), and the density of oxide film (kg/cm³); Q is the quantity of electricity during potentio-static electrolysis (C); and F is Faraday constant (C/mol).

$$n_{\text{Mo}} = \frac{\Delta w - n_{\text{oxide}} M_{\text{oxide}}}{M_{\text{Mo}}} \tag{8}$$

The amounts of the dissolved Mo: n_{Mo}(mol) and the current contribution of Mo dissolution P_{Mo} are given as follows:

$$P_{Mo} = \frac{3 n_{Mo} F}{Q} \times 100 \tag{9}$$

where M_o and Δw are the atomic weight of Mo (kg/mol) and the weight change by electrolysis. The electrolysis current seemed to be spent partly other than the oxide film formation and Mo dissolution in molten $MgCl_2$–$NaCl$–$CaCl_2$, and its contribution P_{other} is given as follows:

$$P_{\text{other}} = 100 - P_{\text{oxide}} - P_{\text{Mo}} \tag{10}$$
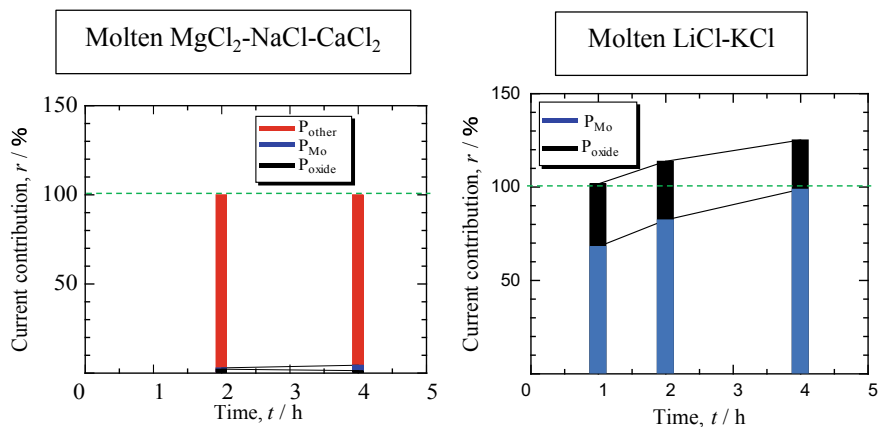
Fig. 4 Current contribution for reactions in molten $MgCl_2$–NaCl–$CaCl_2$ and molten LiCl–LCl. (Color figure online)

Figure 4 shows estimated contributions for electrolysis at 4.7 V (vs. Mg/Mg^{2+}) in molten $MgCl_2$–NaCl–$CaCl_2$ and for electrolysis at 4.2 V (vs. Li/Li^+) in molten LiCl–KCl. P_{oxide} and P_{Mo} in molten $MgCl_2$–NaCl–$CaCl_2$ were very small, whereas most of the current seemed to be consumed to the oxide film formation and Mo dissolution in molten LiCl–KCl.

The current contribution other than the oxide film formation and Mo-dissolved, P_{other} in the molten $MgCl_2$–NaCl–$CaCl_2$ was more than 90%. Since bubbles were continuously generated during electrolysis, it is thought that the electrolysis current was mainly consumed for the gas generation. These results indicated that the oxidation of $MoSi_2$ was inhibited by the oxide film formation in molten $MgCl_2$–NaCl–$CaCl_2$. The oxide film obtained in molten $MgCl_2$–NaCl–$CaCl_2$ seemed thinner and denser than that in molten LiCl–KCl as shown in Fig. 2, and $MgSiO_3$ was contained in it. It is considered that the film consisting of $MgSiO_3$ shows good protectability.

Conclusion

An oxide film consisting of $MgSiO_3$ and SiO_2 was formed by electrolysis in molten $MgCl_2$–NaCl–$CaCl_2$, and it was thinner than the SiO_2 film formed in the molten LiCl–KCl. The current contributions of oxide film formation and Mo dissolution were estimated from the film thickness and weight change; the current contributions other than the oxide film formation and Mo dissolution reached more than 90% under the suitable condition in molten $MgCl_2$–NaCl–$CaCl_2$, while most of the current was consumed in the oxide film formation and Mo dissolution in molten LiCl–KCl. It is considered that the $MgSiO_3$ formation in molten $MgCl_2$–NaCl–$CaCl_2$ strongly affects the anodic behavior of $MoSi_2$.

References

1. The Japan Institute of Metals and Materials (1999) Metal smelting engineering, Maruzen Co., Ltd.
2. Komatu R (1968) Light Metals 18(2):114–123
3. Kobayashi M (1984) J Min Metall Inst Jpn 1152:115–123
4. Paek S, Kim S-H, Yoon D, Kim T-J, Ahn D-H, Lee H (2013) J Radioanal Nucl Chem 295:439–444
5. Park W, Kim J-K, Hur J-M, Choi E-Y, Suk lm H, Hong S-S (2013) J Nucl Mater 432:175–181
6. Takenaka T, Umehara M, Araki D, Morishige T (2012) ECS Trans 50(11):127
7. Takahashi Y, Morishige T, Takenaka T (2016) ECS Trans 75(15):207
8. Miyoshi T, Morishige T, Takenaka T (2020) ECS Trans 9(10):253–260

Part II
Alloy Development

Development of an Mg–RE-Based Die-Cast Magnesium Alloy for Elevated Applications

Xixi Dong, Lingyun Feng, Eric A. Nyberg, and Shouxun Ji

Abstract The development of magnesium (Mg) alloys capable of operating at demanding working temperatures above 200 °C and the ability of using high-pressure die casting for high-volume manufacturing are the most critical advancements required in developing new alloys used to manufacture critical parts for internal combustion (IC) engines used in power tools. Here we introduce the development of a rare earth (RE)-based die-cast Mg alloy for elevated temperature applications in small IC engines. The developed Mg–RE-based die-cast alloy shows good ambient and high temperature strength, and it also has excellent high-temperature creep resistance. In addition, the developed RE-based die-cast Mg alloy shows good stiffness at elevated temperatures. Furthermore, the alloy exhibits good thermal conductivity at ambient and high temperatures, which is a key point normally neglected during the development of high-temperature Mg alloys.

Keywords Magnesium alloy · Die casting · Elevated application · Mechanical properties

Introduction

Magnesium alloys have a great potential for structural applications in industry due to their significant weight savings, thus improving fuel economy and lessening environmental impact [1]. The development of magnesium (Mg) alloys capable of operating at demanding working temperatures above 200 °C and the ability of using high-pressure die casting (HPDC) for high-volume manufacturing are two key advancements required in the development of Mg alloys for use in manufacturing critical

X. Dong · L. Feng · S. Ji (✉)
Brunel Centre for Advanced Solidification Technology (BCAST), Brunel University London, Uxbridge UB8 3PH, UK
e-mail: shouxun.ji@brunel.ac.uk

E. A. Nyberg
Tungsten Parts Wyoming, Laramie, WY 82072, USA

parts for internal combustion (IC) engines used in power tools, for lightweighting, noise reduction, damping, and use comfort [2–4].

In the early stage of development of die-cast Mg alloys for high-temperature applications, significant amount of Al was used for the improvement of die casta-bility, and a group of Mg–Al-based die-cast alloys were developed [5, 6]. Repre-sentative alloys are the widely used AZ91, AM50, and AM60 alloys; the Mg–Al–Si alloys (AS21X, AS31, AS41) [7, 8]; the Mg–Al–Ca alloy (AX51, AX52) [9]; the Mg–Al–Sr alloy (AJ52); the Noranda alloy Mg–6Al–2Sr–Ca (AJ62X) [10–12]; the Mg–Sr–Ca alloy (AJX500) [5]; the General Motors alloy Mg–Al–Ca–Sr (AX52J, AXJ530, AXJ531) [13, 14]; the Mg–9Al–1Ca–Sr alloy (MRI153A); the Mg–8Al–1Ca–Sr alloy (MRI153M) [15, 16]; the Mg–6.5Al–2Ca–1Sn–Sr alloy (MRI230D) [17–19]; the Nissan alloy Mg–Al–Ca–RE [20]; the Honda alloy Mg–5Al–2Ca–2RE (ACM522) [21]; the Mg–0.5Zn–6Al–1Ca–3RE alloy (ZACE05613); the Mg–0.5Zn–4Al–1Ca–1RE alloy (ZACE05411) [22]; the Mg–4Al–RE (La, Ce) alloys (AE42, AE44) [23–25]; the Mg–Al–Ba–Ca alloy [26]; etc. The Mg–4Al–4RE (AE44) alloy is a major achievement among the Mg–Al-based die-cast alloys with good combina-tion of die castability, mechanical properties at elevated temperatures, and good corrosion resistance [25, 27]. However, a common detriment for these alloys is that the general working temperature of the Mg–Al-based die-cast alloys is at a level of approximately 150 °C, due to the formation of the Al-rich phases that are unstable when temperatures are close to or higher than 175 °C [5, 28, 29], and the high-temperature creep resistance of the Mg–Al-based die-cast alloys is also not perfect [30].

In addition to the Mg–Al-based die-cast alloys, Al-free die-cast Mg alloys were developed for applications at elevated temperatures [30–34]. The Al-free die-cast Mg–2.5RE–0.35Zn alloy (MEZ) was developed with good creep resistance, but the ductility and strength of the alloy are low [31]. The Al-free die-cast Mg–RE–Zr–Zn alloys were well investigated with medium as-cast strength [32, 33]. The Al-free die-cast Mg–4 wt%RE (La,Ce,Nd) alloy named HP2+ delivers higher mechanical performance especially creep resistance at elevated temperatures, which is a signifi-cant achievement for potential applications at 150–200 °C [30, 34]. However, 4wt% RE is near the maximum of Al-free die-cast Mg–RE alloys, and further addition of RE for higher working temperatures and elevated mechanical performance will make the Al-free die-cast Mg–RE alloys too brittle, with hot-tearing or die-soldering occurring during die casting [34]. Therefore, it is still hard for the existing Al-free die-cast Mg alloys to work at elevated temperatures of above 200 °C.

In this work, different from the existing die-cast Mg alloys using Al-rich or Al-free, a new design for elevated die-cast Mg alloys was adopted, in which an appropriate addition of Al as a minor element was applied, and a new Mg–RE–Al die-cast alloy was developed for applications at higher elevated temperatures of 200–300 °C.

Experimental

Melt Preparation and HPDC

The newly designed die-cast Mg alloys have compositions in the range of 1.0–3.5 wt% (La + Ce), 1.0–3.5 wt% (Nd + Gd), 0.2–2.5 wt%Al, 0.3–0.5wt%Mn, 0.3–0.5wt%Zn, and balanced Mg [35]. They alloys were melted in a steel crucible using an electric resistance furnace, under a protective cover gas. After melting, the alloy was stirred and held at 720 °C for 30 min before HPDC. HPDC was conducted on a 4500 kN cold chamber machine. During HPDC, the die was heated by mineral oil to a temperature of 225 °C, and the shot sleeve was heated by compressed hot water to a temperature of 180 °C. The pour temperature was controlled at 715 °C, and the intensification pressure was set at 320 bar.

Material Tests

Tensile tests of the die-cast round bars with a gage dimension of ϕ6.35 mm $\times$ 50 mm were performed on an Instron 5500 Universal Electromechanical Testing System equipped with Bluehill software and a 50 kN load cell, at room temperature and elevated temperatures of 150, 250, and 300 °C. The ramp rate for room temperature tensile tests was controlled at 1 mm/min, while the strain rate for high-temperature tensile tests was maintained at 0.0002/s. Young's modulus of the die-cast alloys was determined using a RFDA HT1600 machine from room temperature up to 300 °C. Rectangular-shaped samples with dimensions of 40 mm (L) $\times$ 12 mm (W) $\times$ 2 mm (D) were used for the modulus testing. Modulus was tested during both heating and cooling cycles, in which both the heating rate and the cooling rate were set at 3 °C/min, while the modulus data was collected every minute. Thermal conductivity was measured on a laser flash machine from room temperature up to 300 °C.

Results and Discussion

Microstructure

Figure 1 shows the scanning electron microscope (SEM) microstructure of the die-cast Mg–RE–Al alloy in the as-cast state. The Mg matrix phase was observed having two different grain sizes, i.e., the primary α_1–Mg phase with a size of ~20–50 μm and the secondary α_2–Mg phase with a size of ~2–10 μm. The α_1–Mg phase nucleated in the shot sleeve which has a lower cooling rate, so it was larger in size than the α_2–Mg phase that nucleated in the die cavity with higher cooling rate [36–39]. Network of

Fig. 1 Microstructure of the die-cast Mg–RE–Al alloy in as-cast state. (Color figure online)
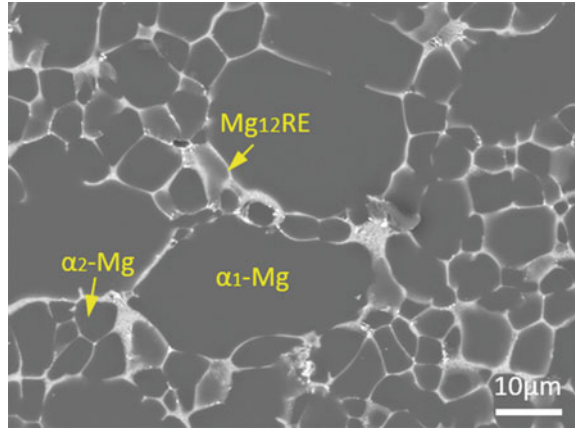
the other phases was found at the grain boundaries of Mg matrix phase, and the main body of the network at the grain boundaries was determined as the $Mg_{12}RE$ phase.

Ambient and Elevated Tensile Properties

Figure 2 displays the statistical mean tensile properties of the die-cast Mg–RE–Al alloy at room temperature and elevated temperatures of 150, 250, and 300 °C. The statistical mean yield strength (YS) of the alloy at room temperature was 170 ± 2.8 MPa, which was 32% higher than that of the benchmark AE44 die-cast Mg alloy [4, 34].

The YS and ultimate tensile strength (UTS) of the alloy decreased gradually with the increase of temperature. The YS of the alloy at 150, 250, and 300 °C were 141 ± 2.5 MPa, 113 ± 2.1 MPa, and 94 ± 1.8 MPa, respectively, which was 30.5%, 37.8%, and 42.4% higher than that of the AE44 alloy, separately [4]. With the increase of the temperature from room temperature to 300 °C, the UTS of the alloy decreased from 197 ± 2.8 to 98 ± 1.7 MPa. The die-cast Mg–RE–Al alloy also showed much

Fig. 2 Statistical mean tensile properties of the die-cast Mg–RE–Al alloy at room temperature and elevated temperatures of 150, 250, and 300 °C. (Color figure online)

better elevated creep resistance than the existing die-cast Mg alloys, and the creep properties will be disclosed elsewhere.

Ambient and Elevated Modulus

High temperature stiffness is important but is seldom reported for die-cast Mg alloys, especially at elevated temperatures above 200 °C. Figure 3 shows the evolution of Young's modulus of the die-cast Mg–RE–Al alloy versus temperature. The measured Young's modulus during heating and cooling test cycles fit well with each other. The room temperature Young's modulus of the alloy was 43.7 GPa, and it was in the normal range of 40–50 GPa ambient Young's modulus that is generally expected for cast Mg alloys [40, 41]. Young's modulus of the alloy decreases nearly linearly with the increase of temperature, and Young's moduli of the alloy at elevated temperatures of 150 °C, 200 °C, 250 °C, and 300 °C were 41.2 GPa, 40.2 GPa, 39.2 GPa, and 38.2 GPa, respectively. With the increase of temperature from room temperature to 300 °C, Young's modulus decreased only 12.6%, which demonstrates good stability of Young's modulus of the alloy at elevated temperatures.

Ambient and Elevated Thermal Conductivity

Thermal conductivity is another key aspect usually neglected during the development of Mg alloys for elevated applications, and mechanical properties normally conflict with thermal conductivity at elevated temperatures. AZ91, a die-cast Mg alloy widely used for elevated engineering applications up to 120 °C, has a low room temperature thermal conductivity of 51 W/m K [42], and the benchmark AE44 die-cast Mg alloy for elevated applications up to 175 °C only has an ambient thermal conductivity

Fig. 4 Thermal conductivity of the die-cast Mg–RE–Al alloy at room temperature and elevated temperatures of up to 300 °C. (Color figure online)
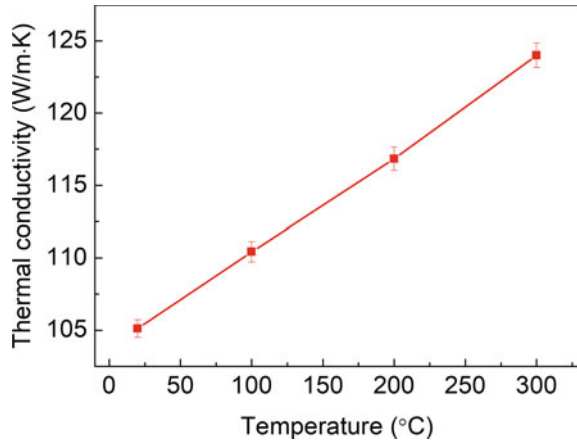
of 85 W/m K [42]. Figure 4 presents the thermal conductivity of the new die-cast Mg–RE–Al alloy at room temperature and elevated temperatures. The Mg–RE–Al alloy has good room temperature thermal conductivity of 105 W/m K, which is 105.9% higher than that of the AZ91 alloy, and it is still 23.5% higher than that of the AE44 alloy. The room temperature thermal conductivity of the alloy is also comparable to the commercially used A380 die-cast Al alloy that has an ambient thermal conductivity of 110 W/m K [42]. The thermal conductivity of the die-cast Mg–RE–Al alloy increases with increasing temperature, up to 124 W/m K at 300 °C.

Conclusions

(1) The developed Mg–RE-based die-cast alloy has good strength at ambient and elevated temperatures. The ambient yield strength of the alloy is 170 MPa, and the alloy can achieve a yield strength of over 90 MPa at the elevated temperature of 300 °C.

(2) The developed Mg–RE-based die-cast alloy can maintain the stiffness well at elevated temperatures. The ambient Young's modulus of the alloy is 43.7 GPa. With the increase of temperature from room temperature to the elevated temperature of 300 °C, Young's modulus of the alloy decreases only by 12.6%.

(3) The developed Mg–RE-based die-cast alloy has good thermal conductivity at ambient and elevated temperatures. The room temperature thermal conductivity of the alloy is 105 W/m K. With the increase of temperature from room temperature to the elevated temperature of 300 °C, the thermal conductivity of the alloy increases to 124 W/m K.

References

1. Luo AA (2013) Magnesium casting technology for structural applications. J Magnes Alloys 1:2–22
2. Hort N, Dieringa H, Kainer KU (2018) Magnesium pistons in engines: fiction or fact? In: Orlov D, Joshi V, Solanki KN, Neelameggham N (eds) Magnesium technology 2018. The minerals, metals & materials society, pp 349–353
3. Dong XX, Nyberg EA, Ji S (2020) A die-cast magnesium alloy for applications at elevated temperatures. In: Jordon B, Miller V, Joshi V, Neelameggham N (eds) Magnesium technology 2020. The minerals, metals & materials society, pp 31–36
4. Dong XX, Feng LY, Wang SH, Nyberg EA, Ji S (2020) A new die-cast magnesium alloy for applications at higher elevated temperatures of 200–300 °C. J Magnes Alloys. https://doi.org/10.1016/j.jma.2020.09.012
5. Pekguleryuz MO, Kaya AA (2003) Creep resistant magnesium alloys for powertrain applications. Adv Eng Mater 5:866–878
6. Hu H, Yu A, Li NY, Allison JE (2003) Potential magnesium alloys for high temperature die cast automotive applications: a review. Mater Manuf Process 18:687–717
7. Hillis JE, Shook SO (1989) Composition and performance of an improved magnesium AS41 alloy. SAE Tech Pap 890205
8. Evangelista E, Gariboldi E, Lohne O, Spigarelli S (2004) High-temperature behaviour of as die-cast and heat treated Mg–Al–Si AS21X magnesium alloy. Mater Sci Eng A 387–389:41–45
9. Luo AA, Balogh MP, Powell BR (2002) Creep and microstructure of magnesium-aluminum-calcium based alloys. Metall Mater Trans A 33A:567–574
10. Pekguleryuz MO, Baril E (2001) Development of creep resistant Mg–Al–Sr alloys. In: Hryn JN (ed) Magnesium technology 2001. The minerals, metals & materials society, pp 119–125
11. Lefebvre M, Pekguleryuz M, Labelle P (2002) Magnesium-based casting alloys having improved elevated temperature performance. US patent 6342180
12. Baril E, Labelle P, Pekguleryuz M (2003) Elevated temperature Mg-Al-Sr: creep resistance, mechanical properties, and microstructure. JOM 55:34–39
13. Powell BR, Rezhets V, Luo AA, Bommarito JJ, Tiwari BL (2001) Creep resistant magnesium alloy die casting. US patent 6264763
14. Powell BR, Luo AA, Rezhets V, Bommarito JJ, Tiwari BL (2001) Development of creep-resistant magnesium alloys for powertrain applications: part 1 of 2. SAE Tech Pap 2001-01-0422
15. Bronfin B, Aghion E, Von Buch F, Schumann S, Katsir M (2001) Die casting magnesium alloys for elevated temperature applications. In: Hryn JN (ed) Magnesium technology 2001. The minerals, metals & materials society, pp 127–130
16. Aghion E, Moscovitch N, Arnon A (2007) Solidification characteristics of newly developed die cast magnesium alloy MRI153M. Mater Sci Technol 23:270–275
17. Aghion E, Bronfin B, Von Buch F, Schumann S, Friedrich H (2003) Dead sea magnesium alloys newly developed for high temperature applications. In: Kaplan HI (ed) Magnesium technology 2003. The minerals, metals & materials society, pp 177–182
18. Aghion E, Bronfin B, Von Buch F, Schumann S, Friedrich H (2003) Newly developed magnesium alloys for powertrain applications. JOM 55:30–33
19. Aghion E, Moscovitch N, Arnon A (2009) Mechanical properties of die-cast magnesium alloy MRI 230D. J Mater Eng Perform 18:912–916
20. Samato K, Yamamoto Y, Sakate N, Hirabara S (1997) Heat-resistant magnesium alloy member. European patent EP0799901A1
21. Koike S, Washizu K, Tanaka S, Baba T, Kikawa K (2000) Development of lightweight oil pans made of a heat-resistant magnesium alloy for hybrid engines. SAE Techn Pap 2000-01-1117
22. Anyanwu IA, Gokan Y, Nozawa S, Suzuki A, Kamado S, Kojima Y, Takeda S, Ishida T (2003) Development of new die-castable Mg–Zn–Al–Ca–RE alloys for high temperature applications. Mater Trans 44:562–570

23. Powell BR, Rezhets V, Balogh MP, Waldo RA (2001) The relationship between microstructure and creep behavior in AE42 magnesium die castings. In: Hryn JN (ed) Magnesium technology 2001. The minerals, metals & materials society, pp 175–182

24. Dargusch MS, Pettersen K, Bakke P, Nogita K, Bowles AL, Dunlop GL (2004) Microstructure and mechanical properties of high pressure die cast magnesium alloy AE42 with 1% strontium. Int J Cast Metal Res 17:170–173

25. Bakke P, Westengen H (2005) The role of rare earth elements in structure and property control of magnesium die casting alloys. In: Neelameggham N, Kaplan HI, Powell BR (eds) Magnesium technology 2005. The minerals, metals & materials society, pp 291–296

26. Gavras S, Zhu SM, Easton MA, Gibson MA, Dieringa H (2019) Compressive creep behavior of high-pressure die-cast aluminum-containing magnesium alloys developed for elevated temperature applications. Front Mater 6:262

27. Zhu SM, Nie JF, Gibson MA, Easton MA, Bakke P (2012) Microstructure and creep behavior of high-pressure die-cast magnesium alloy AE44. Metall Mater Trans A 43A:4137–4144

28. Mordike B (2001) Development of highly creep resistant magnesium alloys. J Mater Process Technol 117:391–394

29. Kiełbus A (2007) Microstructure of AE44 magnesium alloy before and after hot-chamber die casting. J Achiev Mater Manuf Eng 20:459–462

30. Zhu SM, Easton MA, Abbott TB, Nie JF, Dargusch MS, Hort N, Gibson MA (2015) Evaluation of magnesium die-casting alloys for elevated temperature applications: microstructure, tensile properties, and creep resistance. Metall Mater Trans A 46:3543–3554

31. Moreno IP, Nandy TK, Jones JW, Allison JE, Pollock TM (2002) Microstructure and creep behavior of a die cast magnesium-rare earth alloy. In: Kaplan HI (ed) Magnesium technology 2002. The minerals, metals & materials society, pp 111–116

32. Atiya G, Bamberger M, Katsman A (2011) Microstructure, phase evolution and precipitation strengthening of Mg-3.1Nd-0.45Zr-0.25Zn alloy. In: Sillekens WH, Agnew SR, Neelameggham NR, Mathaudhu SN (eds) Magnesium technology 2011. The minerals, metals & materials society, pp 249–253

33. Atiya G, Bamberger M, Katsman A (2012) Microstructure and phase composition in a die cast Mg–Nd alloy containing Zn and Zr. Int J Mater Res 103:1277–1280

34. Easton M, Gibson MA, Zhu, Abbott T, Nie JF, Bettles CJ, Savage G (2018) Development of magnesium-rare earth die-casting alloys. In: Orlov D, Joshi V, Solanki KN, Neelameggham N (eds) Magnesium technology 2018. The minerals, metals & materials society, pp 329–336

35. Dong XX, Nyberg EN, Almgren M, Ji SX (2019) Swedish patent. Application No. 1950219-4

36. Dong XX, Youssef H, Zhang YJ, Yang HL, Wang SH, Ji SX (2019) High performance Al/TiB$_2$ composites fabricated by nanoparticle reinforcement and cutting-edge super vacuum assisted die casting process. Compos Part B-Eng 177

37. Dong XX, Youssef H, Zhang YJ, Yang HL, Wang SH, Ji SX (2020) Advanced heat treated die-cast aluminium composites fabricated by TiB$_2$ nanoparticle implantation. Mater Des 186:

38. Dong XX, Youssef H, Zhu XZ, Zhang YJ, Wang SH, Ji SX (2021) High as-cast strength die-cast AlSi$_9$Cu$_2$Mg alloy prepared by nanoparticle strengthening with industrially acceptable ductility. J Alloys Compd 852

39. Liu LH, Zhang T, Liu ZY, Yu CY, Dong XX, He LJ, Gao K, Zhu XG, Li WH, Wang CY, Li PJ, Zhang LC, Li LG (2018) Near-net forming complex shaped Zr-based bulk metallic glasses by high pressure die casting. Materials 11:2338

40. Sumitomo T, Cáceres CH, Veidt M (2002) The elastic modulus of cast Mg–Al–Zn alloys. J Light Met 2:49–56

41. Xu YL, Wang L, Huang M, Gensch F, Kainer KU, Hort N (2018) The effect of solid solute and precipitate phase on Young's modulus of binary Mg–RE alloys. Adv Eng Mater 20:1800271

42. https://www.leadingedgeonly.com/innovation/view/high-conductivity-mg-alloy

Effect of Adding Third Element on Deformability of Mg–Al Alloy

Kazuki Senoo, Tatsuya Nakatsuji, Naoko Ikeo, Masatake Yamaguchi, and Toshiji Mukai

Abstract In recent years, magnesium is expected to be used as a structural material in vehicles. Since limited slip systems in magnesium induces marked yield anisotropy and poor deformability at room temperature, there is a specific demand for developing magnesium alloys with reduced plastic anisotropy. In this study, we focused on the Mg–Al system alloy, which is widely used in commerce, and examined the third element contributing to the reduction of the plastic anisotropy. Generalized stacking fault energy (GSFE), which corresponds to the energy for sliding atomic layer along a slip plane, was calculated in the first-principles calculations to estimate deformability of ternary Mg–Al-X alloys adding the third element X, to the Mg–Al binary alloy. As the third element X, Zn, Zr, and Gd were selected. The slip properties were evaluated using the unstable stacking fault energy (USFE), which represents the maximum value of GSFE. The result suggested that the addition of zirconium contributes most to the reduction of plastic anisotropy.

Keywords First-principles calculations · Generalized stacking fault energy · Slip systems · Plastic anisotropy · Mg–Al alloy

Introduction

Social demands for energy saving have been increasing. It is expected that the use of magnesium, which is the lightest of all practical metals, as a structural material of transportation equipment will contribute to further improvement of fuel efficiency [1–3]. However, since the crystal structure of magnesium is a hexagonal close-packed structure (HCP), the number of slip systems active at room temperature are small, and it exhibits high plastic anisotropy [4]. Thus, in plastic deformation not only slips but

K. Senoo · T. Nakatsuji · N. Ikeo · T. Mukai (✉)
Graduate School of Engineering Faculty of Engineering, Kobe University, 1-1 Rokkodai-Cho, Nada, Kobe, Hyogo 657-8501, Japan
e-mail: mukai@mech.kobe-u.ac.jp

M. Yamaguchi
Japan Atomic Energy Agency, 765-1 Funaishikawa, Tokai-Mura, Naka-Gun, Ibaraki 319-1184, Japan

also $\{10\bar{1}2\}$ twins with small critical resolved shear stress (CRSS), play a major role. However, twins also cause strong anisotropy, and their activity differs depending on the deformation mode. Due to these properties, it has a feature of lower formability than steel and aluminum alloys. Hence, the application of the current magnesium alloys to structural components in transportation equipment is limited. To increase the practical use of magnesium alloys, it is necessary to reduce the difference in CRSS between basal slip and non-basal slip and enhance ductility by reducing plastic anisotropy. Recent experiments and calculations have shown that the activation of prismatic slips, among non-basal slips, contributes to the ductility improvement of magnesium [5]. Therefore, in order to improve the plastic deformability of magnesium, it is considered important to reduce the relative difference between CRSS for basal slip and prismatic slip. The addition of solute elements can be mentioned as a measure for improving such plastic anisotropy [6, 7]. This study focused on the Mg–Al system alloy, which is widely used in commerce to investigate the effect of the third element X on plastic anisotropy using first-principles calculations. As the third element X, Zn, Zr, and Gd were selected.

Calculation Method

First-Principles Calculation

In this study, the calculation was performed using the Vienna ab initio Simulation Package (VASP) [8, 9], a first-principles calculation package using plane waves and pseudopotential grounds developed by the density functional theory at the University of Vienna. Calculations are performed using Pewdew-Burke-Ernzerhof (PBE) type Projector Augmented Wave (PAW) potential [10] for pseudopotential and Generalized Gradient Approximation (GGA) [11] for exchange-correlation interaction. The cutoff energy was 360 eV, and the 0.2 eV wide Methfessel-Paxton Smearing method was used to improve convergence. In addition, structural relaxation was discontinued when the difference in total energy for each iteration was 1.0×10^{-5} eV or less. The Brillouin zone was sampled with a Monkhorst-Pack k-point mesh. The value of the k-point mesh for each calculation model is described in Sect. 2.3.

Generalized Stacking Fault Energy

The generalized stacking fault energy (GSFE) was used to evaluate the plastic anisotropy. GSFE corresponds to the energy for sliding atomic layer along a slip plane [12]. The value of GSFE represents the energy barrier against slip deformation, or the Peierls potential. It makes possible to evaluate the difficulty of dislocation slip
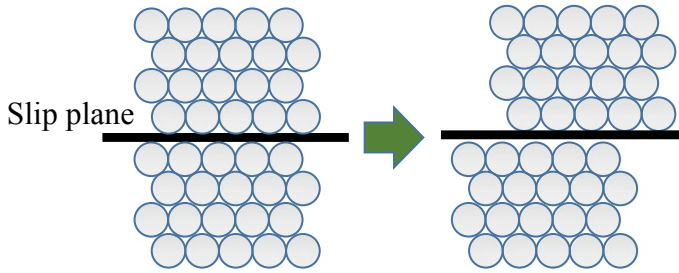
Fig. 1 Schematic image of the cell model used for GSFE calculation. (Color figure online)

and the relative critically resolved shear stress (CRSS). Figure 1 shows a schematic image of the cell model used for GSFE calculation.

A model was created in which the upper and lower layers adjacent to the slip surface were relatively slipped, and the calculation of GSFE was performed. As expressed by Eq. (1), the difference between the total energy of the slipped model E_{tot}(displaced) and the total energy of the non-slip model E_{tot}(undisplaced) is divided by the area of the slip plane $A_{slip\ plane}$. Then, the GSFE value γ_{GSF} was obtained.

$$\gamma_{GSF} = \frac{E_{tot}(\text{displaced}) - E_{tot}(\text{undisplaced})}{A_{slip\ plane}} \# \tag{1}$$

In this study, the CRSS of each slip was relatively evaluated using unstable stacking fault energy (USFE, γ_{us}), which indicates the maximum value of GSFE. In addition, the USFE ratio was calculated to evaluate the slip-plastic anisotropy of the basal slip and the prismatic slip. The USFE ratio refers to the value obtained by dividing USFE of the basal slip γ_{us}(basal) by USFE of the prismatic slip γ_{us}(prism),

$$USFEratio = \frac{\gamma_{us}(\text{basal})}{\gamma_{us}(\text{prism})} \# \tag{2}$$

The closer the USFE ratio is to 1, the smaller the relative difference between CRSS for basal slip and prismatic slip, which means that the deformation is relatively isotropic. On the contrary, the further the USFE ratio is from 1, the higher the plastic anisotropy is.

The Calculation Conditions and Models

A basal slip model with 117 atoms and a prismatic model with 144 atoms were used as each calculation model. The calculation models and calculation conditions of GSFE for each slip are shown in Fig. 2 and Table 1, respectively. The two slip calculation models are supercells with a bulk layer (slab) with a thickness of about 30 Å. Vacuum layer of about 15 Å was introduced between each slab (above and below the bulk layer) so that interaction due to periodic boundary conditions would

(a) (b)
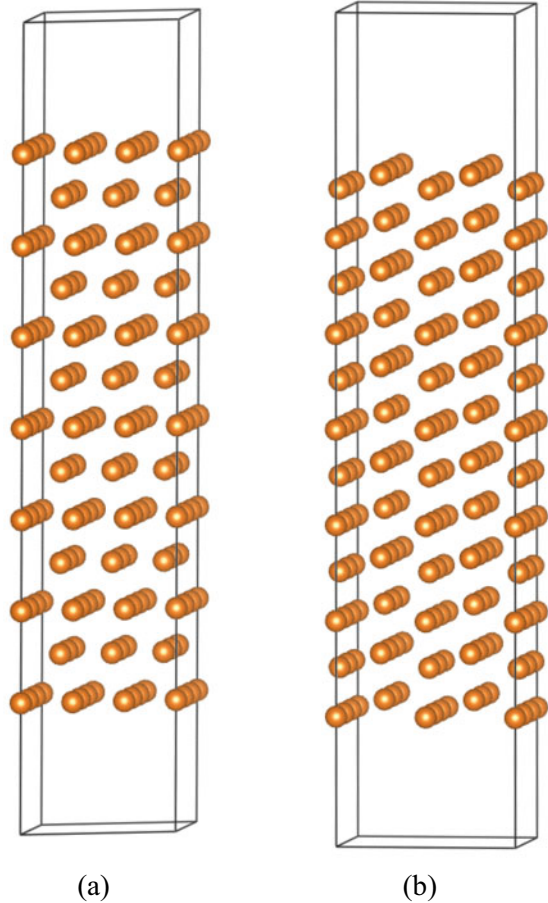
Table 1 The number of atoms and k-points mesh of GSFE on the basal and prismatic slips

Model	Number of atoms	K-point mesh
Basal	117	$5 \times 5 \times 1$
Prism	144	$4 \times 4 \times 1$

not occur. The kinds of alloys to be calculated were pure Mg, Mg–Al, and Mg–Al-X (X = Zn, Zr, Gd) alloys.

In Mg–Al-X alloys, two solute atoms are replaced simultaneously, so it is necessary to estimate the relationship of the atomic configuration due to the bonding force between the solute atoms. In this study, the binding energy $E_{\text{bind}}(\text{Al} - \text{X})$ between aluminum and third element X in Mg–Al-X alloy was calculated, and the most stable configuration of solute atoms was investigated. For the calculation of the binding energy $E_{\text{bind}}(\text{Al} - \text{X})$, a supercell with 54 atoms (Fig. 3), a magnesium unit

Fig. 3 Supercell for determining the most stable configuration in Mg–Al-X (X = Zn, Zr, Gd) alloys. The substitution position of aluminum is fixed, and the third element X is substituted at Site 1–10. (Color figure online)
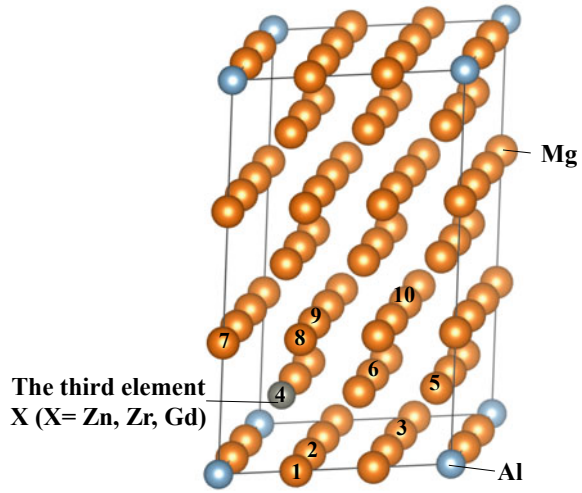
cell expanded to $3 \times 3 \times 3$, was used. As shown in Fig. 3, the substitution position of the aluminum atom was fixed, and one of the magnesium atoms of Site1-10 was substituted with the third element X. $E_{\text{bind}}(\text{Al} - \text{X})$ were calculated for each site, and the site with the largest negative value, or the most energetically stable site, was defined as the most stable configuration of aluminum and the third element X.

Results and Discussion

The Most Stable Configuration of Solute Atoms

The binding energy $E_{\text{bind}}(\text{Al} - \text{X})$ was calculated to determine the most stable configuration of solute atoms in each Mg alloy. As a result, it was found that Site 5 is the most energetically stable for Zr and Gd, and Site 4 is the most stable for Zn. Based on this most stable configuration, multiple alloy models in which solute atoms were substituted near the slip plane of each slip model were prepared. The value in the model with the smallest USFE in each alloy model, or the model in which slip is most likely to occur, is adopted as the result of the USFE in each alloy [13].

Deformability Evaluation Using USFE Ratio

To improve deformability, it is effective to reduce the CRSS difference between basal slip and prismatic slip and improve the plastic anisotropy. Figure 4 shows the USFE
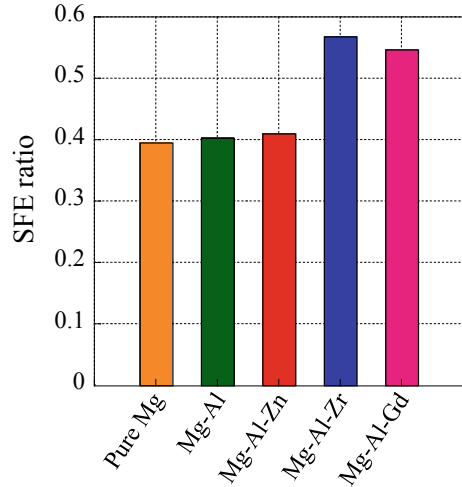
ratio results, which can relatively evaluate the difference in CRSS between basal slip and prismatic slip. The USFE ratio of Mg–Al was higher than that of pure Mg, which confirmed that the addition of Al contributed to the improvement of plastic anisotropy. When Zn was added as the third element, the USFE ratio remained almost unchanged, suggesting that the effect of Zn addition on plastic anisotropy was small. On the other hand, the ternary alloy which contains Zr and Gd as the third element has a significantly higher USFE ratio than Mg–Al. In particular, Zr has the potential as the most effective additive element for improving plastic anisotropy.

Factor for Promoting Prismatic Slip

In order to consider the activation factors of the prismatic slip, Fig. 5 shows a diagram in which the unstable stacking fault energy of the prismatic slip γ_{us}(prism) of the Mg–Al-X alloys are plotted against the atomic radius of the third element X. As the atomic radius of the third element X increases, γ_{us}(prism) decreases almost linearly. This result suggests that the atomic radius of the third element X is an important factor in activating prismatic slip in the Mg–Al-X alloys.

Summary

The purpose of this study was to elucidate the third element contributing to the improvement of plastic anisotropy of Mg–Al alloys using first-principles calculations. The plastic anisotropy was investigated from the ratio of USFE of basal slip

Fig. 5 Relationship between calculated γ_us (prism) of the Mg–Al–X (X = Zn, Zr, Gd) alloys and the atomic radius of the third element X. (Color figure online)
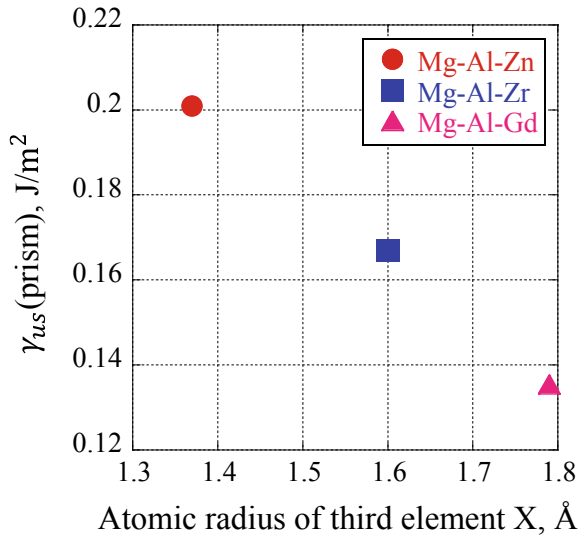
and prismatic slip. The result confirmed that the addition of zirconium reduced the relative difference in USFE between basal slip and prismatic slip, suggesting that zirconium is an effective additive element for improving plastic anisotropy. It was also confirmed that the prismatic slip tends to be activated as the atomic radius of the third element X increases.

References

1. Easton M, Beer A, Barnett M, Davies C, Dunlop G, Durandet Y, Blacket S, Hilditch T, Beggs P (2008) Magnesium alloy applications in automotive structures. JOM 60:57–62
2. Mukai T (2004) Materials technology for weight reduction—possibility of magnesium alloys—Mater. Jpn 43:810–814
3. Suzuki Y (2010) Weight reduction of railway vehicles by applying aluminum alloy and its future problems. J Jpn Inst Light Metals 60(11):565–570
4. Verma R, Hector LG, Krajewski PE, Taleff EM (2009) The finite element simulation of high-temperature magnesium AZ31 sheet forming. JOM 61(8):29–37
5. Chino Y, Ueda T, Otomatsu Y, Sassa K, Huang X, Suzuki K, Mabuchi M (2011) Effects of Ca on tensile properties and stretch formability at room temperature in Mg–Zn and Mg–Al Alloys. Mater Trans 52:1477–1482
6. Somekawa H, Yamaguchi M, Osawa Y, Singh A, Itakura M, Tsuru T, Mukai T (2015) Material design for magnesium alloys with high deformability. Philo Mag 95:869–885
7. Hase T, Ohtagaki T, Yamaguchi M, Ikeo N, Mukai T (2016) Effect of aluminum or zinc solute addition on enhancing impact fracture toughness in Mg–Ca alloys. Acta Mater 104:283–294

8. Kresse G, Hafner J (1993) Ab initio molecular dynamics for liquid metals. Phys Rev B 47:558–561

9. Kresse G, Furthmüller J (1996) Efficient iterative schemes for ab initio total-energy calculations using a plane-wave basis set. Phys Rev B 54:11169–11186

10. Kresse G, Joubert D (1999) From ultrasoft pseudopotentials to the projector augmented-wave method. Phys Rev B 59:1758–1775

11. Perdew JP, Wang Y (1992) Accurate and simple analytic representation of the electron-gas correlation energy. Phys Rev B 45:13244–13249

12. Vitek V (1968) Intrinsic stacking faults in body-centred cubic crystals. Philos Mag 18:773–786

13. Yuasa M, Hayashi M, Mabuchi M, Chino Y (2014) Improved plastic anisotropy of Mg–Zn–Ca alloys exhibiting high-stretch formability: a first-principles study. Acta Mater 65:207–214

Effect of LPSO Phases on Crack Propagation in an Extruded Mg–Dy–Nd–Zn–Zr Alloy Influenced by Heat Treatment

Petra Maier, Benjamin Clausius, Asta Richter, Benjamin Bittner, Norbert Hort, and Roman Menze

Abstract The effect of LPSO phases on the crack propagation in different microstructures modified by heat treatment is investigated. Solution heat treatment on a hot-extruded Mg–Dy–Nd–Zn–Zr alloy (RESOLOY) is done to change the initial fine-grained microstructure, consisting of lamellar LPSO structures within the matrix, into coarser grains of less lamellae but blocky LPSO phases. C-Ring compression tests were done with the focus on crack initiation and propagation. The blocky LPSO phases clearly hinder crack growth, either by increasing the energy to pass through the phases or along its interface. LPSO phases are found to be responsible for crack initiation: by the interface or the softer Mg-matrix in between LPSO lamellae. The softer Mg-matrix layer is providing the possibility for slip band cracking. In the coarser-grained microstructure, the crack propagation is also influenced by twins. The microstructural features were characterized by micro and nanohardness, as well as the amount and location of LPSO phases, in dependence on the heat treatment condition. Blocky LPSO phases show a higher hardness than the grains with or without lamellar LPSO phases— more specific by nanoindentation.

Keywords Magnesium · Microstructure · Crack propagation · Nanoindentation · LPSO phases

P. Maier (✉) · B. Clausius
University of Applied Science Stralsund, Stralsund, Germany
e-mail: petra.maier@hochschule-stralsund.de

A. Richter
Technical University of Applied Sciences Wildau, Wildau, Germany

B. Bittner · R. Menze
MeKo Laserstrahl-Materialbearbeitungen e.K, Stralsund, Germany

N. Hort
Helmholtz-Zentrum Geesthacht, Geesthacht, Germany

Introduction

Considering their pronounced mechanical properties and acceptable corrosion performance, Mg-rare earth (Mg–RE) alloys have attracted considerable attention as structural metals [1–3] as well as for biomedical applications [4–6]. As heavy RE elements of higher solubility, Gd and Dy strengthen Mg by solid solution and Nd, an element of low solubility, forms stable intermetallic phases at the grain boundary [7–9]. Research by Yang et al. [10] shows that the binary Mg–Dy alloy exhibits the best combination of mechanical and corrosion properties at 10 wt.% Dy. Zn is a common alloying element to improve the mechanical properties and in combination with RE, it weakens and modifies the basal texture to obtain excellent properties [11]. Kawamura et al. [12] and Nie et al. [13] reported the long period stacking ordered (LPSO) phases in Mg–Zn–Y and in Mg–RE–Zn alloys (RE = Y, Gd, Tb, Dy, Ho, Er, Tm), which provide high strength, moderate ductility, improved fracture toughness, and good corrosion resistance.

Mg–Dy–Nd and Mg–Dy–Nd–Zn–Zr have been already studied in Refs. [14, 15]. Twins form when the Mg–Dy–Nd alloy is plastically deformed and the crack initiation and growth are mainly influenced by the twin boundaries. Mg–Dy–Nd–Zn–Zr shows a heterogeneous microstructure of grains fully consisting of lamellar LPSO structures within the matrix, blocky LPSO phase, and grains of wider lamellar LPSO structures within the matrix. Solution heat treatment causes grain growth and hardness reduction. The influence of heat treatment on the nanohardness has been studied on Mg-Gd-Nd, where the precipitates exhibit the highest nanohardness [16].

Experimental

The Mg–Dy–Nd–Zn–Zr alloy (Resoloy) was cast at the Helmholtz-Zentrum in Geesthacht, Germany, and indirectly hot-extruded in tubes at the Extrusion Research and Development Center TU Berlin. The detailed process parameter can be found in Ref. [15]. The outer diameter of the as-extruded tubes was 35 mm, and the wall thickness was 5 mm. The chemical compositions of Dy and Zn were analyzed by using X-Ray micro fluorescence M4 Tornado and Nd and Zr by using a spark optical emission spectroscopy Spectrolab M12 Hybrid. Short annealing was performed at 200 °C for 4 h, acting as a stress relief, and solution heat treatment was done at 500 °C for 24, 48, and 72 h. C-Ring samples were compressed with 2 mm/min in a testing machine up to fracture in Ringer solution. The study on Mg–Dy–Nd [14] provides detailed information on the C-Ring compression test in Ringer and the study in Ref. [17] presents data from the force–displacement curves, like force and displacement at crack initiation and its fracture toughness. An optical micrographic investigation was done to characterize microstructural features, like the location, shape, and amount of the LPSO phases. Cross-sectional micrographs of the fractured C-Rings were used to evaluate the influence of the microstructural features like twins and LPSO
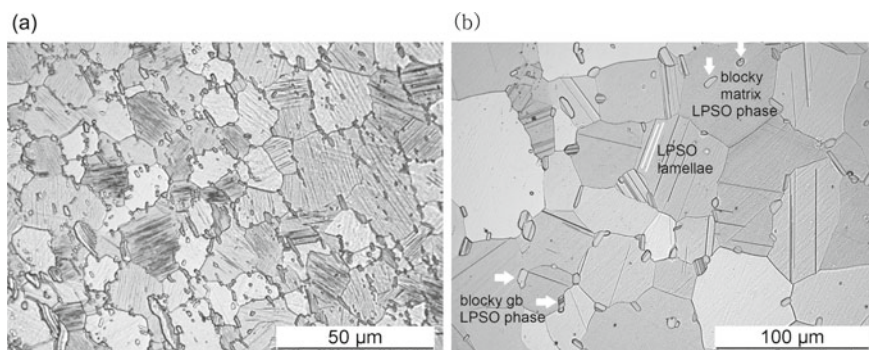
Fig. 1 Optical micrographs of Resoloy in **a** as-extruded and **b** solution heat-treated condition at 500 °C for 48 h

phases, either as lamellar matrix structures or as blocky matrix- or grain boundary phases on the crack propagation (see labeling in Fig. 1b). Microhardness by Vickers (HV0.01) was used to determine the hardness of the specific features and Nanoindentation measurements were performed using the electrostatic transducer of a UBI 1 Hysitron triboscope with a diamond 90° cube corner tip. Detailed methodology is described in Refs. [16, 18]. Two different nanoindentation modes were applied: force controlled single cycles up to a maximum force of 1 mN and progressive multi-cycles in force control applying 12 consecutive loading–unloading cycles with a load being increased to 2 mN.

Results and Discussion

The Mg–Dy–Nd–Zn–Zr alloy (Resoloy) consists of 12.63 wt.% Dy, 1.05 wt.% Nd, 0.94 wt.% Zn and 0.075 wt.% Zr. Figure 1 shows representative examples of the fine-grained microstructure (as-extruded in Fig. 1a) and the coarse-grained microstructure (solution heat-treated condition at 500 °C for 48 h in Fig. 1b). According to Ref. [15] the grain size increases during solution heat treatment at 500 °C from below 10 μm in the as-extruded condition to around 50 μm in the heat-treated condition.

According to the optical micrographic investigation (Fig. 1) the number of LPSO phases decreases with increasing solution heat treatment time from 24 to 72 h. The blocky LPSO phases appear mostly irregular polygon-like shaped, globular and rod-shaped, and they have random orientation. This agrees with studies by Kittner et al. [19] and Dong et al. [20]. The network-like LPSO phases forming along the grain boundaries in the as-extruded condition separate during solution heat treatment. Depending on the "cut" through the blocky LPSO phases, as well as on the dissolution stage, they make the long period stacking derivatives of the Mg-phase and the Zn/RE distributions visible, like described in Ref. [21]. The solution heat-treated condition contains more blocky LPSO phase at the grain boundary than within the grains.

During the C-Ring compression tests, see macroscopic crack growth in Ref. [17], the cracks initiate at the tensile side of the C-Ring, run through the neutral zone, and end in the compression side, which microstructure has meanwhile changed; there are an increased amount of twinned grains. These twin boundaries hinder the crack growth by redirecting it and this leads to higher fracture toughness. Because of the geometrical restriction within the C-Ring compression test (compression to 50%), the samples did not fail completely and besides the crack flanks, the tip could also be investigated. The crack flanks exhibit sub-cracks, either being connected with the main crack or being seen nearby (Fig. 2). The sub-cracks become very pronounced at solution heat treatment at 500 °C towards longer solution times. According to Ref. [17], the highest fracture toughness was found in the solution heat-treated condition at 500 °C for 48 h. The cross-sectional optical micrographs show further, that the sub-cracks mainly branch off via lamellar matrix LPSO structures (Fig. 2a, b, f), where the softer Mg-matrix layer has provided the possibility for slip band cracking [22, 23]. The study in Ref. [22] on Mg–Gd–Y–Zn–Zr shows enriched RE in the LPSO lamellae and a significant increase in Zn. Chemical analysis of the Mg–Dy–Nd–Zn–Zr was already reported in Ref. [15] and also shows increased RE and Zn in the LPSO region, even a higher amount in the matrix containing lamellar LPSO than that in the blocky LPSO phases.

Sub-cracks either start at grain boundaries, are redirected by grain boundaries or by blocky LPSO phases, but always follow the orientation of the lamellar matrix LPSO structure. Figure 2a, b show the crack-path in the as-extruded and heat-treated condition at 200 °C for 4 h, both revealing a fine-grained microstructure, where almost all the grains consisting of lamellar matrix LPSO structures. The grain boundaries acting as barriers for crack propagation, because the orientation of the LPSO lamellae differs in the neighboring grain. Is the disorientation far off a parallel orientation, in an extreme situation (90°), the crack tips blunt and the crack-path carries on by initiation a new sub-crack, see Fig. 2b. The interfaces between the Mg-matrix and the blocky LPSO phases seem also to be the path where the crack grows or the nucleation of new sub-cracks occurs. When there are coarser grains either free of disoriented lamellar matrix LPSO structures in relation to the propagating crack, or blocky LPSO phases in the way, the crack runs continuously across the grain towards the opposite grain boundary (Fig. 2c–f). In this case, the energy depends on the toughness of the grain itself, mainly influenced by its solid solution strengthening. However, more often LPSO lamellae, blocky LPSO phases, and twins hinder crack propagation and are the reason for redirection. Figure 2c (500 °C 24 h) shows crack redirection by inner grain and grain boundary LPSO phases, where either the crack tips blunt before propagating any further (also found in Ref. [24]), find their way through the softer Mg-matrix in between the LPSO lamellae, or propagates via the interface between the Mg-matrix and the blocky LPSO phases. Figure 3d (500 °C 48 h) shows clearly that a crack reaching the disoriented matrix LPSO lamellae, carries on by propagating within these lamellae. This image also shows interfaces between the Mg-matrix and the blocky LPSO phases acting as regions of crack propagation, which is in agreement with studies on Mg−Y−Zn [24]. Figure 2e (500 °C 48 h) shows, that a blocky LPSO phase, which orientation agrees to the crack growth direction, allows the crack to run
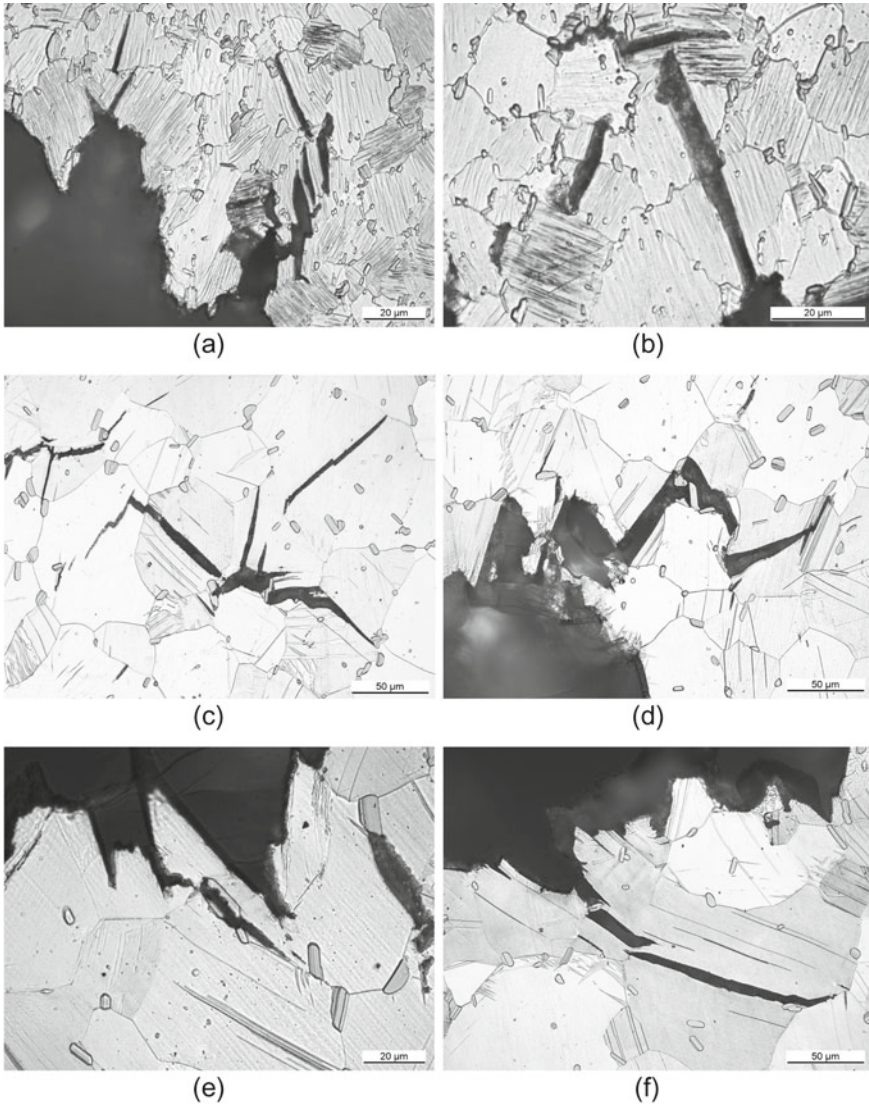
Fig. 2 Cross-sectional optical micrographs of the crack-path in **a** as-extruded, **b** heat-treated 200 °C for 4 h, **c** solution heat-treated 500 °C for 24 h, **d**, **e** solution heat-treated 500 °C for 48 h, and **f** solution heat-treated 500 °C for 72 h

through it, most likely at enhanced energy due to higher hardness and because of its different crystallographic structure. Solution heat treatment at 500 °C for 72 h leads to a reduced fracture toughness [17]. Figure 2f shows a crack-path through a grain without much interaction. Here, the grains have grown and the amount of blocky LPSO phases reached a low number. Even there will be an increased solid solution,
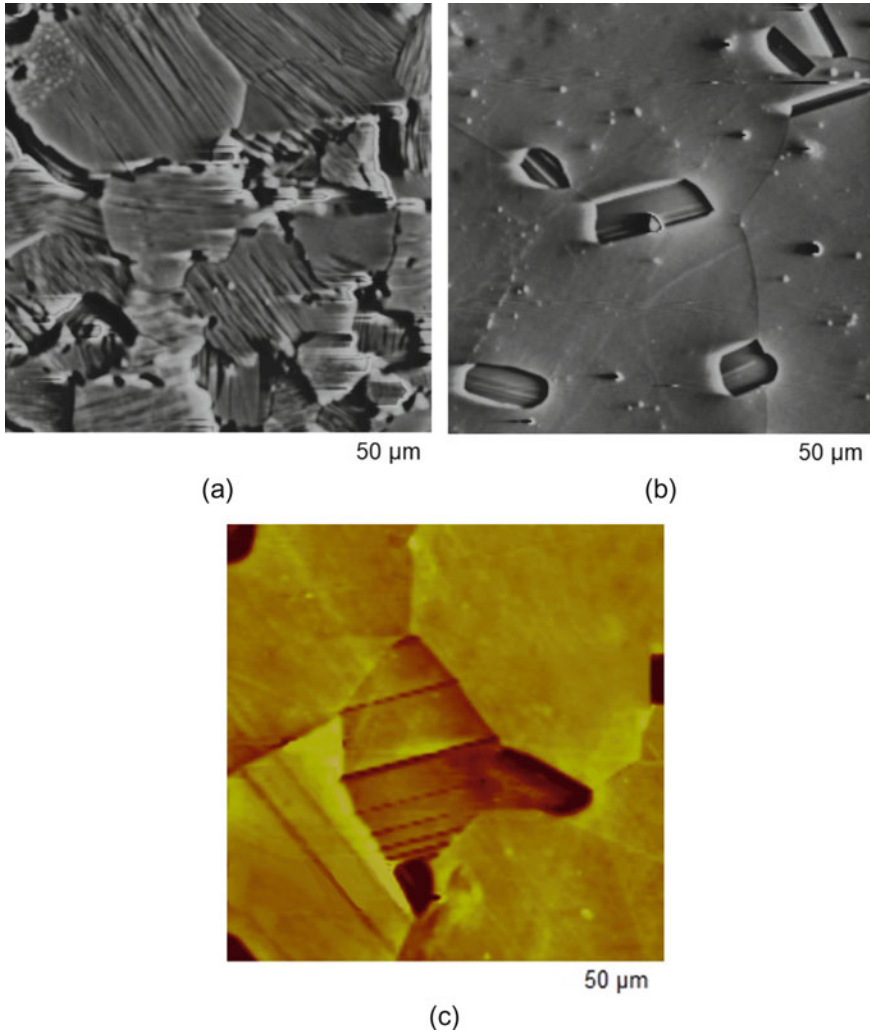
Fig. 3 Nanoindenter AFM image of Resoloy in **a** as-extruded, **b** solution heat-treated condition at 500 °C for 48 h, and **c** solution heat-treated condition at 500 °C for 72 h. (Color figure online)

a certain critical grain size should not be exceeded and blocky LPSO phases seem to be important for hindering crack growth and providing overall enhanced toughness.

Figure 3 shows AFM images of Resoloy in the as-extruded (Fig. 3a) and solution heat-treated condition at 500 °C for 48 h (Fig. 3b) and 72 h (Fig. 3c). The lamellar matrix LPSO structure can be easily seen in Fig. 3a. The network of the blocky LPSO phases at the grain boundaries is less visible. Figure 3b shows the coarser-grained microstructure after solution heat treatment at 500 °C for 24 h with some blocky LPSO phases at the grain boundary. Lamellar matrix LPSO structures cannot be

seen. Figure 3c (solution heat-treated condition at 500 °C for 72 h) shows a grain containing matrix LPSO lamellae of a wider distance. The grain is surrounded by two grain boundary blocky LPSO phases.

Figure 4 shows representative force–displacement curves of Resoloy in the solution heat-treated condition at 500 °C for 24 h of indents in Mg-matrix and blocky LPSO phases, as a single cycle at a force of 1 mN and as multi-cycles progressing the load up to 2 mN. Larger blocky LPSO phases have been indented up to 3 times

(a)

(b)
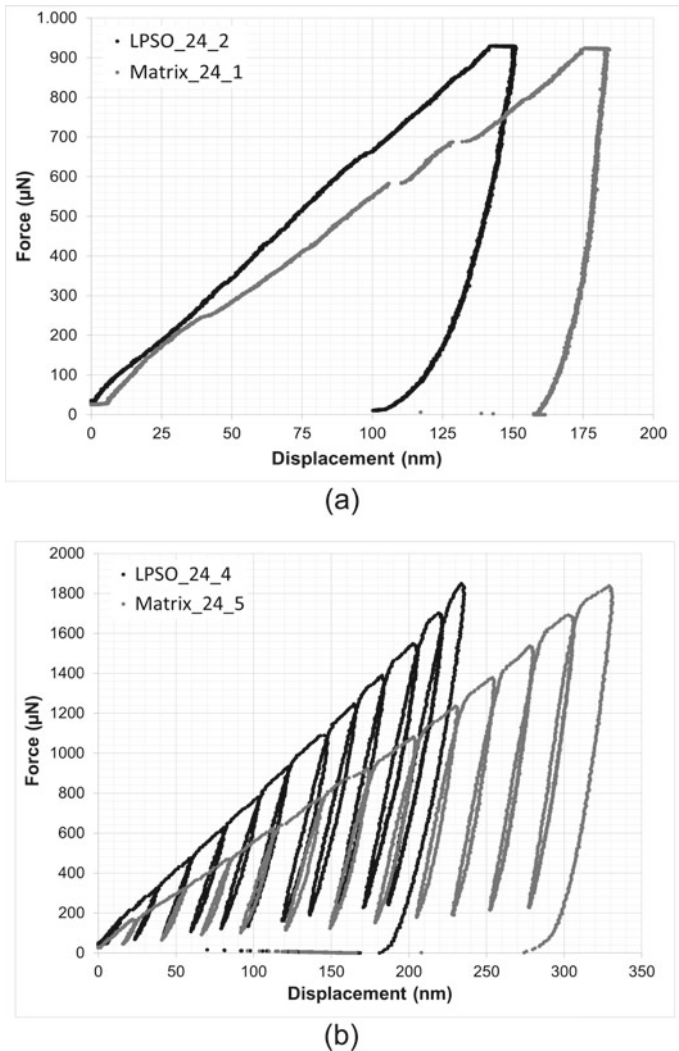
Fig. 4 Force–displacement curves of Resoloy in the solution heat-treated condition at 500 °C for 24 h of indents in Mg-matrix and blocky LPSO phases, **a** at an applied loading force of 1 mN and **b** as multi-cycle progressive loading up to 2 mN

(see three imprints in the blocky phase in Fig. 5a) and its higher hardness compared to the Mg-matrix can be clearly seen. The preliminary nanohardness measurements do not offer any statistical discussion yet. However, the nanohardness of the blocky LPSO phases is 2.6 GPa and of the Mg-matrix 1.7 GPa, in general agreement to Refs. [25, 26]. Detailed investigation will show, how the hardness of the LPSO phases and matrix will change by the solution heat treatment and more precise evaluations on the dependence of the hardness on the applied load are in progress.

The Vickers microhardness values also reveal differences between the blocky LPSO phases and the Mg-matrix. In the as-extruded Resoloy, the blocky LPSO phases have a hardness of 116 HV0.01 and the grains consisting of matrix LPSO lamellae of 109 HV0.01. The blocky LPSO phases in the solution heat-treated condition at 500 °C for 48 h have a hardness of 128 HV0.01, where the matrix with or without LPSO lamellae shows hardness values of 95 HV0.01. The difference in hardness
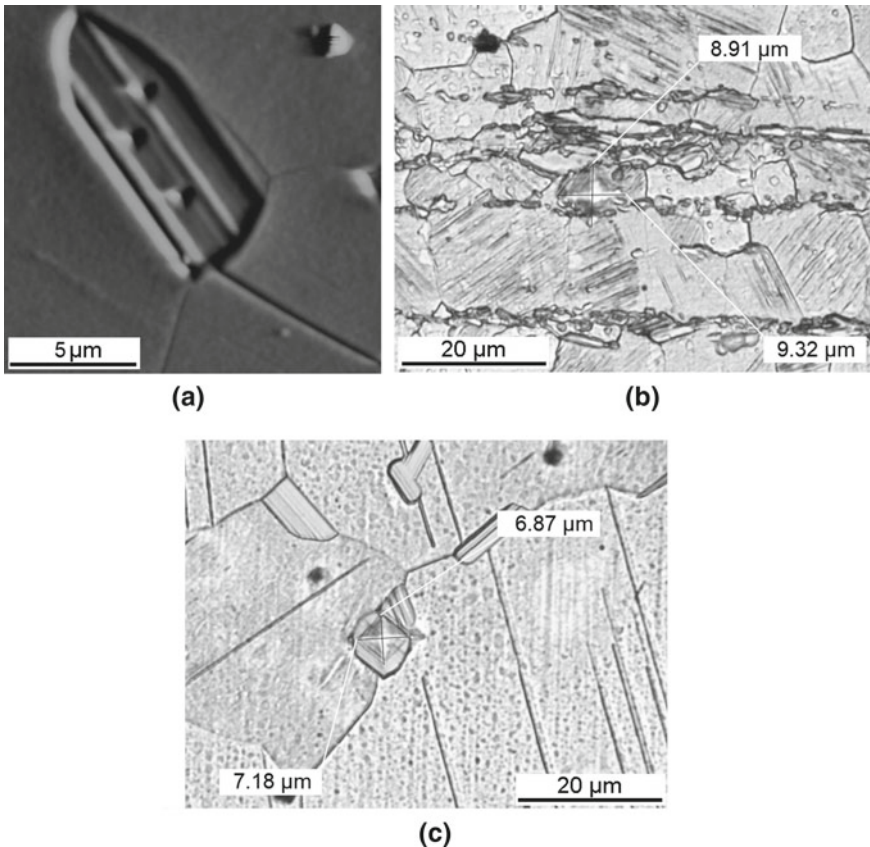
Fig. 5 Nanohardness and microhardness indents in block LPSO phases in Resoloy in **a** solution heat-treated condition at 500 °C for 48 h, **b** as-extruded, and **c** solution heat-treated condition at 500 °C for 48 h

between the blocky LPSO phases and the Mg-matrix is smaller when applying the Vickers microhardness. This can be traced back to the indent size in correlation to the size of the blocky LPSO phase: nanoindentation offers the possibility for measuring the blocky LPSO phase without the interference of the interface to the Mg-matrix. The nanoindents sit within the phase (Fig. 5a); whereas the size of the Vickers microhardness indent is often of the same size as the LPSO phase or it is even larger. Results at this early stage show that the diagonal line of the Vickers microhardness indent (both are labeled with their length values in Fig. 5b, c), where the indent has less LPSO phase around, is often of longer length than the other diagonal line.

This study helps the understanding of the role of blocky and lamellar LPSO phases on the crack propagation and with that on the fracture toughness. The LPSO phases are of a certain high hardness, providing some strength in general, but also serving as obstructions to crack growth; inner grain blocky LPSO phases are here very effective. Current research is focusing on the explanation of the high fracture toughness in the solution heat-treated condition at 500 °C for 48 h, more nanohardness data are to come.

Conclusions

The effect of blocky and lamellar LPSO phases on the crack propagation in different microstructures of Mg–Dy–Nd–Zn–Zr alloy (RESOLOY) has been investigated; in fine-grained microstructure, consisting of lamellar LPSO structures within the matrix and in coarser grains of less lamellae, but blocky LPSO phases. The amount of blocky phases decreases with heat treatment time. The amount and location of LPSO phases, in dependence on the heat treatment condition, were evaluated by optical microscopy. C-Ring compression tests were done to cause sample failure. Crack initiation and propagation were explicitly demonstrated. The blocky LPSO phases clearly hinder crack growth, either by increasing the energy to pass through the phase or along its interface. LPSO phases are found to be responsible for crack initiation. Either the interface or the softer Mg-matrix in between LPSO lamellae is the weak region. The softer Mg-matrix layer provides the possibility for slip band cracking. In the coarser-grained microstructure, the crack propagation is also influenced by twin boundaries, especially on the compression side of the C-Ring. The blocky LPSO phases were characterized by micro- and nanohardness. Blocky LPSO phases show a higher hardness than the grains with or without lamellar LPSO phases. Due to the smaller indents size, nanoindentation is here much more specific. Knowing the size, volume fraction, location, and hardness of the blocky LPSO phases will help to optimize the fracture toughness and properties in general.

References

1. Zhang J, Liu S, Wu R, Hou L, Zhang M (2018) Recent developments in high-strength Mg-RE-based alloys: focusing on Mg–Gd and Mg–Y systems. J Magnes Alloys 6(3):277–291
2. Li Q, Liu W, Song X (2014) Research progress of Mg-RE alloys. Adv Mater Res 937:178–181
3. Wu YP, Zhang XM, Deng YL (2015) Microstructure, texture, and enhanced mechanical properties of an extruded Mg–rare earth alloy after hot compression. J Mater Res 30:3776–3783
4. Feyerabend F, Fischer J, Holtz J, Witte F, Willumeit R, Drücker H, Vogt C, Hort N (2010) Evaluation of short-term effects of rare earth and other elements used in magnesium alloys on primary cells and cell lines. Acta Biomater 6(5):1834–1842
5. Liu D, Yang D, Li X, Hu S (2019) Mechanical properties, corrosion resistance and biocompatibilities of degradable Mg–RE alloys: a review. J Mater Res Technol 8(1):1538–1549
6. Hort N, Huang Y, Fechner D, Störmer M, Blawert C, Witte F, Vogt C, Drücker H, Willumeit R, Kainer KU, Feyerabend F (2010) Magnesium alloys as implant materials-principles of property design for Mg–RE alloys. Acta Biomater 6(5):1714–1725
7. Mirza FA, Chen D, Li D, Zeng X (2012) Effect of rare earth elements on deformation behavior of an extruded Mg–10Gd–3Y–0.5Zr alloy during compression. Mater Design 46:411–418
8. Wu Y, Hu W (2008) Comparison of the solid solution properties of Mg-RE (Gd, Dy, Y) alloys with atomistic simulation. Phys Res Int, Article ID 476812, https://doi.org/10.1155/2008/476812
9. Gorsse S, Hutchinson CR, Chevalier B, Nie JF (2005) A thermodynamic assessment of the Mg-Nd binary system using random solution and associate models for the liquid phase. J Alloys Compd 392(1–2):253–262
10. Yang L, Huang Y, Peng Q, Feyerabend F, Kainer KU, Willumeit R (2011) Mechanical and corrosion properties of binary Mg–Dy alloys for medical applications. Mater Sci Eng B 176:1827–1834
11. Yuan G, Liu Y, Ding W, Lu C (2008) Effects of extrusion on the microstructure and mechanical properties of Mg–Zn–Gd alloy reinforced with quasicrystalline particles. Mater Sci Eng A 474(1–2):348–354
12. Kawamura Y, Yamasaki M (2007) Formation and mechanical properties of Mg97Zn1RE2 alloys with long-period stacking ordered structure. Mater Trans 48(11):2986–2992
13. Nie JF, Zhu YM, Morton AJ (2014) On the structure, transformation and deformation of long-period stacking ordered phases in Mg–Y–Zn alloys. Metall Mater Trans A 45A:3338–3348
14. Maier P, Clausius B, Wicke J, Hort N (2020) Characterization of extruded Mg–Dy–Nd under stress corrosion in C-ring tests. Metals 10:584
15. Maier P, Steinacker A, Clausius B, Hort N (2020) Influence of solution heat treatment on the microstructure, hardness and stress corrosion behavior of extruded resoloy. JOM 72(5):1870–1879
16. Maier P, Richter A, Tober G, Hort N (2013) Effect of grain size and structure, solid solution elements, precipitates and twinning on nanohardness of Mg–RE alloys. Mater Sci Forum 765:491–495
17. Maier P, Clausius B, Joy C, Bittner B, Hort N, Menze R (2021) Microstructure and fracture toughness of an extruded Mg-Dy-Nd-Zn-Zr alloy influenced by heat treatment. Magn Technol *in press*
18. Richter A, Smith R (2011) Nanoindentation of materials: experiment and simulation. J Nanosci Nanotechnol 17(63):375–437
19. Kittner K, Ullmann M, Arndt F, Kawalla R, Prahl U (2020) Microstructure and texture evolution during twin-roll casting and annealing of a Mg–6.8Y2.5Zn–0.4Zr Alloy (WZ73). Crystals 10(6):513
20. Dong B, Zhang Z, Che X, Yu J, Meng M, Zhang J (2020) Microstructure, texture evolution, and mechanical properties of MDFed GWZ alloy containing LPSO phases on the condition of high and low temperature cycle deformation. Metals 10(1):136
21. Kim JK, Jin L, Sandlöbes S, Raabe D (2017) Diffusional-displacive transformation enables formation of long-period stacking order in magnesium. Sci Rep 7(4046):1–8

22. Shao XH, Liu HQ, Yang HJ, He C, Su N, Wu YJ, Chen Q, Ma XL (2020) Enhanced very high cycle fatigue resistance of solution treated Mg–10Gd–3Y–1Zn–0.5Zr magnesium alloy containing long-period stacking ordered phase. Materialia 11:100672
23. Su N, Xue X, Zhou H, Wu Y, Deng Q, Yang K, Chen Q, Chen B, Peng L (2020) Effects of nanoprecipitates and LPSO structure on deformation and fracture behaviour of high-strength Mg–Gd–Y–Zn–Mn alloys. Mater Charact 165:110396
24. Shi X, Long Y, Zhang H, Chen L, Zhou Y, Yu X, Yu X, Cai L, Leng Z (2019) Role of LPSO phase in crack propagation behavior of an As-Cast Mg–Y–Zn alloy subjected to dynamic loadings. Materials 12:498
25. Zhang Z, Zhang Y, Zhang J, Li Y, Ma Y, Xu C (2018) Effect of ZRB2-modified on microstructure and mechanical properties of Mg–Zn–Y–Mn alloy. J Magnes Alloys 6:255–262
26. Zhang HX, Chen SF, Cheng M, Zheng C, Zhang SH (2019) Modeling the dynamic recrystallization of Mg–11Gd–4Y–2Zn–0.4Zr alloy considering non-uniform deformation and LPSO kinking during hot compression. Acta Metall Sinica (Eng. Letters) 32(9)

Improving the Creep Resistance of Elektron21 by Adding AlN/Al Nanoparticles Using the High Shear Dispersion Technique

Hong Yang, Yuanding Huang, Karl Ulrich Kainer, and Hajo Dieringa

Abstract A novel high shear dispersion technique (HSDT) was used for the first time to effectively distribute AlN/Al nanoparticles (NPs) in Elektron21 (El21) Mg alloys. Different high shearing speeds were adopted to investigate the optimum shearing speed for optimum deagglomeration of NPs and enhancing the creep resistance of AlN/Al NPs reinforced El21 alloy. The results showed that the creep resistance of El21 + 0.5% AlN/Al nanocomposite increased with the increasing speed of HSDT. The individual/synergistic roles of AlN and Al were also systematically identified by comparing the microstructural evolutions and creep properties of El21, El21 + 0.25% Al, El21 + 0.75% AlN, and El21 + 1% AlN/Al. The creep results showed that the mixture additions of AlN and Al NPs gave a synergistic improvement on the creep resistance of El21 alloy compared to the single addition of Al or AlN NPs.

Keywords Creep · Metal matrix nanocomposite · MMNC · AlN · Elektron21

H. Yang
State Key Laboratory of Mechanical Transmissions, College of Materials Science and Engineering, Chongqing University, Chongqing 400044, China

National Engineering Research Center for Magnesium Alloys, Chongqing University, Chongqing 400044, China

H. Yang · Y. Huang · H. Dieringa (✉)
MagIC - Magnesium Innovation Centre, Helmholtz-Zentrum Hereon, Max-Planck Straße 1, 21502 Geesthacht, Germany
e-mail: hajo.dieringa@hereon.de

Y. Huang
Institute of Metallic Biomaterials, Helmholtz-Zentrum Hereon, Max-Planck-Str. 1, 21502 Geesthacht, Germany

K. U. Kainer
Chair of Light Elements Engineering, Foundry and Automation, Wrocław University of Science and Technology, W. Wyspianskiego 27, 50-370 Wrocław, Poland

H. Dieringa
Institute of Materials and Process Design, Helmholtz-Zentrum Hereon, Max-Planck-Str. 1, 21502 Geesthacht, Germany

Introduction

Magnesium (Mg) alloys have attracted increasing attention in automobile, aircraft, and commercial electrical product fields owing to their ideal combinations of low density, high specific strength, and good castability [1]. However, their creep resistance is relatively poor at elevated temperatures above 125 °C, which severely limits their wide applications in major powertrain components and automatic transmission cases, such as engine blocks (200 °C) and engine pistons (300 °C) [2]. Commercially used Mg alloys, such as Mg–Al–Zn (AZ series) and Mg–Al–Mn (AM series), usually offer poor creep performances at service temperatures over 120 °C [3–5], which is related to the low thermal stability of $Mg_{17}Al_{12}$ phase in the matrix. Its eutectic temperature is relatively low (437 °C) and could be readily softened and coarsened when the service temperature is above 120 °C, thus made it difficult to pin the grain boundary sliding and inhibit dislocation motions during creep [6]. Therefore, the critical principle to develop creep-resistant Mg alloys is to introduce thermal stable phases/particles in the Mg matrix.

Ceramic particles, such as SiC, Al_2O_3, and AlN, exhibit high hardness, wear resistance, and high thermal stabilities, which are usually chosen as the reinforcements to fabricate Mg-based metal matrix composites (MMMCs) [7–10]. Moreover, an obvious advantage of particles-reinforced Mg alloys is that they could keep more thermally stable when subjected to a long-term creep, while precipitates strengthened Mg alloys often overage with a long period of exposure to elevated temperatures during creep. However, a severe challenge exists for the fabrication of MMMCs, especially for the particles with nano-size, they easily agglomerate due to their large surface area (large van-der-Waals-Forces) and poor wettability [11]. Hence, an effective way to disperse the nanoparticles (NPs) with less clusters is of importance to develop the metal matrix nanocomposites (MMNCs). In this paper, a high shearing dispersion technique (HSDT) was employed to break up the particle clusters, commercial Elektron21 (El21) alloy was chosen as the matrix, AlN/Al NPs were utilized as the reinforcements. Influence of shearing speed and the roles of AlN and Al on the microstructures and creep performances were investigated. Their creep properties and strengthening mechanisms were explored and discussed based on their microstructural evolutions.

Experimental Procedures

Commercial El21 alloy, which was produced by Magnesium Elektron Ltd of Manchester, UK, was utilized as the matrix. It has a chemical composition of Mg−2.85Nd−0.92Gd−0.41Zr−0.29Zn as confirmed by optical emission spectroscopy (OES, Spectrolab M9 Kleve, Germany) and X-ray fluorescence (XRF) analyzer (Bruker AXS S4 Explorer, Germany). A mixture of AlN/Al NPs, which contain 75 wt.% AlN NPs and 25 wt.% Al NPs, was chosen as the reinforcement

Table 1 Casting parameters of El21 alloy and its nanocomposites

Materials	Matrix	Additives	Shearing speed [rpm]	Shearing time [min]
NH−El21	El21	–	0	–
El21−500	El21	–	500	1
El21 + 0.5% NPs−500	El21	0.5% AlN/Al	500	1
El21−3000	El21	–	3000	1
El21 + 0.5% NPs−3000	El21	0.5% AlN/Al	3000	1
El21 + 0.25% Al	El21	0.25% Al	3000	1
El21 + 0.75% AlN	El21	0.75% AlN	3000	1
El21 + 1% AlN/Al	El21	1% AlN/Al	3000	1

(compositions are in wt.% unless specified). The average size of AlN/Al NPs is approximatly 80 nm. Nanoparticles were supplied by Tomsk State University, Russia [12]. Pure AlN NPs with a size range of 60–70 nm were selected as the reinforcements for comparison. In an attempt to reveal the influence of shearing speed on the creep resistance of AlN/Al reinforced El21 alloy, 0, 500 and 3000 rpm were applied to incorporate NPs in El21 matrix. El21 with additions of 0.25% Al and 0.75% AlN were also designed to reveal their individual/synergistic roles on the creep resistance of El21 + 1% AlN/Al alloy. Their detailed casting parameters and compositions are listed in Table 1.

El21 alloy and its nanocomposites were fabricated using direct-chill casting. The equipment for HSDT, which contains a motor driven rotor of 67.5 mm diameter with four blades impeller, was utilized to stir the additives into El21 alloy at 3000 rpm for 1 min, respectively (Table 1). The detailed illustrations and shearing mechanisms of HSDT could be found in [13]. After intensive shearing, the molten nanocomposites with about 3 kg were poured into a preheated cylindrical mold (450 °C) and delivered into a three-zone resistance furnace for 5 min holding time at 670 °C. It was then solidified by water quenching at a descending speed of 100 mm/min. The non-high sheared El21 (NH−El21) alloy and El21 + 0.5% AlN/Al sheared at 500 rpm were also fabricated following the similar process as mentioned above.

Creep tests were performed using Applied Test Systems (ATS) lever arm creep tests in air. Creep stress range was selected in 70–140 MPa at 240 °C. Optical microscopy (OM, Leica DM2500 M, Germany) was employed to characterize the grain morphologies. Scanning electron microscopy (SEM, Tescan Vega3, Czech Republic) equipped with energy dispersive spectroscopy (EDS, IXRF Systems 550i, USA) was adopted to reveal the intermetallic morphologies and identify the compositions of phases.

Results and Discussion

Microstructures

Effect of shearing speed: Fig. 1 shows the optical microstructures of El21 and its nanocomposites sheared at 0, 500, and 3000 rpm using HSDT. NH−El21 exhibits equiaxed grains with an average grain size of 80.1 ± 5.0 μm (Fig. 1). With the assistance of HSDT at 500 rpm in El21 alloy, there is barely any difference visible in the grain size compared to that of NH−El21 (Fig. 1b). When the shearing speed
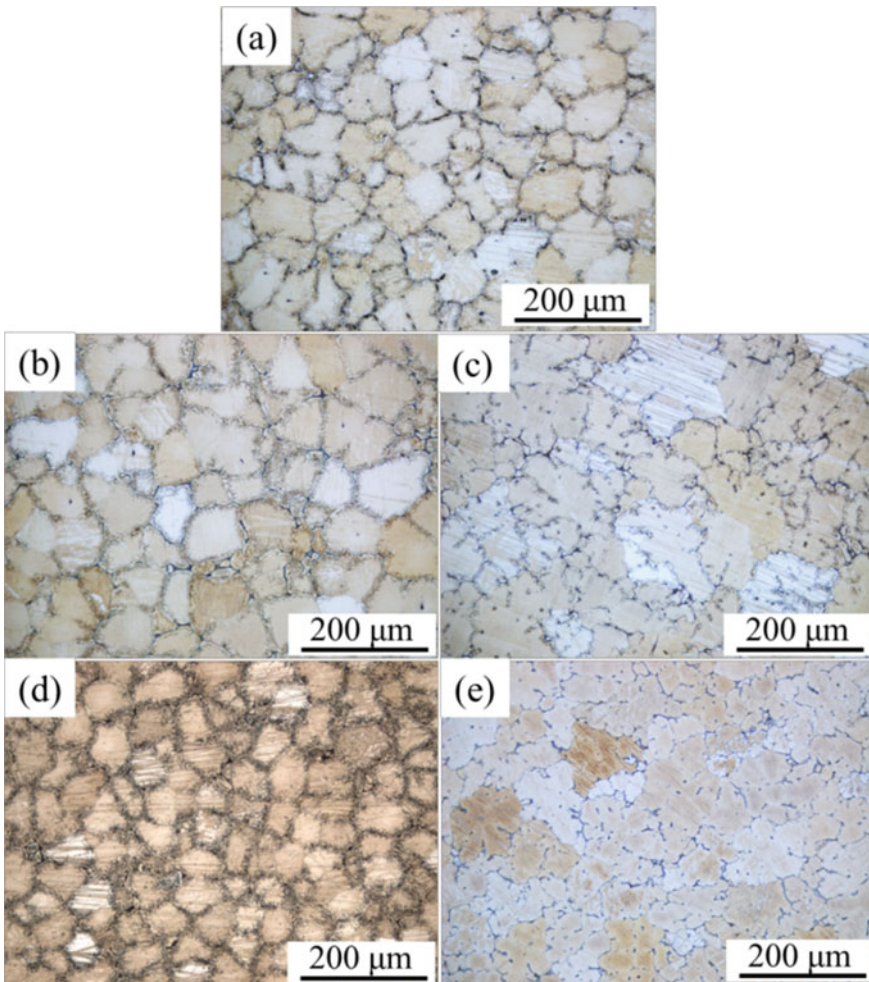
Fig. 1 Optical microstructures of **a** NH−El21, **b** El21−500, **c** El21 + 0.5% NPs−500, **d** El21−3000, and **e** El21 + 0.5% NPs−3000. (Color figure online)

increases up to 3000 rpm, the grain size of El21−3000 decreases to 59.4 ± 1.6 μm
(Fig. 1d). This is ascribed to the grain refinement effect of HSDT, which generated
intensive shear stress within the melt prior to solidification and promoted abundant
formation of MgO particles in the matrix. Fan et al. [14] firstly claimed that the grain
size of AZ91D alloy could be significantly refined from 682 μm to 187 μm with the
application of intensive shearing at 650 °C and 800 rpm for 45 s. They proposed that
intensive shearing is effective in distributing MgO films and oxide skins into discrete
particles with a diameter range of 100–200 nm, which can act as potential nucleation
sites for α−Mg grain refinement. With the addition of 0.5% AlN/Al NPs, the grain
morphologies of El21 + 0.5% NPs−500 and El21 + 0.5% NPs−3000 both changed
to more dendritic with varying degrees of grain coarsening (Fig. 1c, e). This is due
to the poisoning effect of Al in Zr-containing Mg alloys, which interferes with the
grain refinement efficiency of Zr in Mg alloys. It turned out that the grain coarsening
caused by the loss of Zr overwhelmed the grain refinement effect induced by HSDT,
thus giving an increase in the grain size of AlN/Al containing El21 alloy.

Roles of AlN and Al: Figure 2 shows the BSE micrographs of as-cast El21−3000,
El21 + 0.25% Al, El21 + 0.75% AlN/Al, and El21 + 1% AlN/Al. Mg_3RE inter-
metallic phase in El21−3000 exhibits typical network morphology with an area frac-
tion of 5.9% (Fig. 2a). By adding 0.25% Al in El21 alloy, the distribution of eutectic
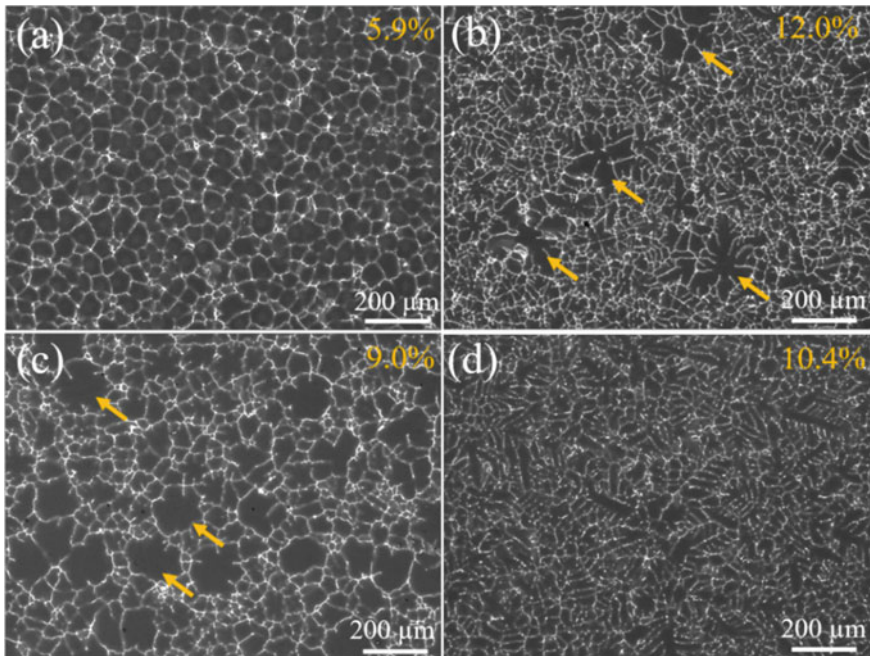
Fig. 2 BSE micrographs of as-cast **a** El21−3000, **b** El21 + 0.25% Al, **c** El21 + 0.75% AlN, and
d El21 + 1% AlN/Al. (Color figure online)

Mg_3RE became denser and dendritic with an area fraction of 12.0% (Fig. 2b). With the addition of 0.75% AlN NPs in El21 alloy, the intermetallic morphology was also modified and shows higher volume fraction of 9% compared to that of El21−3000 (Fig. 2c). With the simultaneous additions of 0.25% Al and 0.75% AlN in El21 alloy, the morphology of the intermetallic phase became much smaller and denser in the matrix (Fig. 2d). Although its area fraction (10.4%) is less than that in El21 + 0.25% Al, its distribution is much more dispersive and homogeneous.

According to Back-Scattered Electron (BSE) micrographs and its corresponding EDS results (Fig. 3a–f), it is found that Mg_3RE phase is dominant both in El21 + 0.25% Al and El21 + 0.75% AlN. However, different levels of chemical reactions between Al and RE elements occurred by the addition of 0.25% Al, 0.75% AlN, and 1% AlN/Al in El21. Some Al_2RE particles were found in El21 + 0.25% Al and El21 + 0.75% AlN, but its amount is quite low and it can only be found in some specific regions. In El21 + 1% AlN/Al nanocomposite, Mg_3RE and Al_2RE phases are the two dominant intermetallic particles in the matrix. Al_2RE phase could be observed throughout the whole matrix, which implies that the formation of Al_2RE phase could be promoted with simultaneous additions of AlN and Al in El21 alloy.
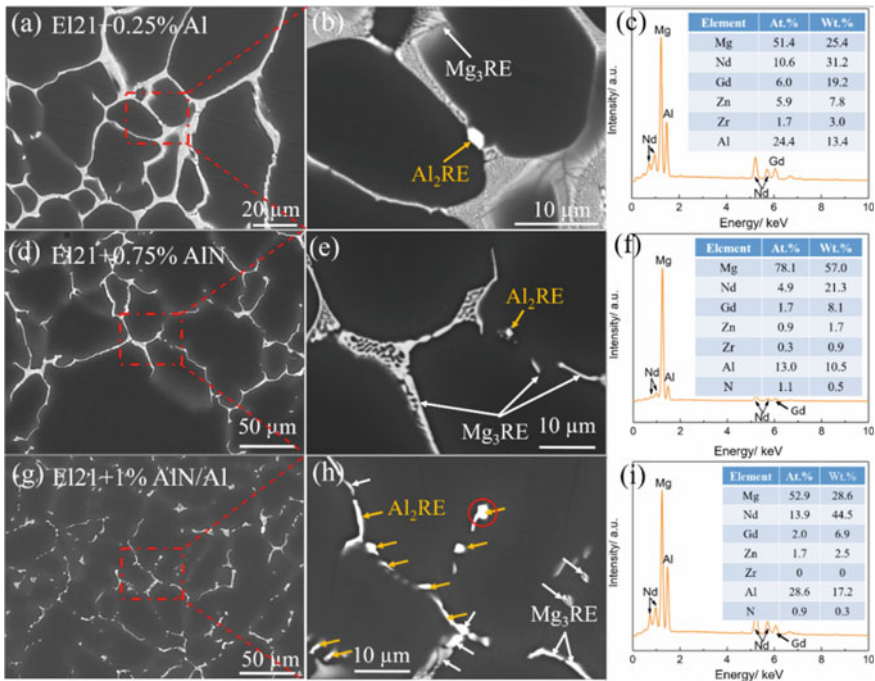
Fig. 3 BSE micrographs at lower and higher magnifications of **a–b** El21 + 0.25% Al, **d–e** El21 + 0.75% AlN, and **g–h** El21 + 1% AlN/Al and their corresponding EDS results of Al_2RE in (**c**), (**f**), and (**i**). (Color figure online)
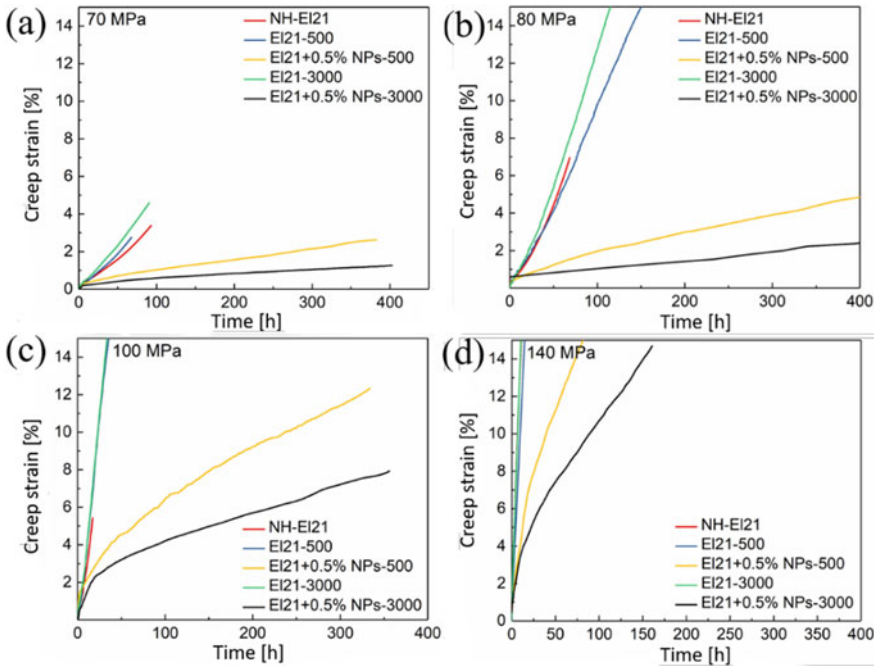
Fig. 4 Creep strain as a function of creep time for NH−El21, El21−500, El21 + 0.5% NPs−500, El21−3000, and El21 + 0.5% NPs−3000 at 240 °C under creep stress of **a** 70 MPa, **b** 80 MPa, **c** 100 MPa, and **d** 140 MPa. (Color figure online)

Creep Properties

Effect of shearing speed: The creep properties of El21 and its nanocomposites under a stress range of 70–140 MPa at 240 °C are shown in Fig. 4. All examples show an instantaneous deformation upon applied stresses and exhibit an increase in creep strain progressively with long exposure time during creep. NP-free El21 alloys, such as NH−El21, El21−500, and El21−3000, share similar creep trends under the stress range of 70–140 MPa, indicating that only the application of HSDT does not have a noticeable influence on the creep resistance of El21 alloy (Fig. 4). Further additions of 0.5% AlN/Al NPs in El21 alloy lead to a much lower creep strain both in El21 + 0.5% NPs−500 and El21 + 0.5% NPs−3000 compared to that of NP−free El21 alloy. This reveals that the combined adoption of 0.5% AlN/Al NPs and HSDT could effectively strengthen the creep properties of El21 alloys. Specifically, El21 + 0.5% NPs sheared at 3000 rpm shows a much lower creep strain under all the applied stresses than that sheared at 500 rpm, indicating that 3000 rpm shearing speed of HSDT is favored to incorporate the AlN/Al NPs reinforced El21 alloy.

The significant increment in the creep resistance of El21 + 0.5% NPs−500 and El21 + 0.5% NPs−3000 is ascribed to the following two reasons. Firstly, AlN NPs

were relatively uniformly dispersed in the matrix with the assistance of HSDT, which cause Orowan strengthening [15] and act as hindrances to inhibit the dislocation motions during creep. Lastly, by adding AlN NPs in El21 alloy using HSDT, the morphology of eutectic Mg_3RE was also modified from network to more homogeneous distributions in the dendritic boundaries and matrix, which could hinder the dislocations and pin the grain boundary sliding simultaneously. It is found that higher shearing speed provides a more uniform distribution of eutectic Mg_3RE, thus giving a higher creep resistance in El21 + 0.5% NPs−3000 than that of El21 + 0.5% NPs−500.

Roles of AlN and Al: Figure 5 shows the creep rate curves as a function of creep time under a stress range of 80–140 MPa. It is found that the creep resistance of El21 alloy could be improved by either adding 0.25% Al or 0.75% AlN NPs, they both show lower creep rate than that of El21−3000. This indicates that single addition of Al or AlN could both contribute to the enhancement of creep resistance in El21 alloy. With the simultaneous additions of 0.25% Al and 0.75% AlN NPs in El21 alloy, it shows even higher creep resistance than that of El21 + 0.25% Al and El21 + 0.75% AlN. The ratio values of $\dot{\varepsilon}$ (El21−3000) /$\dot{\varepsilon}$(El21 + x Al/AlN) reflect the improvement of
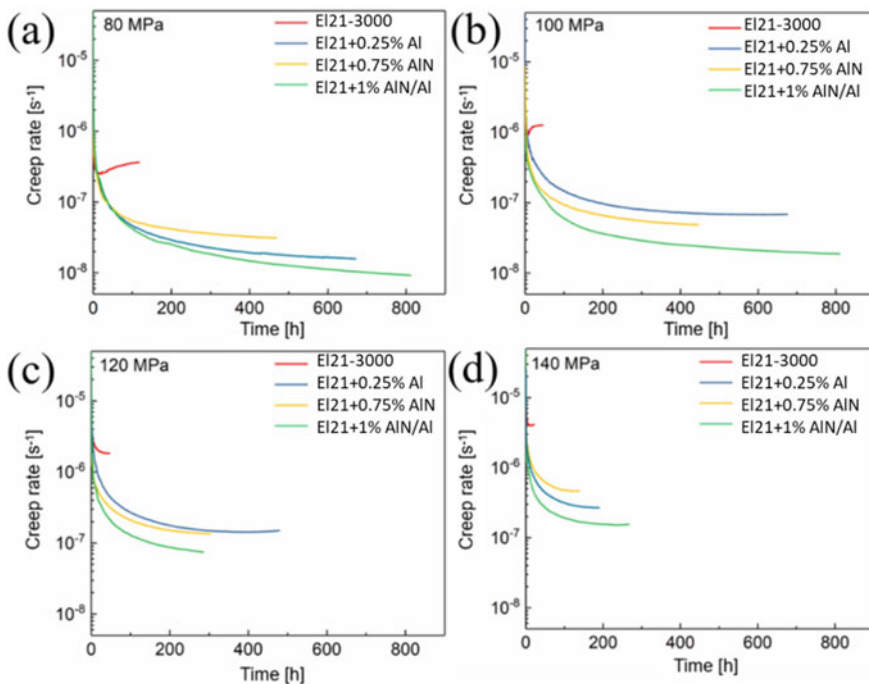
Fig. 5 Creep rate as a function of creep times for El21−3000, El21 + 0.25% Al, El21 + 0.75% AlN, and El21 + 1% AlN/Al under applied stress of **a** 80 MPa, **b** 100 MPa, **c** 120 MPa, and **d** 140 MPa. (Color figure online)

creep resistance quantitatively (Table 2). The increment of creep resistance caused by 1% AlN/Al overwhelmed the sum that gained by 0.25% Al and 0.75% AlN, which manifests a synergistic effect on the improvement of creep resistance in El21 alloy.

In order to determine the creep mechanism during deformation, Eq. 1 was employed to calculate the stress exponent n [16].

$$\dot{\varepsilon}_{min} = A\sigma^n \exp\left(-\frac{Q_C}{RT}\right) \tag{1}$$

where $\dot{\varepsilon}_{min}$ is the minimum creep rate, A is the constant corresponding to the frequency factor and Burgers vector, σ is the applied stress, Q_c is activation energy during creep, R is the universal gas constant with a value of 8.314 J/mol K. Stress exponent n is usually introduced to identify the creep mechanism empirically. Based on previous literature [7], n = 1 is related to diffusion creep, n = 2 is related to grain boundary sliding, n = 3 indicates dislocation glide is the main creep mechanism and n = 4–7 means dislocation climb is the controlling mechanism during creep.

When the temperature is constant in Eq. 1, n value can be calculated by the slope of $ln\dot{\varepsilon}_{min}$ against $ln\sigma$ (Fig. 6a). It is concluded that the n values for all the materials are close to 5. Nevertheless, for the materials containing many dispersoids/phases, the n value does not really reflect the true creep mechanisms [17]. Usually, a relatively high n value is calculated due to the occurrence of threshold stress (σ_{thr}), which indicates the interactions between dispersoid barriers and dislocation motions. As for the materials containing many intermetallic phases and AlN NPs in the present work, it is necessary to consider the influence of threshold stress in Eq. 1. Li and Langdon [17] modified Eq. 1 by replacing σ with σ$_{thr}$ as shown in Eq. 2.

$$\sigma_{eff} = \sigma - \sigma_{thr} \tag{2}$$

Thus, Eq. 1 was given in Eq. 3.

$$\dot{\varepsilon}_{min} = A\sigma_{eff}^{n_t} \exp\left(-\frac{Q_C}{RT}\right) \tag{3}$$

It is suggested [17] that the lowest $\dot{\varepsilon}_{min}$ is considered as 10^{-10} s^{-1}, which is a value of about 1% strain in 3 years in laboratory measurements. Hence, σ_{thr} can be given by extrapolating the curve of minimum creep rate $\dot{\varepsilon}_s$ versus applied stress σ to a strain rate of 10^{-10} s^{-1}. Based on Eqs. 2–3, the true stress exponent n_t was identified in Fig. 6b. The values of n_t for all materials are in a range of 3–4, which indicates that the viscous glide of dislocations and/or dislocation climb might be the main creep mechanism during creep at 240 °C.

The improvement on the creep resistance of El21 alloy induced by 0.25% Al, 0.75% AlN, and 1% AlN/Al NPs is ascribed to the modifications of intermetallic morphologies and dominant intermetallic phases. The area fractions of intermetallic phases in El21 + 0.25% Al, El21 + 0.75% AlN, and El21 + 1% AlN/Al were both

Table 2 Minimum creep rates under the applied stress of 80, 100, 120, and 140 MPa at 240 °C. The ratio values compared to based El21−3000 alloy (ratio=$\dot{\varepsilon}$(El21) / $\dot{\varepsilon}$(El21 + x (x = 0.25% Al, 0.75% AlN, and 1% AlN/Al)) are also listed

Stress [MPa]	El21−3000		El21 + 0.25% Al		El21 + 0.75% AlN		El21 + 1% AlN/Al	
	$\dot{\varepsilon}[\text{s}^{-1}]$	Ratio	$\dot{\varepsilon}[\text{s}^{-1}]$	Ratio	$\dot{\varepsilon}[\text{s}^{-1}]$	Ratio	$\dot{\varepsilon}[\text{s}^{-1}]$	Ratio
80	2.5×10^{-7}	1	1.56×10^{-8}	16.0	3.13×10^{-8}	8.0	9.05×10^{-9}	27.6
100	9.25×10^{-7}	1	6.71×10^{-8}	13.8	4.85×10^{-8}	19.1	1.87×10^{-8}	49.5
120	1.83×10^{-6}	1	1.47×10^{-7}	12.4	1.34×10^{-7}	13.7	7.36×10^{-8}	24.9
140	4.01×10^{-6}	1	2.68×10^{-7}	15.0	4.36×10^{-7}	9.2	1.52×10^{-7}	26.4
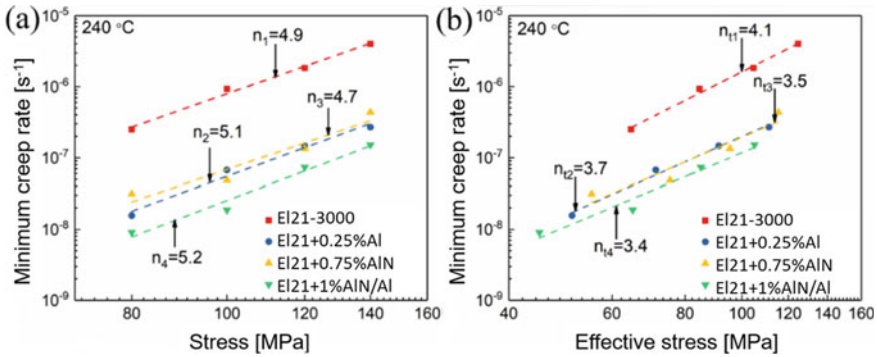
Fig. 6 Double logarithmic plots of **a** the stress dependence of minimum creep rate and **b** the effective stress dependence of minimum creep rate for El21−3000 alloy, El21 + 0.25% Al alloy, El21 + 0.75% AlN composite, and El21 + 1% AlN/Al composite at 240 °C. (Color figure online)

increased compared to that of El21−3000 alloy. Their appearance has also been changed from a more network-like to a homogeneously distributed in the matrix, which has a positive effect on the ability to prevent dislocation movement during creep. In [9], it was shown that another reason for the improved creep resistance of El21 + AlN prepared by an ultrasound-assisted casting method is the fact that the nanoparticles are preferentially located in the eutectic and at the grain boundaries. This probably can hinder the mechanism of grain boundary sliding, resulting in higher creep resistance. However, El21 + 0.25% Al shows the highest area fraction of the intermetallic phase but did not have the highest creep resistance among all the materials. This is highly related to the thermal stability of the intermetallic phase in the matrix. Mg_3RE is the main phase in El21 + 0.25% Al, while Mg_3RE and Al_2RE are two dominant phases in El21 + 1% AlN/Al. In general, it can be assumed that the thermal stability of intermetallic phases that are metallic bonded is proportional to their melting points [18]. It is reported that the Al_2RE phase (1200 °C) has a higher melting point than the Mg_3RE phase (780 °C), demonstrating higher thermal stability than Mg_3RE phase in the magnesium matrix. AlN NPs also have an excellent thermal stability with an even higher melting point of 2800 °C [19]. Therefore, El21 + 1% AlN/Al, which contains AlN NPs and larger amount of Al_2RE phase, was more effective to transfer the load from the matrix and impede the dislocations than El21 + 0.25% Al at elevated temperature during creep.

Conclusions

AlN/Al NPs reinforced El21 nanocomposites were successfully fabricated using HSDT. The optimum shearing speed and the roles of Al and AlN NPs on the creep resistance of El21 alloy were systematically investigated based on microstructures and creep properties. The main conclusions are as follows:

(1) The creep resistance of El21 + 0.5% AlN/Al nanocomposite increased with the increasing speed of HSDT. El21 + 0.5% AlN/Al sheared at 3000 rpm showed more than one order of magnitude lower minimum creep rate than NP-free El21alloy, which was ascribed to the more homogeneous distribution of NPs and eutectic phase in the matrix.

(2) The additions of 0.25% Al and 0.75%AlN + 1% AlN/Al could both contribute to the improvement of creep resistance in El21 alloy. The simultaneous addition of AlN and Al exhibits the best strengthening effect among all the materials.

(3) The synergistic effect caused by 1% AlN/Al was attributed to the increased area fraction of intermetallic phase and higher thermal stable AlN NPs and Al_2RE phase in the matrix, which were more effective to transfer the load from the matrix and impede dislocation movements during creep.

References

1. Dieringa H, Hort N, Letzig D, Bohlen J, Höche D, Blawert C, Zheludkevich M, Kainer KU (2018) Mg alloys: challenges and achievements in controlling performance, and future application perspectives. In: Orlov D, Joshi V, Solanki K, Neelameggham N (eds) Magnesium technology 2018. The minerals, metals and materials series. Springer, Berlin, pp 3–14. https://doi.org/10.1007/978-3-319-72332-7_1

2. Luo AA (2004) Recent magnesium alloy development for elevated temperature applications. Int Mater Rev 49:13–30

3. Mo N, Tan Q, Bermingham M, Huang Y, Dieringa H, Hort N, Zhang M-X (2018) Current development of creep-resistant magnesium cast alloys: a review. Mater Des 155:422–442

4. Celikin M (2010) Creep resistance in magnesium alloys. Int Mater Rev 55:197–217

5. Mordike BL (2002) Creep-resistant magnesium alloys. Mater Sci Eng A 324:103–112

6. Meshinchi Asl K, Tari A, Khomamizadeh F (2009) The effect of different content of Al, RE and Si element on the microstructure, mechanical and creep properties of Mg–Al alloys. Mater Sci Eng A 523:1–6

7. Dieringa H (2011) Properties of magnesium alloys reinforced with nanoparticles and carbon nanotubes: a review. J Mater Sci 46:289–306

8. Dieringa H, Huang Y, Maier P, Hort N, Kainer KU (2005) Tensile and compressive creep behaviour of Al2O3 (Saffil®) short fiber reinforced magnesium alloy AE42. Mater Sci Eng A 410–411:85–88

9. Katsarou L, Mounib M, Lefebvre W, Vorozhtsov S, Pavese M, Badini C, Molina-Aldareguia JM, Jimenez CC, Pérez Prado MT, Dieringa H (2016) Microstructure, mechanical properties and creep of magnesium alloy Elektron21 reinforced with AlN nanoparticles by ultrasound-assisted stirring. Mater Sci Eng A 659:84–92

10. Chen J, Bao C, Chen F (2016) Evolutions of microstructure and mechanical properties for Mg–Al/AlN composites under hot extrusion. Mater Sci Eng A 667:426–434

11. Tjong SC (2007) Novel nanoparticle-reinforced metal matrix composites with enhanced mechanical properties. Adv Eng Mater 9:639–652

12. Dieringa H, Katsarou L, Buzolin R, Szakács G, Horstmann M, Wolff M, Mendis C, Vorozhtsov S, StJohn D (2017) Ultrasound assisted casting of an AM60 based metal matrix nanocomposite. Properties Recyclability, Metals 7:388

13. Yang H, Huang Y, Song B, Kainer KU, Dieringa H (2019) Enhancing the creep resistance of AlN/Al nanoparticles reinforced Mg-2.85Nd-0.92Gd-0.41Zr-0.29Zn alloy by a high shear dispersion technique. Mater Sci Eng A755:18–27

14. Fan Z, Wang Y, Xia M, Arumuganathar S (2009) Enhanced heterogeneous nucleation in AZ91D alloy by intensive melt shearing. Acta Mater 57:4891–4901
15. Ferguson JB, Sheykh-Jaberi F, Kim C-S, Rohatgi PK, Cho K (2012) On the strength and strain to failure in particle-reinforced magnesium metal-matrix nanocomposites (Mg MMNCs). Mater Sci Eng A 558:193–204
16. Athul KR, Pillai UTS, Srinivasan A, Pai BC (2016) A review of different creep mechanisms in Mg alloys based on stress exponent and activation energy. Adv Eng Mater 18:770–794
17. Li Y, Langdon TG (1997) A simple procedure for estimating threshold stresses in the creep of metal matrix composites. Scripta Mater 36:1457–1460
18. Hort N, Huang Y, Kainer KU (2006) Intermetallics in magnesium alloys. Adv Eng Mater 8:235–240
19. Mcnelly GASF (1976) Growth of high purity AlN crystals. J Crystal Growth

Investigation of Microstructural Factors Affecting the Plane-Strain Fracture Toughness of Mg–Zn–Y–Al Alloys Processed by Consolidation of Rapidly Solidified Ribbons

Soya Nishimoto, Michiaki Yamasaki, Shin-ichi Inoue, and Yoshihito Kawamura

Abstract High strength nanocrystalline bulk $Mg_{96.75}Zn_{0.85}Y_{2.05}Al_{0.35}$ (at%) alloys featuring increased fracture toughness were fabricated by the consolidation of rapidly solidified (RS) ribbons. The RS ribbons prepared by single-roller melt-spinning at a cooling rate of ~1.4×10^5 Ks^{-1} were pressed into a copper billet and then consolidated by hot-extrusion. The microstructure of the alloys consists of α-Mg and long-period stacking ordered (LPSO) phases. The two-phase microstructure evolution in the alloys is influenced by conditions of pre-consolidation/extrusion heat treatment. In the alloys without pre-extrusion heat treatment, plate-shaped LPSO phase precipitates in grain interior. On the other hand, in the alloys with pre-extrusion heat treatment, block-shaped LPSO phase forms around grain boundaries. Formation of the block-shaped LPSO phase induces crack deflection and meandering, resulting in improvement of fracture toughness. The alloy subjected to pre-extrusion heat treatment at ~738 K for 24 h exhibited a good balance of plane-strain fracture toughness ($K_{Ic} = $ ~15 MPam$^{1/2}$) and tensile yield strength ($\sigma_{0.2} = $ ~400 MPa).

Keywords Mg–Zn–Y · Long-period stacking ordered structure · Rapid solidification · Fracture toughness

S. Nishimoto
Department of Materials Science and Applied Chemistry, Graduate School of Science and Technology, Kumamoto University, 2-39-1 Kurokami, Chuo-ku, Kumamoto 860-8555, Japan

M. Yamasaki (✉) · S. Inoue · Y. Kawamura
Magnesium Research Center, Kumamoto University, 2-39-1 Kurokami, Chuo-ku, Kumamoto 860-8555, Japan
e-mail: yamasaki@gpo.kumamoto-u.ac.jp

Introduction

To solve environmental problems such as global warming and resource depletion, improvement of fuel efficiency of transportation vehicles by weight reduction is expected. Mg alloys have a great potential as structural materials because of their lightest weight among all metallic structural materials [1]. However, the use of commercially available Mg alloys has been limited due to their low strength and poor ductility. Under these situations, wrought Mg–Zn–Y alloys have attracted attention since they exhibit high strength and superplasticity [2]. It is well known that the $Mg_{97}Zn_1Y_2$ alloy consists of α-Mg matrix and long-period stacking ordered (LPSO) phases [3]. The LPSO phase plays an important role for alloy-strengthening in the wrought alloys because of its short-fiber reinforcement. Application of rapid solidification processing to the LPSO-typed Mg alloys brings about grain refinement and improving electrochemical homogeneity, resulting in enhancement of tensile yield strength and corrosion resistance [2, 4–6]. Although there are various rapid solidification methods, we have adopted the rapidly solidified (RS) ribbon-consolidation processing to fabricate the nanocrystalline bulk Mg alloys. Recently, RS ribbon-consolidated Mg–Zn–Y–Al alloys have been expected to be used in aerospace industries, especially in structural applications, due to their high specific strength, high corrosion resistance, and incombustibility. Meanwhile, new problems to be overcome such as insufficient fracture toughness and poor ductility at room temperature have arisen. Our previous studies indicated that heat treatment before the consolidation of RS ribbons was effective in improving fracture toughness and ductility. Therefore, in this study, optimization of the pre-extrusion heat treatment was conducted for the RS ribbon-consolidated Mg-Zn-Y-Al alloys. Particular attention has been paid to the influence of microstructure evolution on mechanical properties and fracture toughness.

Experimental Procedure

Master alloy ingot of $Mg_{96.75}Zn_{0.85}Y_{2.05}Al_{0.35}$ (at.%) was prepared by high frequency induction heating in an argon atmosphere. RS ribbons were prepared by single-roller melt-spinning at a roll-circumferential velocity of ~42 m·s^{-1}. The cooling rate of the RS ribbon was estimated as 1.4×10^5 Ks^{-1}. RS ribbons were pressed into a copper billet and degassed for 15 min at 523 K. Before extrusion, billets were heat-treated at 738 K for 10, 24, and 48 h. Then, the non-heat-treated billet and the heat-treated billets were extruded with an extrusion ratio of 10, at 623 K, and an extrusion ram speed of 2.5 mms^{-1}. The detail of the RS ribbon-consolidated process was described in previous reports [4–6].

Mechanical properties were evaluated by tensile tests and fracture toughness tests. Tensile tests were carried out using an Instron testing machine (Instron Model 5584) at room temperature with an initial strain rate of 5×10^{-4} s^{-1}. The gauge section of

tensile specimens was 2.5 mm and 15 mm in diameter and length, respectively. The tensile axis was held parallel to the direction of extrusion. The 0.2% proof strength was employed as yield strength. Fracture toughness tests in mode I were performed according to ASTM-E399 [7] using a servo-hydraulic mechanical testing machine (Shimadzu EHF-EM). Compact tension (CT) specimen (thickness: $B = 4.2$ mm, wide: $W = 8.4$ mm) was adopted in the fracture toughness test. The V-notch was normal to the extrusion direction. Before the plane-strain fracture toughness test, the fatigue cracking tests were carried out under load control using maximum stress intensity of 2.3–3.2 MPam$^{1/2}$ at a frequency of 10 Hz with a load ratio $R = 0.1$ in order to insert a fatigue pre-crack in the specimens. At this time, the pre-crack length, a, has to be satisfied $0.45 \leqq a/W \leqq 0.55$. By using pre-cracked specimens, the plane-strain fracture toughness test was carried out at a constant displacement rate of 12 μms^{-1} at room temperature. The average value of stress intensity factor K_Q was determined with the relationship given as follows:

$$K_Q = \frac{P_Q}{B\sqrt{W}} \bullet f\left(\frac{a}{W}\right) \tag{1}$$

where P_Q is the conditional load, and $f\left(\frac{a}{W}\right)$ is the geometrical factor that is defined as

$$f\left(\frac{a}{W}\right) = \frac{\left(2 + \frac{a}{W}\right)\left[0.886 + 4.64\frac{a}{W} - 13.32\left(\frac{a}{W}\right)^2 + 14.72\left(\frac{a}{W}\right)^3 - 5.6\left(\frac{a}{W}\right)^4\right]}{\left(1 - \frac{a}{W}\right)^{3/2}} \tag{2}$$

The value of P_Q is determined from the curve between the P and CMOD by drawing a secant line with a slope which is 5% less than the slope of the linear part of the curve. For a valid plane-strain facture toughness K_{Ic}, the value of K_Q has to satisfy all validity requirements according to the ASTM E399-12 standard given as

$$P_{\max} \leq 1.10 P_Q \tag{3}$$

$$W - a \geq 2.5\left(\frac{K_Q}{\sigma_{ys}}\right)^2 \tag{4}$$

where $P_{\max}$ is the maximum load and σ_{ys} is the yield strength of the specimen.

The microstructure and the fracture surface of the alloys was investigated by scanning electron microscopy (SEM; JEOL JSM-4601F), and transmission electron microscopy (TEM; JEOL JEM-2100F). TEM samples were prepared by ion milling (GATAN PIPS M-691).

Results and Discussion

Figure 1 shows changes in the plane-strain fracture toughness and the tensile yield strength of the RS ribbon-consolidated $Mg_{96.75}Zn_{0.85}Y_{2.05}Al_{0.35}$ alloys as functions of pre-extrusion heat treatment time at 738 K. All specimens satisfied the Eqs. (3) and (4). Thus, K_Q values are regarded as plane-strain fracture toughness values, K_{Ic}. The relationship between the K_{Ic} value and logarithmic heat treatment time is sigmoidal for the RS ribbon-consolidated $Mg_{96.75}Zn_{0.85}Y_{2.05}Al_{0.35}$ alloy, their K_{Ic} values increased from ~9.5 $MPam^{1/2} \cdot s^{-1}$ up to ~15.5 $MPam^{1/2} \cdot s^{-1}$. The yield strength decreased from ~500 MPa to less than 400 MPa with an increase in the pre-extrusion heat treatment time. From those results, it appears that the specimen heat-treated for 24 h has a good balance of fracture toughness and yield strength among four specimens examined in this study. Hereafter, we compare the non-heat-treated (denoted Non-HT) specimen with the heat-treated specimen for 24 h (HT-24 h).

Figure 2 shows SEM images of the Non-HT and HT-24 h specimens. Dark and bright regions correspond to the α-Mg and the LPSO phases, respectively. The LPSO
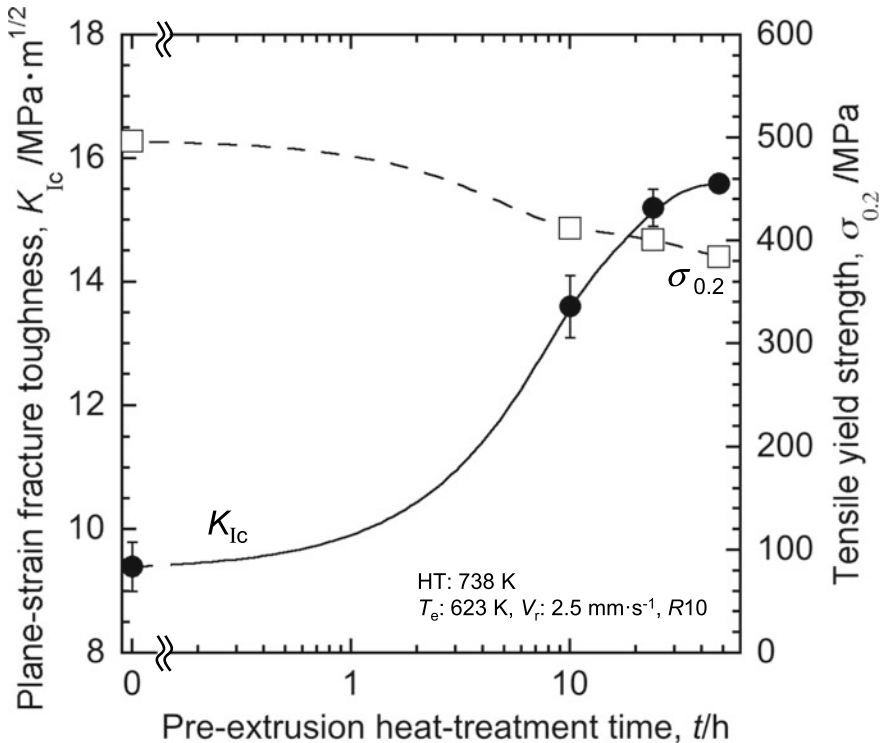
Fig. 1 Change in the plane-strain fracture toughness and tensile yield strength of the RS ribbon-consolidated $Mg_{96.75}Zn_{0.85}Y_{2.05}Al_{0.35}$ alloys as a function of pre-extrusion heat-treatment time
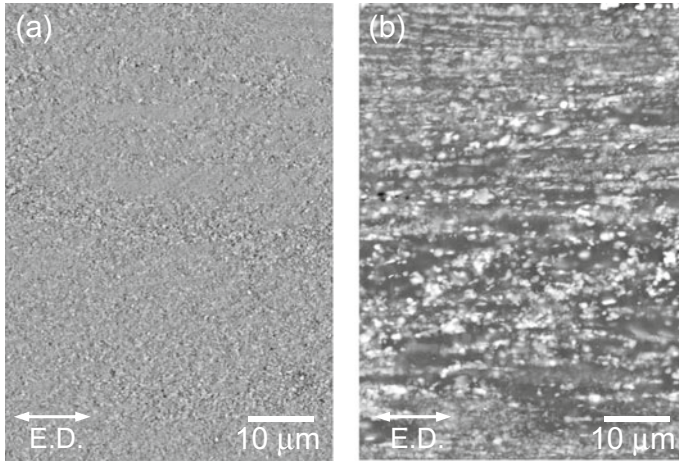
Fig. 2 SEM images of **a** the Non-HT specimen and **b** the HT-24h specimen

phase in the Non-HT specimen seems to disperse finely and homogeneously. On the other hand, the LPSO phase in the HT-24 h specimen coarsely disperses.

Figure 3 shows HAADF-STEM images of the Non-HT and HT-24 h specimens. In the Non-HT specimen, profuse bright lines corresponding to the plate-shaped LPSO phase were observed. Selected area electron diffraction (SAED) patterns exhibited diffraction spots of α-Mg with a strong streak along c^*-axis. These streaks indicate the formation of solute-segregated stacking-faults in the basal plane of α-Mg matrix. In the HT-24 h specimens, the bright lines in the α-Mg matrix grains disappeared. Instead, block-shaped LPSO phases were formed around the grain boundary.

Figure 4 shows SEM images in macroscopic view and cross-sectional view of fracture-tested samples of the Non-HT and HT-24 h specimens. The Non-HT specimen showed a flat fracture surface. On the other hand, the HT-24 h specimen showed a relatively rough fracture surface. This indicates that crack deflection or meandering frequently occurred when fracture toughness tests in mode I were conducted for the HT-24 h specimen. Furthermore, some secondary cracks (indicated by arrow in
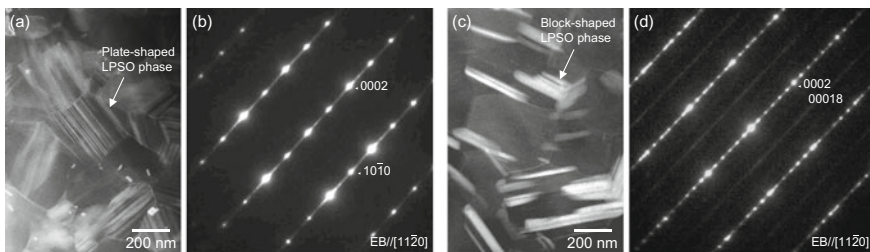
Fig. 3 HAADF-STEM images and SAED patterns of **a**, **b** the Non-HT specimen and **c**, **d** the HT-24h specimen
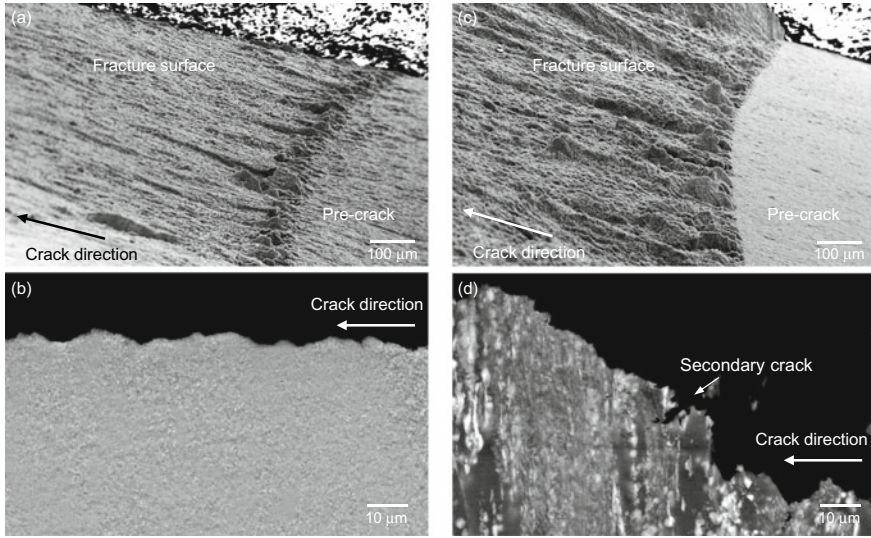
Fig. 4 Macroscopic and cross-sectional SEM images of fracture toughness test samples: **a**, **b** the Non-HT, and **c**, **d** the HT-24h specimens

Fig. 4d) were also observed. It is known that those fracture behaviors improve fracture toughness of materials as extrinsic toughening [8]. The difference between fracture behaviors of the Non-HT and HT-24 h specimens may be due to differences in the morphology of the LPSO phase. The Non-HT alloy consists of α-Mg fine grains containing solute-segregated stacking fault and plate-shaped LPSO phase. The crack tends to propagate along grain boundaries. The plate-shaped precipitates of LPSO phase in the α-Mg grains do not seem to hinder the crack propagation. Whereas the HT-24 h alloy possesses the block-shaped LPSO phase around grain boundaries. These huge block-shaped LPSO grains induced crack deflection and meandering, resulting in improved fracture toughness.

Conclusions

(1) The plane-strain fracture toughness of the RS ribbon-consolidated $Mg_{96.75}Zn_{0.85}Y_{2.05}Al_{0.35}$ alloys falls in the range from 9.1 $MPam^{1/2}$ to 15.7 $MPam^{1/2}$. The alloy heat-treated at 738 K for 24 h showed a good balance of fracture toughness ($K_{Ic} = $ ~15 $MPam^{1/2}$) and yield strength (~400 MPa).

(2) Pre-extrusion heat treatment condition affects the morphology of LPSO phase in the RS ribbon-consolidated Mg–Zn–Y–Al alloys. In the alloys without heat treatment, plate-shaped LPSO phase precipitates in the grain interior. On the other hand, in the heat-treated alloys, block-shaped LPSO phase forms around the grain boundaries.

(3)   Formation of the block-shaped LPSO phase promotes the crack deflection and meandering. It probably improves the fracture toughness.

References

1. Pollock TM (2010) Weight loss with magnesium alloys. Science 328:986–987
2. Kawamura Y, Hayashi K, Inoue A, Masumoto T (2001) Rapidly solidified powder metallurgy $Mg_{97}Zn_1Y_2$ alloys with Excellent Tensile Yield Strength above 600 MPa. Mater Trans 42:1172–1176
3. Abe E, Kawamura Y, Hayashi K, Inoue A (2002) Long–period ordered structure in a high–strength nanocrystalline Mg–1 at% Zn–2 at% Y alloy studied by atomic–resolution Z–contrast STEM. Acta Mater 50:3845–3857
4. Izumi S, Yamasaki M, Kawamura Y (2009) Relation between corrosion behavior and microstructure of Mg–Zn–Y alloys prepared by rapid solidification at various cooling rates. Corros Sci 51:395–402
5. Yamasaki M, Izumi S, Kawamura Y, Habazaki H (2011) Corrosion and passivation behavior of Mg–Zn–Y–Al alloys prepared by cooling rate-controlled solidification. Appl Surf Sci 257:8258–8267
6. Okouchi H, Seki Y, Sekigawa T, Hira H, Kawamura Y (2010) Nanocrystalline LPSO Mg–Zn–Y–Al alloys with high mechanical strength and corrosion resistance. Mater Sci Forum 638–642:1476–1481
7. ASTM E399–12, Standard Test Method for Plane–Strain Fracture Toughness of Metallic Materials, ASTM, West Conshohocken, PA (2012).
8. Ritchie RO (1988) Mechanisms of fatigue crack propagation in metals, ceramics and composites: role of crack tip shielding. Mater Sci Eng A 103:15–28

Part III
Solidification and Casting Processes

Contemporary Magnesium Die-Casting Research and Technology: A Canadian Viewpoint

J. P. Weiler

Abstract For the last 20 years, Canada has been a world leader in magnesium die-casting research and development. The breadth of research faculty and facilities, presence of a strong industrial sector, and the participation of government funded programs and agencies have fueled significant developments. This paper provides an overview of the developments led by Canadian researchers in the field of magnesium die-casting in alloy development, property, and microstructural characterization, development of ICME models, joining and corrosion technologies, and automotive product development with focus on developments funded by large-scale government funded research programs.

Keywords Die-casting · Research and development · Canada

Introduction

The research and development ecosystem of magnesium die-casting technology in Canada is considered world leading due to the existence of involved raw metal suppliers and die-cast manufacturers, an innovative academic sector, engaging government funded agencies, and a strategic vision to fund Canada's innovation in lightweight materials. Canada is home to Alliance Magnesium, a producer of magnesium metal located in Quebec, and Meridian Lightweight technologies, a world leader in magnesium die-cast components for the automotive industry located in Southwestern Ontario. The Canada Centre for Mineral and Energy Technology (Canmet) MATERIALS (CMAT) research laboratory, a branch of Natural Resources Canada is located in Southwestern Ontario as shown in Fig. 1. CanmetMATERIALS extensive state-of-the-art laboratory equipment includes a medium tonnage cold-chamber High-Pressure Die-Cast (HPDC) machine for non-ferrous metals research installed as part of an expansion and relocation (Fig. 1). This facility is dedicated to develop

J. P. Weiler (✉)
Meridian Lightweight Technologies, 25 MacNab Avenue, Strathroy, ON N7G 46, Canada
e-mail: jweiler@meridian-mag.com

Fig. 1 Natural Resources Canada CanmetMATERIALS (CMAT), located in Hamilton, Ontario, left, and CanmetMATERIALS' pilot plant HPDC machine, right (Copyright, 2019, Government of Canada, used with permissions) [1]. (Color figure online)

and deploy technologies for improved materials fabrication and production with a focus on automotive materials.

Finally, the Natural Sciences and Engineering Research Council of Canada (NSERC) and Innovation, Science and Economic Development Canada (ISED) support discovery research, and foster innovation to enhance Canada's innovation performance through various funding programs.

With these resources and Canada's strong academic sector in materials and manufacturing, Canadian researchers have demonstrated a strong insight and expertise in magnesium die-casting technology. In fact, Canada has published the second most publications in Scopus-indexed journals on magnesium die-casting per million capita in the last 20 years in the world, as shown in Fig. 2 [2]. Only Australia has a published a greater ratio of investigations on magnesium die-casting. We find then, that this
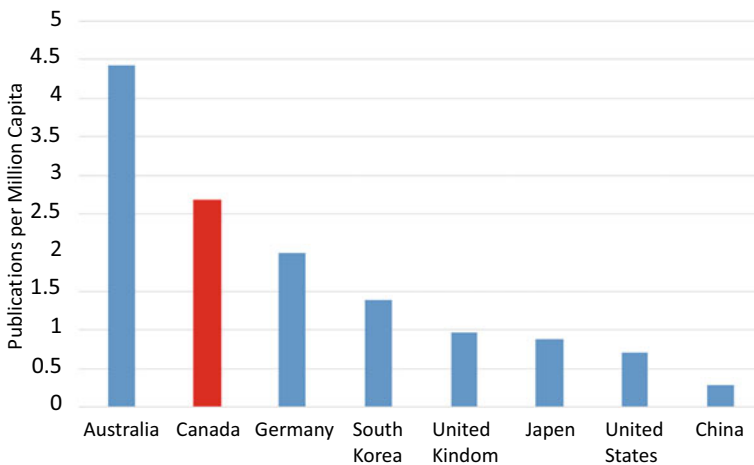
Fig. 2 Publications per million capita identified in Scopus-indexed journals since 2000 [2]. (Color figure online)

is a good opportunity to summarize and highlight the contributions that Canadian researchers have made to the development of magnesium die-casting technology. This paper strives to provide a thorough summary of Canadian-led research and development in magnesium die-casting technology. The structure of this paper is divided into different topics, including alloy development, property, or microstructural characterization of magnesium die-castings, Integrated Computational Materials Engineering (ICME) developments and modeling, joining and corrosion technology, novel products developed for the automotive industry, and large-scale research programs.

Alloy Development

The most prevalent magnesium die-casting alloys used in automotive applications include AZ91D [3] primarily used in powertrain application, and AM50A/AM60B [3] primarily used in automotive applications possessing increased ductility and toughness qualities, typically used for structural applications. These alloys contain primarily aluminum, zinc, and manganese as alloying elements. However, due to the advancement of engine technologies in the 1970s, resulting in increased engine temperatures, there was a need for magnesium alloys with higher operating temperature exposure limits. Several different research groups worldwide explored various alloying elements to improve the high-temperature creep properties of die-cast magnesium alloys, while not decreasing castability, and maintaining room temperature mechanical properties. These alloying elements included rare earths and alkaline earth elements, among others. Some of these alloy formulations have successfully been utilized in automotive applications [4]. Noranda, a Quebec-based magnesium producer, began developing a magnesium die-casting alloy for high-temperature automotive applications based on alloying with Aluminum and Strontium [5–13]. This Mg–Al–Sr system takes advantage of the addition of strontium to the typical magnesium–aluminum alloy system to form Al-Sr intermetallic particles resulting in an improved thermal stability at temperatures greater than 125 °C [5]. Noranda completed extensive work documented by numerous publications describing the benefits of the alloy system for high-temperature powertrain automotive applications [5–13]. Noranda characterized the creep performance [5–12] high-temperature mechanical properties [5, 6], thermophysical properties [7, 8], castability evaluations [5, 7, 9–11], alloy composition stability through thermal cycling [12], melt protection studies [13], and recyclability evaluations in a fluxless system of the alloy system [12]. The work of Noranda resulted in the promotion of two of these compositions for high-temperature automotive applications—AJ52X and AJ62X. Figure 3 shows the microstructure of several of these AJ-series formulations.

The AJ52X composition is promoted to possess excellent creep and bolt-load retention properties up to 175 °C [5, 6, 10], a thermal conductivity that is the greatest of any magnesium die-casting alloy [7, 8], chemical consistency through a fluxless recycling process [6], and good castability characteristics, although, with a limited process window [6, 7, 9] utilizing increased metal and die temperatures and
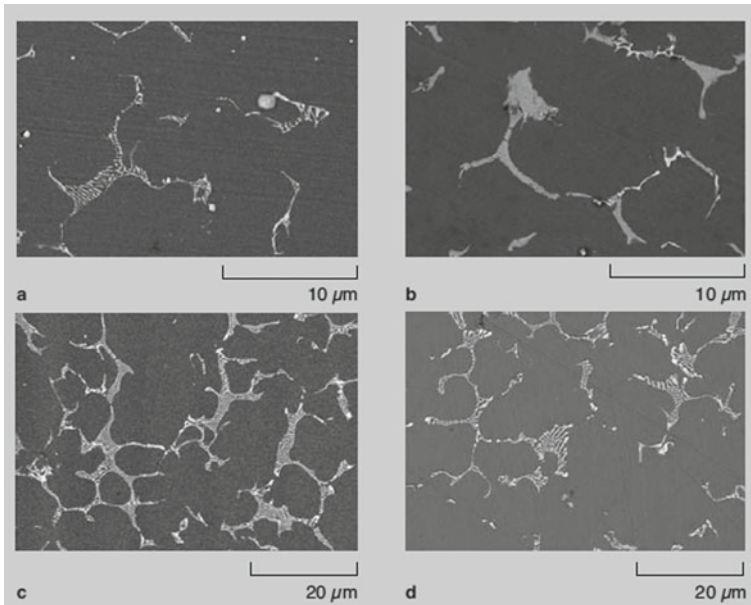
Fig. 3 SEM micrographs of Mg–Al-Sr alloy series in the as-cast condition: **a** AJ51x, **b** AJ52x, **c** AJ62x, and **d** AJ62L (Copyright TMS, 2003, used with permission) [5]

short fill times [6]. The AJ62X version was promoted as having generally similar high-temperature properties [5, 9, 10], an improved castability due to the increased aluminum content that widens the freezing range [5, 9, 10], and good corrosion resistance [5, 10]. Noranda suggests that the AJ62X alloy formulation is recommended for transmission cases and engine block components that are exposed to higher stresses at elevated temperatures [9]. The AJ62X alloy formulation was successfully implemented in a BMW aluminum–magnesium composite crankcase housing found on 3- and 6-series vehicles from 2004–2015, as shown in Fig. 4 [11].

Characterization of Magnesium Die-Castings

The understanding of magnesium die-casting material has been an important field of research as automotive use of magnesium die-cast components has progressed into structural applications over the last 20 years. The microstructure, mechanical properties, corrosion properties, strain-rate properties, and solidification characteristics among others are important to improve the knowledge of magnesium die-casting. Canadian researchers have contributed significantly to the understanding of magnesium die-casting over the last 20 years through extensive studies focusing on the characterization of the microstructure and mechanical properties of thin-walled automotive die-cast magnesium through several different research groups [15–37]. These works primarily focus on the AM50 and AM60 magnesium alloys. From these
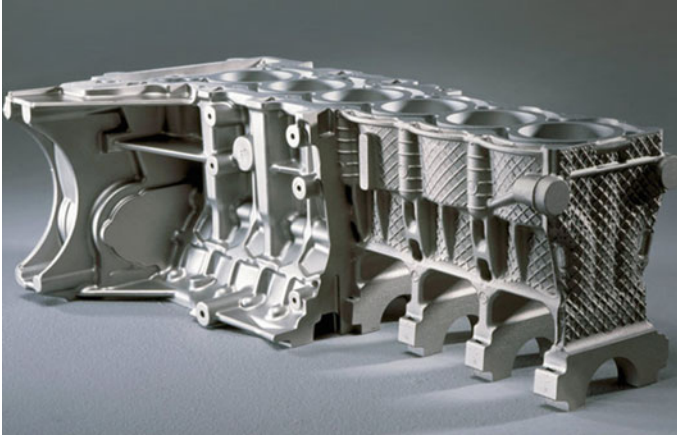
Fig. 4 The AJ62X BMW aluminum–magnesium composite crankcase housing [14]. (Color figure online)

research works, the microstructure of die-cast magnesium is described with a bimodal grain distribution [15], where a region of fine-grained grains is found close to the die surface [16], and a region of relatively coarse grains is found in the center of the cross section [17]. The microstructure of die-cast magnesium is further described as a primary magnesium matrix with relatively high aluminum concentration, containing both Mg–Al particles and Al–Mn inclusions [15, 17, 18]. This microstructure has a random texture [15] with a mean grain size in the range of tens of microns [18]. The skin region found close to the die surface resulting from faster solidification times is relatively free from porosity, and its thickness is dependent upon the local solidification conditions [16]. The core region found in the center of the casting consists of increased amounts of porosity [17], an increased amount of dendritic structures, and decreased hardness values [19]. Figure 5 shows microstructures of the skin and core region demonstrating these characteristics [20].
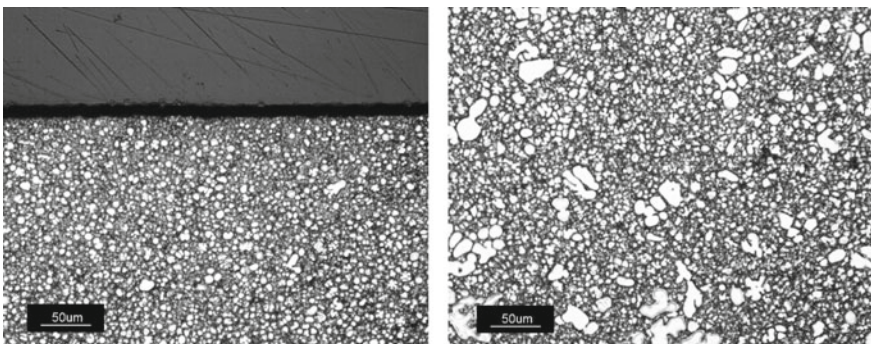
Fig. 5 Typical skin, left, and core, right, microstructures found in magnesium alloy die-castings [20]
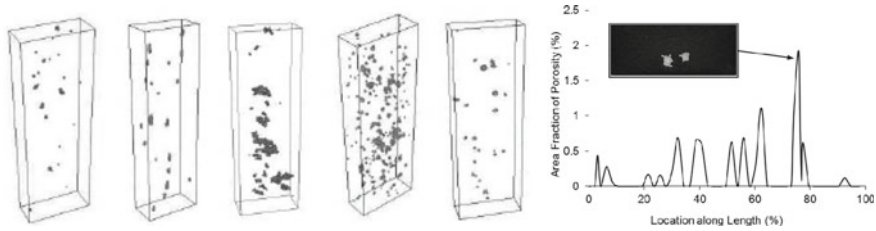
Fig. 6 Internal porosity detected by computed tomography of samples excised from regions of different solidification condition in a large magnesium die-cast component, left, and variation of areal fraction of porosity along length of coupon #4 from computed tomography data, right (Copyright Elsevier, 2005, used with permission) [25]

The properties of die-cast magnesium alloys have been found to depend upon the local microstructure [16, 17, 21–26] or casting conditions [27]. The size and location of internal porosity have demonstrated a significant effect on the tensile [17, 23–25, 28] and fatigue properties of die-cast magnesium [22]. In three separate studies completed on tensile samples with different solidification conditions, the internal porosity was characterized using x-ray tomography, as shown in Fig. 6, the evolution of porosity was described [28, 29], and the size of internal porosity was found to correlate analytically with the tensile elongations, and empirically with the fracture location in the gauge length [25, 28].

A smaller grain size in magnesium alloy die-castings results in improved creep resistance [19], a greater strain-hardening rate [24], greater tensile yield strengths [26], and improved corrosion rates compared with the core region [30]. The skin region, formed at the die walls during solidification from a rapid cooling rate forming a fine-grained microstructure, is primarily responsible for the shape of the tensile stress–strain flow curve [21] following a power-law hardening rule [15] and correlates with 4-point bending [23] and tensile flow strength [16] experimental results from different locations in a large thin-walled die-cast component. The tensile yield strength of die-cast magnesium can be accurately predicted using a modified Hall–Petch relationship developed through spherical microindentation considering both the skin and core regions [26]. At higher strain rates, the tensile yield strength [15] and compressive strength [31] were found to increase, while decreases in strain-hardening rate [15] were observed.

Several Canadian researchers have performed casting, solidification, and heat transfer studies on magnesium die-casting alloys through either die-casting experiments [27, 32, 33], simulated solidification studies [34, 35], or instrumented custom-designed equipment [36, 37]. Detailed analyses of different cooling rates of magnesium die-casting alloys have found that an increase in the cooling rate results in a larger quantity of intermetallic phases [32, 34] that also is affected by solute content [32]. The data created with these studies was also used to model the evolution of phase formation during solidification [34], and the latent heat of solidification [35]. These studies have also found that there is a strong influence of metal cleanliness on tensile elongation of die-cast magnesium [27]. Oxide contents less than 1000 ppm

were found to result in very little effect on AM60B tensile properties. Researchers investigating the influence of calcium content between 0.2% and 0.8% in AM50 found that an increasing amount of calcium resulting in reduced visual appearance, affected the operation of the die-cast cell, resulted in more dross, and decreased mechanical properties [33]. Finally, in a set of studies completed to determine the heat flow capability of different cooling devices, it was found that copper rods are capable of transferring heat with a rate of 435.5 BTU/hr [36], while isobars were found to result in 14% improved cooling capability when compared with copper rods [37], demonstrating their effectiveness.

Development of ICME Framework for Magnesium Die-Castings

The development of Integrated Computational Materials Engineering (ICME) tools for magnesium die-cast components is a very important research field with the advancement of automotive applications into more structural components, such as instrument panels and liftgate inners, among others. The designer of a magnesium die-cast component requires confidence that the material properties being represented by a material card in FE (finite element) simulations of the performance provide both an accurate and robust representation of the material in order to optimize the design. Further, new applications for magnesium die-casting will necessitate alloy compositions designed with specific properties to meet the requirements. Canadian researchers have contributed significantly to developing tools to optimize the alloy design process through thermodynamic databases [38], computationally developing predictive behavior of the solidification process of magnesium die-castings [39–41], developing models predicting process-structure-property relationships of magnesium die-cast alloys [29, 42–48], and applying process-structure-property relationships into material codes to predict the structural behavior of magnesium die-cast components [49–51]. Thermodynamic software and database packages, such as FactSage™, are routinely used to model phase diagrams and phase equilibria in alloy systems to predict freezing ranges and phase formations for magnesium die-cast alloys, among other data [38]. Canadian researchers have developed an optimization algorithm that searches these databases for the optimal conditions of multicomponent alloy systems to meet given criteria. The example of optimizing corrosion resistance of an existing magnesium alloy while maintaining existing properties is given, resulting in a complex composition [38]. Several Canadian researchers have developed computational and empirical models that predict the complicated solidification process during high-pressure die-casting of magnesium alloys considering directional solidification and precipitation of hydrogen gas over the entire solidification range [39], and the governing equations for fluid, solid, and mushy regions [40] both to predict shrinkage porosity, and the simulated local volumetric flow rate over the filling process to predict poor metal front conditions [41]. Figure 7 shows the
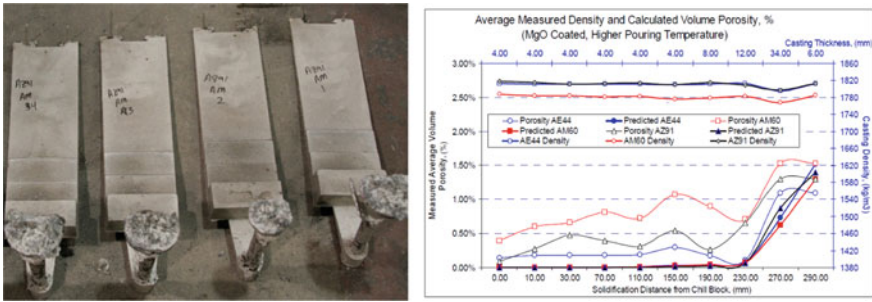
Fig. 7 Castings produced, left, and measured versus predicted volumetric porosity for three different alloys as part of the development of a computational model to predict porosity in magnesium die-castings. (Color figure online) (Copyright TMS, 2008, used with permission) [39]

castings produced and predicted and measured levels of volumetric porosity from a Canadian research group's work in developing a computational model to predict porosity [39].

Further, other groups have developed empirical relationships to predict the average local grain size for cooling rates typical of both sand- and die-cast processes [44], and the skin thickness in magnesium die-castings using heat transfer equations and predictive equations of the local grain size from cooling rates [42]. The local yield strength of magnesium die-castings has been predicted using a modified Hall–Petch relationship originally developed using spherical microindentation cyclic load–unload experiments on samples of varying average grain size [26]. This method, which utilizes the average grain sizes and relative thicknesses of the skin and core regions, was originally developed for the AM60B alloy and has shown validity for yield strengths of tensile coupons excised from an alternative AM60B cast component [42], from AZ91D, AE44, and AM60 gravity castings, and AZ91D and AE44 die-cast test plates [43–45]. The prediction of local tensile properties in a large die-cast component—ultimate tensile strength and elongation—has been predicted using a critical strain model and knowledge of the local porosity conditions [25]. The framework of the critical strain model was improved with additional investigations [43, 47, 48] to consider a strain concentration factor and the spatial location of the porosity in the cross-sectional area within the casting. These improvements simplified the input required and improved the predictions. The failure model predicts a maximum condition for porosity found centered in the cross-sectional area, and a reduced elongation as the porosity is located closer to the cast surface, reaching a minimum prediction using the thickness of the skin region [44]. This model was found to accurately predict the range of tensile elongations of coupons excised from AM60B cast components [42], and extended to AM60, AE44, and AZ91 gravity castings, and AE44 and AZ91 die-castings [46]. Figure 8 demonstrates the range of predicted tensile ductility of AM60B magnesium alloy from the location of the porosity in the cross-sectional area compared with experimental data of the size and location of porosity and the associated fracture strains [25, 42–44, 47, 48].
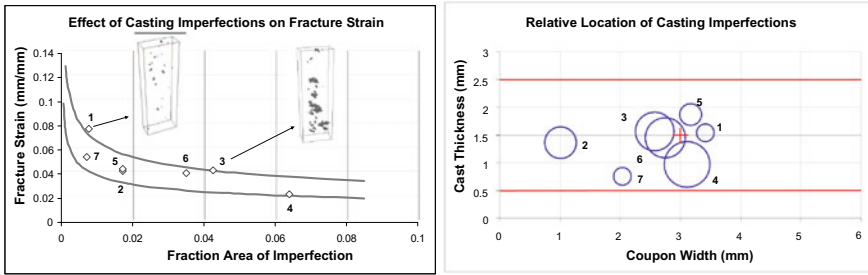
Fig. 8 Predicted range of tensile ductility from an analytical failure model, left, compared with experimental data considering both size and location of porosity, shown on right. (Color figure online) (Adapted from [43])

Canadian researchers have developed ICME tools for FE simulations of structural performance based on either material data obtained from coupon testing [49], reverse engineering a flow curve with a conservative failure prediction [50], or incorporating process-structure-property relationships into property predictions [51]. An FE material card was developed for AM50A die-cast magnesium alloy based upon coupon test results and fit to a Johnson–Cook constitutive model accounting for effects of strain and strain rate [49]. The validation of the material card was completed using static and dynamic testing of steering wheel armature cast components. From this study, it was determined that the largest error in the prediction of component performance was due to the non-homogeneous microstructure in the casting [49]. An alternative approach was taken by Alain et al. [50] who developed a material card for AM60B magnesium alloy by reverse engineering component performance coupled with a conservative failure criterion based on empirical data. The results of this work find a statistical conservative prediction of component performance failure, however, these authors state that a better understanding of structure–property relationships for large die-cast components is required [50]. This statistical conservative approach was refined in work completed more recently [51] where process-structure-property relationships were integrated into an FE material model to predict the performance of component bench testing. Figure 9 demonstrates the methodology. Local property variability and robustness were incorporated into FE performance simulations with the use of
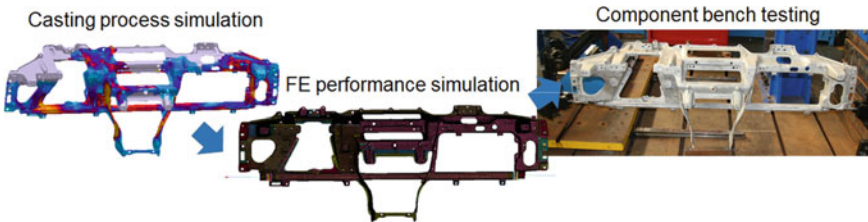

Fig. 9 Methodology presented to predict component performance incorporating process-structure-property relationships in FE models. (Color figure online) (adapted from [51])

casting process simulation results to calculate a unique material response for each FE element based upon its simulated process history. Validation of this approach shows excellent prediction of force–displacement characteristics and statistically conservative failure prediction to experimental results [51].

Joining and Corrosion Technologies for Magnesium Die-Castings

In a study completed by the United State Automotive Materials Partnership (USAMP), it was reported that joining and corrosion concerns were two of the major technology challenges to more magnesium usage in North American vehicles [52]. These are two of the areas of key research and development work by Canadian researchers for furthering magnesium die-casting implementation in the automotive industry. Canadian researchers have contributed to the research areas of joining and corrosion by developing a set of guidelines for utilizing self-threading fasteners with magnesium die-cast components [53, 54], and by developing design considerations and research into corrosion solutions and coatings for corrosion mitigation for magnesium die-castings [55–58]. A design for assembly using self-threaded fasteners is presented describing the approach to designing the hole diameter and tolerances to provide a sufficient torque assembly window for cast holes in die-cast magnesium components [53, 54]. These works further describe the effects of hole diameters, draft angles, and lengths of engagement upon the prevailing and failure torques and failure method of self-threaded fastened joints in magnesium die-castings. Design guidelines for magnesium die-cast components in automotive exterior applications are developed by Canadian researchers highlighting the considerations for sub-assembly processes with magnesium die-castings and mitigation methods for galvanic corrosion [55]. Canadian researchers investigate the severity of various accelerated cyclic corrosion test procedures to cosmetic and galvanic corrosion of die-cast magnesium and compare with in-field underbody exposure [56]. These comparisons find that each lab exposure results in a range of results, however, a more severe condition for cosmetic and galvanic corrosion than the 5 years of underbody exposure, providing validation of these exposures for a conservative magnesium die-cast product development. Further, Canadian researchers complete detailed electrochemistry investigations into various magnesium alloys, including a die-cast alloy, calculating breakdown, and repassivation potentials [57]. These researchers find that there is a difference in cyclic potentiodynamic curves between exposures to the skin and core regions of the die-cast magnesium alloy. Canadian researchers have also investigated developing low-energy plasma electrolytic coatings for die-cast magnesium alloys to reduce voltage and energy costs of these coating processes [58]. One particular study investigates a novel electrolyte solution and different exposure times to change the growth behavior of the resulting coating, as shown in Fig. 10 [58].
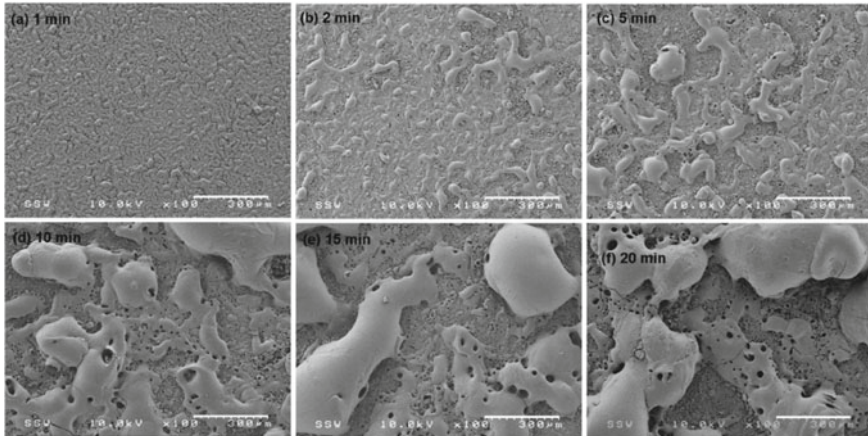
Fig. 10 SEM images of the different surface morphologies of PEO coating developed on AM50 for different durations from 1 to 20 min (Copyright 2019 Elsevier, used with permission) [58]

Development of Automotive Applications for Magnesium Die-Castings

Traditional application of magnesium die-casting in the automotive industry include transfer cases, brackets, and cross-car beams. However, more recently, new applications have been developed including roof frames, liftgate inners, door inners, and engine cradles [59]. Canadian researchers have been instrumental in leading the development of new automotive applications for magnesium die-castings and solving technical challenges to ensure successful products. These applications include developments to improve cross-car beams [60–62], front-end carriers [63, 64], and closure inners [61, 65, 66]. Canadian researchers have developed cross-car beams for numerous automobile manufacturers in the last 20 years, including General Motors [59], Mercedes Benz [60], Jaguar Land Rover [62], and Honda [61]. The performance-led design process [67], typical of these types of structural applications, resulted in significant weight reductions and part consolidation. These researchers developed products that, in one case, resulted in a weight reduction of 3.4 kg and a consolidation of 28 components into a single die-casting compared to an aluminum design [61]. An excellent example of the potential of magnesium die-castings in automotive applications is given in Ref. [62], where a platform-wide development for a cross-car beam was completed. The automobile manufacturer, in this case, improved attachment points and inefficiencies in attaching components to the cross-car beam to reduce mass, enable a dual-cavity die-cast tool, and eliminate all machining operations in the design [62]. Canadian researchers have also contributed to the development of front-end carriers through flexible design strategies for both welding-in and clip-on assembly methods [63, 64]. These designs have incorporated such features as headlamp locations and attachments, radiator mountings, and the hood latch [63]
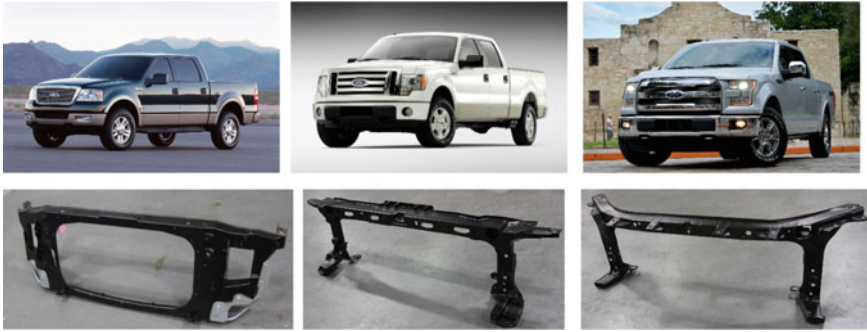
Fig. 11 Generations of magnesium radiator supports found on F-150 full-sized trucks, MY 2004, left, MY 2009, center, and MY 2015, right. (Color figure online) (Copyright 2017, IMA, Used with permissions) [64]

resulting in 8–9 kg of mass savings and a 16 component reduction compared with steel designs [63, 64]. An excellent example of design strategy evolution is provided in Ref. [64], where three generations of a magnesium radiator support casting for Ford F-150 full-sized trucks are summarized, and shown in Fig. 11. The design and corrosion mitigation evolution is detailed resulting in successive mass savings over the first generation magnesium design of nearly 60%, and 70%, respectively [64], while the improved design allowed for dual-cavity die-cast tools for the second and third generation designs. Canadian researchers have also been instrumental in developing closure inners for automotive applications, for both side doors [66] and rear liftgates [61, 65, 66]. These applications presented significant technical developments that required solutions for structural adhesives, coatings, corrosion, fastening, sealing, and sub-assembly, among others [65]. The magnesium die-casting liftgate inners in vehicle production resulted in mass savings of at least 40%, with a part reduction of at least 4 [61, 65, 66].

Key Canadian Magnesium Die-Casting R&D Programs

With a strong magnesium industry, as well as well-organized funding programs for automotive research, several different key R&D programs have been undertaken by Canadian researchers over the past 20 years. Two key programs that have been completed using federally funded R&D are the Canadian Lightweight Materials Research Initiative (CLiMRI) and Auto 21 Network of Centres of Excellence [68]. The Auto 21 R&D program was a 15 year Canadian program focusing upon automotive research and developing strong academic–industry connections [69]. Auto 21 was launched in 2001 at the University of Windsor, and coordinated and funded research programs through 48 academic institutions and academic partners focusing upon developing an improved Canadian automotive industry [69]. Successfully

funded projects ranged from materials and manufacturing through social sciences and humanities, including a project focusing on developing, mapping, and correlation mechanical properties with microstructure in complex magnesium die-cast components [68]. A project funded by Automotive Partnerships Canada (APC) and four Canadian companies contributed to reducing vehicle weight by up to 40% by using lightweight materials, including magnesium [70]. This project focused upon multi-material aspects in the automobile, including dissimilar metal corrosion, joining technologies, durability, computer modeling, crash modeling, and die-casting. A key component to this project is the high-pressure die-cast infrastructure developed at the CanmetMATERIALS laboratory in Hamilton, Ontario [70]. Further, a collaborative project completed by Meridian Lightweight Technologies, General Motors, and The Ohio State University focused on developing an integrated die-casting process for large thin-walled structural magnesium alloy panels [71]. This project was designed to improve the energy productivity of traditional steel stamping and joining processes by up to 50% and focused on developing new technologies for magnesium die-cast tooling, super vacuum, new alloy formulations, overcasting technology, and advanced process simulation tools [71]. Figure 12 shows the resulting side door assembly featuring the magnesium die-cast inner structure. Finally, in an international collaborative project between China, Canada, and the US, sponsored by Natural Resources Canada, magnesium as a major automotive structural material for a subsystem level material was evaluated [72]. Enabling technologies such as NVH, crashworthiness, corrosion and surface treatments, and joining and fastening technologies were researcher with the goal of creating and entire front-end structure with 50–60% mass savings [72].

Fig. 12 Side door assembly featuring a die-cast magnesium inner resulting from collaborative project completed by Meridian, General Motors, and The Ohio State University. (Color figure online) (Copyright, 2018, IMA, Used with permission) [71]

Conclusions

This paper endeavors to provide a thorough summary of the Canadian-led research and development of magnesium die-casting technology over the last 20 years. The work published in technological areas of alloy development, characterization of magnesium die-castings, ICME development for magnesium die-casting, corrosion and joining technologies, product development, and large-scale R&D programs was summarized by demonstrating the significant contribution to the field from Canadian researchers.

References

1. Government of Canada (2019) About CanmetMATERIALS website. https://www.nrcan.gc.ca/science-and-data/research-centres-and-labs/canmetmaterials/canmetmaterials/8234. Accessed 9 June 2020
2. Elsevier (2020) Scopus document search. https://www.scopus.com/home.uri. Accessed 6 May 2020
3. American Society for Testing and Materials (2018) ASTM B94–18. Standard specification for magnesium-alloy die castings, ASTM international, West Conshohocken, PA
4. Aragones J et al (2005) Development of the 2006 corvette Z06 structural cast magnesium crossmember. SAE Technical Paper 2005–01–0340. https://doi.org/10.4271/2005-01-0340
5. Baril E, Labelle P, Pekguleryuz MO (2003) Elevated temperature Mg-Al-Sr: Creep Resistance, Mechanical properties, and microstructure. JOM 55:34–39. https://doi.org/10.1007/s11837-003-0207-7
6. Forakis P, Richard E, Argo D (2002) Fluxless Refining of Clean Diecast Scrap for Noranda's AJ52 high temperature Mg-Al-Sr alloys. In: Kaplan HI (ed) Magnesium technology 2002. The minerals, metals and materials society, Warrendale, pp 12–17
7. Argo D et al (2002) Process parameters and diecasting of Noranda's AJ52 high temperature Mg-Al-Sr alloy. In: Kaplan HI (ed) Magnesium technology 2002. The minerals, metals and materials society, Warrendale, pp 18–24
8. Labelle P et al. (2002) New aspects of temperature behavior of AJ52x, creep resistant magnesium alloy. SAE Technical Paper 2002–01–0079. https://doi.org/10.4271/2002-01-0079
9. Pekguleryuz M et al (2003) Magnesium diecasting alloy AJ62X with superior creep resistance, ductility and diecastability. In: Kaplan HI (ed) Magnesium technology 2003. The minerals, metals and materials society, Warrendale, pp 201–206
10. Pekguleryuz M, Labelle P, Argo D (2003) Magnesium die casting Alloy AJ62x with superior creep resistance, ductility and die castability. SAE Technical Paper 2003–01–0190. doi: https://doi.org/10.4271/2003-01-0190
11. Baril E, Labelle P, Fischersworring-Bunk A (2004) AJ (Mg-Al-Sr) alloy system used for new engine block. SAE Technical paper 2004–01–0659. doi: https://doi.org/10.4271/2004-01-0659
12. Argo D, Forakis P, Lefebvre M (2003) Chemical composition and cleanliness during recycling of the AJ52 magnesium strontium alloy. In: Kaplan HI (ed) Magnesium technology 2003. The minerals, metals and materials society, Warrendale, pp 33–37
13. Argo D, Lefebvre M (2003) Melt protection for the AJ52 magnesium Strontium alloy. In: Kaplan HI (ed) Magnesium technology 2003. The minerals, metals and materials society, Warrendale, pp 15–21
14. Joslin B (2006) Inside the N52 Engine. In: merks.com. https://www.mwerks.com/artman/publish/features/printer_960.shtml. Accessed 11 June 2020

15. Xu S et al (2013) Dependence of flow strength and deformation mechanisms in common wrought and die cast magnesium alloys on orientation, strain rate and temperature. J Mag Alloys 1(4):275–282. https://doi.org/10.1016/j.jma.2013.11.003

16. Weiler JP et al (2006) Variability of skin thickness in an AM60B magnesium alloy die-casting. Mater Sci Eng A 419(1):297–305. https://doi.org/10.1016/j.msea.2006.01.034

17. Zhou M et al. (2006) Microstructure and mechanical properties of diecast magnesium alloy AM50 with varying section thickness. In: Luo AA, Neelameggham NR, Beals RS (eds) Magnesium technology 2006. The minerals, metals and materials society, Warrendale, pp 121–127

18. Gertsman VY et al (2005) Microstructure and Second-phase particles in Low- and High-Pressure die-cast magnesium alloy AM50. Metall Mater Trans A 36:1989–1997. https://doi.org/10.1007/s11661-005-0319-5

19. Han L et al. (2005) Observation of the microstructure and characterization of local mechanical properties of AM50 using a micro-indentation technique. In: Neelameggham NR, Kaplan HI, Powell BR (eds) Magnesium technology 2005. The minerals, metals and materials society, Warrendale, pp 197–202

20. Coultes BJ (2003) Mechanical property variations in a magnesium high-pressure die-cast component. M.E.Sc. thesis, University of Western Ontario

21. Weiler JP et al. (2005) Stress-strain response in skin and core regions of die cast magnesium alloy AM60B determined from spherical microindentation. In: Neelameggham NR, Kaplan HI, Powell BR (eds) Magnesium technology 2005. The minerals, metals and materials society, Warrendale, pp 191–196

22. Koch TA, Gharghouri MA (2003) Fatigue properties of die-cast magnesium alloy AM60B. In: Kaplan HI (ed) Magnesium technology 2003. The minerals, metals and materials society. Warrendale, pp 71–76

23. Coultes BJ et al. (2003) Mechanical properties and microstructure of magnesium high pressure die castings. In: Kaplan HI (ed) Magnesium technology 2003. The minerals, metals and materials society. Warrendale, pp 45–50

24. Hu H et al (2008) Tensile behavior and fracture characteristics of die cast magnesium alloy AM50. J Mater Pro Tech 201(1–3):364–368. https://doi.org/10.1016/j.jmatprotec.2007.11.275

25. Weiler JP et al (2005) Relationship between internal porosity and fracture strength of die-cast magnesium AM60B alloy. Mater Sci Eng A 395(1–2):315–322. https://doi.org/10.1016/j.msea.2004.12.042

26. Weiler JP et al (2005) The effect of grain size on the flow stress determined from spherical microindentation of die-cast magnesium AM60B alloy. J Mater Sci 40:5999–6005. https://doi.org/10.1007/s10853-005-1295-2

27. Wang GG, Froese B, Bakke P (2003) Process and Property relationships in AM60B die-castings. In: Kaplan HI (ed) Magnesium technology 2003. The minerals, metals and materials society, Warrendale, pp 65–69

28. Weiler JP et al (2006) Tensile fracture characteristics of die cast magnesium alloy AM60B determined from high-resolution X-ray tomography. In: Luo AA, Neelameggham NR, Beals RS (eds) Magnesium technology 2006. The minerals, metals and materials society, Warrendale, pp 405–410

29. Weiler et al (2007) Damage modeling of die-cast magnesium alloy AM60B. In: Paper presented at the 3rd international conference on light metals technology. Saint-Sauveur, Quebec

30. Zhang W et al. (2006) Skin and bulk corrosion properties of die cast and thixocast AZ91D Magnesium alloy in 0.05M NaCl solution. Can Metall Quart 45(2):181–188. https://doi.org/10.1179/000844306794408968

31. Weiler JP, Wood JT (2012) Strain-rate Effects of sand-cast and die-cast magnesium alloys under compressive loading. In: Mathaudhu SN, Sillekens WH, Neelameggham NR, Hort N (eds) Magnesium technology 2012. The minerals, metals and materials society, Warrendale, pp 365–370. https://doi.org/10.1007/978-3-319-48203-3_67

32. Kang DH et al (2010) Experimental studies on the As-cast microstructure of Mg-Al binary alloys with various solidification rates and compositions. In: Agnew SR, Neelameggham NR,

Nyberg EA, Sillekens WH (eds) Magnesium technology 2010. The minerals, metals and materials society, pp 533–536

33. Berkmortel J et al (2000) Die castability assessment of magnesium alloys for high temperature applications: Part 1 of 2. SAE Technology Paper 2000–01–1119. https://doi.org/10.4271/2000-01-1119

34. Marchwica PC et al (2012) Combination of cooling curve and microchemical phase analysis of rapidly quenched magnesium AM60B alloy. In: Mathaudhu SN, Sillekens WH, Neelameggham NR, Hort N (eds) Magnesium technology 2012. The minerals, metals and materials society, pp 519–524. https://doi.org/10.1007/978-3-319-48203-3_92

35. Gesing AJ et al (2013) Cooling curve and microchemical phase analysis of rapidly quenched magnesium AM60B and AE44 alloys. J Achiev Mater Manuf Eng 58(2):59–73

36. Farrokhnejad M, Berkmortel R (2016) Investigation of the effectiveness of cooling bars used in the die for magnesium high pressure die-casting (HPDC). In: Paper presented at the North American die casting association 2016 die casting congress and tabletop. Columbus, Ohio

37. Farrokhnejad M, Weiler J (2017) Investigation of the effectiveness of heat pipes used in the die for magnesium high pressure die casting. In: Paper presented at the North American die casting association 2017 die casting congress and tabletop. Atlanta, Georgia

38. Gheribi AE et al (2012) Identifying optimal conditions for Mg alloy design using thermodynamic and properties databases, the Factsage software and the mesh adaptive direct searches algorithm. In: Paper presented at the 9th international conference on magnesium alloys and their applications. Vancouver, British Columbia

39. Li JM et al (2008) Thermodynamic modeling of porosity formation during non-equilibrium solidification in magnesium alloy castings. In: Pekguleryuz MO, Neelameggham NR, Beals RS, Nyberg EA (eds) Magnesium technology 2008. The minerals, metals and materials society, pp 105–111

40. Farrokhnejad M, Straatman AG (2012) Advances on a VOF based numerical simulation of Mg Die-casting process on a general unstructured grid. In: Paper presented at the 9th international conference on magnesium alloys and their applications. Vancouver, British Columbia

41. Weiler JP et al (2012) Prediction of knit line formations in complex high pressure die cast magnesium alloy components. Int J Cast Metal Res 25(6):379–382. https://doi.org/10.1179/1743133612Y.0000000029

42. Sharifi P (2015) Process-structure-property correlations for HPDC AM60B. In: Manuel MV, Singh A, Alderman M, Neelameggham NR (eds) Magnesium technology 2015. The minerals, metals and materials society, pp 351–356. https://doi.org/10.1007/978-3-319-48185-2_65

43. Weiler JP et al (2010) Structure-property relationships for die-cast magnesium alloys. In: Agnew SR, Neelameggham NR, Nyberg EA, Sillekens WH (eds) Magnesium technology 2010. The minerals, metals and materials society, pp 413–318

44. Weiler JP, Wood JT (2012) Predicting mechanical performance from process parameters in cast magnesium alloys: a review of the UWO research programme. In: Paper presented at the 9th International conference on magnesium alloys and their applications. Vancouver, British Columbia

45. Sharifi P (2014) Predicting the flow stress of high pressure die cast magnesium alloys. J Alloy Comd 605:237–243. https://doi.org/10.1016/j.jallcom.2014.03.043

46. Weiler JP, Wood JT (2012) Modeling the tensile failure of cast magnesium alloys. J Alloy Comd 537:133–140. https://doi.org/10.1016/j.jallcom.2012.05.090

47. Weiler JP, Wood JT (2009) Modeling fracture properties in a die-cast AM60B magnesium alloys I—Analytical failure model. Mat Sci Eng A 527(1–2):25–31. https://doi.org/10.1016/j.msea.2009.08.060

48. Weiler JP, Wood JT (2009) Modeling fracture properties in a die-cast AM60B magnesium alloy II—The effects of the size and location of porosity determined using finite element simulations. Mat Sci Eng A 527(1–2):32–37. https://doi.org/10.1016/j.msea.2009.08.061

49. Alternof W et al (2004) Numerical simulation of AM50A magnesium alloy under large deformation. Int J Impact Eng 30(2):117–142. https://doi.org/10.1016/S0734-743X(03)00060-5

50. Alain R et al (2004) Robustness of large thin wall magnesium die castings for crash applications. SAE Technical Paper 2004–01–0131. https://doi.org/10.4271/2004-01-0131
51. Weiler JP (2018) Incorporating an ICME approach into die cast magnesium alloy component design. JOM 70:2338–2344. https://doi.org/10.1007/s11837-018-2985-y
52. USAMP (2011) Magnesium vision 2020: a north american automotive strategic vision for magnesium. USCAR, Detroit, Michigan
53. Wang GG, Bos J (2018) A study on joining magnesium alloy high pressure die casting components with thread forming fasteners. J Mag Alloy 6(2):114–120. https://doi.org/10.1016/j.jma.2018.04.002
54. Burns JR, Jekl J, Berkmortel R (2012) Designing for Assembly with thread forming fasteners in magnesium. In: Paper presented at the 9th international conference on magnesium alloys and their applications. Vancouver, British Columbia
55. Wang GG et al (2001) Corrosion prevention for external magnesium automotive components. SAE Technical Paper 2001–01–0421. https://doi.org/10.4271/2001-01-0421
56. Weiler JP, Wang G, Berkmortel R (2018) Assessment of cyclic corrosion test protocols for magnesium substrates. SAE Int J Mater Manuf 11(4):481–490. https://doi.org/10.4271/2018-01-0103
57. Hu Y et al (2012) Effect of some microstructural parameters on the corrosion resistance of magnesium alloys. In: Mathaudhu SN, Sillekens WH, Neelameggham NR, Hort N (eds) Magnesium technology 2012. The minerals, metals and materials society, pp 271–276. https://doi.org/10.1007/978-3-319-48203-3_50
58. Dehnavi V et al (2018) Growth behavior of low-energy plasma electrolytic oxidation coatings on a magnesium alloy. J Mg Alloy 6(3):229–237. https://doi.org/10.1016/j.jma.2018.05.008
59. Luo AA (2013) Magnesium casting technology for structural applications. J Mg Alloy 1(1):2–22. https://doi.org/10.1016/j.jma.2013.02.002
60. Fackler H, Berkmortel R (2016) Design and optimization of magnesium cross car beam for the new mercedes GLC. In: Paper presented at the international magnesium association's 73rd annual world magnesium conference. Rome, Italy
61. Berkmortel R et al. (2015) Magnesium applications in the automotive industry and the development trends. In: Paper presented at China Die casting 2015, Shanghai, China
62. Tippings A et al (2014) Development of a high pressure die cast magnesium cross car beam for automotive 'platform" application. In: Paper presented at the international magnesium association's 71st world magnesium conference, Munich, Germany
63. Tippings A, Lawson T (2005) Design and development of a high pressure die 'FEC' (Front End Carrier) for exterior automotive applications. In: Paper presented at the international magnesium association's 62nd World Magnesium Conference, Berlin, Germany
64. Adams A et al (2017) Third generation Ford F-150 die-cast magnesium radiator support evolution. In: Paper presented at the international magnesium association's 74th world magnesium conference, Singapore
65. Weiler JP et al (2016) Next generation magnesium liftgate—utilizing advanced technologies to maximum ass reduction in a high volume vehicle application. In: Paper presented at the International magnesium association's 73rd annual world magnesium conference. Rome
66. Weiler JP (2019) A review of magnesium die-castings for closure applications. J Mag Alloy 7(2):297–304. https://doi.org/10.1016/j.jma.2019.02.005
67. Simonds G, Wang J (2002) Structural Magnesium Die castings. Developing a robust solution. In: Paper presented at the international magnesium association's 59th world magnesium conference. Montreal, Quebec
68. Jackman JA et al (2005) Overview of key R&D activities for the development of high-performance magnesium materials in Canada. Mater Sci Forum 488–489:21–24. https://doi.org/10.4028/scientific.net/MSF.488-489.21
69. Macaluso G (2016) A look back at 15 years of research and innovation at Auto21. Windsor Star. https://windsorstar.com/business/local-business/a-look-back-at-15-years-of-research-and-innovation-at-auto21/. Accessed 9 June 2020

70. Automotive Partnerships Canada (2013) Industry drives Canadian research effort to build lighter and greener vehicles. Automotive Partnerships Canada website, https://www.apc-pac.ca/About-Renseignements/Project-Project_eng.asp?ID=19. Accessed 9 June 2020
71. Jekl J et al (2015) Development of a Thin-Wall Magnesium Side Door Inner Panel for Automobiles. Paper presented at the International Magnesium Association's 72nd World Magnesium Conference, Vancouver, British Columbia
72. Luo AA et al (2008) Magnesium front end research and development: a Canada-China-USA Collaboration. In: Pekguleryuz MO, Neelameggham NR, Beals RS, Nyberg EA (eds) Magnesium technology 2008. The minerals, metals & materials society, Warrendale, pp 3–10. https://doi.org/10.1007/978-3-319-48099-2_6

MAXImolding: Vertical Semi-Solid Magnesium Alloy Injection Molding Machine for Mega Volume Production

Edo Meyer and Ashley Stone

Abstract The four semi-solid metal casting processes Thixomolding®, Thixocasting®, rheocasting, and stress induced melt activation are very complex and highly maintenance intensive. The cold chamber die-casting and the hot chamber die-casting did not fulfill end user expectations for quality, energy savings, and environmental sustainability. We dedicated all our working life to solve two problems: production of high-integrity net-shape light metal parts, while reducing porosities in moldings (castings). We are fully committed to improving the current non-sustainable approach of molding, inspecting, separating, and re-melting. The Team of MAXImolding invented and patented [1–5] a new vertically oriented, environmentally friendly Semi-Solid Metal Alloy Injection Molding Machine. The molding processing parameters are optimized without a human operator by closing a real-time X-ray feedback control loop based on the parts "quality indicators and proper AI algorithms" [2, 5]. This is an intrinsically safe, energy and material efficient, environmentally sound magnesium-molding self-learning smart factory with no emissions outside of factory parameters limits.

Keywords Thixomolding® · Maximolding · Semi-solid · Semi-solid metal alloy injection molding · Magnesium alloy molding · Multi-injector metal molding · Multi-layer metal molding · High-integrity net-shape light metal parts · Zero emission

Introduction

The continuous quest for weight reduction has focused our technological developments on magnesium alloys as the most promising material. Magnesium is the eighth most abundant element in the Earth's crust and the fourth most common element in the Earth. Magnesium is the lightest of all structural metals, see Fig. 1. A unique blend of low density, high specific strength, stiffness, high electrical conductivity,

E. Meyer (✉) · A. Stone
MAXImolding! Technology GmbH, Scheichenbergstraße 36, 83313 Siegsdorf, Germany
e-mail: em@maxi-molding.com
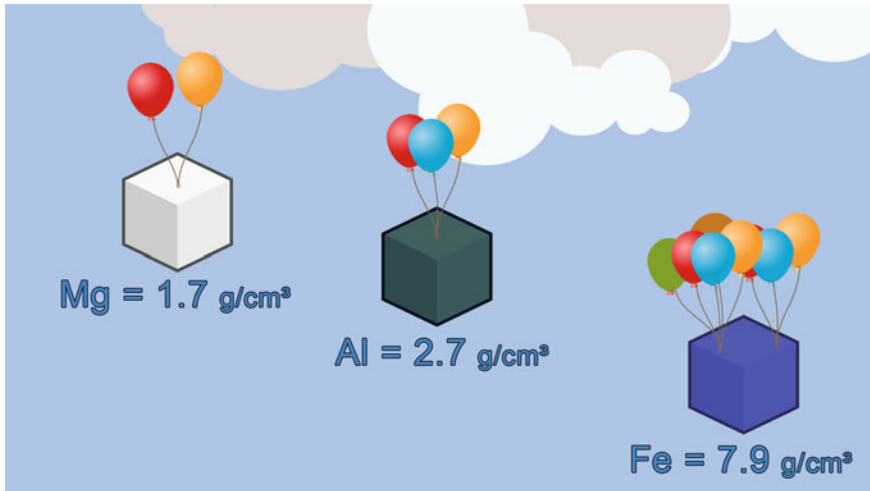
Fig. 1 Lightweight of magnesium is 2/3 of that of aluminum and 1/4 of steel. (Color figure online)

high heat dissipation, and absorption of vibration makes the magnesium best suitable to support daily activities of humans in almost every aspect of our lives and to sustain a higher quality of life. When combined with easy machining, molding, forming, and very simple recycling, magnesium can be the material of the future. And, even if you do not recycle it, it becomes MgO and thus a part of nature. Compared with plastics, which had huge growth over the last 50 years, magnesium improves on many qualities, without downsides. Magnesium does not adversely affect wildlife and humans and is readily available.

Semi-solid metal injection molding is a molding process that involves filling a mold with the metal in a partially molten state in which globules of solid are homogeneously dispersed in the liquid. The four currently used semi-solid metal casting processes, Thixomolding®, Thixocasting®, Rheocasting®, and stress induced melt activation (SIMA), are complex to start and very highly maintenance intensive. The processes, cold or hot chamber die-casting or vacuum die-casting, do not fulfill end user expectations for quality, simplicity, energy savings, safety, economy, and environmental responsibility. This is where our MAXImolding process comes in and further simplifies and improves the Thixomolding® process. We start with mechanically stressed chips or favorably configured chips. The selected chips are fed into a pre-conditioning unit and pre-heating processor. The chips are heated with a precise temperature control under Argon in our vertical injection molding machine.

We call this process solid-to-solid molding because we start with solid chips, produce semi-solid slurry, and end with solid net-shape parts out of the mold. Process is fully enclosed in MAXImolding machine. We use a very small amount of Argon to prevent the oxidation of chips.

Solid-To-Solid: New Magnesium Semi-Solid Metal Injection Molding Process

Thixomolding® is very similar to plastic injection molding in its machinery, tooling, and process fundamentals. Designers with experience in plastic injection part design are typically familiar with designing Thixomolded products. Table 1 gives an overview of historical semi-solid process steps.

Dr. Frank Czerwinski has been working for decades in the research fields of "Semi-Solid Metal Metallurgy" and improvements of Magnesium Injection Molding Machines. He wrote in his book [3] that the generation of thixotropic slurry containing spherical solid particles in the melt can be done in the thermal mass reactor under the sole influence of heat. Figure 2 shows the process and the microstructure of the alloy.

The adopted process does not require screw rotation. It is not necessary to shear the chips to produce semi-solid slurry that contains spherical solid particles in the melt. Precise temperature control of chips fed under gravitation from the top to the bottom of the reactor is only what is required. Elimination of screw for shearing is a major simplification of the process.

The adopted process does not require screw rotation. It is not necessary to shear the chips to produce semi-solid slurry that contains spherical solid particles in the melt. The generation of thixotropic slurry that contains spherical solid particles in the melt can be done in the thermal mass reactor under the sole influence of heat.

Table 1 Historical semi-solid process steps

Process	Feed material	Conditions in the processing barrel	Inventive steps comparisons
Rheocasting (Flemings '544) US Pat. No. 3,902,544	Semi-solid metal slurry produced in separate slurry producer	Constant temperature—no shear	2-step (requires slurry producing machine)
Thixocasting (Flemings 1976)	Partially remelted SSM slugs	Constant temperature—no shear	2-step (requires SSM billets or Ingots)
Thixomolding® (Bradley '589) US Pat. No. 5,040,589	Metal pellets	Heating and shear	1-step
Rheomolding Cornell WO 95/34,393 (Cornell Research Foundation)	Liquid metal	Cooling and shear	1-step
S2S™- MAXImolding (Stone '386) US Pat. No. 10,046,386	Comminuted chips or chips already made with preferred metallurgical spherical structure	Fast Heating—No shear	1-step
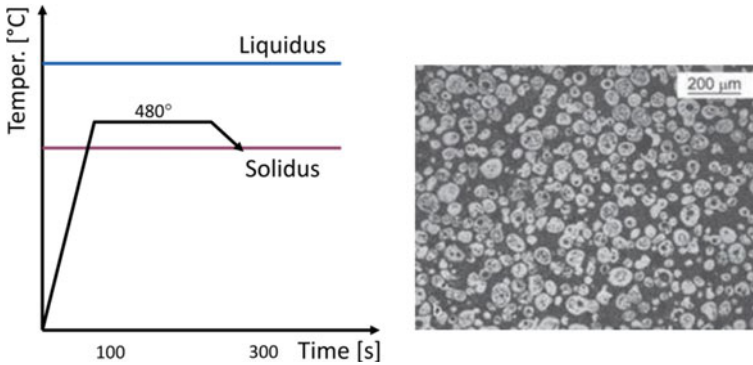
Fig. 2 MAXImolding works in the semi-solid temperature range between 480 and 580 °C for the AZ91 alloy. The microstructure of the alloy has spherical, non-dendritic features with 50% solids (Dr. Frank Czerwinski). This avoids the formation of defects. (Color figure online)

Precise temperature control of chips fed under gravitation from the top to the bottom of the reactor is only what is required.

Vertical Semi-Solid Magnesium Alloy Injection Molding Machine

The core of the idea starts with the question: How can you build a hybrid machine that can produce highly integrated parts that are nearly defect-free with little energy and material very quickly and without environmentally harmful gas emissions? A machine that combines the advantages of Thixomolding® and hot and cold chamber high pressure die-casting machines (HPDC) and avoids their disadvantages? The answer to this is offered by semi-solid (semi-liquid) metal injection molding. A molding process in which a mold is filled with the metal in a partially molten state. The advantages of this procedure are as follows:

- lower energy consumption and increased mold life,
- no handling of liquid metal,
- less solidification shrinkage,
- less susceptible to gas inclusions or defects,
- better yield from the raw material,
- and much more.

The MAXImolding machine is the result of an advanced development of the magnesium injection molding machine. Advancing Thixomolding® technology and eliminating major disadvantages of Thixomolding®, namely, the extruder with a screw, resulted in MAXImolding vertical oriented processor—many improvements

compared to the environmentally un-friendly, high-energy consumption hot and cold chamber high pressure die-castings (HPDC) machines.

As known, most products made from magnesium today are being made by die-casting. Magnesium casting was left behind in the technology curve. However new semi-solid metal injection molding machines offer much improved processing capability. For example, the new machine does not require a melting pot of overheated molten magnesium during casting that requires the SF_6, SO_2, or R134a cover gas (greenhouse gas pollutant) and does not need the energy to maintain the molten metal in an overheated molten state. Rather, solid magnesium particulates can be used. The chips, with preferred structure, are fed into the magnesium main processor that (by adding heat) converts the solid magnesium into a semi-solid slush of material. This material structure flows like a mixture of water and fine ice and operates at temperatures often 200 °C below the current Magnesium die-casting processing temperatures resulting in significant energy advantages. This semi-solid magnesium alloy is injected into a permanent mold, very similar to plastic molding processing. Our process is fully enclosed; solid-to-solid part injection molding machines can be operated in ordinary manufacturing plants.

The simplicity of the process makes it easy to operate in any region of the world without the need for extensive training. The MAXImolding vertical orientation saves floor space and improves material flow. Fully automated part removal is easily integrated by simple robotic devices. Magnesium solidification in the mold releases captured heat via an innovative heating/cooling process. MAXImolding recycles this heat by pre-heating the input magnesium chips. The energy savings alone allow the costs of parts to be competitive in the market compared to any other magnesium process known today. Carbon credits generated by this technology could be suitably marketed and sold as carbon shares on the open market to those who need to operate plants with high CO_2 output.

To be able to improve on energy, reduce maintenance and improve on output quality, we replaced the barrel and screw with a new high thermal mass reactor in form of a revolver cylinder. We drilled eight smaller processing cavities for AZ91D-chips entering from the top, four on each left and right side and a larger one in the middle of cylinder for injection piston. Heaters are placed around the cylinder and nuzzle from the top to bottom for uniform and precise heating. Lower platen with mold opens downwards. The removal of parts is simply done by any side entry device. Replacing the extruder with a high thermal mass reactor led to a precise temperature control and thus a more efficient and less maintenance intensive process is accomplished. Figures 3 shows the schematic of the MAXImolding machine.

Processing the Magnesium

Let's start with the source material and preparation in the MAXImolding machine. Metal shavings, also called chips, are fed to a hopper with a levitation preprocessor for cleaning, where the chips are heated up to 200 °C with a precise temperature
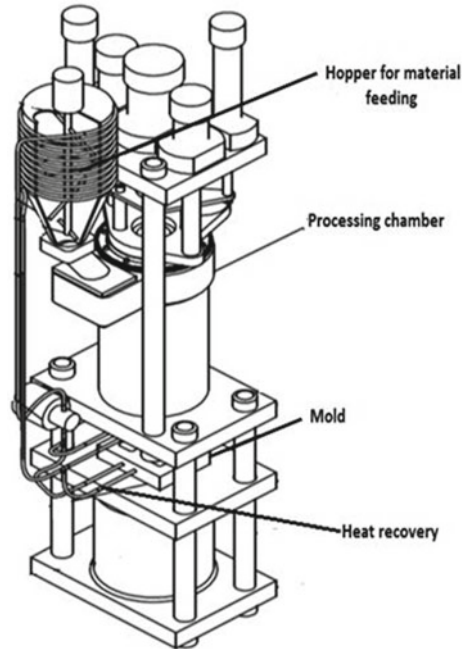
control under argon. Oxidation is avoided by flooding with argon. The chips are then continuously dosed into the vertical injection molding machine and slowly heated from top to bottom. The heat returned from the mold is used to preheat the starting material (chips). The Mg chips coming from the preprocessor are preheated to approx. 200 °C. Further heating happens with argon in the thermal reactor in the form of a revolver. This is done through several heating zones attached to the outside wall of the cylinder. The semi-solid slurry is collected in a chamber. This viscous mass is then precisely injected into the mold via two positive valves through a centrally positioned injection piston at a high pressure of 1.000 bar and high speed up to 12 m/s. The whole process requires a vertical path of only 1.5 m, which means that the foundry line is shrinking to 4, 5 m only. This makes the process more manageable.

In the new machine, the stock material (AZ91D chips) or specially formulated chip alloys are then re-heated to the desired forming temperature and injected into the mold while in the semi-solid state. The semi-solid metal mixture (slurry) is produced on demand and injected directly into the mold. The heated magnesium pathways and nozzle shutoff greatly reduces the total cycle time and improve part quality while keeping energy consumption low.

MAXImolding: Less Energy and Material Usage

A recent study done by Neue Materialien Fürth GmbH, Germany [4] compared a number of currently used processes for energy and material consumption for finished engine bracket (net weight 430 g, red line). It shows the great advantage of the Thixomolding® (injection molding). The reduction of energy consumption is at around 60% and material usage at around 50% in comparison to cold chamber die-casting. The MAXImolding machine reduces estimated energy consumption by approx. 30% compared to a 220t-JSW Thixomolding® machine with hot runner as seen on chart in Fig. 4.

Advanced applications for the MAXImolding machine should be explored in future research. Possible advancements could be

- molding parts consisting of different layers,
- the use of different feedstock composition in different areas of the part,
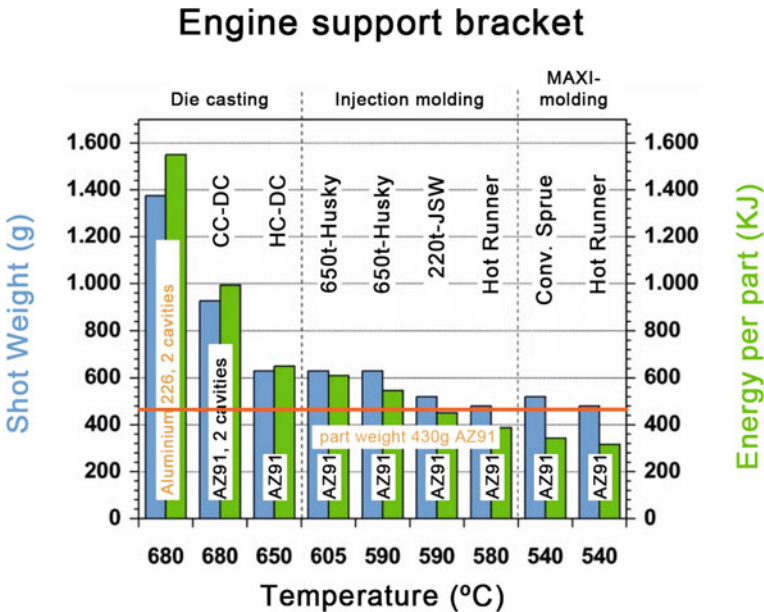- multi-injector usage for molding parts with large surface areas.

Fig. 4 Representation of the energy input and the shot weight for a 430 g engine support bracket depending on the process (Dr. Lohmüller, NMF GmbH). (Color figure online)

Conclusion

This new solid-to-solid process, combined with an X-ray feedback control loop and applied mathematics (AI, machine learning, big data mining, etc.) as well as the use of self-contained fully operated modules based on the new HyperComMachinery [6] concept, can revolutionize the classical die-casting and injection metal molding industry. The semi-solid magnesium metal alloy injection molding machine is able to operate and create a fully automated molding factory. It will ensure the fast production of good parts and maintain a stable automatic closed-loop process control.

This is an intrinsically safe, energy and material efficient, environmentally sound magnesium-molding factory with no emission of gases outside of factory parameters. All molding machines and X-ray inspection machines, as well as proprietary linear robotics and machine vision systems integrated into this semi-solid injection molding process, will ensure the fast production of good parts and maintain stable automatic closed-loop process control wherever you are on this planet. The collection of process data for the same or similar parts worldwide (planetary molding) will be accessible via cloud and everybody can use it to start up and improve their processes of magnesium molding.

Appendix

Additional material (Table 2).

Table 2 MAXImolded parts have several advantages compared with die-casting and Thixomolding®

Item	Die-Casting		Thixomolding®	MAXImolding
	Hot-Chamber	Cold-chamber		
Molding temp. (°C)	630–650	680–700	580–600	480–580
Injection speed (m/s)	1–4	1–8	1–4	1–12
Injection pressure (kgf/cm^2)	250–350	400–2.000	500–1.200	500–1.200

(continued)

Table 2 (continued)

Item	Die-Casting		Thixomolding®	MAXImolding
	Hot-Chamber	Cold-chamber		
Material	Ingot direct in machine at 650 °C	Ingot in melting pot at 700 °C	Chip direct in machine	Pre-processor takes feedstock paletts and de-contaminates, degreases, dries and pre-heats them uniformly to max. 200 °C and doses them in the machine
Projected area at same clamping force	Large	Medium	Medium	Larger because of direct gate injection, no sprue, no runners
Max. machine size	900t	4.500t	1.600t	5.000t + , limited by press tonnage only; multi-injector usage
Air inclusions	Small	Many	Few	Few
Surface defect	Small	Many	Few	Few
Shrinkage crack	Small	Few	Few	Few
Fluidity	Good	Good	Excellent	Excellent + +
Surface roughness	Good	Good	Excellent	Excellent
Flash	Few	Much	Small	Few
Shrinkage	Small	Many	Few	Few
Mold shrinkage(%)	0,5–0,55	0,7–0,8	0,38–0,45	0,38–0,45
Dimension accuracy	Good	Poor	Excellent	Excellent
Warp	Small	Much	Few	Few
Mechanical properties	Good	Good	Excellent	Excellent + +
Corrosion resistance	Good	Poor	Good	Good
Shot cycle	0.8	0.9	1 (Standard)	0.8
Material cost	0.85	0.9	1 (Standard)	1
Material yield	1	1.2	1 (Standard)	0.8
Die's life	0.9	0.8	1 (Standard)	1.4
Safe operation	Good	Poor	Excellent	Excellent +
Protection gas	SF6/SO2	SF6/SO2	Ar	Ar
Dross/Sludge	Much	Much	Nothing	Nothing

References

1. Stone A (2018) Device For Casting. US. Patent 10,046,386. 14 August 2018
2. Stone A (2020) Self-learning production systems with good and/or bad part variables inspection feedback. US. Patent 10,528,024
3. Czerwinski F (2008) Magnesium injection molding. Springer, New York
4. Lohmüller A, Körner C, Singer RF (2012) Neue Gießtechnologien: Ressourceneffizient und wirtschaftlich. In: Neugebauerv R (ed) (Hrsg.): Ressourceneffiziente Technologien für den Powertrain; International Chemnitz Manufacturing Colloquium ICMC 2012, S. 67–81
5. Stone A (2020). In: Portal Spotlightmetal. Vogel Communications Group, Germany. https://www.spotlightmetal.com/part-4--new-casting-machine-replaces-complete-casting-line-a-903753/ https://www.spotlightmetal.com/part-5--fully-automated-self-learning-digital-casting-factory-a-903305/ Accessed 9 January 2021
6. HyperComMachinery concept from Jacobsen X-Ray Canada defines self-contained fully operated modules that flow seamlessly into factory SCADA system according to the CEO's ultimate wish—one software for the whole factory!

The Effect of Process Parameters on the Microstructure of Semi-solid Slurry of AZ91 Magnesium Alloy Produced Through Inert Gas Bubbling

S. G. Shabestari and Y. Najafi

Abstract The inert gas bubbling causes local and rapid heat extraction combined with the convection using a stainless steel porous tube in temperatures above liquidus of the magnesium alloy. In this investigation, the effect of argon inert gas bubbling on the microstructure of AZ91 magnesium alloy has been studied. Different parameters such as the argon gas flow rate of 2, 4 L/min; the injection temperature of 610, 620 °C; and the injection duration of 10, 15, 20 s have been investigated. Thermal analysis has been carried out in AZ91 alloy to find the liquidus temperature and the solid fraction at different temperatures during solidification. Microstructural study showed that this semi-solid process changed the microstructure of AZ91 from dendritic to globular state. Image analysis has been used to study the microstructural constituents. Among key parameters studied, the inert gas flow rate had the major effect on the globularity and the grain size. The results showed that at the optimum condition of the gas flow rate of 4 L/min, gas purging temperature of 610 °C, gas purging time of 10 s, the globularity of 0.75, the average α-Mg globule size of 58.4 μm, and the average number of 168 α-Mg globules per unit area were achieved.

Keywords AZ91 magnesium alloy · Thermal analysis · Gas-induced semi-solid process · Globular structure

Introduction

Magnesium alloy is the lightest commercial structural metallic material. Magnesium alloys have been widely used in automotive, communication, electronics, and aerospace industries because of their high specific strength and stiffness, good damping properties, excellent machinability, cast ability, and recyclability [1–3]. However, Mg alloys have poor formability and limited ductility at room temperature due to their hexagonal closed packed (hcp) structure with limited slip systems. Many attempts have been made to improve the formability of wrought magnesium alloys.

S. G. Shabestari (✉) · Y. Najafi
School of Metallurgy and Materials Engineering, Iran University of Science and Technology (IUST), Narmak, Tehran, Iran
e-mail: shabestari@iust.ac.ir

Microstructural refinement is a best and effective way for increasing both ductility and strength of these alloys [3–5].

The solidification characteristics of AZ magnesium alloys in various cooling conditions were investigated through computer-aided cooling curve thermal analysis technique (CA-CCTA) [6]. The effects of different alloying elements such as Sr and Sn additions on solidification parameters, microstructure, and mechanical properties of AZ magnesium alloys were also studied [7, 8]. These elements can act as the grain refiner or create different intermetallic compounds to improve mechanical properties of the alloys.

Flemings et al. [9–11] introduced semi-solid as a new concept in metals during modeling of hot tear propagation in steel casting in 1972. Since then, a variety of semi-solid techniques have been developed. Semi-solid processes postpone the onset of dendrites impingement and lead to produce sound casting parts. To achieve superior mechanical and physical properties, semi-solid casting methods were developed in order to improve the microstructure morphology and formation of a non-dendritic microstructure of the alloy during the casting and solidification. A number of processes have been developed to prepare high-quality semi-solid slurry, such as mechanical stirring, electromagnetic stirring, and ultrasonic vibration [12–15]. Gas-Induced Semi-Solid (GISS) process is a newly developed technique, in which the preparation of semi-solid slurry is carried out by applying Ar gas bubbling during the early stage of solidification. Compared with other processes, GISS seems to be more convenient, sufficient, and economic [16]. Wannasin et al. [17, 18] proved that GISS process was capable of preparing fine semi-solid slurry of several Al alloys. They also found that GISS was well coordinated with die casting, squeeze casting, and gravity casting processes. Shabestari et al. [19, 20] studied the semi-solid processing of Al-4.3%Cu (A206) alloy through GISS process in different conditions. They found that inert gas purging into the melt led to temperature drop of the melt to its liquidus temperature. In fact, copious nucleation is induced by cooling effect of inert gas bubbles and leads to the microstructural modification from fully dendritic to globular structure.

However, there were not many researches done on the semi-solid slurry of Mg alloys and the influence of the process parameters in GISS. A systematic study of effects of inert gas bubbling parameters on semi-solid microstructure of Mg alloy is scarce. In this study, the effect of semi-solid process of AZ91 magnesium alloy through inert gas bubbling on the solidification parameters and microstructural features has been investigated.

Table 1 Chemical composition of AZ91 magnesium alloy

Element	Al	Zn	Mn	Mg
Content (wt%)	9.45	0.91	0.14	Bal.

Experimental Procedure

Material

Commercial AZ91 magnesium alloy ingot was used in this research. The chemical composition of AZ91 magnesium alloy used in this study was determined by an inductively coupled plasma analyzer (ICP) and the result is presented in Table 1.

Thermal Analysis

Cooling curve thermal analysis was conducted by re-melting and pouring of approximately 200 g of AZ91 magnesium alloy into a thin-wall stainless steel cup at the temperature of 650 °C. Thermal analysis was implemented in this research as well as conventionally cast sample via CA-CCTA new technique which was described elsewhere [6, 14]. The thermocouple was used, shielded by stainless steel sheath, and linked to a high-speed data acquisition system connected to a notebook computer. The analog-to-digital converter ADAM-4018 used in this study has a sensitive 16-bit microprocessor-controlled sigma-delta A/D converter, which has a response time of 0.02 s and eight channel analog input modules that provide programmable input ranges on all channels.

Semi-solid Process

The semi-solid process was performed by purging argon gas through a diffuser into the molten metal which is called GISS process [21]. The diffuser was prepared from a stainless steel tube of 200 mm in length with outer diameter of 10 mm and inner diameter of 9 mm which was closed from one end. A series of small holes (0.3 mm in diameter) were drilled on the tube near the closed side up to 50 mm in height.

The flow rate of the inert gas, the gas purging temperature, and the duration of gas purging period were three key process variables which were changed during this study. Table 2 shows the process parameters and the nomenclature of samples. The liquidus temperature was 600 °C and the solidus temperature of the alloy was 425 °C. They were determined using cooling curve thermal analysis. The liquidus

Table 2 The nomenclatures of the semi-solid samples and their respective GISS variables

Nomenclature	Gas flow rate (L min^{-1})	Starting temperature (°C)	Gas purging period (s)
G-2-610-15	2	610	15
G-2-610-20	2	610	20
G-4-610-10	4	610	10
G-4-610-15	4	610	15
G-4-610-20	4	610	20
G-4-620-10	4	620	10
G-4-620-20	4	620	20

temperature is necessary for choosing the starting temperature of argon gas purging in the semi-solid process.

Semi-solid processing was carried out on 300 g of the alloy melted in an electrical resistance furnace. The melt was covered by a protective coverall flux (Magrex powder), pure argon gas, and treated with different GISS process variables. After duration of the predetermined gas purging period at a fixed starting temperature as presented in Table 2, the diffuser was removed and semi-solid slurry was immediately poured into a small stainless steel mold to study the microstructures of the samples. A schematic of the process equipment which was used in this research for preparation of AZ91 semi-solid slurry is illustrated in Fig. 1.
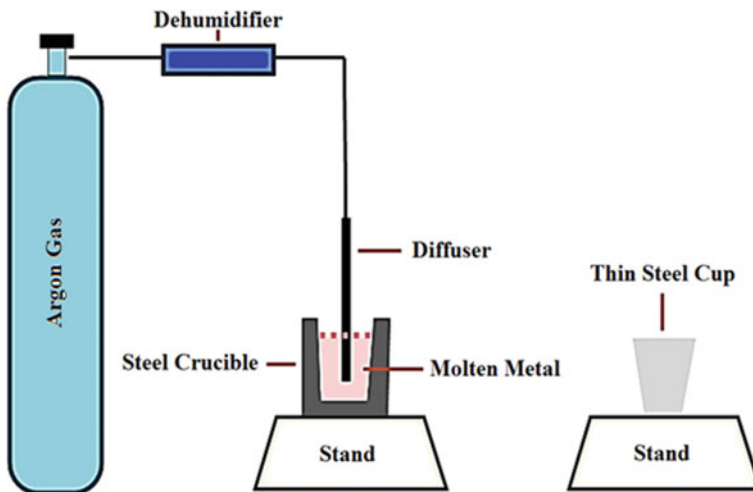
Fig. 1 Schematic of the preparation of AZ91 semi-solid slurry by gas bubbling. (Color figure online)

Microstructural Evaluation

GISS samples as well as conventionally cast sample were sectioned and prepared according to the standard methods for metallography study. They were etched by Nital 2% (Volume Fraction Nitric Acid Ethanol Solution) after polishing. Microstructural evaluations were carried out using optical microscope (OM) and Tescan-Vega scanning electron microscope (SEM). To quantify the results, the microstructures of the samples were analyzed by image J® image analyzer software and the linear intercept method was used to calculate the shape factor, average grain size, and average grain number per square millimeter.

Results and Discussion

The cooling curve recorded for AZ91 alloy, its first derivative curve, and the solid fraction curves are exhibited in Fig. 2. There are two distinct peaks on the first derivative curve of AZ91 alloy. The first peak at 600 °C and the last one at 425 °C are the representative of the formation of α-Mg matrix and β-$Mg_{17}Al_{12}$ phase in the eutectic reaction, respectively. According to these curves, the solidification of this alloy starts
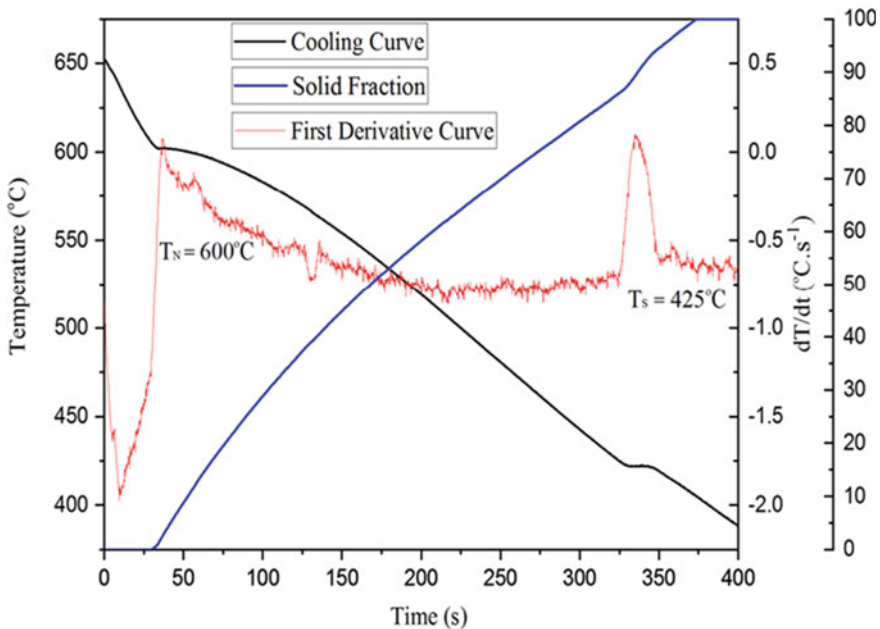
Fig. 2 Cooling curve, its first derivative curve, and solid fraction for AZ91 alloy. (Color figure online)

by nucleation of primary α-Mg at 600 °C. The solidification continues as the melt cools down in AZ91 alloy. Finally, at 425 °C, the remaining melt solidifies with the formation of [α-Mg + β-$Mg_{17}Al_{12}$] eutectic phases in the spaces among the primary α-Mg globules. Therefore, the freezing temperature range of AZ91 magnesium alloy is 175 °C and this alloy is suitable to be treated through semi-solid process, because AZ91 is a long freezing range alloy and has a mushy zone.

The microstructure of AZ91 ingot (original sample) is shown in Fig. 3. SEM micrograph and X-ray mapping analysis of original sample are also illustrated in Fig. 4. As seen, the microstructure of AZ91 alloy consists of primary α-Mg dendrites and the inter-dendritic eutectic phases of [α-Mg + β-$Mg_{17}Al_{12}$].

The microstructures of the GISS samples are shown in Fig. 5. As shown in Fig. 5, when the gas flow rate was 2 L min^{-1} and the gas purging temperature was 620 °C, primary α-Mg phase was a mixture of coarse dendrites and non-dendritic particles. The tips of the dendrites seemed to be partly spheroidized. As the gas flow rate increased to 4 L min^{-1} and the gas purging temperature decreased to 610 °C, dendritic particles disappeared and the primary α-Mg particles changed to non-dendritic structure. At the optimum condition, primary α-Mg particles come to a globular state completely.

It is clear that regardless of the effects of GISS key parameters, the microstructures have completely changed from dendritic to globular as treated through semi-solid process. In the early stage of solidification, the solid fraction in semi-solid slurry increases significantly. Gas purging into the melt leads to the formation of a lot of nuclei around diffuser at the early stage of solidification because of the heat extraction effect of the inert gas [22]. These nuclei will be distributed everywhere in the melt and could survive because of the temperature drop to the mushy zone. The agitation due to gas purging unifies the temperature and the chemical composition of the melt. As known, unified chemical composition reduces the possibility of constitutional under cooling (C.U.C) and dendritic growth. On the other hand, the homogeneity of the temperature encourages a multi-directional growth. The overall results of these

**Fig. 3** Microstructure of AZ91 alloy ingot

200μm
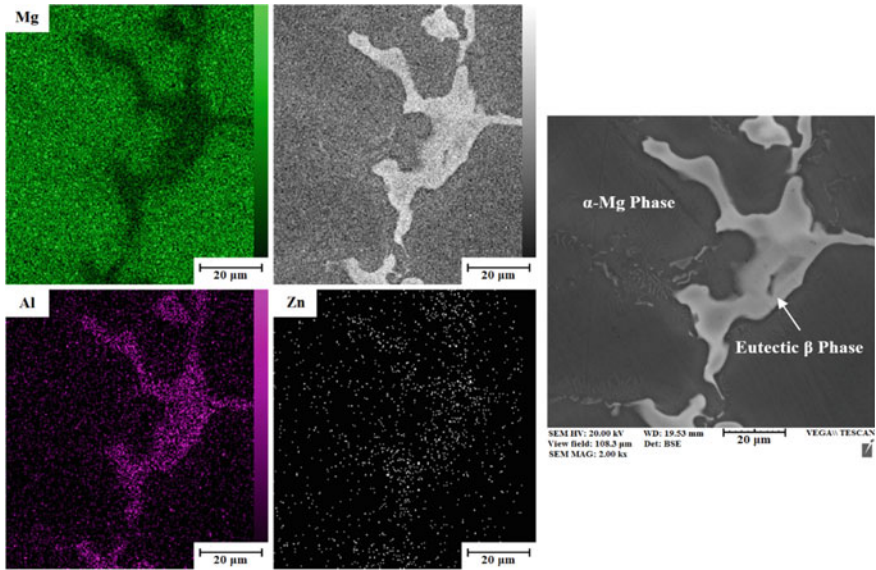
Fig. 4 SEM micrograph and X-ray maps of elemental distribution in AZ91 magnesium alloy. (Color figure online)

events lead the nuclei to grow spherically. In previous studies, it was suggested that the fragmentation of dendrites was responsible for the formation of non-dendritic particles in GISS process [23, 24]. However, it seems that primary α-Mg particles were more likely to nucleate and grow into spherical particles directly in the melt during gas bubbling process. As the temperature of Ar gas was always lower than the melt, effective localized chilling could be achieved near the diffuser during gas bubbling. Heterogeneous nucleation was likely to occur in the undercooled regions and the nuclei could distribute uniformly in the melt driven by the gas flow. Also, due to the presence of continuous gas bubbling, forced stirring was achieved and homogeneous temperature and concentration field were created in the bulk melt, which had favorable influence on the non-dendritic growth of primary α-Mg particles [25].

Figure 6 indicates the shape factor, the particle size, and particle number for GISS samples. The amounts of grain size and shape factors are determined from the average of at least 10 micrographs related to each sample. The grain size has decreased by increasing the flow rate of the inert gas. According to the results, gas purging duration has a limited effect on the grain size in comparison with the gas flow rate. By increasing the starting temperature from 610 °C to 620 °C at a constant gas flow rate and period, the amount of heat extraction from the alloy in the mushy zone diminishes. In fact, some of the cooling effects of the inert gas compensate for the melt with higher temperature to achieve the liquidus temperature. Therefore, increasing the gas purging temperature leads to increase in the grain size. The best globularity, particle size, and the maximum number of particles per unit area occurred
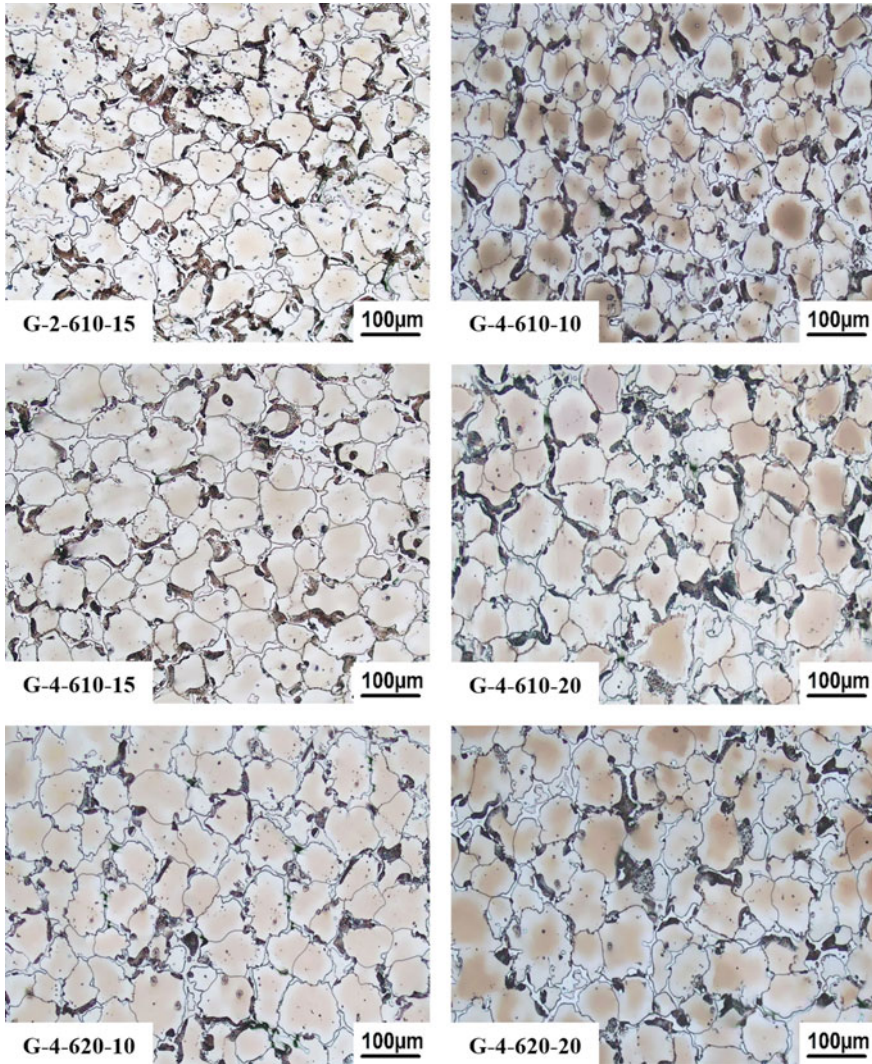
Fig. 5 Microstructures of AZ91 GISS samples. (Color figure online)

when the alloy was treated at 610 °C with the inert gas flow rate of 4L/min for 10 s or G-4-610-10. At this optimum condition, the average α-Mg globule size was 58.4 μm and the average number of α-Mg globule per unit area was 168/mm^2. This happens because of the increase of the heat extraction from the melt and the agitation which result in the homogeneity in temperature and composition of the melt. Therefore, numerous nucleation [20, 25] and multi-directional grain growth occur and cause fine globular grain structure.
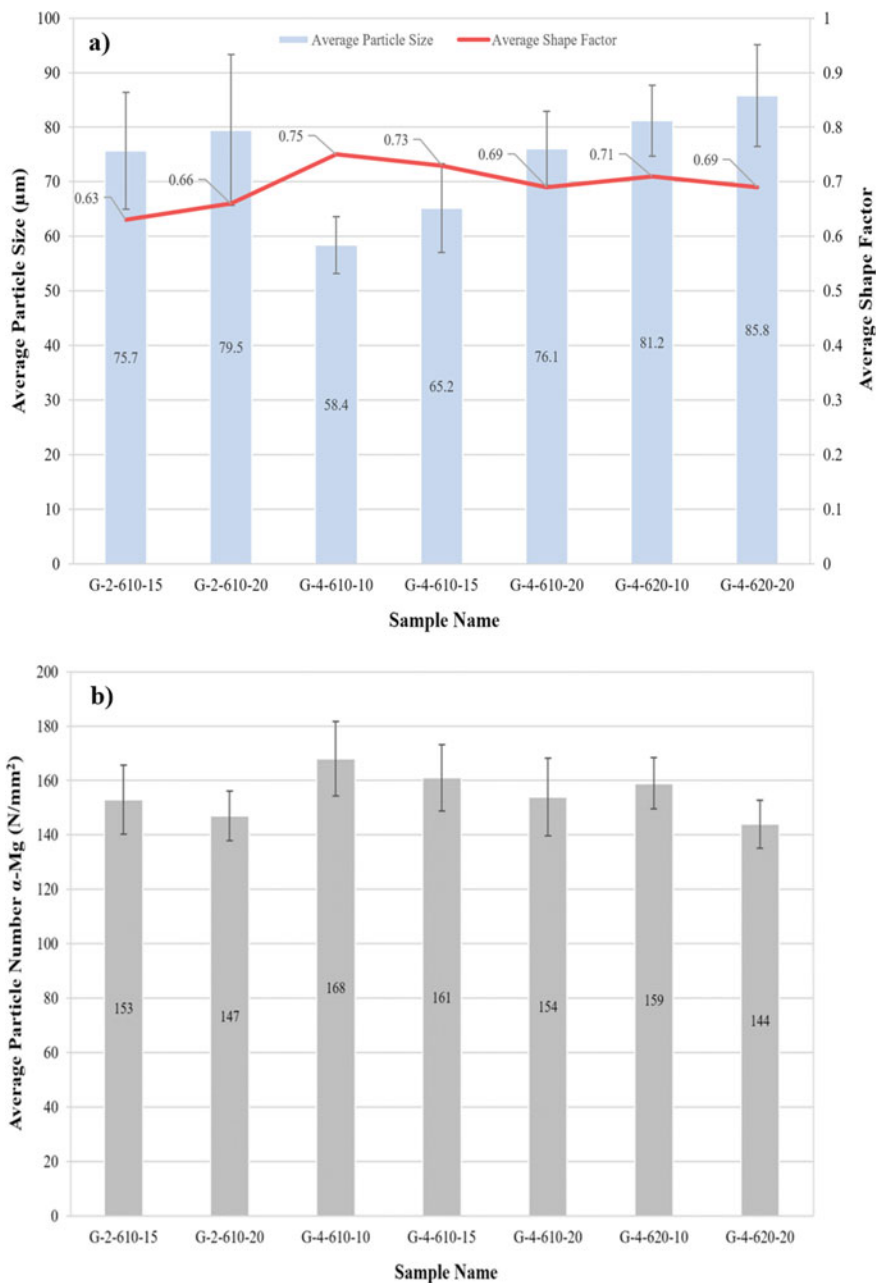
Fig. 6 **a** Average particle sizes and shape factors, **b** average particle number α-Mg of GISS samples. (Color figure online)

Conclusions

In present work, semi-solid slurry of AZ91 magnesium alloy was prepared by gas bubbling process successfully. The effects of processing parameters on the microstructure of AZ91 alloy were investigated. The main conclusions are listed as follows:

(1)   The cooling curve of the AZ91 magnesium alloy showed that the freezing temperature range of the alloy was 175 °C and it was a long freezing range alloy. Therefore, it was a suitable material to be treated through semi-solid process.
(2)   The liquidus temperature was 600 °C and the starting temperatures of 610 and 620 °C were chosen for argon gas purging in the semi-solid process.
(3)   The inert gas flow rate, the gas purging temperature, and the gas purging period were three key process parameters which changed the grain morphology and the grain size of the primary α-Mg in AZ91 magnesium alloy. As the gas flow rate increased to 4 L min^{-1} and the gas purging temperature decreased to 610 °C, the structure completely changed from dendritic to globular.
(4)   Among the GISS key parameters, the inert gas flow rate had the major effect on the globularity and the grain size. It created the numerous nucleation and multi-directional grain growth and caused the formation of fine globular grain structure.
(5)   At the optimum condition of the gas flow rate of 4 L min^{-1}, gas purging temperature of 610 °C, gas purging time of 10 s, the globularity of 0.75, the average α-Mg globule size of 58.4 µm, and the average number of 168 α-Mg globules per unit area were achieved in G-4-610-10 sample. The best mechanical properties and toughness can be predicted at this situation.

References

1. Mordike BL, Ebert T (2001) Magnesium: properties-applications-potential. Mater Sci Eng A 302:37
2. Yang MB, Pan FS, Zhang J (2005) An analysis of the development and applications of current and new Mg-Al based elevated temperature magnesium alloys. Mater Sci Forum 923:488–489
3. Cao P, Qian M, Stjohn DH (2004) Effect of iron on grain refinement of high-purity Mg–Al alloys. Scr Mater 51:125–129
4. Roberto B, Figueiredo S, Terence G (2009) Principles of grain refinement and superplastic flow in magnesium alloys processed by ECAP. Mater Sci Eng A 501:105
5. Wu SS, Xie LZ, Zhao JW (2008) Formation of non-dendritic microstructure of semi-solid aluminum alloy under vibration. Scr Mater 58:556–559
6. Yavari F, Shabestari SG (2017) Effect of cooling rate and al content on solidification characteristics of AZ magnesium alloys using cooling curve thermal analysis. J Therm Anal Calorim 129 (2):655–662
7. Yavari F, Shabestari SG (2020) Assessment of the microstructure, solidification characteristics and mechanical properties of AZ61 + xSr magnesium alloys. Metall Mater Trans B 51(6):3089–3097

8. Sedighi O, Shabestari SG, Yavari F (2018) Investigation on the effect of Sn on solidification and microstructure of AZ91 magnesium alloy using cooling curve thermal analysis. Thermochim Acta 667:165–172
9. Spencer DB, Mehrabian R, Flemings MC (1972) Rheological behavior of Sn-15Pb in the crystallization range. Metall Trans 3:1925–1932
10. Flemings MC, Riek RG, Young KP (1976) Rheocasting. Mater Sci Eng 25:103–117
11. Flemings MC (1991) Behavior of metal alloys in the semi-solid state. Metall Trans A 22:957–981
12. Hashmi S, Macgeough J (2014) Comprehensive material processing (casting), semi-solid forming and hot metal forming, vol 5. Elsevier, pp 109–190
13. Nafisi S, Ghomashchi R (2016) Semi-solid processing of aluminum alloys. Springer, pp 1–43
14. Ghoncheh MH, Shabestari SG (2015) Effect of cooling rate on the dendrite coherency point during solidification of Al2024 alloy. Metall Mater Trans A 46:1287–1299
15. Yavari F, Shabestari SG (2019) Assessment of the effect of cooling rate on dendrite coherency point and hot tearing susceptibility of AZ magnesium alloys using thermal analysis. Int J Cast Metals Res 32(2):85–94
16. Wannasin J, Martinez RA, Flemings MC (2006) Grain refinement of an aluminum alloy by introducing gas bubbles during solidification. Scr Mater 55(2):115–118
17. Wannasin J, Junudom S, Rattanochaikul T, Canyook R, Burapa, T. Chucheep T, Thanabum-rungkul S (2010) Research and development of gas induced semi-solid process for industrial applications. Trans Nonferrous Metals Soc China 20:1010–1015
18. Thanabumrungkul S, Janudom S, Burapa R, Dulyaprahant P, Wannasin J (2010) An industrial development of the Gas Induced Semi Solid (GISS) process. Trans Nonferrous Metals Soc China 20:1016–1021
19. Abdi M, Shabestari SG (2019) Effect of gas induced semi-solid process on solidification parameters and dendrite coherency point of Al-4.3Cu alloy using thermal analysis. J Therm Anal Calorim 136(6):2211–2220
20. Abdi M, Shabestari SG (2019) Semi-solid slurry casting using gas induced semi-solid technique to enhance the microstructural characteristics of Al-4.3Cu alloy. Solid State Phenom 285:253–258
21. Wannasin J, Martinez RA, Flemings MC (2006) A novel technique to produce metal slurries for semi-solid metal processing. Solid State Phenom 116–117:366–369
22. Czerwinski F (2017) Modern aspects of liquid metal engineering. Metall Mater Trans B 48:367–393
23. Canyook R, Wannasin J, Wisuthmethangkul S, Flemings MC (2012) Characterization of the microstructure evolution of semi-solid metal slurry during the early stages. Acta Mater 60:3501–3510
24. Canyook R, Petsut S, Wisutmethangoon S, Flemings MC, Wannasin J (2010) Evolution of microstructure in semi solid slurries of rheocast aluminum alloy. Trans Nonferrous Metals Soc China 20:1649–1655
25. Fan Z, Liu G (2005) Solidification behaviour of AZ91D alloy under intensive forced convection in the RDC process. Acta Mater 53(16):43–45

Part IV
Forming and Thermomechanical Processing

Comparison of Effects of Heat Treatment on Mechanical Properties and Microstructural Behavior of Extruded AZ31 and AM50 Magnesium Alloys

Irem Sapmaz, Enes Kurtulus, Asım Zeybek, and Emrah F. Ozdogru

Abstract Magnesium alloys provide wide application areas due to their low density, high specific strength, and stiffness. However, the HCP (hexagonal close pack) crystal lattice structure of the magnesium can limit its formability. Thermomechanical processes like extrusion provide refined microstructure, better mechanical properties, and higher ductility than casting. Heat treatment is an effective way to enhance mechanical properties using precipitation hardening. In this study, tubular extruded profiles produced from AZ31 and AM50 magnesium alloys were investigated. Profiles were artificially aged to get T5 condition. Tensile and hardness tests were carried out with the longitudinal specimens taken out parallel to the extrusion direction. The heat treatment effect was presented with microstructural investigation via both optical microscopy and scanning electron microscopy analysis of fracture surfaces. As a result, the effect of the heat treatment process on the mechanical properties and microstructural behaviors of AZ31 and AM50 will be revealed.

Keywords Extrusion · AZ31 · AM50 · Heat treatment · Tensile strength · Aging · SEM · Microstructure

Introduction

Magnesium alloys exhibit the attractive combination of low densities and high strength per weight ratios [1] (comparable or greater than that of precipitation strengthened Al alloys), along with adequate damping capacity, castability, weldability, and machinability [2, 3]. Magnesium alloy is typically a close-packed hexagonal structure. At room temperature, plastic deformation of magnesium alloy usually acts on a slip system of {0001} [4], and it causes magnesium to have poor formability. Because of these characteristics, Mg alloys are being increasingly used in

I. Sapmaz (✉) · E. Kurtulus · A. Zeybek
Yeşilova Holding R&D Center, Bursa, Turkey
e-mail: irem.sapmaz@yesilova.com.tr

E. F. Ozdogru
TRI Metalürji, Istanbul, Turkey

electronics, automobile, and aerospace industries [5]. Of the various commercial magnesium alloys, those developed from the Al–Zn ternary system (i.e., the as-named AZ alloys) have found the largest number of industrial applications [6, 7]. Besides, AM-series magnesium alloys are widely used due to their adequate strength, good castability, and corrosion resistance, especially in the automotive industry [8].

Some different studies investigate the microstructure of AM50 and AZ31 magnesium alloys under different conditions in the literature. They generally contain texture effect, strain rate, grain refinement, etc. [9, 10]. So far, systematic information about the effects of heat treatment is relatively limited for these alloys. Heat treatment through which the microstructures of magnesium alloys are improved to realize the strengthening and toughening is an essential method in improving and adjusting the mechanical properties and forming properties of magnesium alloys [11]. Thus, it is significant to investigate the effects of different heat treatment ways on improving the deformation microstructures, refining grains, and raising the mechanical properties. The heat treatment process for magnesium alloys such as AZ31 up to higher temperatures results in the nucleation of new grains and a pronounced decrease of the volume fraction of twins. Namely, at 350 °C and 400 °C, the initially deformed grains are replaced by new finer ones [12]. The heat treatment process is suitable for eliminating twin bands in the microstructure.

In this study, the effects of the heat treatment process were investigated on the microstructural and mechanical properties of the hot-extruded AZ31 and AM50 magnesium alloys. The tensile and hardness tests were performed to define the mechanical properties of the alloys based on the heat treatment process. The microstructural investigation was performed with the help of an optical microscope (OM). The fracture surface of the tensile test specimens was characterized via the Scanning Electron Microscope (SEM). As a result, changes of both the mechanical and microstructural properties will be revealed for the extruded AZ31 and AM50 alloy after the heat treatment process.

Experimental Method

AZ31 and AM50 were used for the extrusion process. The chemical composition of the magnesium ingots is shown in Table 1. The homogenization process was performed in the annealing furnace, as 15 h at 410 °C for AM50 alloy and 15 h at 375 °C for AZ31 alloy.

Table 1 Chemical composition of AZ31 and AM50 alloy tubes (values in weight percent, wt%)

Alloy	Al	Zn	Mn	Si	Fe	Cu	Mg
AM50	4.5–5.3	<0.02	0.28–0.5	<0.05	<0.004	<0.008	Balance
AZ31	2.4–3.5	0.6–1.4	0.2–1.0	<0.1	<0.005	<0.05	Balance

Heat treatment studies were performed via the Piri Thermnevo furnace. Heat treatment parameters are shown in Table 2. The heat treatment condition for AM50 alloy was chosen from ASTM B661-03 (Table 2) and for AZ31 alloy from ASTM Standard (Table 2).

Hollow profiles were air-cooled after the extrusion process. They were subjected to heat treatment in order to analyze the effect of it on the microstructure, tensile, and hardness properties. The hollow profile that is to be used as a test specimen is 70 mm in diameter with 3.35 mm thickness, as shown in Fig. 1, respectively. The extrusion ratio was 36.91.

Tensile test specimens were machined along the longitudinal direction of the tubes according to the DIN 50125 standard. The tensile properties of the alloy samples were evaluated using a universal testing machine (Shimadzu AG—IS 250 kN) at room temperature according to ISO EN 6892-1. Minimum of four and maximum of six tests were done for analyzing tensile properties statistically.

Hardness tests were performed according to EN 6506-1 standard using a universal hardness measurement machine (DIGIROCK-RBV Brinell, Vickers) at room temperature. The Brinell hardness values (HB) of the samples were measured using an indenter ball with a diameter of 2.5 mm. The load used was 62.5 kg. Five measurements were done for each sample.

Table 2 Heat treatment parameters of magnesium alloys

Alloy	Temperature (°C)	Duration (h)
AM50	232 ± 2	5
AZ31	177 ± 2	16

Table 3 The average grain size of magnesium alloys

Alloy	Conditions	The average grain size (μm)
AM50	Heat-treated	45
AM50	Non-heat-treated	53
AZ31	Heat-treated	36
AZ31	Non-heat-treated	39

Fig. 1 Section view of extruded tube
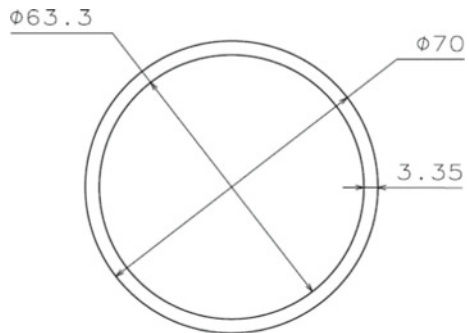
The metallographic specimens were taken from cross section of the hollow profiles, and they were ground 180, 800, 1200, and 2000 sandpaper and polished using 6 μm, diamond pastes. Then, specimens were etched by using 3.5 mL acetic acid, 3 mL water, and 50 mL picral for 6 s. The grain size analysis was characterized on selected specimens using a Nikon LV150NA optical microscope (OM). The mean linear intercept method was used to measure the average grain size, and analysis was performed by image analysis software called Clemex. The fracture surfaces after the tensile tests for the best-the worst tensile test specimens in each parameter were observed by scanning electron microscopy (SEM) (JEOL NeoScope JCM-6000 Plus), and the EDX analysis is performed with the help of the same device.

Results and Discussion

The average grain size of the AZ31 and AM50 alloys based on the heat treatment process is shown in Table 3. According to the average grain size results of the extruded AM50 and AZ31 alloys, the heat treatment process decreased the grain size of both alloys. According to the average grain size values of the alloys, the heat treatment process caused to decrease around 8 μm remarkably for the AM50 alloy.

The microstructural images of extruded AZ31 alloy are shown in Fig. 2. According to the microstructure of the alloy, the fragmented areas of grain are clearly seen due to the observation of heterogeneous fragmentation of structure, but it also appears that areas not deformed as much. In the microstructure of all examined areas, fine recrystallized grains surrounded by larger grains were observed. The shape and size of grains were found similar for both heat-treated and non-heat-treated samples. A large grain can be observed, which can be caused by not full dynamic recrystallization during the extrusion process [13]. Heat-treated extruded AZ31 magnesium alloy showed a smaller grain size. Additionally, it was found that a mass of twins has been generated in the material due to extrusion temperature [14]. After the heat treatment process, the number of twins decreased in the structure.

The microstructural images of extruded AM50 alloy are shown in Fig. 3. According to the microstructure of the alloy, the fragmented areas of grain due to observation of heterogeneous fragmentation of structure are clearly seen, but it also appears that areas are not deformed as much. In the microstructure of all examined areas, mostly larger grains were observed, including a higher mass of twins inside. It is the same for AM50 alloy that the cause of larger grains is not full dynamic recrystallization during the extrusion process [13]. After the heat treatment process, the average grain size decreased remarkably. According to the microstructural images after the heat treatment process, it is seen that the smaller grains were surrounded by larger grains like AZ31 alloy, and the mass of twins decreased in the structure.

The average tensile and hardness properties of the AZ31 and AM50 alloys are shown in Table 4. According to the hardness test results of the alloys that are shown in Fig. 4, both AZ31 and AM50 alloys have close hardness properties without heat treatment process. After the heat treatment, the hardness properties of AZ31 alloy

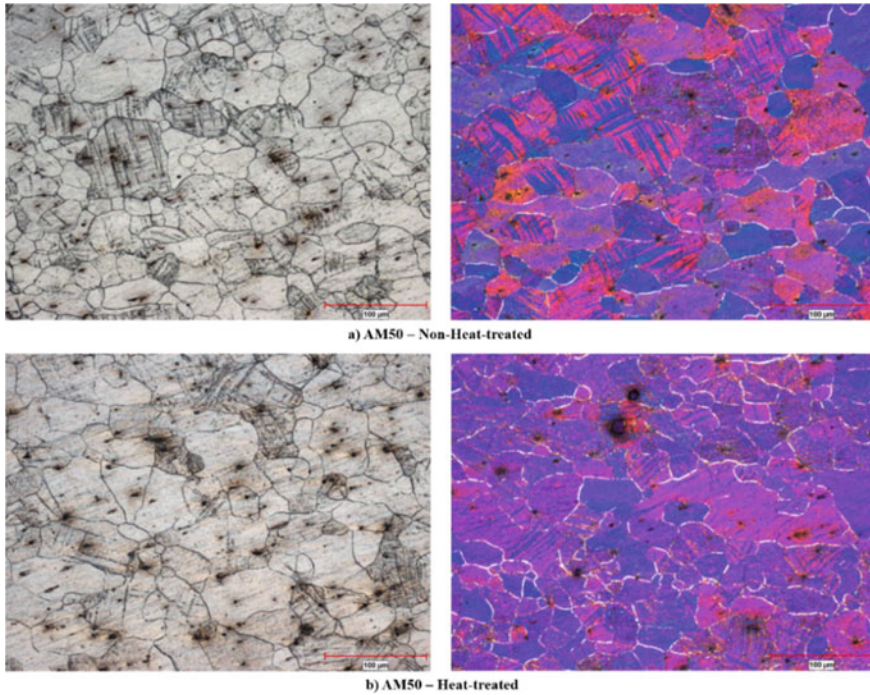a) AZ31 – Non-Heat-treated
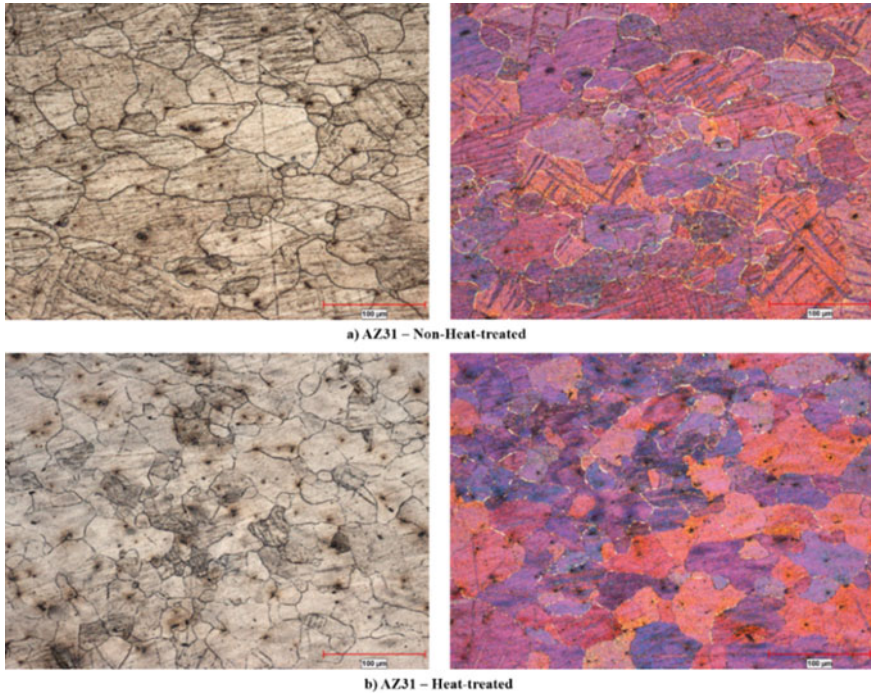
b) AZ31 – Heat-treated

Fig. 2 Microstructural images of the extruded AZ31 alloy: **a** Non-heat-treated, **b** Heat-treated. (Color figure online)

improved significantly, but the hardness property of the AM50 alloy did not change remarkably after the heat treatment process [15].

Comparing the tensile properties of the AZ31 and AM50 alloys based on the heat treatment is shown in Fig. 5. According to the results, the yield strength of AZ31 and AM50 alloys shows almost the same value when the heat treatment was not implemented on the extruded profiles. The ultimate tensile strength value of the AZ31 alloy was found around 10 MPa higher than AM50 alloy. When the strain values of the extruded magnesium alloys are compared, AZ31 alloy shows a better strain value strikingly. In conclusion, the yield strength and the hardness properties of both AZ31 and AM50 alloy were found quite closer. The extruded AZ31 alloy showed better ultimate tensile strength and strain properties when compared to extruded AM50 alloy.

According to the results, when the heat treatment applied on the extruded profiles, both yield strength and ultimate tensile strength values of AZ31 alloy increased around 20 MPa by the help of the heat treatment process. Additionally, the heat treatment process did not significantly affect the strain properties of the AZ31 alloy. When the tensile properties of the heat-treated and non-heat-treated profiles of the AM50 alloy are compared, it is clearly seen that both the yield strength and tensile strength values of the AM50 extruded profiles decreased around 20 MPa remarkably

Fig. 3 Microstructural images of the extruded AM50 alloy: **a** Non-heat-treated, **b** Heat-treated. (Color figure online)

Table 4 Average mechanical properties of the magnesium extruded alloys

Alloy	Conditions	Yield strength (MPa)	Tensile strength (MPa)	Strain (%)	Hardness (HB)
AM50	Heat-treated	164.903	216.046	7.127	55.32
	Non-heat-treated	175.768	234.193	8.144	58.63
AZ31	Heat-treated	193.400	261.462	12.098	73.98
	Non-heat-treated	174.480	241.958	12.088	58.90

after the heat treatment [16]. The strain property of the AM50 alloy decreased when the heat treatment was applied. The formation of coarse, secondary phase precipitates in the grain boundary region may lead to a low elongation in AM50 alloy [17]. In conclusion, the heat treatment process positively affects both the tensile and hardness properties of the extruded AZ31 alloy. As it is well known that the mechanical properties of Mg alloys are strongly related to microstructure formation during the deformation process, such as rolling and extrusion. Deformation twins generally form after mechanical processing, and the density of RX grains can be linked to the
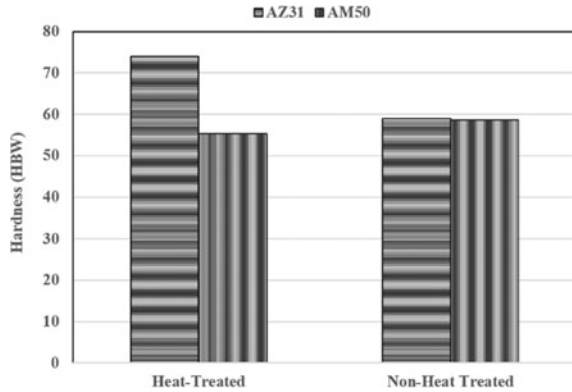
density of deformation twins. Deformation twins generally weaken the mechanical
deformation. Thus, the extruded AM50 alloy indicated lower mechanical properties.

The typical SEM micrographs of the fracture surface of the extruded AZ31 magne-
sium alloy after the tensile test are shown in Fig. 6. The pictures below show the
fracture process in the final rupture region. According to the images, there were found
many dimple patterns [18], and the fracture surface showed ductile behavior. The
size of dimples was found different when they compare the heat treatment process.
During the investigation of the fracture surface, lots of inclusion were seen, and
it is well known that the dimple is mainly caused by the existence of inclusions
[19]. For AZ31 alloys, the polygonal-shaped inclusions were seen on the dimples
which are based on the Mn based, as shown in Fig. 7. In conclusion, there was
found no remarkable difference between the fracture surface of heat-treated and
non-heat-treated specimens.

The typical SEM micrographs of the fracture surface of the extruded AM50
magnesium alloy after the tensile test are shown in Fig. 8. In the typical case, the
fracture mode of as-cast AM50 magnesium alloy is quasi-cleavage fracture [16].
The pictures below show the fracture process in the final rupture region. According
to the images, there were found many cleavage steps and cracks on the fracture
morphology, and some dimples were observed on both specimens. The torn and
river-like pattern with raised edges was seen on the fracture surface of the non-heat-
treated specimens. After the heat treatment process, the cleavage plains were seen on
the fracture surface, and the crack initiations were seen mainly at the grain boundaries
for AM50 alloy. So, twin boundaries that were seen on the microstructural images
of Fig. 4 may also be crack initiation sites [20]. For AM50 alloys, the aciculiform
inclusions were seen in the Mn based as shown in Fig. 9a, and the polygonal-shaped
inclusions were seen in the Mn-Si based as is shown in Fig. 9b. In conclusion, there
was found no remarkable difference between the fracture surface of heat-treated and
non-heat-treated specimens.

Fig. 5 Comparison graphs of the tensile properties based on the heat treatment process

Yield Strength Comparison Graph

U. Tensile Strength Comparison Graph

Strain Comparison Graph
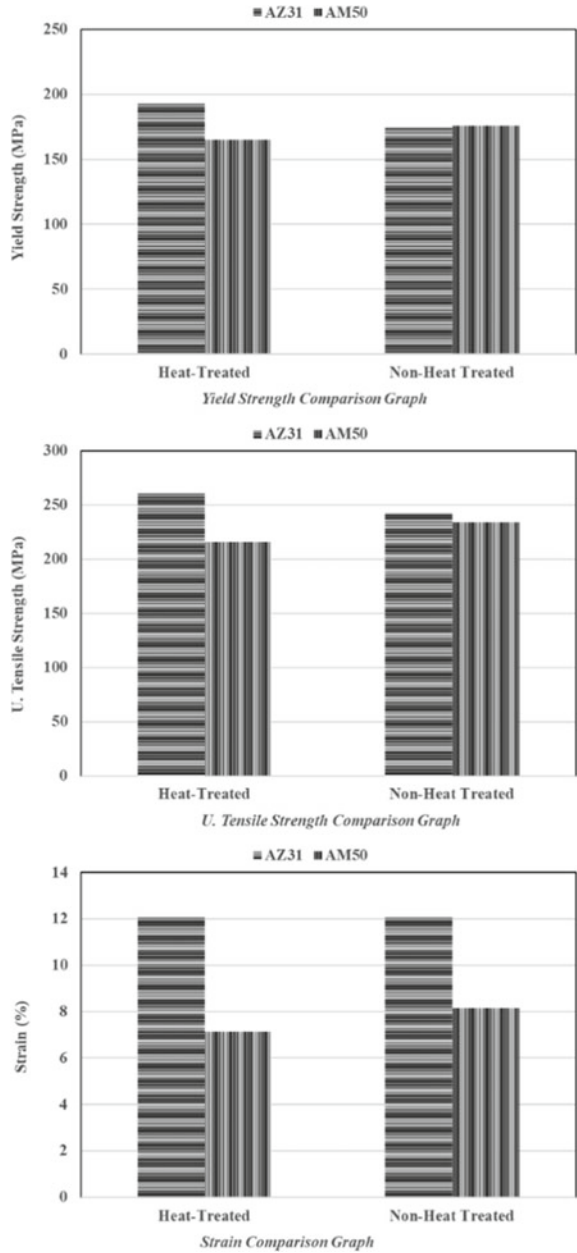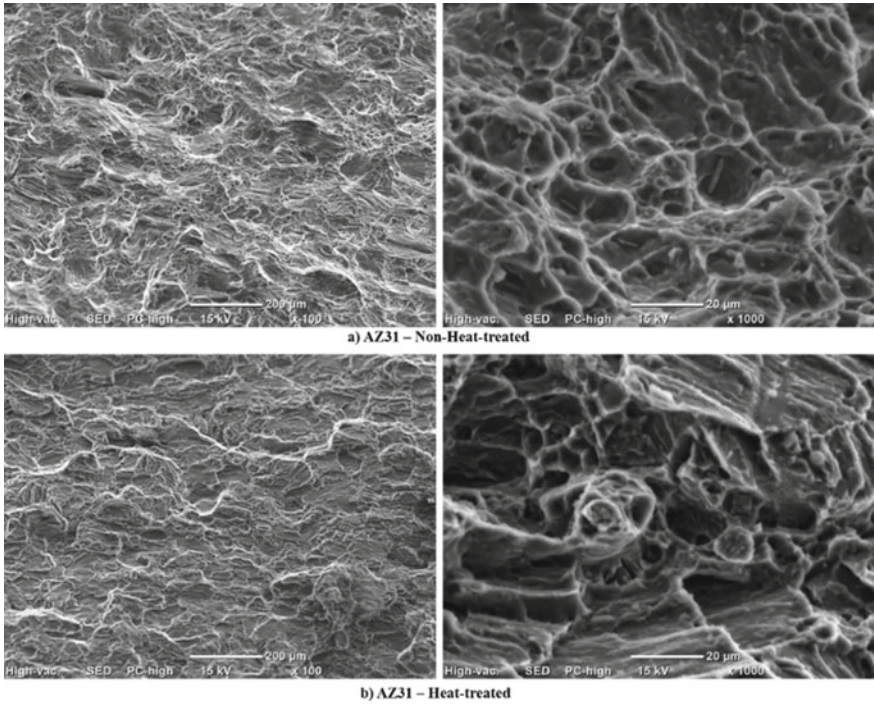
Fig. 6 Fracture surfaces of the extruded AZ31 alloy after the tensile test: **a** Non-heat-treated, **b** Heat-treated
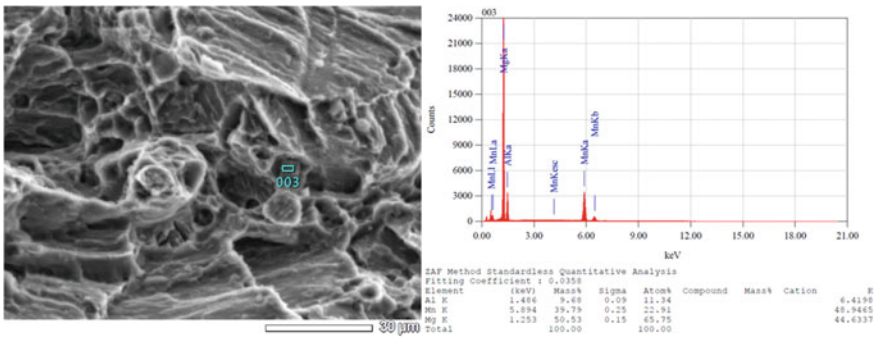
Fig. 7 Mn-based inclusion from the fracture surface of the extruded AZ31 alloy after the tensile test. (Color figure online)

a) AM50 – Non-Heat-treated
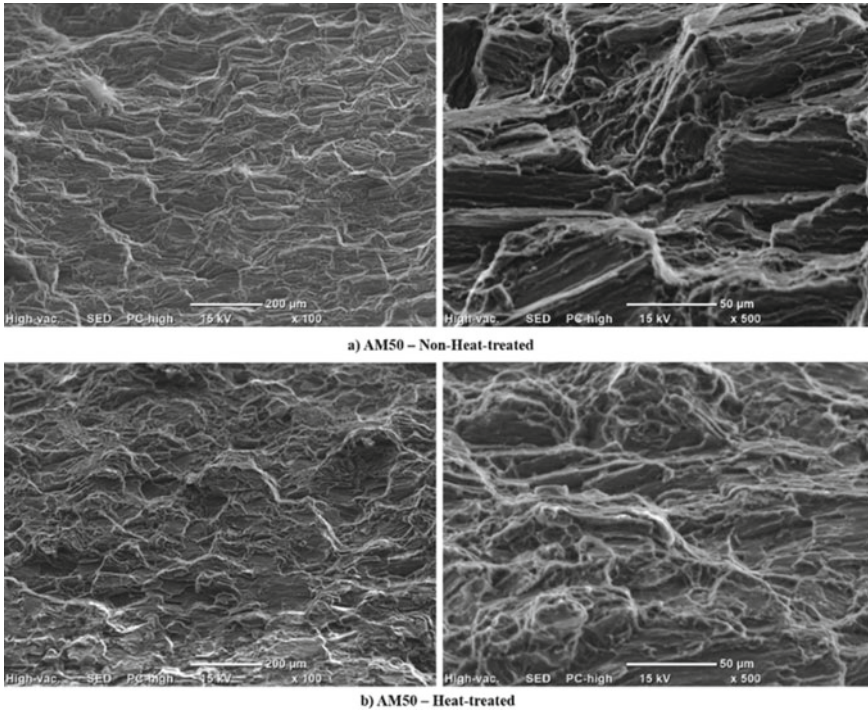
b) AM50 – Heat-treated

Fig. 8 Fracture surfaces of the extruded AM50 alloy after the tensile test: **a** Non-heat-treated, **b** Heat-treated

Conclusion

In this investigation, heat treatment effects on the microstructure and mechanical properties of an extruded AZ31 and AM50 magnesium alloys were reported. The results suggest that the heat treatment process was beneficial for improving the tensile and hardness properties of the profiles. The main findings of the study were given as follows:

- AZ31 and AM50 alloys show quite similar yield strength and hardness properties as a non-heat-treated condition, but AZ31 has higher tensile strength and strain properties.
- The strain value of the AZ31 alloy does not be effected on the part of the heat treatment process.
- The heat treatment process improves both tensile and hardness properties of the extruded AZ31 alloy strikingly, but AM50 alloy negatively affects the heat treatment process, and it causes lower tensile and hardness properties.
- The heat treatment causes a decrease in the average grain size of both AZ31 and AM50 alloys. According to the microstructural images of the alloys in both
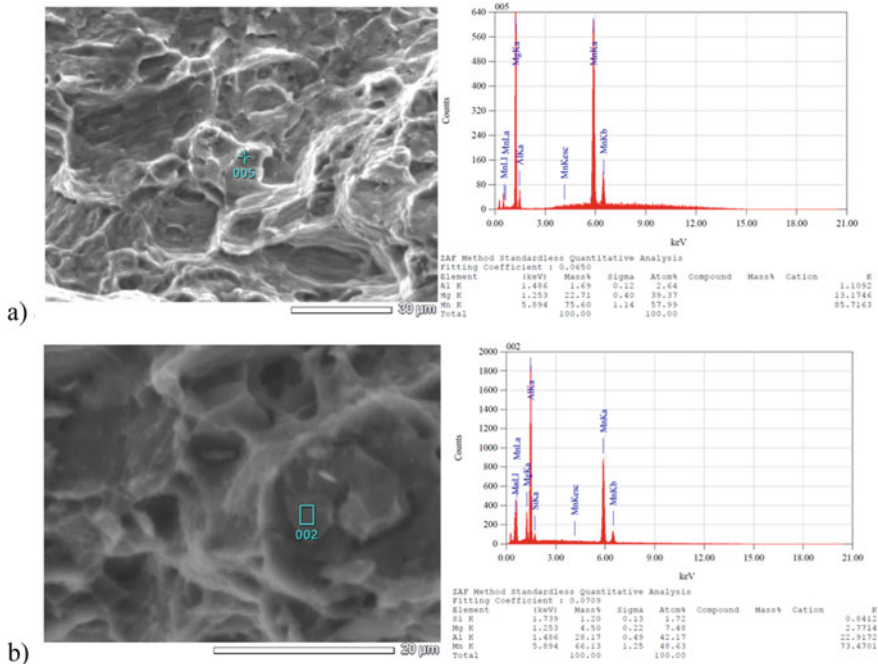
Fig. 9 The inclusions from the fracture surface of the extruded AM50 alloy after the tensile test: **a** Mn based, **b** Mn-Si based. (Color figure online)

conditions, the heat treatment process provides a more uniform and refined grain structure and the elimination of twins.

- Mn-based inclusion was found out for both AZ31 and AM50 alloys. The Mn-Si-based inclusions were seen just on the fracture surface of the AM50 alloy distinctively.
- Deformation twins may cause weak mechanical deformation, and it may cause the lower mechanical properties for the extruded AM50 alloy.

References

1. Polmear IJ (1994) Magnesium alloys and applications. Mater Sci Technol (United Kingdom) 10:1–16. https://doi.org/10.1179/mst.1994.10.1.1

2. Li W-j, Deng K-k, Zhang X, Nie K-b, Xu F-j (2016) Effect of extrusion speed on the microstructure and tensile properties of AZ31 alloy. Mater Sci Eng A 677:367–375. https://doi.org/10.1016/j.msea.2016.09.059

3. Marya M, Hector LG, Verma R, Tong W (2006) Microstructural effects of AZ31 magnesium alloy on its tensile deformation and failure behaviors. Mater Sci Eng A 418:341–356. https://doi.org/10.1016/j.msea.2005.12.003

4. Yang Y-b, Wang F-c, Tan C-w, Wu Y-y, Cai H-n (2008) Plastic deformation mechanisms of AZ31 magnesium alloy under high strain rate compression. Trans. Nonferrous Metals Soc. China (English Ed.) 18:1043–1046. https://doi.org/10.1016/s1003-6326(08)60178-8

5. Pardo A, Merino MC, Coy AE, Arrabal R, Viejo F, Matykina E (2008) Corrosion behaviour of magnesium/aluminium alloys in 3.5 wt.% NaCl. Corros Sci 50:823–834. https://doi.org/10.1016/j.corsci.2007.11.005

6. Feliu S, Maffiotte C, Galván JC, Barranco V (2011) Atmospheric corrosion of magnesium alloys AZ31 and AZ61 under continuous condensation conditions. Corros Sci 53:1865–1872. https://doi.org/10.1016/j.corsci.2011.02.003

7. Walton CA, Martin HJ, Horstemeyer MF, Wang PT (2012) Quantification of corrosion mechanisms under immersion and salt-spray environments on an extruded AZ31 magnesium alloy. Corros Sci 56:194–208. https://doi.org/10.1016/j.corsci.2011.12.008

8. Blawert C, Hort N, Kainer KU (2004) Automotive applications of magnesium and its alloys. Trans Indian Inst Metals 57:397–408

9. Rama M, Sadiku A, Zeka B, Gashi Z (2016) Study of effects distribution of alloying elements in formation of intermetallic phases for Mg alloys AZ91 and AM50. J Int Environ Appl Sci 11:36–41

10. Ma Y, Zhang J, Yang M (2009) Research on microstructure and alloy phases of AM50 magnesium alloy. J Alloys Compd 470:515–521. https://doi.org/10.1016/j.jallcom.2008.03.047

11. Czerwinski F, Kasprzak W (2013) Heat treatment of magnesium alloys - current capabilities. Mater Sci Forum 765:466–470. https://doi.org/10.4028/www.scientific.net/MSF.765.466

12. Zimina M, Bohlen J, Letzig D, Kurz G, Poková M, Knapek M, Zrník J, Cieslar M (2015) The study of the behavior of constrained groove pressed magnesium alloy after heat treatment. Acta Phys Pol A 128:775–778. https://doi.org/10.12693/APhysPolA.128.775

13. Stefanik A, Szota P, Mróz S, Bajor T, Dyja H (2015) Properties of the AZ31 magnesium alloy round bars obtained in different rolling processes. Arch Metall Mater 60:3002–3005. https://doi.org/10.1515/amm-2015-0479

14. Gao CY, Zhang LC, Guo WG, Li YL, Lu WR, Ke YL (2014) Dynamic plasticity of AZ31 magnesium alloy: experimental investigation and constitutive modeling. Mater Sci Eng A 613:379–389. https://doi.org/10.1016/j.msea.2014.06.012

15. Yanlong M, Pan F, Yang M (2007) Effects of heat treatments on microstructure of AM50 magnesium alloy. Adv Mater Res 24–25:103–106. https://doi.org/10.4028/www.scientific.net/amr.26-28.103

16. Yang M, Liu YH, Liu JA, Song YL (2015) Effect of T6 heat treatment on corrosion resistance and mechanical properties of AM50 magnesium alloy. Mater Res Innov 19:259–264. https://doi.org/10.1179/1432891715Z.0000000002160

17. Kottuparambil RR, Bontha S, Rangarasaiah RM, Arya SB, Jana A, Das M, Balla VK, Amrithalingam S, Prabhu TR (2018) Effect of zinc and rare-earth element addition on mechanical, corrosion, and biological properties of magnesium. J Mater Res 33:3466–3478. https://doi.org/10.1557/jmr.2018.311

18. Somekawa H, Mukai T (2005) Effect of texture on fracture toughness in extruded AZ31 magnesium alloy. Scr Mater 53:541–545. https://doi.org/10.1016/j.scriptamat.2005.04.048

19. Somekawa H, Singh A, Mukai T (2007) Effect of precipitate shapes on fracture toughness in extruded Mg-Zn-Zr magnesium alloys. J Mater Res 22:965–973. https://doi.org/10.1557/jmr.2007.0112

20. Qiu W, Han EH, Liu L (2010) Effect of heat treatment on microstructures and mechanical properties of extruded-rolled AZ31 Mg alloys. Trans. Nonferrous Metals Soc. China (English Ed.) 20:s481–s487. https://doi.org/10.1016/s1003-6326(10)60523-7

Effects of Adding Zinc and Calcium Solute on Mechanical Properties in Magnesium Fine Wires

Hiroki Sannomiya, Shinsuke Sawaguchi, Tatsuya Nakatsuji, Naoko Ikeo, Kunimitsu Nakamura, and Toshiji Mukai

Abstract Drawing is suitable for manufacturing fine metal wire. This study was designed to clarify the effects of additive elements, calcium or zinc, on mechanical properties of drawn magnesium wires. Binary alloys of Mg-0.3 at. % Ca and Mg-0.1 at. % Zn were cast followed by extrusion. The extrusion bars were drawn to fabricate a fine wire with a diameter of 0.2 mm. Tensile tests were conducted for the wires. The results of the tensile tests confirmed that yield stress increased as the content of the solute element increased, while the work hardening rate and tensile ductility differed depending on the types of additive element. Inspection of the drawn microstructure revealed that the additive element plays an important role in microstructure evolution in magnesium.

Keywords Mg–Ca alloy · Mg–Zn alloy · Wire · Cold drawing · Tensile properties · Microstructure evolution

Introduction

In recent years, surgical sutures have been made from bioabsorbable polymers with the advantage of avoiding removal procedure. Magnesium alloys are possible candidates for bioabsorbable suture materials because of their biocompatibility and degradability [1]. Most fine metal wires are manufactured by drawing. The drawing process of magnesium alloys such as pure magnesium [2, 3], AZ31 [4], WE43 [5], Mg–Ca alloy [6], and Mg-Zn alloy [7, 8] has been studied so far. However, magnesium

H. Sannomiya (✉) · S. Sawaguchi · T. Nakatsuji · N. Ikeo · T. Mukai
Departments of Mechanical Engineering, Graduate School of Engineering, Kobe University, 1–1 Rokkodai, Nada, Kobe, Hyogo 657–8501, Japan
e-mail: sannomiya@jpfs.co.jp

H. Sannomiya · K. Nakamura
Japan Fine Steel CO., LTD., 1-19-1 Ishiide, Sanyoonoda, Yamaguchi 756-0063, Japan

T. Mukai
Center for Advanced Medical Engineering Research and Development, Kobe University, Kobe, Hyogo, Japan

alloy wires composed only of living body essential elements without second phase precipitates have not been well understood. Besides, these magnesium alloys are inferior in mechanical properties to biocompatible metals such as stainless steel and titanium alloys, which highlights the need for enhancing the mechanical properties for surgical devices such as a suture.

This study attempted to elucidate the effects of trace addition of zinc or calcium on magnesium alloy fine wires. The effects of cold drawing and heat treatment were investigated on the alloy wire's mechanical properties with a diameter of 0.2 mm. The drawn microstructure was also inspected to study the correlation between the thermomechanical processes and mechanical properties.

Experimental Procedure

Mg-0.3 at.% Ca and Mg-0.1 at.% Zn alloy ingots were produced by direct chill casting. The chemical compositions of the alloys are shown in Table 1. After extrusion was conducted twice to obtain a round rod with a diameter of 4 mm, cold drawing and annealing were repeated to produce a wire with a diameter of 0.218 mm.

The drawn wires were annealed in a muffle furnace in air. The annealing temperature was selected to be 653 K for Mg-0.3Ca and 523 K for Mg-0.1Zn, respectively, and holding time was fixed to be 3 min. After the annealing, cold drawing was performed to φ0.200 mm (area reduction of 15.8%). The area reduction is expressed by the following equation:

$$\text{Area reduction} = \left[1 - \left(D / D_0\right)\right]^2 \times 100 (\%)$$

These φ0.2 mm cold-drawn wires were cut to a length of 0.3 m and re-annealed. The annealing temperature was selected to be 523–673 K for Mg-0.3Ca and 423–573 K for Mg-0.1Zn, respectively, and holding time was fixed to be 3 min.

Tensile tests were performed for the cold-drawn wires and annealed wires without any processing. The tests were conducted at a distance between chucks of 100 mm at a pulling speed of 10 mm/min and at room temperature. After the tests, a nominal stress-nominal strain relation was obtained. Furthermore, the microstructure of the wires was observed using scanning electron microscope (SEM) and electron backscatter diffraction (EBSD) for the cold-drawn and the annealed states.

Table 1 Chemical compositions of the experimental alloys

Alloy (at%)	Analyzed compositions (wt%)				
	Ca	Zn	Si	Fe	Mg
Mg-0.3Ca	0.48	–	0.002	<0.001	Bal.
Mg-0.1Zn	–	0.26	0.002	<0.001	Bal.
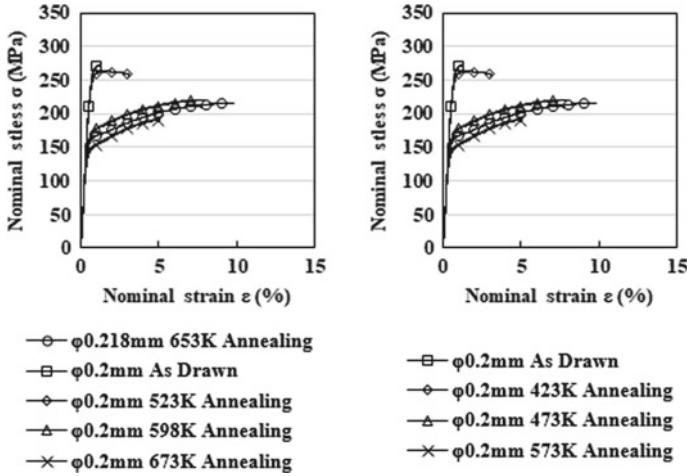
Fig. 1 Tensile mechanical properties of the cold-drawn and the annealed wires of **a** Mg-0.3Ca and **b** Mg-0.1Zn

Results and Discussion

Tensile Mechanical Properties

Tensile mechanical properties of the cold-drawn and the annealed wires of Mg-0.3Ca and Mg-0.1Zn are shown in Fig. 1. Focusing on the wires of both alloys with a diameter of φ0.2 mm, the as-drawn wire had the highest ultimate tensile strength and the smallest fracture elongation. An increase in the annealing temperature decreased the yield strength and the ultimate tensile strength, and the fracture elongation exhibited a maximum at 598 K for Mg-0.3Ca and 473 K for Mg-0.1Zn. Comparing both alloys, Mg-0.1Zn showed superior strength and elongation overall.

Work hardening exponent (n value) was calculated and compared with the 0.2% yield stress. Figure 2 shows the correlation between the 0.2% yield stress and the work hardening exponent (n value). In this figure, good workability in drawing and/or toughness was obtained by combining the 0.2% yield stress and the work hardening exponent (n value). While comparing the examined alloys, Mg-0.1Zn showed higher n values than Mg-0.3Ca at the same yield strength. These results suggest that, compared with calcium, the addition of zinc contributes to toughness enhancement.

Microstructure Evolution

The microstructure of the as-drawn and annealed wire is shown in Fig. 3. Inverse pole figure (IPF) map and kernel average misorientation (KAM) map were obtained

Fig. 2 The correlation between the 0.2% yield stress and the work hardening exponent (n value) of the cold-drawn and the annealed wires of Mg-0.3Ca and Mg-0.1Zn
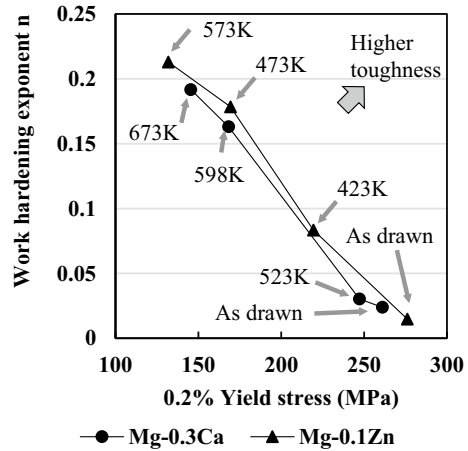
using SEM and EBSD. Accumulation of dislocations was expected in the KAM map for the cold-drawn wires of both alloys. Further, focusing on the accumulated areas of both alloys, a difference was observed. In Mg-0.3Ca, a marked accumulated area existed near grain boundaries, while some strained regions were dispersed inside the grains. However, in Mg-0.1Zn, the accumulated area was concentrated near the grain boundaries, while the strained region inside the grains was small. A previous investigation of extruded Mg-Zn-Ca alloys has reported that solute of zinc and calcium tended to segregate near the grain boundaries [9]. The difference in the distribution of accumulated area in as-drawn wire suggested that zinc solute might be segregated near the grain boundary and caused the accumulation of dislocations by drawing. Moreover, Mg-0.1Zn was considered to have shown higher strength and elongation due to this difference in accumulation. These findings suggested that in the drawing process of the magnesium alloy, the dislocations were expected to be concentrated near the grain boundaries, leading to increased toughness.

In both alloys' annealed wires, the number of subgrain boundaries increased inside the grains annealed at low temperatures (Mg-0.3Ca at 573 K, Mg-0.1Zn at 423 K, respectively). At these temperatures, elongation increased without lowering tensile strength. Therefore, in order to enhance toughness, an optimized annealing process was considered essential.

In the wires annealed at intermediate temperatures (Mg-0.3Ca at 598 K, Mg-0.1Zn at 473 K, respectively), equiaxed grains were formed, and the area of strained regions became smaller. Thus, the subsequent drawing should be performed after annealing around these temperatures.

After the annealing at higher temperatures (Mg-0.3Ca at 673 K, Mg-0.1Zn at 573 K, respectively), grain coarsening was observed. At these temperatures, annealed wire exhibited lower strength and fracture elongation, resulting in excessive annealing.
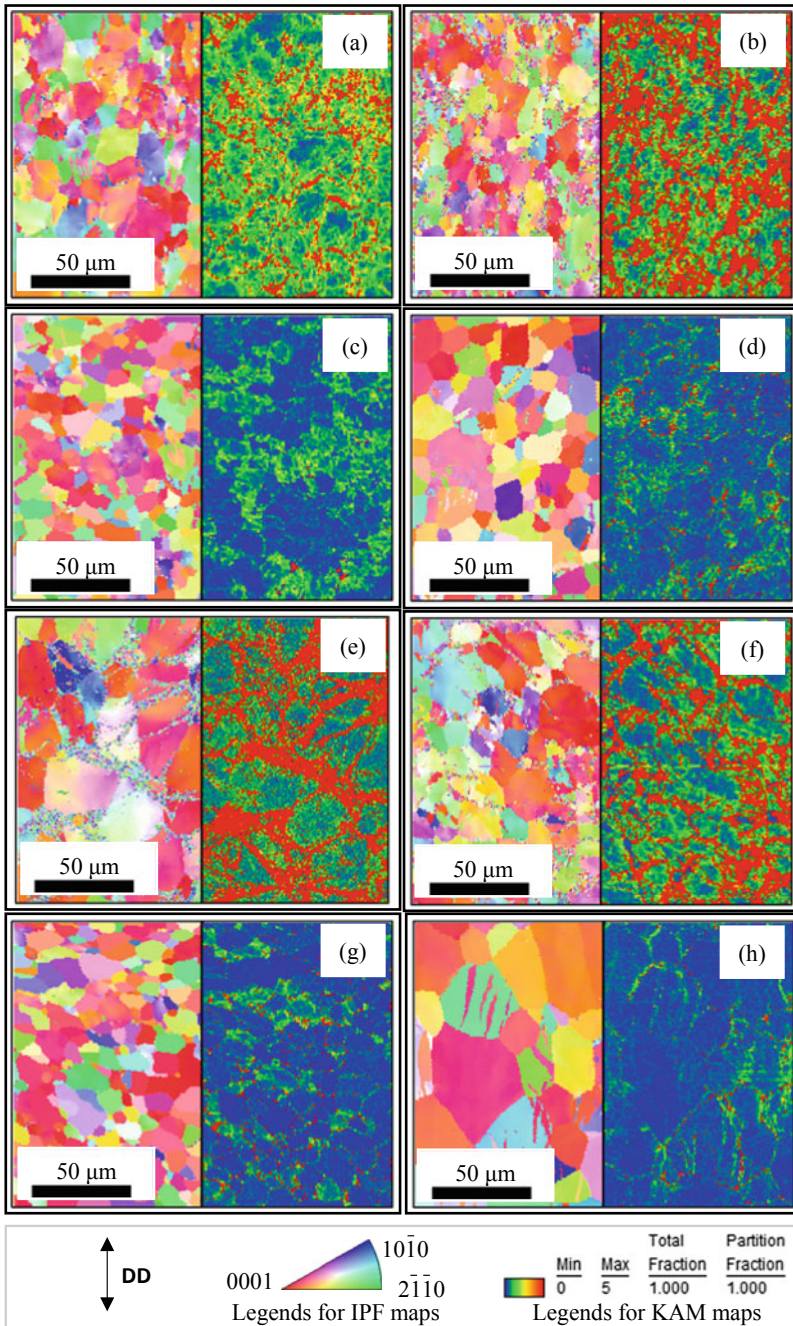
Fig. 3 IPF maps (left figure) and KAM maps (right figure) of the wires of **a** Mg-0.3Ca as drawn (reduction 15%), **b** Mg-0.3Ca annealed at 523K, **c** Mg-0.3Ca annealed at 598K, **d** Mg-0.3Ca annealed at 673K, **e** Mg-0.1Ca as drawn (reduction 15%), **f** Mg-0.1Zn annealed at 423K, **g** Mg-0.1Zn annealed at 473K, **h** Mg-0.1Zn annealed at 573K. (Color figure online)

Microstructure observation suggested that the degree of the accumulated region changed depending on the annealing temperature. While comparing the microstructural evolution in the annealed alloys, the trend was similar; however, the optimum temperature for annealing in Mg-0.3Ca was approximately 100 K higher than in Mg-0.1Zn. This result suggests that calcium solute is effective in suppressing recovery and/or recrystallization in magnesium.

Summary

This study investigated the effects of additive elements, calcium or zinc, on tensile mechanical properties of drawn magnesium wires. The as-drawn wire with a diameter of 0.2 mm had the highest ultimate tensile strength and the smallest fracture elongation. An increase in the annealing temperature decreased the yield strength and the ultimate tensile strength, and the fracture elongation exhibited a maximum at 598 K for Mg-0.3Ca and 473 K for Mg-0.1Zn. Comparing both alloys, Mg-0.1Zn showed superior strength and elongation overall. The difference in the distribution of accumulated area in as-drawn wire suggested that zinc solute might be segregated near the grain boundary, which resulted in higher strength and elongation in Mg-0.1Zn. On the other hand, it was found that calcium solute effectively suppressed recovery and/or recrystallization in magnesium.

References

1. Witte F (2010) Acta Biomater 6:1680–1692
2. Chen XM, Li LT, Chen WZ, Zhang WC, Zhang LX, Qiao YD, Wang ED (2017) Mater Sci Eng, A 708:351–359
3. Sun L, Bai J, Xue F, Chu C, Meng J (2018) Materials 11(4):602
4. Liu D, Bian MZ, Zhu SM, Chen WZ, Liu ZY, Wang ED, Nie JF (2017) Mater Sci Eng A 706:304–310
5. Griebel AJ, Schaffer JE, Hopkins TM, Alghalayini A, Mkorombindo T, Ojo KO, Xu Z, Little KJ, Pixley SK (2018) J Biomed Mater Res B Appl Biomater 106(5):1987–1997
6. Milenin A, Kustra P, Byrska-Wójcik D, Wróbel M, Paćko M, Sulej-Chojnacka J, Matuszyńska S, Płonka B (2020) Arch Civ Mech Eng 20:60
7. Sun L, Bai J, Xue F, Tao L, Chu C, Meng J (2017) Mater Des 135:267–274
8. Yan K, Sun J, Bai J, Liu H, Huang X, Jin Z, Yuna W (2019) Mater Sci Eng, A 739:513–518
9. Singh A, Dudekula AB, Ikeo N, Somekawa H, Mukai T (2016). In: Singh A, Solanki K, Manuel VM, Neelameggham NR (eds), Magnesium technology 2016, The minerals, metals & materials society, pp 83–88

Effect of Ca Addition on Microstructure of AZ61 Magnesium Alloy During High-Temperature Deformation

K. B. Kim, J. H. Lee, and K. H. Kim

Abstract Magnesium and its alloys have been restricted to wide adoption in the industrial field because of low formability due to lack of slip system on room temperature. It is necessary to control the texture to improve the plasticity. In order to investigate the Ca concentration and effect on microstructure deformation behavior, Ca addition on AZ magnesium alloy was experimentally investigated with AZ61 and AZX611. Through the analysis with XRD, EDS, due to Ca on AZ61, a new Al2Ca phase was formed. Plain strain compression was conducted at 723 K with a strain rate of $5.0 \times 10^{-2} \text{s}^{-1}$. The working softening was observed and flow stress of AZX611 was higher than AZ61. Also, PSN effect was shown at AZX611, and the microstructure was finer than AZ61.

Keywords Magnesium · Phase analysis · Precipitate · Ca content · Microstructure

Introduction

Magnesium and its alloys have been given attention in the industrial fields such as transportation and mobility due to high specific strength and low density. However, their lack of active slip system on the room temperature caused from HCP structure has restricted their wide adoption in industry. Furthermore, magnesium alloys worked at high temperature has strong basal texture parallel to working direction. The occurrence of basal texture causes the low formability and plastic anisotropy [1, 2]. Thus, it is important to control the texture formation to improve the plastic formability.

The researchers have studied the correlation between initial texture and texture development of AZ80 magnesium alloy. It was found that there is stable orientation

K. B. Kim · J. H. Lee · K. H. Kim (✉)
Department of Marine Convergence Design Engineering, Pukyong National University, 45 Yongso-ro, Nam-gu, Busan 48513, Republic of Korea
e-mail: mrppeng@pknu.ac.kr

J. H. Lee · K. H. Kim
Department of Metallurgical Engineering, Pukyong National University, 45 Yongso-ro, Nam-gu, Busan 48513, Republic of Korea

and grain growth occurs consuming adjacent unstable grains [3] Also, Park et al. have investigated the effect of Al content on AZ magnesium alloy and texture formation behavior. They reported that texture's main component and sharpness during high-temperature deformation can be varied by increasing Al concentration [4].

Ca as an alloying element has been reported that can make magnesium increase the flame resistance and mechanical properties. The authors found that Ca content forms the second-phase particle in magnesium alloy and these become the main reason to change the properties [5, 6].

However, the study about effect of Ca addition to magnesium alloy with texture formation behavior is still insufficient. In this study, in order to investigate the effect of Ca addition on phase formation and microstructural development during hot deformation in AZ61 magnesium alloy, conventional AZ61 and Ca-added AZ61 magnesium were investigated by high-temperature plain strain compression. A compression test was conducted at 723 K with a strain rate of $5 \times 10^{-2} s^{-1}$ and microstructure was observed by optical and scanning electron microscope.

Experimental Procedure

The AZ61, AZX611 magnesium alloy was used in this study. Before hot rolling, X-ray fluorescence was conducted with as-cast ingot and each composition of alloys is shown in Table 1.

Starting materials were rolled at 673 K with 25% rolling reduction and water quenched. After rolling, they were machined in rectangular shape with $6.7 \times 10 \times 10$ mm. The direction of thick and width was parallel to rolling and transverse direction. And then all specimens were quartz sealed with Ar gas after formation of vacuum inside. AZ61 specimens were annealed at 773 K for 2H and AZX611 specimens were annealed for 4H to make specimens have homogeneous distribution of second phases and microstructure. After annealing, all specimens were all water quenched. Figure 1 shows the initial microstructure of AZ61 and AZX611 annealed. All of grains were fully annealed and second-phase distribution is homogenized.

AZ61 was shown in second phase in the grain boundary, and AZX611 exist both on matrix and grain boundary. To distinguish the composition of second phase, X-ray diffraction and energy dispersive spectroscopy analysis were conducted.

High-temperature plain strain compression was conducted on both AZ61 and AZX611 specimens at the 723 K, strain rate was $5x10^{-2} s^{-1}$, and strain was up to –0.4 ~ –1.0. Deformed specimens were water quenched to prevent the change of

Table 1 Chemical composition of AZ61 and AZX611 magnesium alloy (wt%)

	Al	Zn	Ca	Mn	Mg
AZ61	6.15	0.52	–	0.20	Bal.
AZX611	6.12	0.51	1.51	0.21	Bal.
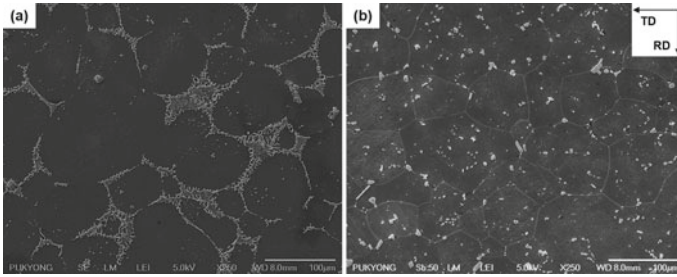
Fig. 1 As annealed microstructure of **a** AZ61, **b** AZX611 specimen

microstructure. They were cut perpendicular to compression direction and mechanically grinded using sandpaper up to #4000 and polished with OP-s suspension. After that, they were chemically etched with picric acid. The microstructure was investigated with optical and scanning electron microscopy.

Results and Discussion

Composition of Second Phase

Figure 2 shows the results of XRD diffraction of AZ61 and AZX611 as received specimens. AZ61 specimen showed α (Mg) + γ ($Mg_{17}Al_{12}$) two phase peak. However, AZX611 showed α + γ ($Mg_{17}Al_{12}$) + C15(Al_2Ca) triple phase peak.

Figure 3 and Table 2 show the results of SEM-EDS analysis of AZ61 and AZX611 as received specimen. In the case of AZ61, point (a) showed magnesium matrix that is Al solutes. point (b), (c) was $Mg_{17}Al_{12}$ phase. Otherwise, AZX611 showed magnesium matrix with Al solutes (point (d)) and point (b) was $Mg_{17}Al_{12}$ phase. But point (c), (d) was Al_2Ca phase. Moreover, $Mg_{17}Al_{12}$ phase particles were less seen in AZX611.

Figure 4 shows the EDS mapping of particle point of AZX611 in Fig. 3b point g. Mapping elements were selected as Mg, Al, and Ca. They are shown in Fig. 4b–d each. Magnesium is not shown in the particle only Al, Ca elements are shown. Consequently, second-phase particles shown in AZX611 are mostly Al_2Ca phase and low amount of $Mg_{17}Al_{12}$.

Janz et al. have reported that Mg–Ca alloy with 4wt%, 8wt% Al component has triple phase (α + γ + C15) under 473 K and $Mg_{17}Al_{12}$ phase fraction get decreased with a decrease in Al content and an increase in Ca [7]. This result shows that AZX611 mostly follows the Mg–Al–Ca phase diagram. Also, $Mg_{17}Al_{12}$ phase has been known as thermally unstable phase [8] and it solutes over 573 K. But, C15 (Al_2Ca) laves phase is thermally stable. Therefore, During the compression at the
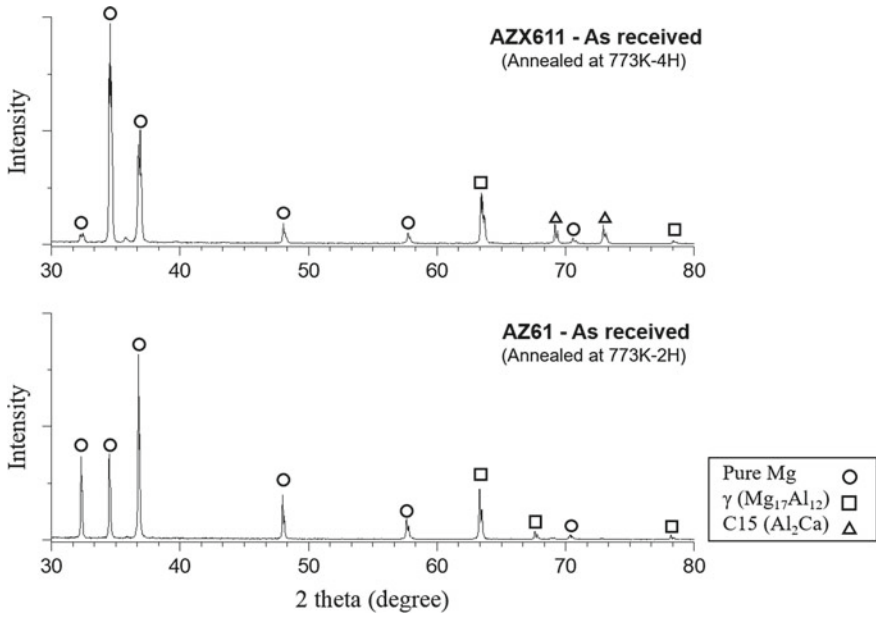
Fig. 2 Result of XRD diffraction of AZ61 and AZX611 specimens
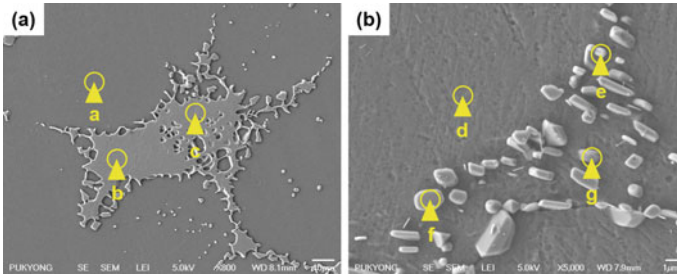
Fig. 3 EDS analysis point of AZ61 (**a**) and AZX611 (**b**). (Color figure online)

Table 2 The results of EDS analysis for AZ61, AZX611 s phase particle (at.%)

Site	Mg	Al	Ca	Zn	Phase
a	94.9	5.1	–	–	α
b	57.9	31.6	–	2.7	γ
c	57.0	30.7	–	3.8	γ
d	96.2	3.8	–	2.2	α
e	58.2	29.2	–	2.9	γ
f	6.9	61.1	22.4	–	C15
g	–	69.9	28.7	–	C15
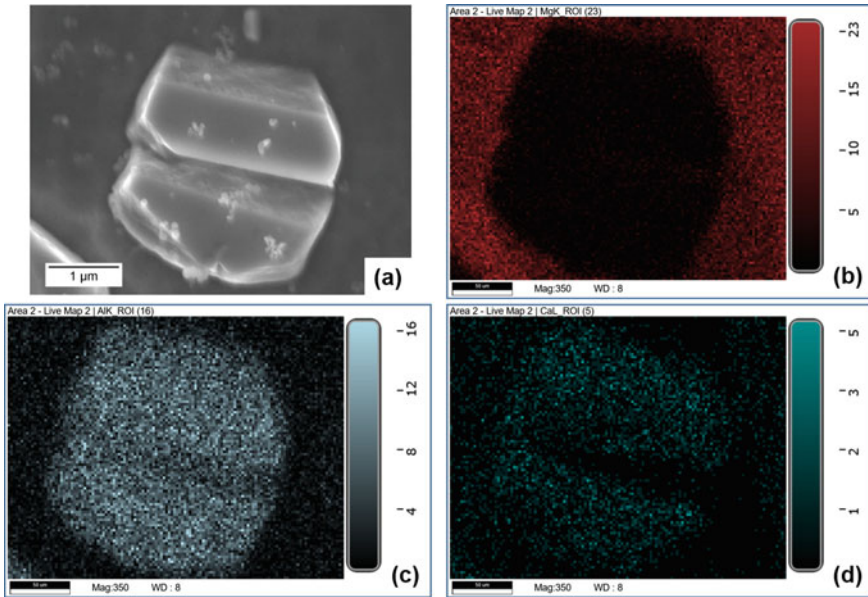
Fig. 4 The results of EDS mapping of point (g) in Fig. 3. **a** SEM image, mapping element, **b** Mg, **c** Al, **d** Ca. (Color figure online)

723 K, grains of AZ61 and AZX611 are composed of α single phase and α + C15 phase each.

Behavior of Plain Strain Compression

Figure 5 shows the true stress-true strain curve during high-temperature plain strain compression at the 723 K, strain rate $5 \times 10^{-2} s^{-1}$. The flow stresses of both alloys increased during the compression and work softening was observed. This behavior has been reported by Kim et al. regarding AZ80 magnesium alloy's high-temperature deformation [3].

And AZX611 showed higher flow stress than AZ61. This phenomenon seems to be due to C15 phase and still exists at 723 K that compression is conducted.

Behavior of Microstructure During Deformation

Figure 6 shows the microstructure after plain strain compression with strain up to –0.4 at 723 K under a strain rate of $5 \times 10^{-2} s^{-1}$ of AZ61 and AZX611. Figure 5a shows microstructure of AZ61. Coarse and fine grains exist uniformly distributed. This is
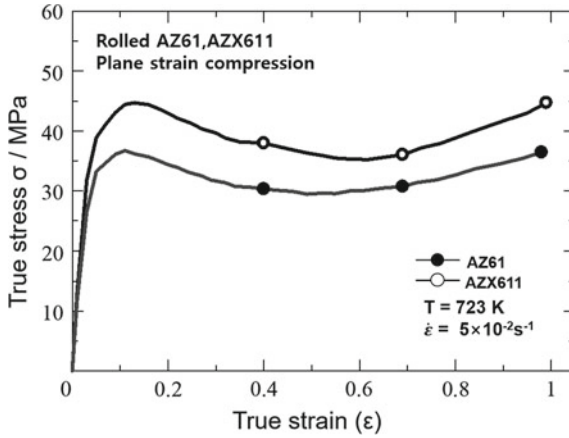
Fig. 5 True stress-true strain curves for the plain strain deformation at 723 K, under a strain rate of $5 \times 10^{-2}s^{-1}$ up to a strain of –1.0
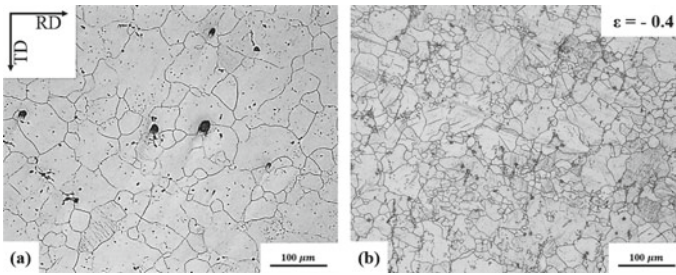
Fig. 6 Microstructure of **a** AZ61 and **b** AZX611 specimen observed by optical microscopy. The deformation condition was up to the strain –0.4, with the strain rate of $5.0 \times 10^{-2}s^{-1}$ at 723 K

general behavior that occurs at AZ system magnesium alloy during hot deformation [3]. However, in the case of AZX611, mostly fine grains are distributed around the second phase.

Figure 7 shows the microstructure after plain strain compression with strain up to –0.7. The overall grain size becomes decreased with increasing strain in two alloys either. Also, microstructure deformation behavior is similar for each other.

Figure 8 shows the microstructure after plain strain compression with strain up to –1.0. AZ61 specimen at strain –1.0 shows fine and uniform grain and average grain size lasts getting decreased to the end of deformation. As Kim et al. have reported, this means dynamic recrystallization has occurred during high-temperature deformation [3].

Either with AZ61, overall grain size of AZX611 gets decreased with strain increased. But, they are more fine than AZ6. It seems that the second phase refines the grains of AZ61 magnesium alloy.
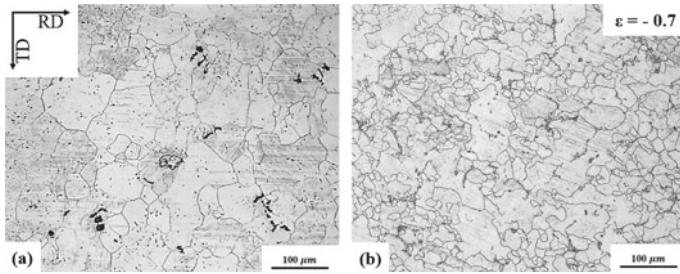
Fig. 7 Microstructure of **a** AZ61 and **b** AZX611 specimen. The deformation condition was up to the strain –0.7 with the strain rate of $5.0 \times 10^{-2} \text{s}^{-1}$ at 723 K
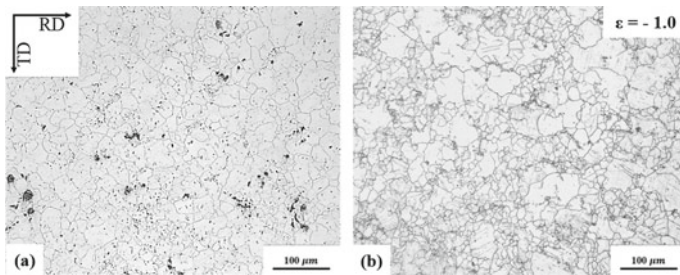
Fig. 8 Microstructure of **a** AZ61 and **b** AZX611 specimen. The deformation condition was up to the strain –1.0 with the strain rate of $5.0 \times 10^{-2} \text{s}^{-1}$ at 723 K

The researcher has reported that for M1 alloy which has particle inside the matrix, Particle Stimulated Nucleation (PSN) effect occurs. After deformation, particle was surrounded by new fine grain developed [9]. Also, it seems that Al_2Ca particle in AZX611 does same role with Mn contents in M1 alloy. They stimulate particle stimulated nucleation and work as a new site.

In this study, the effect of Ca addition on AZ61 microstructural deformation behavior with AZ61 and AZX611 magnesium alloy was discussed. However, texture deformation behavior during hot compression with PSN effect needs to be investigated.

Conclusion

In this study, effect of Ca addition about microstructure and second phase on AZ61 magnesium alloy was investigated. AZ61 and AZX611 magnesium alloy was investigated by high-temperature plain strain compression and major results are as follows:

(1)   Adding Ca on AZ61 magnesium alloy makes $C15(Al_2Ca)$ second phase increased and γ $(Mg_{17}Al_{12})$ phase decreased.
(2)   Ca concentration makes AZ61 alloy to have higher strength at high temperature.
(3)   During the high-temperature deformation, dynamic recrystallization occurs. But, existence of C15 phase changed the DRX mechanism of AZX611 from AZ61.
(4)   Thermally stable C15 phase is contribute to grain refinement of AZ61 during hot working and stimulates PSN effect.

References

1. Mordike BL, Ebert T (2001) Magnesium: properties — applications — potential. Mater Sci Eng A 302(1):37–45
2. Amjad J, Mark K, Frank C (2018) Overcoming barriers to magnesium rolling. Adv Mater Process 176:16–21
3. Kim K, Okayasu K, Fukutomi H (2015) Influence of the initial texture on texture formation of high temperature deformation in AZ80 magnesium alloy. Mater Trans 56(1):17–22
4. Park MS, Park HG, Choi JH, Kim KH (2016) Effect of aluminium content on texture formation behaviors in magnesium alloy. Mater Sci Forum 879:1449–1453
5. Kawabata H, Yagi Y, Aoki Y, Kato H, Kitayama K, Hibi K (2018) Effect of calcium on the combustion behavior of molten AZ91 magnesium alloy. Mater Trans 59(2):272–279
6. Hakamada M, Watazu A, Saito N, Iwasaki H (2010) Dynamic recrystallization during hot compression of as-cast and homogenized noncombustible Mg–9Al–1Zn–1Ca (in mass%) alloys. Mater Sci Eng 527(26):7143–7146
7. Janz A, Gröbner J, Cao H, Zhu J, Chang YA, Schmid-Fetzer R (2009) Thermodynamic modeling of the Mg–Al–Ca system. Acta Mater 57(3):682–694
8. Wang L, Liu H (2006) The microstructural evolution of $Al_{12}Mg_{17}$ alloy during the quenching processes. J Non-Cryst Solids 352(26–27):2880–2884
9. Robson JD, Henry DT, Davis B (2009) Particle effects on recrystallization in magnesium–manganese alloys: particle-stimulated nucleation. Acta Mater 57(9):2739–2747

Investigation of the Effect of Extrusion Speed on Mechanical and Microstructural Characteristics in a Tubular Profile Extruded from AM50 Magnesium Alloy

Enes Kurtulus, Irem Sapmaz, and Emrah F. Ozdogru

Abstract During the extrusion process of magnesium alloys, the extrusion speed has different effects on the microstructure and mechanical properties of the material. In this study, tubular extruded profiles produced from AM50 magnesium alloy were investigated. Extrusion production was carried out with 1 mm/s, 1.5 mm/s, and 2 mm/s ram speed, respectively. Tensile tests were carried out on the tensile test samples taken in the extrusion direction. As a result of these tests, yield strength, tensile strength, and elongation values were achieved for different extrusion speeds and compared with each other. In addition, microstructure investigation was carried out, including particle sizes and hardness measurements on tensile test samples via both optical and SEM analysis techniques. Finally, the fracture surfaces of the samples were examined by the SEM method, and the differences were examined.

Keywords Magnesium alloy · AM50 · Extrusion speed · Microstructure · SEM

Introduction

The use of lightweight magnesium alloys is according to the demand for a better fuel economy and higher operating efficiency, and related reduction of exhaust gases in automotive applications [1]. Magnesium alloys provide a higher weight reduction ratio due to their lower density than aluminum and steel [2]. According to the comparison between Mg and other engineering materials, Mg alloys show similar or even better specific Young's modulus and high specific strength values [3]. In industry, magnesium casting products are generally preferred because of their high productivity, good surface quality, and dimensional precision accuracy. Even though wrought magnesium alloys that have been used in structural applications have better mechanical and ductility properties than casting products, their ability to plastic

E. Kurtulus (✉) · I. Sapmaz
Yeşilova Holding R&D Center, Bursa, Turkey
e-mail: enes.kurtulus@yesilova.com.tr

E. F. Ozdogru
TRI Metalürji, Istanbul, Turkey

deformation is low due to having a hexagonal crystal structure [4]. Even though extruded Mg alloys provide higher mechanical properties, the extrusion process has crucial obstacles like lower extrusion speed and a narrower range of extrusion temperatures [5].

Containing aluminum and manganese, AM50 magnesium alloy allows high-energy absorption and elongation at high strengths. It is typically used in the automotive industry for steering wheels, dashboards, and seat frames [6]. Some different studies in the literature investigate the microstructure of AM50 magnesium alloy under different conditions [7]. They contain die casting, rheo-casting, and extruded solution treated conditions [8]. So far, systematic information about the relationship between extrusion speed and mechanical properties is relatively limited for this alloy. For Mg alloy extrusions, extrusion speed is one of the critical factors which influence the extent of the dynamic recrystallization (DRX) process [9]. So, the mechanical properties of Mg alloy extrusions are mainly dependent on the extrusion speed. This study was carried out to investigate the influence of extrusion speed on the microstructure and mechanical properties of the extruded AM50 magnesium alloy.

Experimental Method

The employed material is AM50 magnesium alloy. The chemical composition of the alloy is shown in Table 1. The homogenization process was performed in the annealing furnace, as 15 h at 400 °C for AM50 alloy.

The dimension of the extruded tube is 70 mm in diameter with 3.35 mm thickness (Fig. 1a). The extrusion ratio is 36.90. The ram speeds are 1 mm/s, 1.5 mm/s, and 2 mm/s, respectively. While determining the limits, the evaluation was made in terms of press capacity and appropriate product quality. When the speed of 2 mm/s

Table 1 Chemical composition of AM50 alloy tubes (values in weight percent, wt%)

Alloy	Al	Zn	Mn	Si	Fe	Cu	Mg
AM50	4.5–5.3	<0.02	0.28–0.5	<0.05	<0.004	<0.008	Balance

Fig. 1 **a** Section view of extruded tube, **b** tensile specimens machined from extruded tube. (Color figure online)

is exceeded in the extrusion trials, hot cracking problems have been observed on the extruded profile surface, and if the speed is below 1 mm/s, the extrusion press force requirement exceeds the capacity.

Tensile test specimens were machined along the longitudinal direction of the tubes according to the DIN 50125 standard (Fig. 1b). The tensile properties of the alloy samples were evaluated using a universal testing machine (Shimadzu AG—IS 250 kN) at room temperature according to ISO EN 6892-1. Minimum of four and maximum of six tests were done for analyzing tensile properties statistically.

Hardness tests were performed according to EN 6506-1 standard using a universal hardness measurement machine (DIGIROCK-RBV Brinell, Vickers) at room temperature. The Brinell hardness values (HB) of the samples were measured using an indenter ball with a diameter of 2.5 mm. The load used was 62.5 kg. Five measurements were done for each sample.

The metallographic specimens were taken from cross section of the hollow profiles, and they were ground 180, 800, 1200, and 2000 sandpaper and polished using 6 μm, diamond pastes. Then, specimens were etched by using 3.5 mL acetic acid, 3 mL water, and 50 mL picral for 6 s. The grain size analysis was characterized on selected specimens using a Nikon LV150NA optical microscope (OM). The mean linear intercept method was used to measure the average grain size, and analysis was performed by image analysis software called Clemex. The fracture surfaces after the tensile tests specimens in each parameter were observed by scanning electron microscopy (SEM) (JEOL NeoScope JCM-6000 Plus). EDX analysis was performed with the help of the same device.

Results and Discussion

The average grain size of the AM50 alloys based on the extrusion speed is shown in Table 2. According to the average grain size results of the extruded AM50 alloy, there is no direct correlation between the ram speed and the average grain size of the extruded magnesium alloy.

The microstructural images of extruded AM50 alloy are shown in Fig. 2. According to the microstructures of the alloy, there can be observed a substructure inside analyzed large grain which can be caused by not full dynamic recrystallization during the extrusion process [10, 11]. The arrangement of large and small grains in the microstructure has changed with the increased extrusion speed. It was found that twinning bands have been generated in the material due to die exit temperature above

Table 2 Average grain sizes according to ram speeds

Alloy	Ram speed (mm/s)	The average grain size (μm)
AM50	1	45
	1.5	43
	2	44
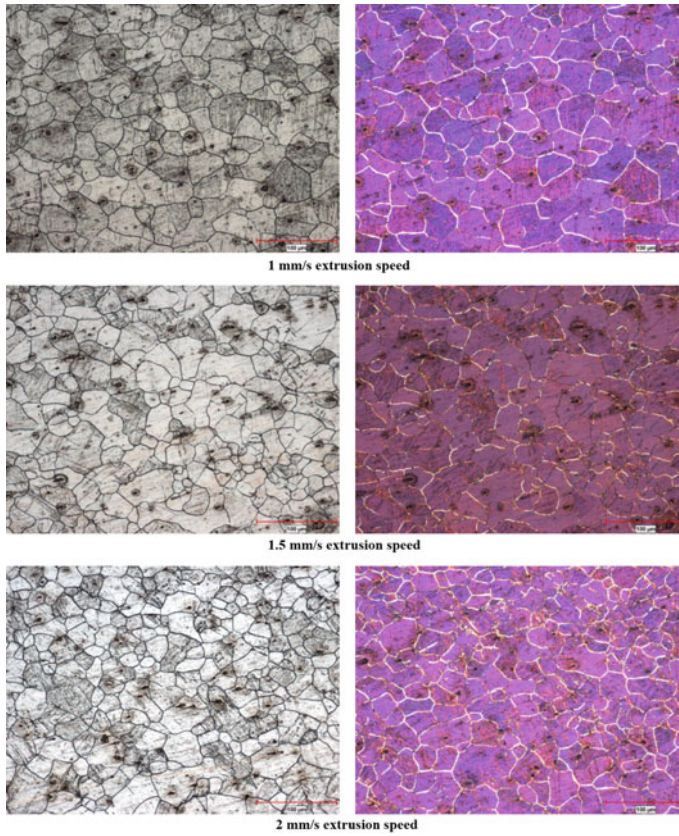
Fig. 2 Microstructural images of the extruded AM50 magnesium alloy with different extrusion speeds. (Color figure online)

460 °C. However, there is no correlation between the extrusion speed and the mass of twinning bands for the extruded AM50 alloy.

The average mechanical properties of the tube extruded at different speeds are shown in Table 3 and Fig. 3, respectively.

The typical SEM micrographs of the fracture surface of the extruded AM50 magnesium alloy after the tensile test are shown in Fig. 4. According to the fracture

Table 3 Average mechanical properties of the magnesium extruded alloys

Alloy	Ram speed (mm/s)	Yield strength (MPa)	Ultimate tensile strength (MPa)	Strain (%)	Hardness (HB)
AM50	1	138.834	253.085	9.320	68.33
	1.5	134.147	242.389	9.510	64.03
	2	136.106	246.509	10.443	71.81
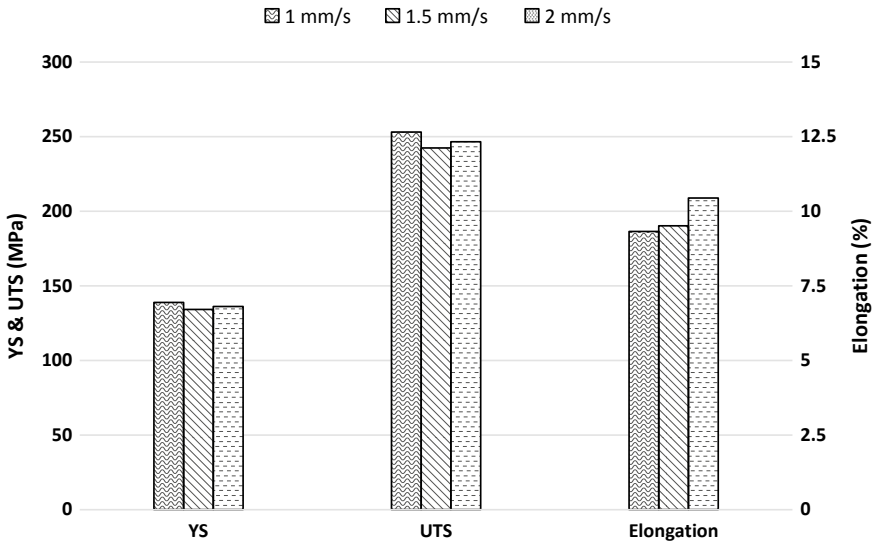
Fig. 3 Mechanical properties of AM50 alloy at different ram speeds

surfaces of the tensile test specimens regarding the extrusion speed, the specimen that extruded with 1 mm/s speed showed a brittle fracture. The fracture type was found out as an intergranular. The fracture surface of the sample that extruded 1.5 mm/s speed, lots of dimples, and cleavage steps revealed the mixture fracture mode of ductile fracture and brittle fracture. When the extrusion speed increased to 2 mm/s, the surface morphology included dimples were found more than planar, and the surface morphology was found out a more likely ductile fracture. The interrelation was investigated between a fracture surface and the strain value from the tensile test, and the results were correlated with each other. The highest strain value was observed in samples produced at 2 mm/s and had a more ductile fracture surface.

Additionally, the fracture type is affected slightly by the extrusion speed and is more prone to change into a ductile fracture. However, there is hardly any link between the extrusion speed and mechanical properties. In conclusion, when the extrusion speed is increased, the number of polygonal-shaped particles and their intensity in the structure were found to increase. The EDX analysis of the main inclusions found out from the fracture surfaces of the tensile test specimens is shown in Fig. 5. There were found two main polygonal shaped inclusions. These inclusions are based on Mn and Mn-Si regarding the EDX results.
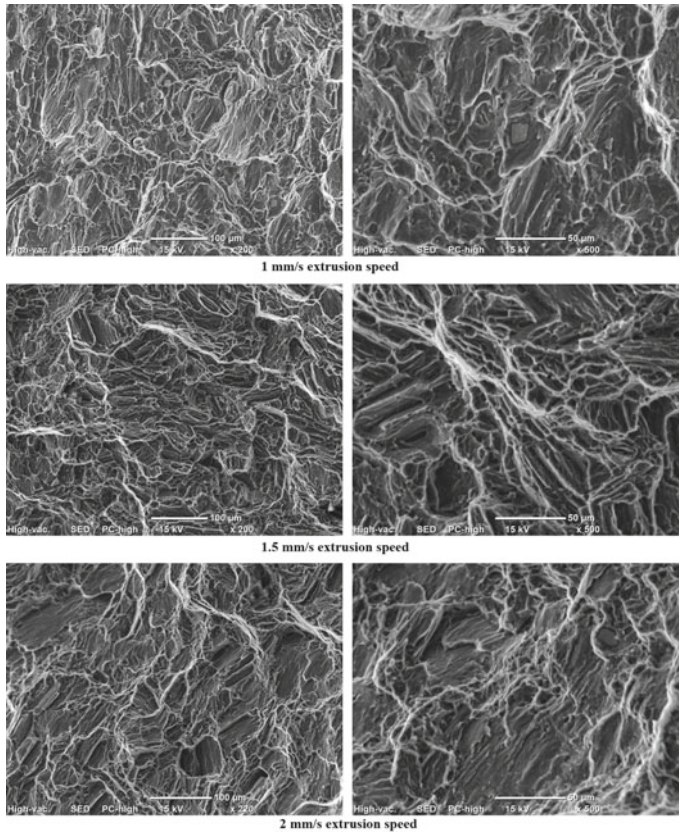
Fig. 4 Fracture surfaces of the extruded AM50 alloy after the tensile test according to ram speed

Conclusion

In this study, the effects of extrusion speed on the microstructure and mechanical properties of an extruded AM50 magnesium alloy were reported. The main findings of the study were as follows:

- There is no direct correlation between yield strength and ultimate tensile strength values with extrusion speed.
- The strain values of the AM50 alloy increase when the extrusion speed is higher.
- Hardness values do not show a direct correlation with the extrusion speed, but it is found that the hardness values are maximum with 2 mm/s ram speed.
- The specimen extruded with 1 mm/s speed showed brittle fracture while it had a ductile fracture surface at 2 mm/s extrusion ram speed.

Mn-based inclusion

Mn-Si based inclusion
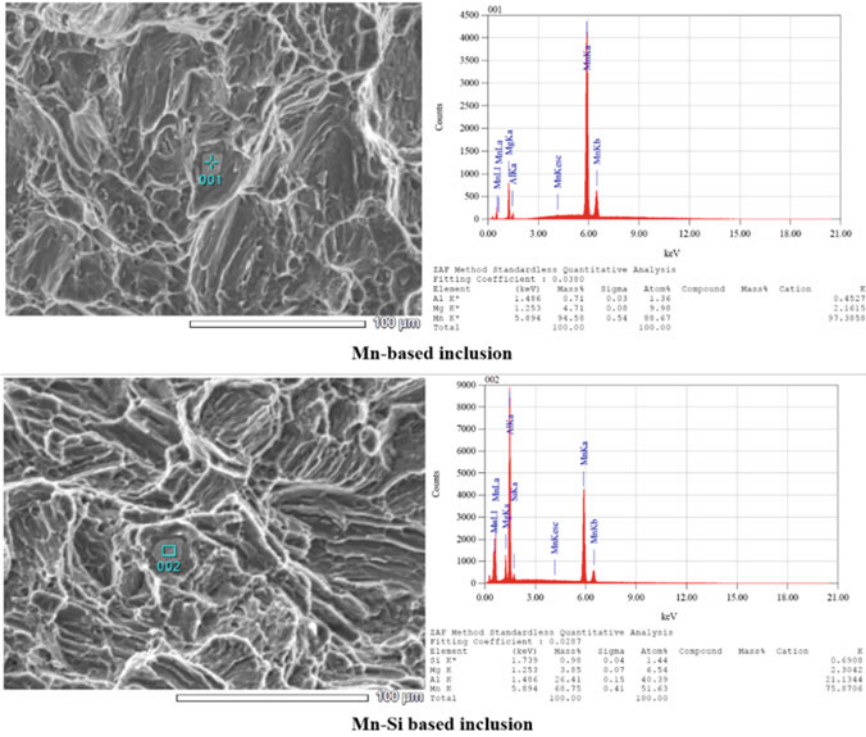
Fig. 5 EDX results of the main inclusions of extruded AM50 alloy. (Color figure online)

- It was found that twinning bands have been generated in the material, and the arrangement of large and small grains in the microstructure has changed with the increased extrusion speed.

References

1. Luo AA (2005) Wrought magnesium alloys and manufacturing processes for automotive applications. Trans-J Mater Manuf SAE, PA, U.S.A. 411–421
2. Polmear IJ (1994) Magnesium alloys and applications. Mater Sci Technol 10:1–16
3. Blawert C, Hort N, Kainer KU (2004) Automotive applications of magnesium and its alloys. Trans Indian Inst Metals 57:397–408
4. Ariffin AK, Mohamed NAN, Abdullah S (2009) A review of workability of wrought magnesium. Adv Manuf Res Group 3:1–15

5. Atwell DL, Barnett MR (2007) Extrusion limits of magnesium alloys. Metall Mater Trans A Phys Metall Mater Sci 38A:3032–3041

6. Kiełbus A, Rzychoń T, Cibis R (2006) Microstructure of AM50 die casting magnesium alloy. J Achiev Mater Manuf, Eng, p 18

7. Esmaily M, Shahabi-Navid M, Mortazavi N, Svensson JE, Halvarsson M, Wessén M, Jarfors AEW, Johansson LG (2014) Microstructural characterization of the Mg–Al alloy AM50 produced by a newly developed rheo-casting process. Mater Charact 95:50–64

8. Wang Q, Chen Y, Peng J, Liu M, Ding W, Suery M, Blandin JJ (2005) Microstructure and mechanical properties of AM50+xTi magnesium alloys extruded from as-cast and solution treated conditions. Mater Sci Forum 488–489:629–632

9. Hsiang SH, Lin YW (2007) Investigation of the influence of process parameters on hot extrusion of magnesium alloy tubes. J Mater Process Technol 192–193:292–299

10. Stefanik A, Szota P, Mróz S, Bajor T, Dyja H (2015) Properties of the AZ31 magnesium alloy round bars obtained in different rolling processes. Arch Metall Mater 60(4):3002–3005

11. Gao CY, Zhang LC, Guo WG, Li YL, Lu WR, Ke YL (2014) Dynamic plasticity of AZ31 magnesium alloy: Experimental investigation and constitutive modeling. Mater Sci Eng A 613:379–389

Understanding Deformation Behavior of AM50 and AZ31 Magnesium Extrusions with Various Heat Treatments in Comparison with AA6063 and AA6082 Aluminum Extrusions

Baris Kara, Enes Kurtulus, Asım Zeybek, Meryem Altay, and Hakan Aydın

Abstract The effect of the cooling methods after extrusion and subsequent heat treatment on mechanical properties of AM50 and AZ31 were studied. For each alloy, the influence of orientation of the specimen with respect to the extrusion direction was also investigated in comparison with 6063 and 6082 aluminum extrusions. The results obtained by hardness tests and Charpy impact tests demonstrate that heat treatments have no significant effect on AZ31 and AM50 extrusions. Tensile test results also generally support this statement; however, the elongation values of Mg alloys display fluctuations and do not show any relation with the corresponding tensile and yield strength values. As a result, any relations between the elongation values and the heat treatment conditions are not detected. AZ31 and AM50 extrusions exhibit highly anisotropic behaviour. AA6063 and AA6082 aluminum extrusions display low anisotrophy and provide high fracture energy values corresponding to their elongation values. However, AM50 and AZ31 alloys provide low fracture energy values regardless of their elongation values.

Keywords Magnesium alloy · Heat treatment · AM50 · AZ31 · Energy absorption

B. Kara (✉) · E. Kurtulus · A. Zeybek
Yesilova Holding, Bursa, Turkey
e-mail: baris.kara@yesilova.com.tr

M. Altay · H. Aydın
Engineering Faculty, Mechanical Engineering Department, Bursa Uludag University, Bursa, Turkey

Introduction

The elemental density of magnesium is 1.74 g/cm^3, which is one-third that of aluminum (Al). Therefore, magnesium extrusions can provide significant lightweight for automobile applications due to their high specific strength, low density, and high damping capacity [1, 2].

AZ (Mg-Al-Zn) types of alloys are the most popular magnesium extrusion alloys. On the other hand, AM (Mg-Al-Mn) types of alloys are mostly used as cast parts due to good ductility and toughness. However, AM types of extrusions have not been widely investigated in the literature. In general, magnesium alloys exhibit a lower extrusion speed than Al alloys and a re-carried out at a higher pressure level [3, 4]. For magnesium extrusions, there exists a great discrepancy between tensile samples taken from the direction parallel and perpendicular to the extrusion direction. Consequently, it exhibits anisotropic mechanical properties [5, 6]. Usage of Mg alloys is restricted because of the limited ductility at room temperature, which can be attributed to its hexagonal close-packed (hcp) structure [7, 8].

Mg-Al-based alloys may improve strength through the precipitation of the β–Mg$_{17}$Al$_{12}$ phase in the matrix based on the alloy content. Al is the most effective alloying element to strengthen magnesium through the precipitation of β–Mg$_{17}$Al$_{12}$ [9]. Zinc is next to Al in effectiveness as an alloying element for magnesium. Manganese does not have much effect on tensile strength, but it does slightly increase the yield strength of magnesium alloys [10, 11].

In this study, heat treatment responses and anisotropic behaviors of AZ31 and AM50 magnesium extrusions and their reflections on energy absorption capabilities of the alloys are investigated in comparison with AA6063-T6 and AA6082-T6 aluminum alloys.

Experiment

Materials used in the research were AZ31, AM50, AA6063, and AA6082 alloys whose typical compositions are presented in Table 1. The magnesium plates were extruded at 400 °C, quenched in water or air, and stretched by %1,3.

Table 1 Chemical compositions of the alloys (%)

	Al	Zn	Mn	Fe	Cu	Si	Ni	Ca	Cr	Ti	Mg
AZ31	3.36	1.12	0.345	0.001	0.0003	0.0110	0.0002	/	/	/	Balance
AM50	4.74	0.004	0.38	0.0022	0.0006	0.0224	0.0007	/	/	/	Balance
AA6063	Balance	0.10	0.10	0.35	0.10	0.2–0.6	/	/	0.10	0.10	0.45–0.9
AA6082	Balance	0.20	0.4–1	0.50	0.10	0.7–1.3	/	/	0.25	0.10	0.6–1.2
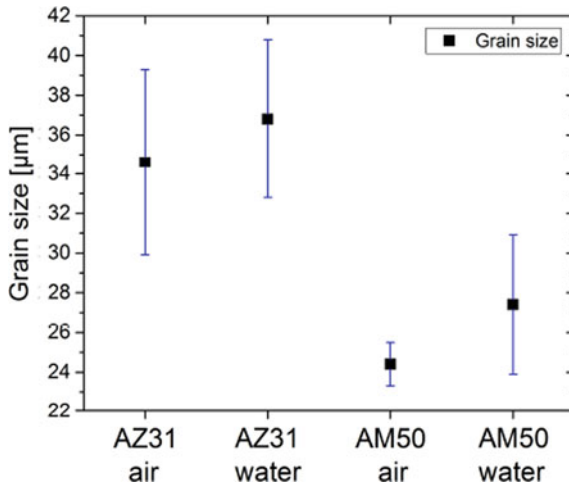
Fig. 1 Microstructural analysis of extruded plates. (Color figure online)

The graph of grain size analysis of the magnesium extrusions is presented in Fig. 1. The microstructure of AM50 is less inhomogeneous and the grain size of AM50 plates is smaller.

Experimental details in this study are presented in Table 2.

To investigate the effect of cooling methods after extrusion on mechanical properties and subsequent heat treat treatments, the trials were carried out. For trial 1, extruded magnesium plates were naturally aged for 3 months. For trial 2, extruded and naturally aged magnesium plates were subsequently artificially aged at 220 °C for different times. For trial 3, extruded magnesium plates were solution heat treated at 400 °C for 2 h and subsequently artifically aged at 220 °C for different times. For trial 4, extruded and naturally aged Al plates were subsequently artificially aged at 185 °C for 6 h.

Table 2 Experimental approach and flows

Trials No.	Code	Material	Quenching Method During Extrusion	Natural Aging (NA) After Extrusion	Solution Heat Treatment (SHT)	Natural Aging (NA)After SHT	Artificially Aging (AA)	Tests		
Trial 1	T1.1-W	AM50 extruded plate - 4 mm	Water	3 months	None	None	None	Hardness (HB)	Tensile Test	Charpy Impact Test
	T1.2-A	AM50 extruded plate - 4 mm	Air							
	T1.3-W	AZ31 extruded plate - 4 mm	Water							
	T1.4-A	AZ31 extruded plate - 4 mm	Air							
Trial 2	T2.1-W	AM50 extruded plate - 4 mm	Water	3 months	None	None	220°C (0-8 h)			
	T2.2-A	AM50 extruded plate - 4 mm	Air							
	T2.3-W	AZ31 extruded plate - 4 mm	Water							
	T2.4-A	AZ31 extruded plate - 4 mm	Air							
Trial 3	T3.1-W	AM50 extruded plate - 4 mm	Water	3 months	400°C for 2 hours	None	220°C (0-6 h)			
	T3.2-A	AM50 extruded plate - 4 mm	Air							
	T3.3-W	AZ31 extruded plate - 4 mm	Water							
	T3.4-A	AZ31 extruded plate - 4 mm	Air							
Trial 4	T4.1	6063-T5 extruded plate - 3 mm	Water	2 days	None	2 days	185°C for 6 hr			
	T4.2	6062-T5 extruded plate - 3 mm	Water	2 days	None	2 days	185°C for 6 hr			

Brinell hardness was tested by applying a test load (62.5 kgf) with a 2.5 mm diameter indenter. The hardness was measured at 3 points on each specimen. Hardness-time data of the heat-treated specimens were plotted for trial 2 and trial 3. Additionally, the effect of natural aging after the solution heat treatment (400 °C for 2 h.) was also illustrated.

Sub-size tensile specimens were prepared according to ASTM E8/E8m-16a and the tensile testing was carried out on a Shimadzu testing machine with a crosshead speed of 0.5 mm/min to the yield point and 4.2 mm/min to the fracture. Charpy (Simple-Beam) impact test specimens were prepared according to ASTM E23-07a (Type C). The tests were repeated twice and the average values were presented.

The coupons for tensile tests and impact tests were machined in three directions, 0°, 45° and 90° with respect to the extrusion direction of the plates to investigate the effect of the different heat treatment procedures on mechanical properties of the magnesium alloys in comparison with AA6063 and AA6082 extrusions (Fig. 2).
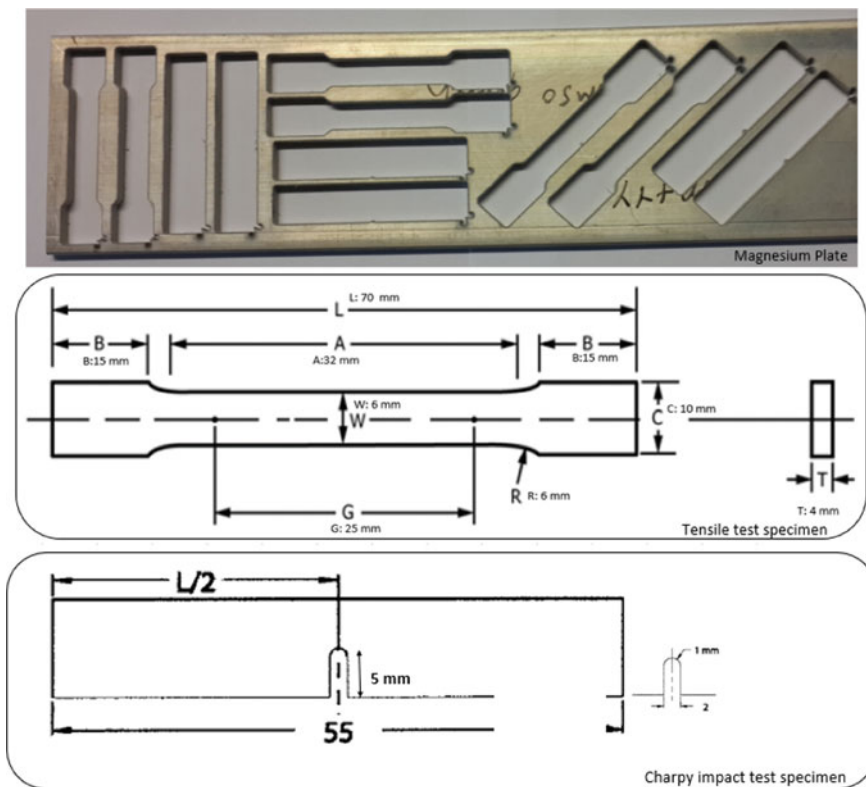
Fig. 2 Tensile and Charpy test specimens used for trials. (Color figure online)

Results

Hardness Test:

Natural aging curves for AM50 and AZ31 plates after solution heat treatment at 400 °C for 2 h are presented in Fig. 3.

The hardness values as a function of the heat treatment time for trial 2 and trial 3 were measured and illustrated in Fig. 4.
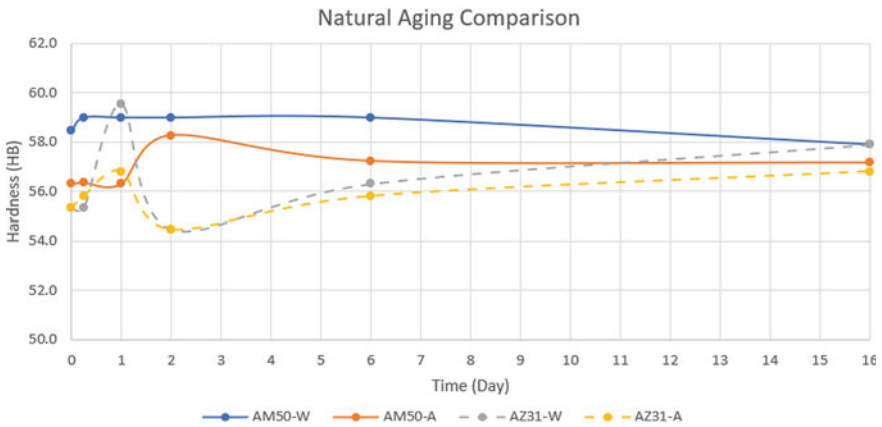
Fig. 3 Natural aging curve obtained after solution heat treatment at 400 °C for 2 h (W: Water quenched after extrusion A: Air quenched after extrusion). (Color figure online)
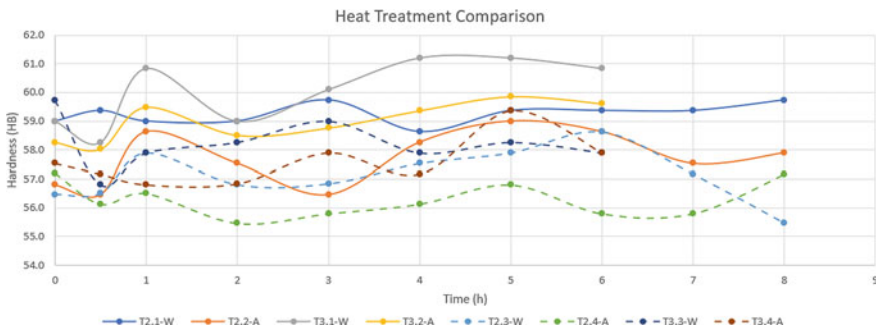
Fig. 4 Hardness versus time curves for trial 2 and trial 3. (Color figure online)

Tensile and Charpy Impact Tests:

Mechanical properties of AM50 and AZ31 under different heat treatments processes were investigated by comparing tensile strength, yield strength, ductility, and impact energy properties. AA6063 and AA6082 aluminum extrusions are also analyzed in the figures below.

Anisotropic behavior of AM50 and AZ31 in the extruded condition, AA6063-T5 and AA6082-T5 were also investigated by comparing tensile strength, yield strength, ductility, and impact energy properties (Fig. 6).

Discussion

In this paper, the mechanical properties of AM50 and AZ31 extrusions subjected to the different heat treatments have been studied in comparison with AA6063 and AA6082 aluminum alloys.

The hardness results plotted in figure 3 and figure 4 demonstrates that natural aging and also different heat treatments have no significant effect on hardness values of AZ31 and AM50 extrusions. Tensile test results in Figure 5 also generally support this statement; however, the elongation values of Mg alloys display fluctuations and do not show any relation with the corresponding tensile and yield strength values. As a result, any relations between the elongation values and the heat treatment conditions are not detected. Energy absorption capacity of AM50 alloy is slightly higher than AZ31 alloy according to the Charpy test results. This may be attributed to the fine grain structure of AM50 extrusions. Based on the results, heat treatment has no significat effect on fracture energy of AM50 and AZ31 extrusions.

The anisotropy of the alloys was characterized through tensile tests performed in the extrusion, diagonal and transverse directions and shown in Fig. 6. AZ31 extrusions exhibit highly anisotropic behavior based on the yield strength and the elongation values and less anisotropic behavior in terms of the tensile strength. AM50 extrusions also show anisotropic behavior based on the elongation values. However, the tensile and the yield strength values of AM50 extrusions exhibit less anisotropy compared to AZ31 alloy. The Charpy impact test results (Fracture energy) do not show a good agreement with the elongation values of the magnesium extrusions.

AA6063 and AA6082 aluminum extrusions exhibit less anisotropic behavior. Additionally, the impact test results of these alloys correspond to their elongation values. Energy absorption capacities of aluminum alloys are much higher than both magnesium alloys according to the Charpy impact test.
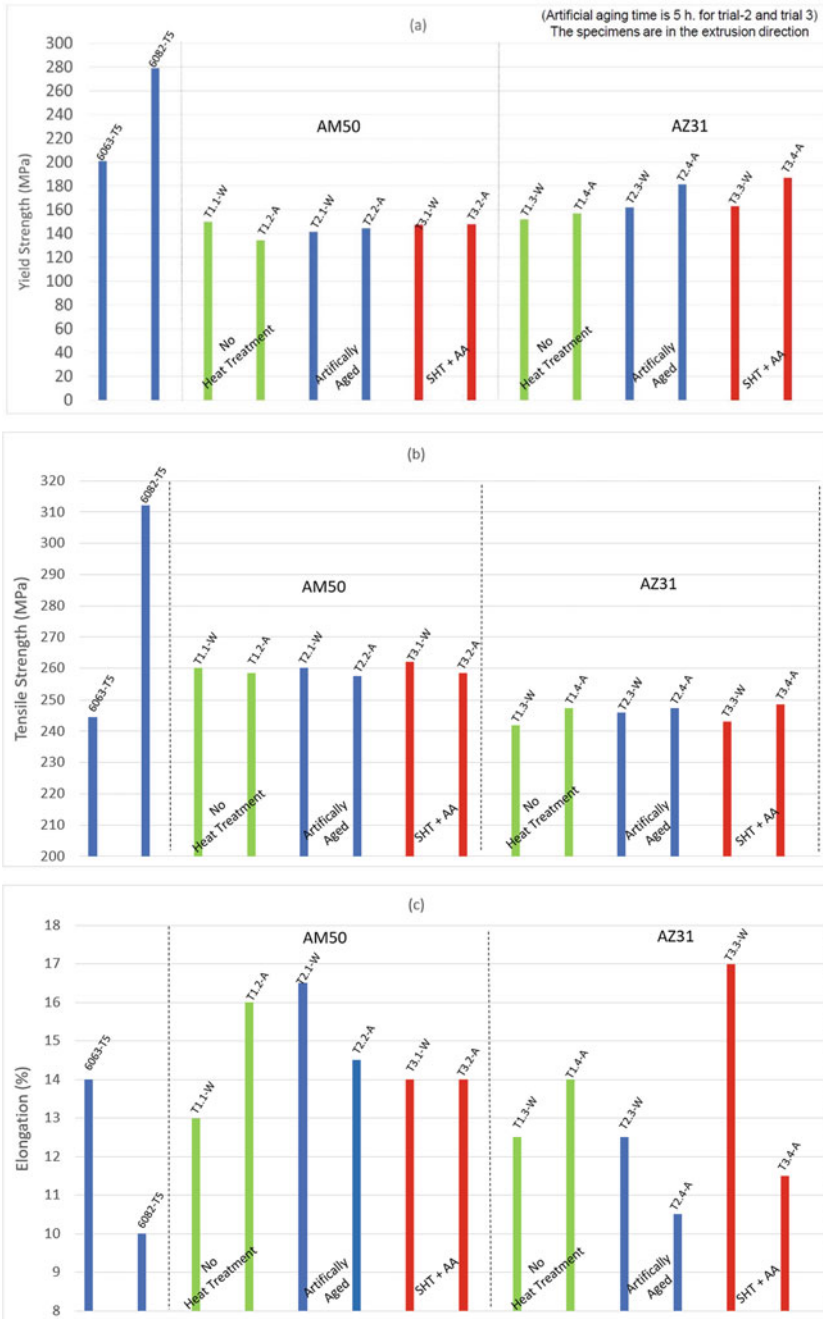
Fig. 5 Heat treatment effect on mechanical properties on **a** Yield strength **b** Tensile strength **c** Elongation **d** Fracture energy (Note: Artificial aging time is 5 h. for trial 2 and trial 3). (Color figure online)
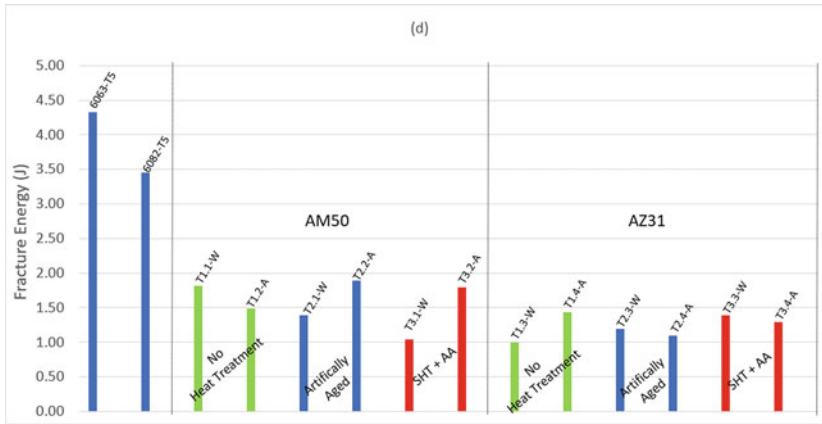
Fig. 5 (continued)

Conclusion

The effect of the cooling methods after extrusion and subsequent heat treatment on mechanical properties of magnesium alloys were studied. For each alloy, the influence of orientation of the specimen with respect to the extrusion direction was also investigated.

The results show that the heat treatment processes have no significant effect on fracture energy AM50 and AZ31 magnesium alloys. Additionally, AZ31 and AM50 extrusions display anisotropic behavior during deformation, which has a profound influence on their elongation values.

AA6063 and AA6082 aluminum extrusions display low anisotropy and provide high fracture energy values corresponding to their elongation values. However, AM50 and AZ31 alloy provide low fracture energy values regardless of their elongation values. Therefore, the low energy absorption capacities of AM50 and AZ31 extrusions must be taken into account when these alloys are used in the automotive safety crash parts.
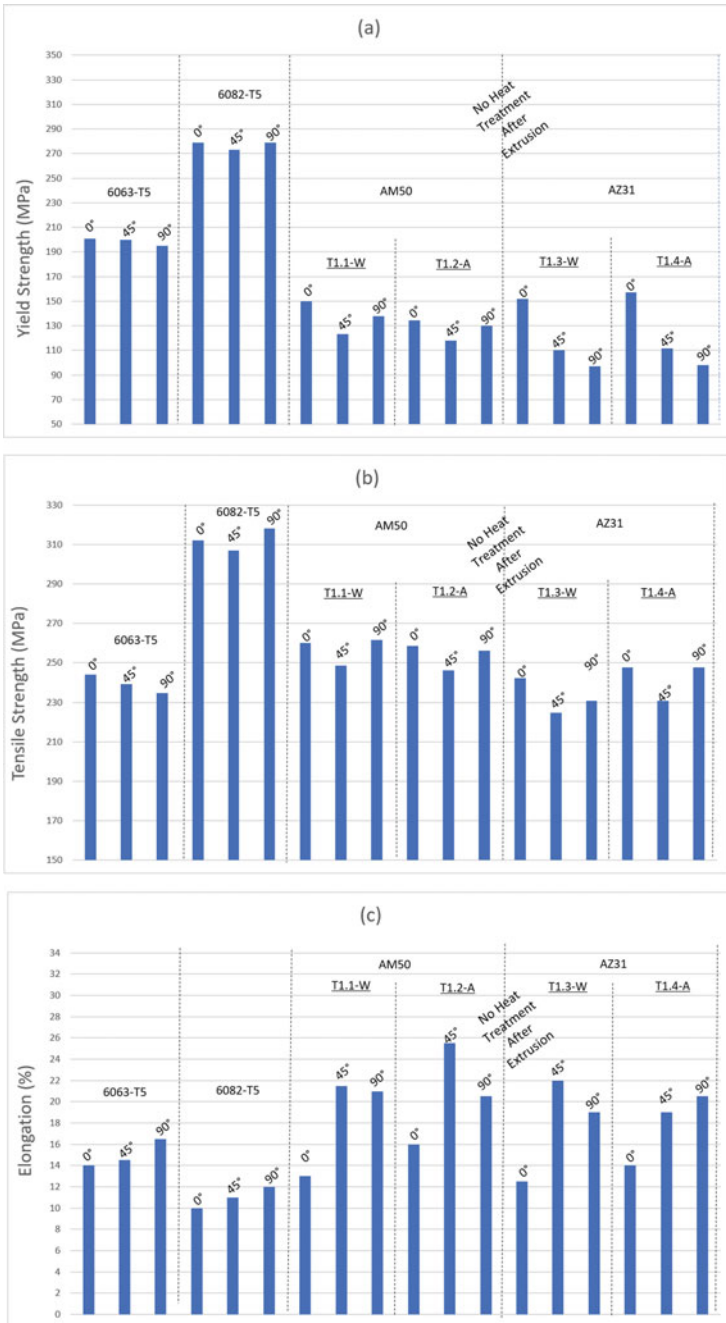
Fig. 6 Orientation effect of the specimens on mechanical properties on **a** Yield strength **b** Tensile strength **c** Elongation **d** Fracture energy. (Color figure online)
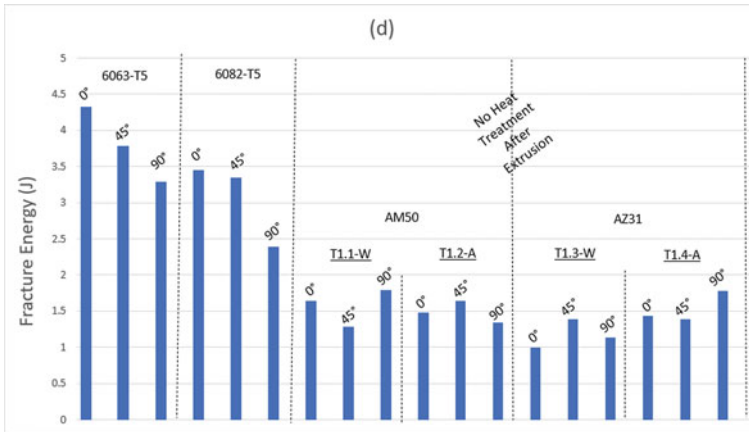
Fig. 6 (continued)

References

1. Dargusch MS, Pettersen K, Nogita K, Nave MD, Dunlop GL (2006) Mater Trans 47:977–982
2. Jurkovic Z, Jurkovic M, Buljan S (2006) Optimization of extrusion force prediction model using different techniques. J Achiev Mater Manuf Eng 17(1–2):353–357
3. Sillekens W, Schade van Westrum J, den Bakker AJ et al. Hydrostatic extrusion of magnesium: process mechanics and performance. Mater Sci Forum. 426:629–636 (2003)
4. Sillekens W, Van Hout M, Pravdic F (2005) Extrusion technology for magnesium: avenues for improving performance. In: 2nd International light metals technology conference; St. Wolfgang, Austria; LKR-Verl, pp 137–142
5. Kleiner S, Uggowitzer PJ (2004) Mater Sci Eng A A379:258–263
6. Ball E, Prangnell P (1994) Scr Metall Mater 31:111–116
7. Yi SB, Davies CHJ, Brokmeier HG, Bolmaro RE, Kainer KU, Homeyer J (2006) Acta Mater 54:549–562
8. Wang H, Wu PD, Gharghouri MA (2010) Mater Sci Eng A 527:3588–3594
9. Zeng Z, Stanford N, Davies CHJ, Nie J-F, Birbilis N (2019) Magnesium extrusion alloys: a review of developments and prospects. Int Mater Rev 64(1):27–62
10. Polmear IJ (1999). In: Avedesian MM, Baker H (eds) Magnesium and magnesium alloys. ASM International, pp 3–5
11. Pekguleryuz MO, Kainer KU, Arslan Kaya A (2013) Fundementals of magnesium alloy metallurgy, pp 275

Part V
Corrosion and Protection

Corrosion Protection of AZ80 and ZK60 Forged Magnesium Alloys with Micro-arc Oxidation and Composite Coating

Yuna Xue, Xin Pang, Sheji Luo, Xiaoyong Zhang, and Hamid Jahed

Abstract Wrought Mg alloys have attracted increasing attention for automotive applications due to their homogeneous microstructure and enhanced mechanical properties compared to as-cast alloys. However, in real service conditions, Mg structural components are susceptible to early failures due to the synergistic effects of corrosion and mechanical loading, which severely hinder their high penetration in the automotive industry. Therefore, the corrosion protection of Mg structural components is of crucial importance. In this work, AZ80 and ZK60 Mg alloys were forged under different temperatures, and then treated with micro-arc oxidation (MAO) and micro-arc composite coating (MCC) which is the MAO plus E-powder coating. The effects of forging processing parameters on the microstructure and corrosion properties of the alloys were analyzed, and the corrosion performances of the MAO-, MCC-coated Mg alloys were characterized through salt spray corrosion test. Experimental results demonstrated that the MCC coating provided robust corrosion protection for the wrought Mg alloys.

Keywords Wrought magnesium alloys · Micro-arc oxidation coating · E-powder coat · Corrosion protection · Forge

Y. Xue (✉) · S. Luo · X. Zhang
School of Materials Science and Engineering, Xi'an Shiyou University, No.18 Dianzi Second Road East, Xi'an, Shaanxi 710065, China
e-mail: xynlina@163.com

X. Pang
CanmetMATERIALS, Natural Resources Canada, 183 Longwood Road South, Hamilton, ON L8P 05, Canada

H. Jahed
Department of Mechanical & Mechatronics Engineering, University of Waterloo, 200 University Avenue West, Waterloo, ON N2L 3G1, Canada

Introduction

Magnesium and magnesium alloys, owning to their low density and favorable mechanical properties have attracted considerable attention for lightweight applications [1, 2]. At present, the magnesium components have not only focused on internal parts in the automotive industry but also considered for external components, such as the lower control arm of the front suspension [3–6]. However, low corrosion resistance of magnesium and its alloys has significantly limited their applications in the automobile industry, especially when they are exposed to aqueous solutions containing aggressive species such as chloride [7]. The focus of this research project is to explore advanced materials processing technologies improving the corrosion resistance for manufacturing next-generation suspension components in passenger cars.

A lot of research attention has been attracted to investigations on corrosion mechanisms of Mg alloys and approaches to improve corrosion resistance of Mg alloys. Among the various corrosion mitigation strategies, surface coating is considered one of the most effective and economic ways to prevent corrosion of Mg alloys [8]. Micro-arc oxidation (MAO) technique is considered very effective as it enables the formation of thick ceramic surface coatings. The MAO coating has been reported to enhance the corrosion resistance of Mg alloys significantly [9, 10]. A topcoat, as a part of a typical coating system, is almost always necessary to achieve a high-quality surface finish of Mg parts. E-powder coating was brought into this research which is formed the micro-arc composite coating (MCC) with MAO coating to investigate their effectiveness on the protection of the Mg alloys [11].

In this work, AZ80 and ZK60 alloys are selected as extrusion materials because of their high aluminum and zinc contents, good forgeability, and outstanding strength. Through investigating and comparing the microstructures and corrosion resistance of extruded, extruded-forged AZ80 and ZK60 alloys before and after MAO and MCC surface treatment, the corrosion mechanism of the forged magnesium alloys with MAO and MCC coatings will be systematically discussed.

Materials and Experiments

Materials

Commercially available AZ80 and ZK60 magnesium materials in the forms of extrusion (8.2 Al, 0.42 Zn, 0.31 Mn, wt.% for AZ80E; 5.5 Zn, 0.71 Zr, wt.% for ZK60E; other elements content as per ASTM B91-17 standard [12]) were studied in this investigation. The forging was conducted at CanmetMATERIALS (Hamilton, Canada) using the billets which were cut down to a length of 680 mm. The direction in which the billet was forged was perpendicular to the extrusion orientation of AZ80E and ZK60E materials. Then the forging process was accomplished in a single step at a

Fig. 1 Control arm and the location of the cut coupons. (Color figure online)

displacement rate of 20 mm/s. A forging was carried out at 250 °C for AZ80 and 300 °C for ZK60, respectively. The finished control arm and the coupons ($65 \times 10 \times 3$ mm^3) extraction location from the control arm are represented in Fig. 1.

MAO and MCC Treatments

The MAO process was subjected using a single-pulse direct current power supply developed by Xi'an University of Technology (China) at a constant current mode with pulsed current at a frequency of 500 Hz. And, the electrolyte used for the MAO process contained 0.065 mol/L of Na_2SiO_3, 15 mol/L of KF, and 0.18 mol/L KOH. The pH of the silicate electrolyte solution was adjusted to 13 using KOH solution. During the MAO process, the Mg alloy specimens were used as the anode, and a stainless steel plate was served as the cathode. The processing parameters optimized by our previous work [31] were a constant current density of 34 mA/cm^2, a pulse width of 80 µs for 10 min. After MAO processing, the specimens were first cleaned ultrasonically in trichloroethylene, rinsed with deionized water, and then air-dried and stored in the desiccator for further analysis.

E-powder coating was provided by the company JP Powder Coating Inc in Kitchener, Ontario, Canada. E-powder coating is a "dry" process in which a spray gun is usually used to apply the dry powder consisting of chemicals such as epoxy resin and some curing agents onto the Mg surface. Curing in an oven is also necessary to finalize the coating.

Specimen Examination and Test Methods

For metallographic characterization of the base alloys, optical microstructure of the specimens were studied using the etching reagents, and the etching procedure was immersing specimen face up with gentle agitation until face turns brown. The surface

and cross-sectional morphologies of the MAO- and MCC-coated different substrates were investigated by XL30 SEM. Phase composition of uncoated and MAO-coated specimens was identified by XRD analysis.

To characterize the corrosion performances of Mg alloys in the different processing condition, the uncoated and coated specimens were put in a Salt Fog Chamber (Singleton Corp. SCCH) and subjected to a fully static environment of a salt fog according to ASTM B 117 and SAE J2334 standards [13, 14]. The corrosion rate was analyzed by gravimetric measurements.

Results and Discussion

Microstructure and Surface Characterization

Figure 2 illustrates the optical micrographs of the microstructure of (a, b) AZ80 extrusion and AZ80 forged at 250 °C alloys. It can be seen that AZ80 extrusion alloy has an α-Mg matrix embedded with secondary β-phase (β-$Mg_{17}Al_{12}$). It shows a reasonably bimodal grain structure, with basal poles oriented perpendicularly to
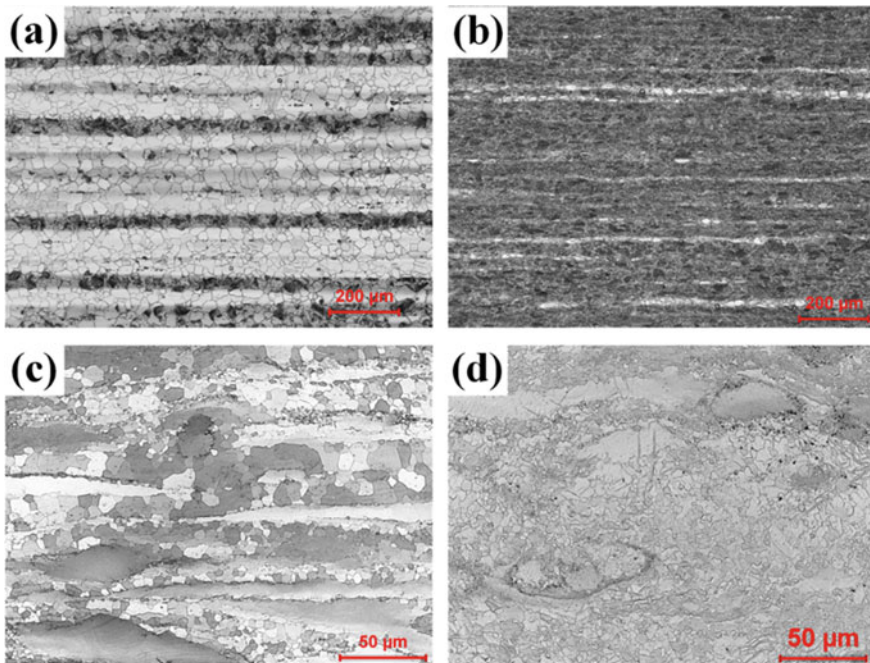
Fig. 2 Typical LOM micrographs of **a** AZ80 extrusion, **b** AZ80 forged, **c** ZK60 extrusion and **d** ZK60 forged. (Color figure online)

the extrusion axis. The α-Mg matrix and β-phase in AZ80 extrusion alloy form a multilayer structure paralleled to the extrusion direction (Fig. 2a). And the majority of β-phase precipitates show a discontinuous lamellar aggregate similar to other researchers reported by Zeng et al. [15]. The microstructure of AZ80 forged at 250 °C had a significantly finer grain structure relative to that of AZ80 extrusion alloy (Fig. 2b). This finer grain structure is attributed to the process of dynamic recrystallization (DRX) that is motivated by the forging processing temperature of 250 °C [16].

The microstructure of the ZK60 extrusion alloy is shown in Fig. 2c. It can be observed that the microstructure consists of a mixture of small equiaxed grains and large bright elongated grains. Visible streamlines of the second phase particles (β-$MgZn_2$) parallel to the extrusion direction concentrate around the small grains. In Fig. 2d, it is clearly shown that incomplete DRX was obtained at the forging temperature of 300 °C for ZK60 extrusion alloy. The average DRX grain size is small which is much finer than the initial ZK60 grain size (Fig. 2c), but the elongated strip grains that are not completely recrystallized are still present. No twins are found in the initial and forged microstructure of the ZK60 Mg alloys. ZK60 is prone to twinning in forging at a low temperature (250 °C). When twins appear, twins can accelerate the corrosion [17].
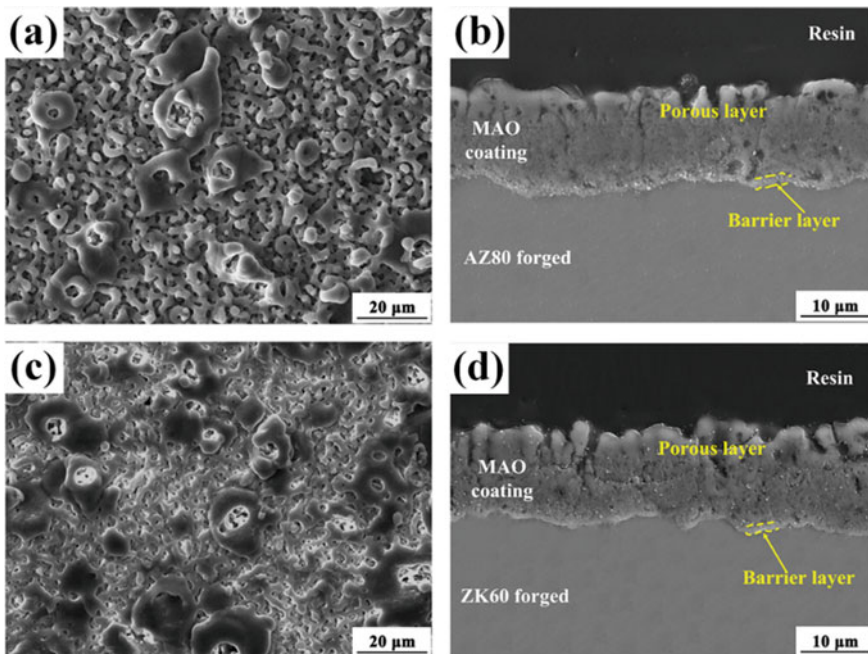
Fig. 3 The SEM micrographs of the surface and cross section of MAO coatings on AZ80 (**a**, **b**) and ZK60 (**c**, **d**) forged alloys. (Color figure online)

   Corrosion protective MAO coatings were deposited on AZ80 and ZK60 forged alloy substrates. The surface and cross-sectional morphologies are presented in Fig. 3. Micro-pores with different sizes and some large oxide particles are apparent on their surface (Fig. 3 a, c). There is no obvious difference in the surface morphology of MAO-coated forged alloy substrates, relatively uniform micro-pores and the randomly molten oxide particles were seen on the coating surface and integrated each other, which can be attributed to the throwing out of molten compound and gas bubbles from the micro-arc discharge channels during the MAO processing [18]. To evaluate the coating thickness and compactness of the MAO coating, the cross-sectional micrographs are shown in Fig. 3b, d. The coatings were observed to have a uniform and compact ceramic coating with strong adhesion to the matrix interface, which may be the result of the initial dissolution of the substrate in the process of MAO surface treatment. We can also see that these MAO coatings are composed of a barrier layer which is relatively dense and compact at the coating/substrate interface and a porous outer layer as displayed in Fig. 3b, d, which agrees very well with what has been reported in the literature [19] for the microstructure of MAO coating on Mg alloy. The average thickness of the MAO-coated AZ80 and ZK60 forged alloys are 15.4 and 15.5 μm, respectively, which are very similar.

   Figure 4 gives the SEM images of the cross-sectional microstructure of the MAO-coated AZ80 and ZK60 forged alloys with a topcoat of powder coating. It can be clearly seen that the coating system (MCC) consisting of two dense and uniform layers were formed on the forged Mg alloys. And the average thickness of the E-powder coating is 53.8 μm.

   The XRD analysis of forged Mg substrates and MAO coatings follows that the uncoated AZ80 forged alloy exhibit primarily α-phase (α-Mg) and secondary β-phase (β-$Mg_{17}Al_{12}$), ZK60 for α-phase (α-Mg) and secondary β-phase (β-$MgZn_2$). MAO-coated specimens showed characteristic substrate and the ceramic compounds corresponding to Mg, MgO, Mg_2SiO_4, and MgF_2. Previous works have been investigated the mechanism of formation of different phases during the MAO process [19, 20].
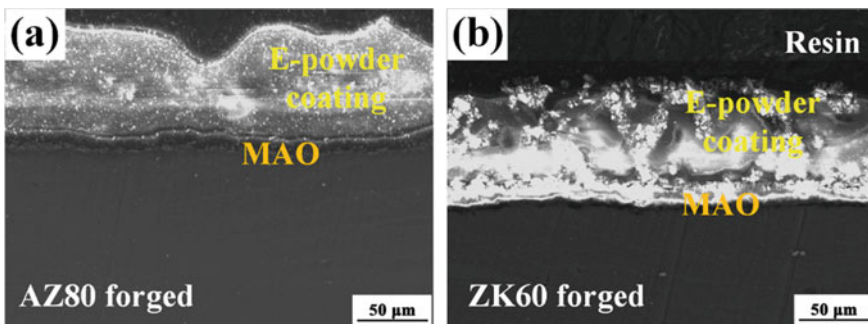
Fig. 4 SEM images of cross-sectional microstructure of the AZ80 forged alloy (**a**) and ZK60 forged alloy (**b**) with MCC coatings. (Color figure online)

Corrosion Characterization

A comparison of the mass change (as shown in Fig. 5) between uncoated AZ80 substrates and MAO coating on different AZ80 and ZK60 Mg alloys exposed to 5 wt.% NaCl neutral salt fog environment at 35 °C after 35 corrosion cycles (840 h). The AZ80 extrusion alloy shows a trend of severe deterioration of the mass loss rate than the other alloys. After forging at 250 °C, the enhancement of corrosion resistance is significantly evident. For MAO coating on AZ80 substrates, the corrosion resistance mainly depends on the formation of the ceramic MAO layer in the early stages of corrosion. When the MAO layer begins to break down, it is easier for the corrosive aqueous medium to penetrate the coating, through the breakdown areas in the coating, eventually reach the substrate surface, thus accelerating the occurrence of corrosion and worsening the corrosion resistance. For untreated and MAO-treated ZK60 alloys, as shown in Fig. 5, they exhibit lower mass loss values than AZ80 alloys. Compared to bare substrates, significantly less mass loss was seen for the specimens with MAO coatings, which verified the robust protectiveness of the MAO coating on ZK60 alloys against corrosion.

At the desired time duration, the first break down sites on the surface of the MAO-coated specimens after 6 days for AZ80 extrusion and forged alloys, 14 days for ZK60 extrusion, and forged alloys. In the salt spray corrosion test, due to the covering effect and the chemical compounds of MAO coating, the corrosion of these substrates was suppressed. The main difference between MAO-coated AZ80 and ZK60 alloys is that the chemical composition contains Al element in the outer porous layer for the MAO coating on AZ80 alloys and Zn element in the inner dense layer for the MAO coating on ZK60 alloys, respectively. MAO-coated ZK60 alloys show better corrosion resistance than MAO-coated AZ80 alloys, which is mainly due to the Zn element being more stable than the Al element in MAO coating. Previous work confirms these results by the MAO-coated cast Mg alloys [20].

Fig. 5 Comparative studies of the mass loss of the bare and MAO-coated AZ80 and ZK60 in 5 wt.% NaCl in 35°C environment for 35 days. (Color figure online)
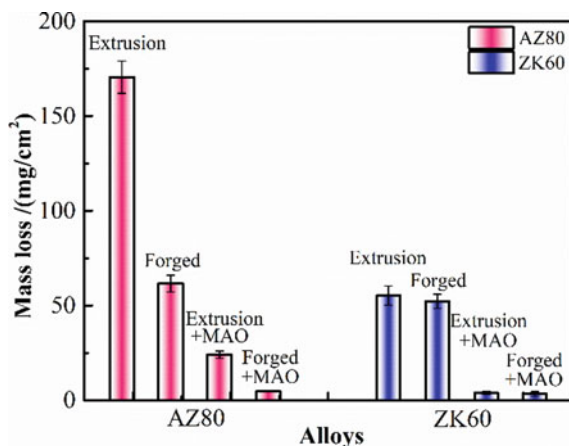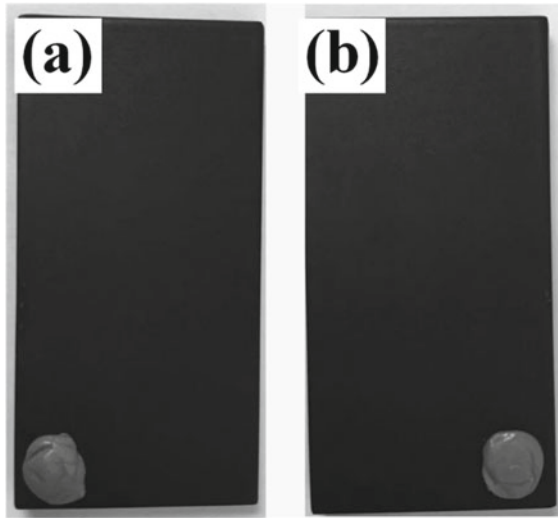
Fig. 6 Optical images of the MCC-coated specimens after salt spray test for 77 days

The MCC coating on AZ80 and ZK60 forged alloys were the salt fog environment as per SAE J2334 standard after 77 corrosion cycles (1848 h) which is closer to the service environment of the automobile components. At each time point, two repetitive specimens of each type were taken out of the salt chamber for observation. As can be seen from Fig. 6, for the MAO-coated ZK60 and AZ80 specimens with E-powder coating, almost no corrosion was seen even after 77 days of salt spray testing, especially on the coated ZK60 coupons.

Overall, E-powder as a topcoat is very effective as a top coating in the case of the MAO pretreated Mg alloys for corrosion protection. The best corrosion performance without a scribe was provided by the MAO powder coating system on the ZK60 alloy. Corrosion fatigue tests were conducted by our previous research for various coating systems with E-coat as a topcoat [21, 22]. It was found that the coating systems involving an MAO coating showed poor corrosion fatigue resistance because of the ceramic brittle structure. But when the MAO tape with E-coat, it can seal the micro-pores and micro-cracks in the MAO coating and created strong adhesion at the E-paint/MAO coating interface. Therefore, the E-powder coating also possesses similar effects as the E-paint coat. Furthermore, compared with the E-paint, the E-powder can obtain a thicker, denser topcoat, and has a great protection effect on the MAO coating.

Conclusion

The corrosion and corrosion properties of the AZ80 and ZK60 extrusion and forged alloys with MAO and MCC coatings were evaluated using advanced microstructural and surface analysis techniques and long-term salt spray corrosion testing method. The main findings are summed up as follows:

(1) The corrosion performance of AZ80 and ZK60 alloys depends considerably on their microstructure, including the grain size and β-phase. It indicated that the fine grain size and better β-phase (β-$Mg_{17}Al_{12}$ or β-$MgZn_2$) can obtain at different forging temperatures. The forged alloys greatly improved the corrosion resistance.

(2) The MAO coatings provided robust protection of AZ80 and ZK60 series alloys as compared to the corresponding bare Mg substrates. When the MAO coating was broken down, then the corrosion performances mainly depended on the corrosion resistance of their substrates. The breakdown time of MAO-coated ZK60 alloys is longer than that of MAO-coated AZ80 alloys, which shows excellent corrosion resistance.

(3) The MCC coating shows a better corrosion performance than MAO coating; MAO-coated ZK60 with powder coating showed the best corrosion performance among all the investigated coat systems. The ability of coated Mg alloys to resist general corrosion largely depends on the corrosion susceptibility of the substrate, surface coating strategies, and the adhesive bonding between them.

References

1. Joost WJ, Krajewski PE (2017) Towards magnesium alloys for high-volume automotive applications. Scr. Mater. 128:107–112
2. Jian YG (2018) Sound Package Design for Lightweight Vehicles. SAE Tech Pap 2–3.
3. Gryguc A, Behravesh SB, Shaha SK et al (2018) Low-cycle fatigue characterization and texture induced ratcheting behaviour of forged AZ80 Mg alloys. Int J Fatigue 116:429–438
4. Gryguc A, Shaha SK, Behravesh SB et al (2017) Monotonic and cyclic behaviour of cast and cast-forged AZ80 Mg. Int J Fatigue 104:136–149
5. Toscano D, Shaha SK, Behravesh B et al (2017) Effect of forging on the low cycle fatigue behavior of cast AZ31B alloy. Mater Sci Eng a 706:342–356
6. Prahash P, Toscano D, Shaha SK et al (2020) Effect of temperature on the hot deformation behavior of AZ80 magnesium alloy. Mater Sci Eng a 794(9):139923
7. Liu LJ, Schlesinger M (2009) Corrosion of magnesium and its alloys. Corros Sci 51:1733–1737

8. Wang J, Pang X, Jahed H (2019) Surface protection of Mg alloys in automotive applications: a review. Mater Sci 6(4):567–600
9. Jiang BL, Ge YF (2013) Micro-arc oxidation (MAO) to improve the corrosion resistance of magnesium (Mg) alloys. Woodhead Publishing Limited, pp 163–196
10. Vladimirov BV, Krit BL, Lyudin VB et al (2014) Microarc oxidation of magnesium alloys: a review. Surf Eng Appl Electrochem 50:195–232
11. Duan HP, Du K, Yan CW et al (2006) Electrochemical corrosion behavior of composite coatings of sealed MAO film on magnesium alloy AZ91D. Electrochim. Acta 51:2898–2908
12. ASTM B91–17 (2017) Standard specification for Magnesium-Alloy forgings. ASTM 1–5
13. B117 A (2017) Standard practice for operating salt spray (fog) apparatus. ASTM 1–12
14. SAE J2334 (1998) Surface vehicel standard-Cosmetic corrosion lab test. SAE 1–10
15. Zeng RC, Xu YB, Ke W, Han EH (2009) Fatigue crack propagation behavior of an as-extruded magnesium alloy AZ80. Mater Sci Eng a 509:1–7
16. Gryguc A, Behravesh SB, Shaha SK et al (2019) Multiaxial cyclic behaviour of extruded and forged AZ80 Mg alloy. Int J Fatigue 127:324–337
17. Merson D, Vasiliev E, Markushev M, Vinogradov A (2017) On the corrosion of ZK60 magnesium alloy after severe plastic deformation. Lett Mater 7:421–427
18. Guo HF, An MZ (2005) Growth of ceramic coatings on AZ91D magnesium alloys by micro-arc oxidation in aluminate-fluoride solutions and evaluation of corrosion resistance. Appl Surf Sci 246:229–238
19. Duan H, Yan C, Wang F (2007) Effect of electrolyte additives on performance of plasma electrolytic oxidation films formed on magnesium alloy AZ91D. Electrochim Acta 52:3785–3793
20. Xue Y, Pang X, Jiang B et al (2020) Characterization of the corrosion performances of as-cast Mg-Al and Mg-Zn magnesium alloys with microarc oxidation coatings. Mater Corros 71:992–1006
21. Shaha SK, Dayani SB, Xue Y (2018) Improving corrosion and corrosion-fatigue resistance of AZ31B cast Mg alloy using combined cold spray and top coating. Coatings 8(12):443–465
22. Xue Y, Pang X, Jiang B, Jahed H (2019) Corrosion and corrosion fatigue performances of micro-arc oxidation coating on AZ31B cast magnesium alloy. Mater Corros 70(2):268–280

Effect of Cation Species in the Electrolyte on the Oxidized Film on the Anodizing of Mg–Li–Al Alloys

Yuka Ichigi, Taiki Morishige, and Toshihide Takenaka

Abstract Mg–14mass%Li–3mass%Al (LA143) alloy has higher corrosion resistance than previous Mg-Li alloys such as Mg–14mass%Li–1mass%Al (LA141). However, the corrosion properties of the alloy are not enough to apply for practical use without corrosion protection coatings. The anodization for Mg alloys is an effective technique to prevent metal surface from exposure to corrosion environment. Phosphoric acid-based solutions containing metal cation are useful electrolytes to form a thick oxide layer on the Mg surface. In this study, the effect of cation species on the oxidized film was investigated. The film formed by each electrolytic solution was mainly composed of $Mg_3(PO_4)_2$, $AlPO_4$, $MgAl_2O_4$, and the phosphate and oxide-containing each additive element were slightly present. Particularly, in the electrolyte containing Ca, the dissolution of LA143 was suppressed about twice as much as other electrolytes, and the most uniform and thick film was formed.

Keywords Magnesium alloy · Magnesium–lithium alloy · Anodizing · Corrosion · Oxidized film

Introduction

Mg alloys are expected to be widely used as lightweight materials. However, since it is difficult to cold-work hcp-structured Mg alloys, bcc-structured Mg–Li alloy was developed to improve workability. Mg alloys easily corrode in a practical environment and require surface treatment to prevent corrosion. Anodizing, which is one of the surface treatments, can obtain a better film thickness than the conversion coating and can be expected to have a high anticorrosion effect.

Y. Ichigi (✉)
Graduate School of Science and Engineering, Kansai University, 3-3-35 Yamate-cho, Suita 564-8680, Osaka, Japan
e-mail: k789549@kansai-u.ac.jp

T. Morishige · T. Takenaka
Department of Chemistry and Materials Engineering, Kansai University, 3-3-35 Yamate-cho, Suita 564-8680, Osaka, Japan

Furthermore, anodizing using a phosphoric acid-based solution has been established for industrial Mg alloys. These films have better corrosion resistance than films composed of only MgO and $Mg(OH)_2$[1]). It has been reported that Mg–9mass% Al–1mass% Zn (AZ91), which forms a film containing $Mg_3(PO_4)_2$, exhibits corrosion resistance of 1000 h and more at a film thickness of 10 μm[2]). Therefore, it is desirable that these methods can be applied to Mg–Li alloys. Furthermore, it has been reported that when AZ91 was anodized in a Ca-based solution in which Ca^{2+} was added to a phosphoric acid-based solution, the film showed good anticorrosion properties. However, the cause of the difference in the amount of substrate dissolved and the corrosion resistance due to the difference in the cation species in the solution has not been clarified[3]). For highly reactive Mg–Li alloys, studying appropriate treatment bath conditions has become a very important issue for further improving corrosion resistance.

In this study, we focused on the solution and investigated the effect of the cation species added to the solution on the film formation and anticorrosion action of Mg–Li alloy by adding the element forming phosphate.

Experimental Procedures

The specimen used was LA143 (Mg–14.1 mass% Li–3.25 mass% Al) alloy prepared by melting. The sample was cut to about 10 mm × 10 mm × 5 mm, and a copper wire (φ1.00) as conductive leads was fixed. The treated area was exposed by 10 mm × 10 mm, and the sample was embedded using a cold-embedded resin. The surface of the sample was subjected to wet mechanical polishing to remove oxides on the surface. In addition, a sample from which organic substances on the surface had been removed by degreasing with acetone was used for anodizing.

Ca, Fe, Mn, Zn, and Ni were selected as the cation species to be added to the solution. The solution was based on 0.1 mol/L H3PO4 (85.0% content). 0.05 mol/L $Ca(OH)_2$ (>96.0%), $FeSO_47H_2O$ (99.0~102.0% content), $MnSO_45H_2O$ (99.0% content), $ZnSO_47H_2O$ (99.5% content), and $NiSO_46H_2O$ (99.0~102.0% content) were mixed with the phosphoric acid solution, respectively. The anodizing was treated at a voltage of 80 V and a time of 6 min. The surface and cross section of anodized films were analyzed by XRD (RIGAKU RINT 2500 V) and SEM (JEOL JCM-6000) -EDX (MP-00040EDAP). The effect of cation species was evaluated by the amount of substrate dissolved and the film thickness. In addition, in order to evaluate the corrosion resistance of each film, each sample was immersed in a 5 mass% NaCl (>99.5%) aqueous solution for 4 h, and the amount of hydrogen generated was measured. The corrosion rate was calculated on the assumption that (1) it is in the standard state and (2) the amount of Al dissolution is negligibly small. The reaction formula and calculation formula are shown below.

$$Mg + 2H^+ \rightarrow Mg^{2+} + H_2 \tag{1}$$

$$2Li + 2H^+ \rightarrow 2Li^+ + H_2 \tag{2}$$
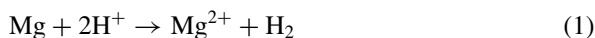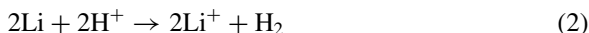
$$X = \frac{Y}{4 \cdot S \cdot 22.4 \times 10^3 (ml \cdot mol^{-1})} \times \{(M_{Mg} \cdot c_{Mg}) \, (2M_{Li} \cdot c_{Li})\} \tag{3}$$

X: corrosion rate (g·cm^{-2}·h^{-1}) Y: H2 generation amount (ml) S: sample surface area (cm^2).

M: molar mass (g·mol^{-1}) c: composition in atomic percent.

Results and Discussion

Anodized Film Characteristics

Figure 1 shows SEM images of the anodized LA143 surfaces with each solution. The film formed in the Fe-, Mn-, and Ni-based solutions had large cracks spread over the entire surface. On the other hand, in the Zn-based solution, although the surface was relatively uniform, small cracks were observed in the oxide film. In particular, the film formed in the Ca-based solution had no cracks and had the most uniform surface. According to SEM–EDX and XRD analyses, the film was mainly composed of AlPO$_4$, Mg$_3$(PO$_4$)$_2$, and MgAl$_2$O$_4$. In each solution, the anodized film also contained phosphates and oxides formed by each cation species. These compounds are known to be a film-constituting phase that exhibits an excellent anti-corrosive effect on AZ91[1) 2)]. However, according to XRD analysis, the β-phase (Li-solid solution) was detected in all the anodized films, the film formation was insufficient regardless of the added cation species.

Figure 2 shows SEM images of the anodized LA143 cross section with each solution. Similar to the surface, the film formed in the Fe-, Mn-, Ni-based solution had large cracks spread inside. Particularly, the adhesion of the film was poor because cracks were observed at the substrate/film interface. In the Zn-based solution, fine cracks were observed inside, but no large cracks were observed at the substrate/ film interface. The film formed in the Ca-based solution had no cracks inside, and the interface adherence of the film was enough.

Figure 3 shows the relationship between the amount of substrate dissolution and the film thickness. When the dissolution of the substrate was suppressed, there was a tendency to form a thick film. Therefore, it is considered that dissolution of the substrate is most suppressed in the presence of Ca^{2+}, and a thick and uniform film is formed.
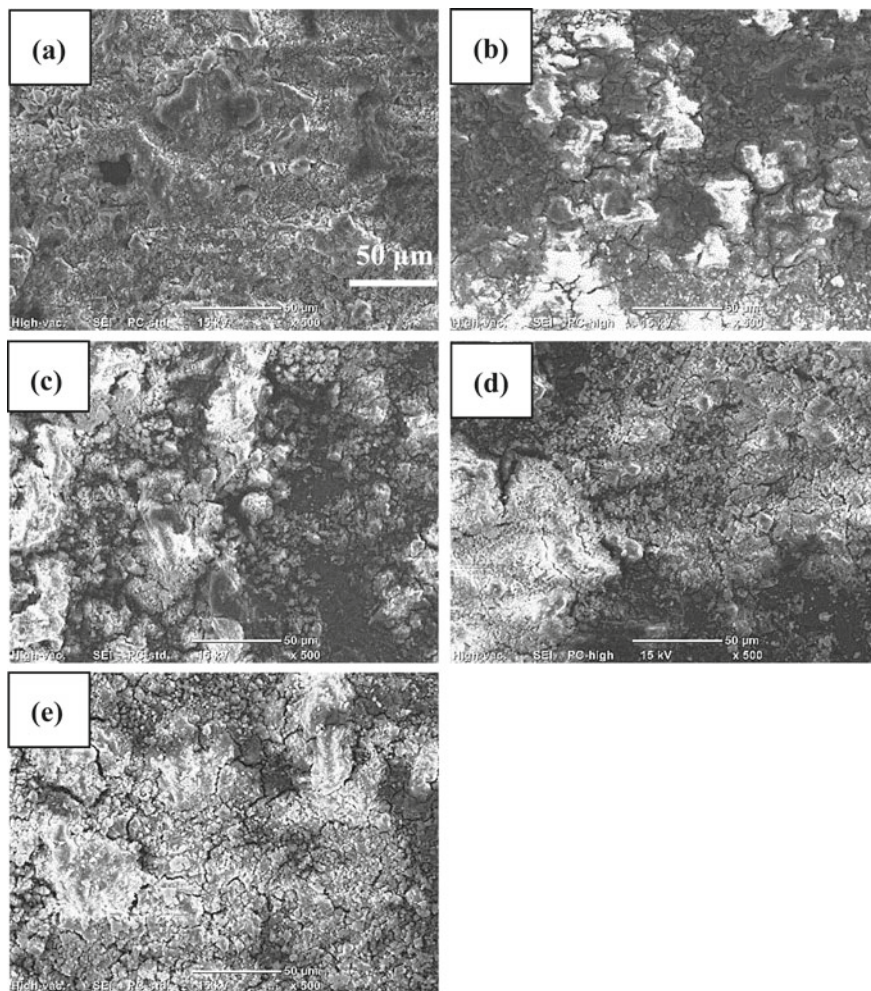
Fig. 1 SEM images of the anodized LA143 surfaces with each solution. **a** Ca-based **b** Fe-based **c** Mn-based **d** Zn-based **e** Ni-based

Effect of Cation Species

Since the amount of base metal dissolution differed depending on the added cation species, it is considered that each cation affects the ease of forming a film. The chemical reaction of the main constituent phases of the film and the dissolution reaction of the base metal are as follows:
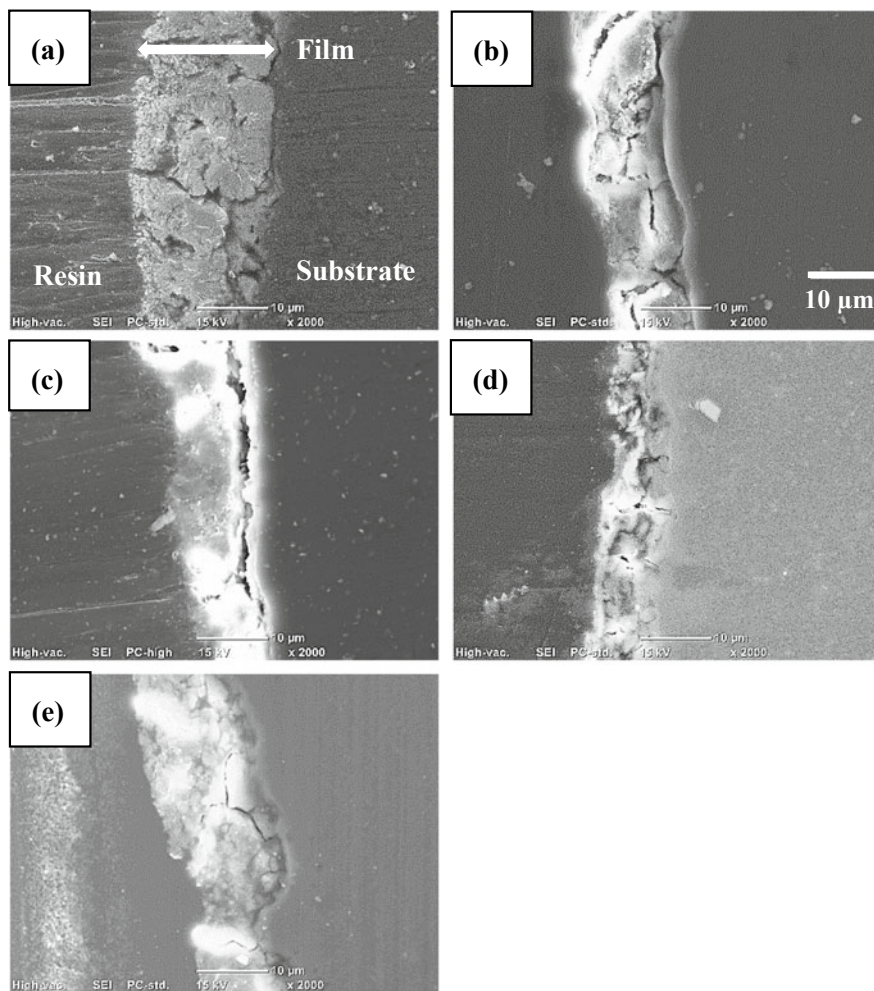
$$3Mg^{2+} + 2PO_4^- \rightarrow Mg_3(PO_4)_2 \; \Delta rG° = -349 \, kJ \, mol^{-1} \, ^{4)} \tag{4}$$

Fig. 2 SEM images of the anodized LA143 cross section with each solution. **a** Ca-based **b** Fe-based **c** Mn-based **d** Zn-based **e** Ni-based

$$MgO + Al_2O_3 \rightarrow MgAl_2O_4^{27)} \; \Delta rG° = -333.3 \, kJ \, mol^{-1} \qquad (5)$$

$$Al^{3+} + PO_4^{3-} \rightarrow AlPO_4 \; \Delta rG° = -224 \, kJ \, mol^{-14)} \qquad (6)$$

$$Mg + 2H^+ \rightarrow Mg^{2+} + H_2 \; \Delta rG° = -455 \, kJ \, mol^{-1} \qquad (7)$$
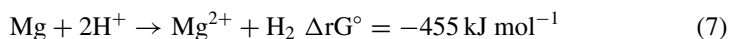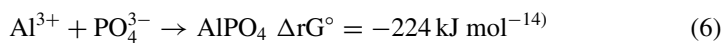
The film is considered to be formed by the reaction of Eq. (4) with the dissolved Mg^{2+} and the reaction of Eq. (5) between the oxides formed by the dissolved oxygen
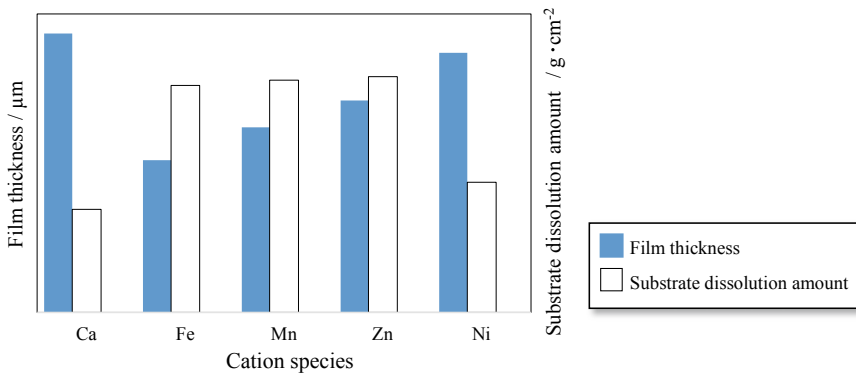
Fig. 3 The relationship between the amount of substrate dissolution and the film thickness. (Color figure online)

in the solution. In addition, since AlPO$_4$ was observed, the reaction of Eq. (6) can be considered, but because the dissolution of Al is negligibly small, it can be said that another formation mechanism is involved. Composite oxides such as MgAl$_2$O$_4$ in the film are easily dissolved and are thought to be involved in the formation of compounds containing Al. However, the substrate dissolution reaction of Eq. (1) is more likely to occur spontaneously than these film formation reactions. Therefore, dissolution of the substrate will proceed in all solutions. In particular, in Fe-, Mn-, Zn-, and Ni-based solutions, the dissolution amount is considered to have increased because the substrate dissolution reaction is the most spontaneous. On the other hand, the film-forming reaction generated in the Ca-based solution is as follows:

$$3Ca^{2+} + 2PO_4^- \rightarrow Ca_3(PO_4)_2 \; \Delta rG^\circ = -447kj \; mol^{-1}{}^4) \tag{8}$$

Equation (7) is about the same as Gibbs energy of the Mg dissolution reaction, and it is considered that Ca^{2+} in the solution formed Ca$_3$(PO$_4$)$_2$ in the initial stage of anodizing and slightly suppressed the dissolution of the substrate. Then, it is suggested that the film-forming reaction of [4–6] changed to a more spontaneous reaction so that the film grew and promoted the suppression of the dissolution of the substrate.

Figure 4 shows SEM mapping images of phosphorus of the anodized LA143 cross section with each solution. The film formed in Fe-, Mn-, and Ni-based solutions did not have phosphorus concentrated on the substrate. Therefore, it was found that even if Fe^{2+}, Mn^{2+}, and Ni^{2+} were added, stable phosphate was not formed on the substrate. In the Ca, Zn-based solution, phosphorus was concentrated inside the film, suggesting that phosphate was formed. However, with the addition of Zn^{2+}, the amount of the substrate dissolved was large, as shown in Fig. 3, suggesting that the formation of phosphate and the dissolution of the substrate continued to proceed at the same time. On the other hand, when Ca^{2+} is added, the formation of Ca$_3$(PO$_4$)$_2$ and the dissolution of the substrate have the same Gibbs energy, so it is considered
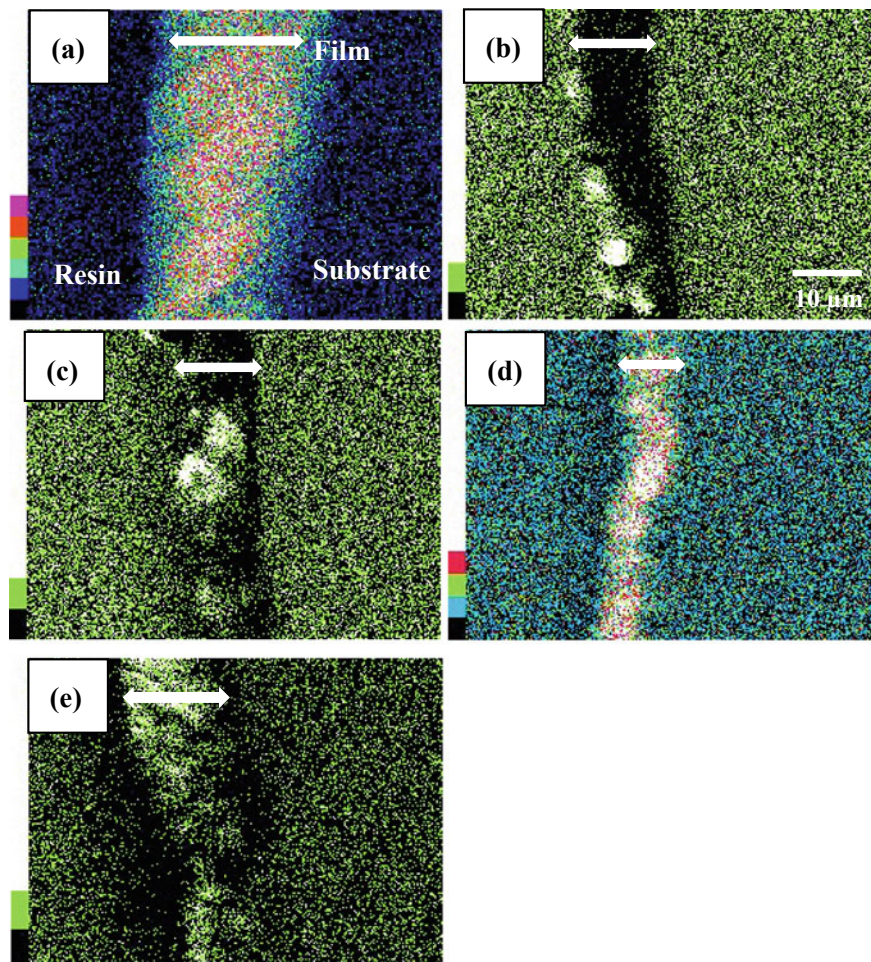
Fig. 4 SEM mapping images of phosphorus of the anodized LA143 cross section with each solution. **a** Ca-based **b** Fe-based **c** Mn-based **d** Zn-based **e** Ni-based. (Color figure online)

that stable calcium phosphate is likely to be formed on the substrate. As a result, it can be said that the phosphate formed on the substrate suppressed the excessive dissolution of the substrate and promoted stable film growth.

Corrosion Test

Figure 5 shows a surface SEM images of LA143 and the anodized sample after 4 h immersion. White areas indicate corrosion products in all SEM images. Filiform

corrosion progressed in LA143 that had not been anodized. More corrosion products were present in Fe-, Mn-, and Ni-based solutions than in LA143. Many cracks and gaps were present on the surface and inside of these films, and gap corrosion proceeded inside the films. Corrosion products similar to LA143 were produced in the Zn-based solution. In particular, there were almost no corrosion products in the Ca-based solution. Since these films had few cracks and the inside of the films was dense, they expressed an anticorrosive effect and suppressed corrosion. It was found that in such a film, the larger the film thickness, the higher the anticorrosion effect. As shown in Fig. 4, when Ca^{2+} is added, the formation of $Ca_3(PO_4)_2$ and the dissolution of the substrate have the same Gibbs energy, so it is considered that stable calcium phosphate is likely to be formed on the substrate. As a result, it can be said that the phosphate formed on the substrate suppressed the excessive dissolution of the substrate and promoted stable film growth.

Conclusion

In this study, we evaluated the anticorrosion performance of LA143 alloy, which was anodized with a phosphoric acid-based solution containing a cation species that forms a phosphate and clarified the effect of the cation species on film formation. When Ca^{2+} was added to the solution, $Ca_3(PO_4)_2$ was spontaneously formed at the initial stage of anodizing, and excessive dissolution of the substrate was suppressed. Even when a cation species other than Ca^{2+} was added to the solution, the dissolution of the substrate proceeded because the phosphate was not formed spontaneously. As a result, a film with many cracks was formed. From the results of the corrosion test, the anodized sample with the Ca-based solution showed good anticorrosion performance. This is because the film without cracks suppresses the occurrence of crevice corrosion.
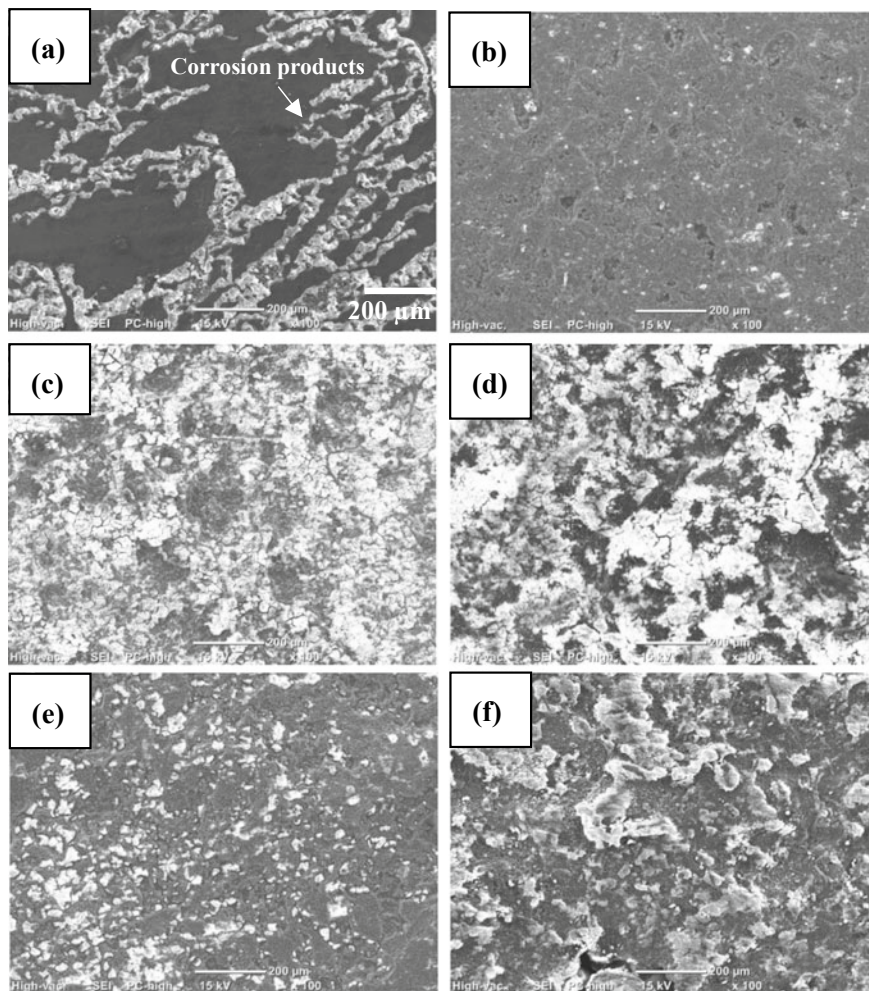
Fig. 5 Surface SEM images of LA143 and the anodized sample after 4 h immersion. **a** LA143 **b** Ca-based **c** Fe-based **d** Mn-based **e** Zn-based **f** Ni-based

References

1. Ono S (2011) Surface finishing 62(4):198–203
2. Hino M, Murakami K, Muraoka K, Saijo A, Kanadani T (2007) J Jpn Inst Light Met 57(12):583–588
3. Nakano K, Koga H (2009) Fukuoka industrial technology research report, 19
4. Kanazawa T, Monma H, Umegaki T (1971) Gypsum & Lime. 112:109–116

Effect of Microstructure on Corrosion Behavior of Cold-Rolled Mg–Li–Al Alloy

Taiki Morishige, Hayato Ikoma, and Toshihide Takenaka

Abstract Mg–Li system alloy has excellent formability at room temperature due to its crystal structure. However, exfoliation corrosion appears during the progress of corrosion. Therefore, it is difficult to apply for the actual metallic products without corrosion protection. Previously, the suppression of exfoliation could be attained by recrystallization of cold-rolled alloy. The microstructural characteristics were completely changed by recrystallization, so a detailed investigation is required for the explanation of exfoliation corrosion origination. In this study, the origination of exfoliation corrosion of Mg–14 mass%Li–1 mass%Al alloy with various microstructures such as as-rolled, only recovered and recrystallized state. As the results, the induced strain during severe deformation is a major factor of expression of exfoliation corrosion.

Keywords Magnesium · Exfoliation · Corrosion · Microstructure

Introduction

Mg–Li system alloy with over 11 mass% Li has body-centered cubic crystal structure, therefore this alloy is able to severe plastic forming at room temperature. It is expected that this system alloy such as LA141 (Mg–14 mass% Li–1 mass% Al) is the lightest structural metal material with excellent formability for practical use. However, bcc-structured Li solid solution alloy has poor corrosion resistance because Li element has less noble potential than Mg. It has also been reported that the exfoliation corrosion appeared in cold-rolled Mg–Li alloys [1–4]. The microstructure of as-rolled alloy has elongated grains and includes high dislocation density and residual stress by severe cold-rolling. These are the factor of expression of exfoliation corrosion. Previously, authors reported that the elongated grains in cold-rolled LA141

T. Morishige (✉) · T. Takenaka
Department of Chemistry and Materials Engineering, Kansai University, Osaka, Japan
e-mail: tmorishi@kansai-u.ac.jp

H. Ikoma
Graduate School of Science and Engineering, Kansai University, Osaka, Japan

Table 1 The chemical composition of as-received LA141 alloy (in wt.%)

Li	Al	Ca	Zn	Si	Fe	Cu	Ni	Mn	Mg
13.74	1.09	0.29	0.004	0.024	0.003	<0.001	0.001	0.038	Bal.

alloy brought the filiform corrosion along the grain boundary and this resulted in exfoliation origination. It is important to make a detailed investigation of the initial stage of exfoliation corrosion to improve the reliability of this alloy. In some literatures, the exfoliation is caused by a wedge effect by corrosion products in the grain boundary [4]. On the other hand, microcracks at the track of filiform corrosion were observed and the crack expands during corrosion progression [2]. It is considered that the cause of crack propagation may be evoked by residual stress by cold-rolling. In this study, the effect of annealing without recrystallization of cold-rolled LA141 alloy on exfoliation corrosion resistance was investigated.

Experimental Procedures

The chemical composition of the as-received Mg–14 wt.% Li–1 wt.% Al alloy (LA141) is shown in Table 1. The ingot was cut off with the size of 20 × 30 × 10 mm^3. This ingot was subjected to homogeneous heat treatment at 400 °C for 8 h in an argon atmosphere. Cold rolling was performed with 85% of rolling reduction at room temperature. The annealing temperature after rolling was at 100 °C only for recovery of the work hardening without static recrystallization. The hardness test was conducted using a micro-Vickers hardness test with 0.1−N load and 10 s of holding time. Corrosion tests were performed for 12 h with the as-rolled and the annealed conditions. The longitudinal section of the as-rolled and the annealed specimens were mirror-like polished and immersed in the solution of 5 wt.% NaCl in distilled water. Microstructures of as-rolled specimens were observed after mounted epoxy resin and etched by 10 mL HNO$_3$ + 90 mL methanol solution after polishing. The exfoliation corrosion was determined by macroscopic observation and thickness change of the specimens. The thickness change ratio was calculated as the thickness of the specimen after immersion divided by the thickness of the as-rolled specimen.

Results and Discussion

The microstructure of as-rolled LA141 alloy has elongated grains along the rolling direction. The homogenized LA141 (before CR) alloy has equiaxial large grains with >200 μm. There were no precipitates such as AlLi and other intermetallic phases in the grain boundary. The grain thickness was approximately 2 μm and all annealed specimens have almost the same microstructure as shown in Fig. 1. The relation-
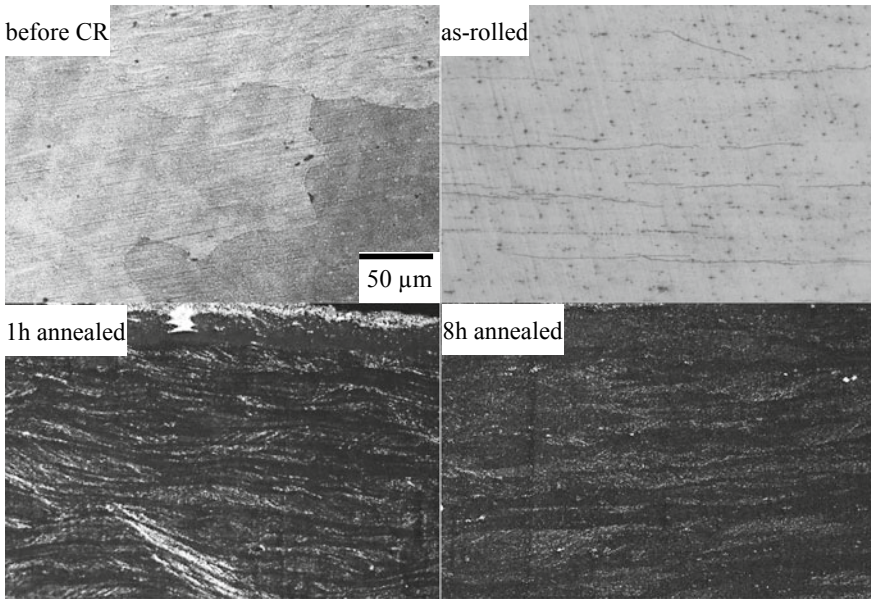
Fig. 1 Microstructures of LA141 alloy before corrosion test

ship between hardness and annealing time of specimens were shown in Fig. 2. The hardness decreased with increasing annealing time because the introduced strain by severe plastic deformation during cold-rolling was released by annealing. The corrosion immersion tests were performed on these as-rolled and annealed specimens until the occurrence of exfoliation corrosion. The expression time of exfoliation corrosion increases with the progression of recovery. In the initial stage of corrosion, corrosion pits were observed and the filiform corrosion, originated by pits, progresses as

Fig. 2 The relationship between hardness and annealing time. (Color figure online)
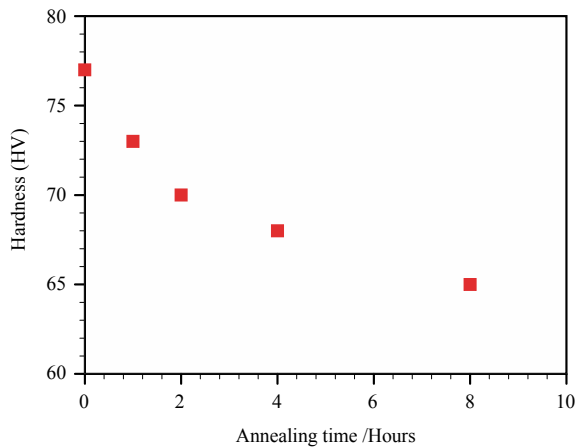
Fig. 3 The relationship between annealing time of cold-rolled LA141 alloy and the exfoliation origination time. (Color figure online)
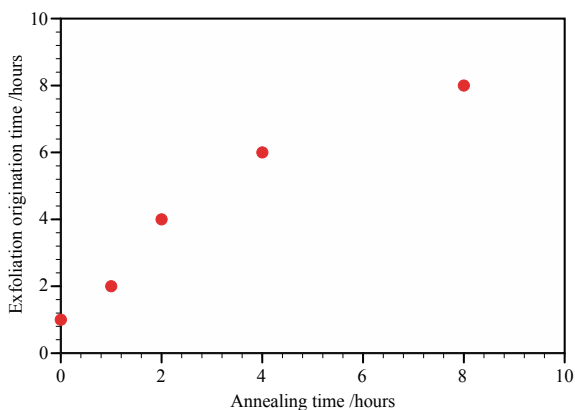
intergranular corrosion along the elongated grains. Even though the fully annealed condition, the exfoliation corrosion was observed at 8 h of immersion as indicated in Fig. 3. It is considered that there are some factors for the origination of exfoliation corrosion such as grain geometry, corrosion products in the crack, residual stress by plastic deformation. All the specimen has elongated grains in this work. Therefore, the microcracks and cleavage were formed by filiform corrosion progression. As a result of microstructural observation of immersed specimens, there are corrosion products of $Mg(OH)_2$ on the corrosion microcracks in all specimens. The corrosion products in the grain-eliminated gaps provide the tensile stresses through-thickness direction. This stress operates the tearing the grains neighboring the corrosion products. This is one of the factors to propagate the crack when the corrosion progression [4]. The residual stress introduced during the cold-rolling accelerates the crack propagation and tearing the grains at the grain boundary. This is the reason that the origination of exfoliation corrosion was delayed with increasing annealing time. The relationship between the annealing time and the thickness change ratio after 8 h immersion was shown in Fig. 4. The thickness change ratio decreased with the progression of recovery. This result means the exfoliation corrosion dominantly developed in the specimen includes residual stress. This stress by cold-rolling was released during annealing. Nonetheless, fully annealed specimen appeared exfoliation corrosion at 8 h of immersion test because the corrosion products formed at the grain-eliminated gaps and tearing the grains. However, the initiation of microcracks is affected by residual stresses during cold-rolling. The relaxation of residual stresses by annealing could decreases the sensitivity of microcrack origination and tearing at the grain boundary. As a result, even though the exfoliation corrosion appears the cold-rolled LA141 alloy with the microstructure of elongated grains with the fully annealed condition.

Fig. 4 The relationship between annealing time and the thickness change ratio at 8 h of immersion test
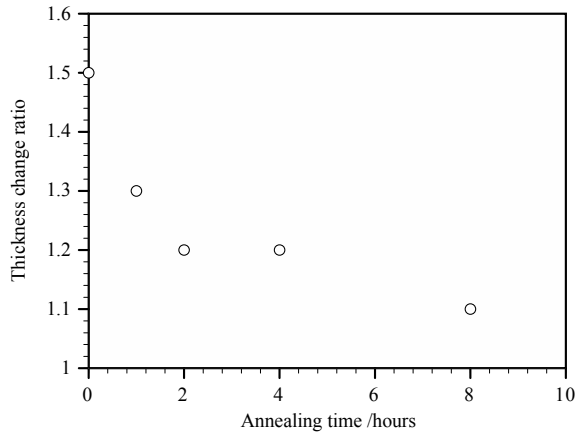
Conclusion

The effect of annealing on the origination of exfoliation corrosion in LA141 alloy was investigated. The exfoliation corrosion appeared not only in as-rolled but in fully annealed specimen with elongated grain microstructure in as-rolled. However, the sensitivity of exfoliation corrosion decreased by annealing to release the residual stresses during cold-rolling. The corrosion products in the microcracks facilitate the progression of exfoliation.

References

1. Song Y-W, Shan D-Y, Chen R-S, Han E-H (2009) Corros Sci 51:1087–1094
2. Morishige T, Doi H, Goto T, Nakamura E, Takenaka T (2013) Materials transaction 54(9):1863–1866
3. Sekiguchi Y, Morishige T, Goto T, Nakamura E, Takenaka T (2018) Mater Sci Forum 941:1743–1747
4. Ding ZY, Cui LA, Zeng RC, Zhao YB, Guan SK, Xu DK, Lin CG (2018) J Mater Sci Technol 34:1550–1557

Improvement in the Corrosion Resistance of AZ31 Magnesium Alloy Via a Composite Coating of the Zn–Ce LDH/Oxide

Vahdat Zahedi Asl, Jingmao Zhao, and Yahya Palizdar

Abstract The pH values of the solution, ratios of the cations, intercalated compounds, and hydrothermal conditions are the main parameters that influenced the layered double hydroxides (LDHs) efficiency. In this paper, the composite of the Oxide/LDH coatings, containing Zn^{2+} and Ce^{3+}/Ce^{4+} as metal cations, were prepared on the AZ31 substrate by a combined co-precipitation and hydrothermal processing method for the first time. To investigate the effect of Ce ions on the deposition of the suitable coating on AZ31, the LDHs with different ratios of the cations were synthesized. The comprehensive characterizations of the morphology, composition, structure, of the synthesized coatings, were investigated by SEM, XRD. PDP and EIS measurements were conducted to compare the corrosion behaviors of the coatings. The self-healing ability of the scratched samples was investigated. The finding of this study proves that a composite coating composed of the uniform scaffold-like clusters of the oxides incorporated with the LDH plates is successfully produced which can retard the corrosion of the AZ31 effectively.

Keywords LDH coating · Magnesium alloy · Corrosion protection · Self-healing · Cerium · Oxide

V. Zahedi Asl · J. Zhao (✉)
College of Materials Science and Engineering, Beijing University of Chemical Technology, Beijing 100029, China
e-mail: jingmaozhao@126.com

Beijing Key Laboratory of Electrochemical Process and Technology for Materials, Beijing 100029, China

Y. Palizdar
Nanotechnology and Advanced Materials Department, Materials and Energy Research Center, Karaj, Iran

Introduction

Recently, the layered double hydroxide (LDH) structures which are shown by the general formula of $M_{1-x}^{2+}M_x^{3+}(OH)_2^{x+}(A)_{x/2}^{n-}.mH_2O$, have attracted the scientist's attention as a promising smart structure to be utilized in the anti-corrosion coatings [1]. Generally speaking, these LDH structures are formed from the hydroxides of the divalent and trivalent cations which are designated as the M^{2+} and M^{3+}, respectively. The total valence of the hydroxide layers is positive, but it becomes inert via intercalating the anions (A^{n-}) such as carbonates and nitrates, which can be exchanged by other ions, between the hydroxide layers. Thus, the ion-exchange ability of the LDH sheets makes these structures more efficient in the anti-corrosion performances and self-healing properties of the coatings [2]. Various methods have been investigated to apply the LDH nanosheets into the coatings such as adding the powders of the LDHs in the polymer matrix, direct deposition of the LDHs on the surface by electrodeposition methods, and growth of the LDH structures on the surface via chemical conversion process (in situ and coprecipitation method) which is attracted much attention recently for the deposition of the LDH coatings on the light alloy materials [3]. Thus, one of the most valuable cost-effective environmentally smart coatings for magnesium alloys is the LDH coating. However, increasing the protection efficiencies of the LDH coating was taken into the consideration by the scientists, recently. In order to enhance the anti-corrosion performances as well as the self-healing properties of the LDH coatings, the main parameters such as pH values of the solution, ratios of divalent and trivalent cations, intercalated compounds, and hydrothermal conditions, etc., during the synthesizing have been investigated. In this regard, various studies such as increasing the hydrophobicity of the LDH coatings [4, 5], intercalation of the different anions [6, 7], and the growth behavior of the LDH coating in different pH values [8, 9] have been investigated. Also, Hoshino et al. have reported that in the high pH values of the hydrothermal process, the composite coating of the oxides (ZnO) and LDHs could be deposited on the surfaces [9]. Additionally, an effect of the different kinds of the trivalent cations on the microstructures and anti-corrosion performance of the LDHs where the pores of the film were sealed by Nanoplates oriented nearly perpendicular to the substrate, have been reported by Wu et al. [10]. The cerium is one of the effective cations that could intercalate into the LDH structures and enhance the anti-corrosion performances of the coatings [11].

During the last decade, scientists have tried to apply composite coatings on magnesium alloys in order to enhance various properties (anti-corrosion, self-healing, wear resistance, adhesion) of the coating altogether [12]. The combination of the LDHs coatings with the cerium compounds, which are known as environmentally friendly inorganic inhibitors, has attracted the attention of scientists recently [12, 13]. Incorporation of the cerium cations with Zn–Al LDH film has been investigated and the results confirmed the enhancement of the anti-corrosion performances [14]. Also, Smalenskaite et al. found that Ce^{3+} can dope into the LDH structure and revealed that the brucite-like layers of the $Mg_3Al_{1-x}Ce_x$ LDHs could be synthesized [15]. The intercalation of the cerium cations into the LDH structures as trivalent or tetravalent

cations and combining with the divalent cations (Zn and Mg) has also been previously reported [11, 15–18]. It is worth mentioning that the intercalation of the high amount of the cerium cations into the LDH structures is limited; thus, it is not easy to intercalate the cerium cations in high percentages due to the big ionic size of the cerium cations, especially in the trivalent form where the free aluminum cations exist in the solution [19]. It was, however, seen that by increasing the pH values of the solution consisting of the Zn and Ce cations, the Ce ions with different valance charges (higher amount of the tetravalent with small ionic size compared to the trivalent form) appeared, and its combination with hydroxides, oxides, and carbonates was observed [20].

In this study, the higher pH values (above 12.5) where the hydrothermal solution contains only the Zn and Ce cations were utilized to investigate the one-step in situ fabricability and feasibility of depositing the Oxide/LDH composite coating on AZ31 magnesium alloy. Also, the anti-corrosion performances and the microstructures of the coatings with different Zn/Ce ratios were investigated to compare the protection efficiencies of the prepared coatings.

Experimental Process

Synthesizes of the Coating

The mechanically polished AZ31 magnesium alloy plates with the size of the pieces of $25 \times 25 \times 2$ mm^3 were used as substrates. The Oxide/LDH composite coating was synthesized via a two-step hydrothermal process [11]. In this regard, two kinds of the solution with different Zn/Ce ratios (3 and 2) were prepared by dissolving Zn $(NO_3)_2.6H_2O$ (0.2 and 0.3 M) and Ce $(NO_3)_3.6H_2O$ (0.1 M) in the 75 ml DI water. The prepared solution was placed in three-neck flasks while stirring in an oil bath at 80 °C. Then 75 ml DI water containing 2 gr Na_2CO_3, 1 gr NaOH were dropped into the solutions. Finally, the pH of the precursor solution was adjusted to approximately 13 and then poured into the Teflon-lined autoclave in which the surface-treated AZ31 substrates have been vertically placed. After heating the Teflon-lined autoclave for 24 h. at 125 °C, the coated samples were taken out, washed with DI water, and dried with warm air. The samples were named ZC213 and ZC313, respectively.

Surface Characterization

The crystallographic investigation has been done by the (Rigaku D/Max2500X, Rigaku, Japan) equipment with a Cu target ($\lambda = 0.154$ nm). Also, the data was processed by X'Pert HighScore software (Version 1.0). The microstructural morphology and chemical composition of the coatings were investigated by the

field-emission scanning electronic microscopy (FE-SEM) equipped with an energy dispersive X-ray spectrometer (EDS). The entire sample was pre-sputtered with gold to obtain an excellent conductivity for the SEM observation.

Electrochemical Tests

Gamry (Interface 1000) equipment was used to investigate the corrosion resistance of the AZ31 magnesium alloys with and without coatings in 3.5wt.% NaCl solution and the conventional three-electrode system. After leaving the samples in the solution for 1 hr. the electrochemical impedance spectroscopy (EIS) was measured in the range between 100 kHz and 10 MHz and the results were fitted with ZSimpWin 3.5 software. The polarization curves were prepared within -500 mV to + 1500 mV with respect to the OCP and the potential scan rate was $2mVs^{-1}$.

Self-healing Properties

After scratching the surface of the ZC213 sample with a sharp knife, the sample was placed in 3.5 wt.% NaCl solution for 2, 7, and 21 days, respectively. OLYMPUS-BX61 optical microscope (OM) was utilized to observe the self-healing phenomenon in the scratched coating. Also, after 21 days process, the SEM equipped with the energy dispersive spectroscopy (EDS) was utilized to study the morphological features and the composition of the scratched area.

Results and Discussion

Characterization of the Coatings

The XRD patterns that identify the phases and the crystalline structures of the coatings are shown in Fig. 1. The peaks of the (003) and (006) planes that illustrate the existence of the LDHs flakes in the coating occur at around the 2θ position of 11° and 22°, respectively. However, the sharp intensities of the diffracted peaks of the LDHs for the ZC213 sample are approximately higher than the ZC313 sample which could indicate the higher percentage of the LDHs flakes in the composite coating. The peaks at around 2θ position of the 28°, 32°, and 34° are related to the cerium oxide, cerium hydride, and zinc oxide which indicates the oxide form of the elements due to the higher pH values of the synthesizes process. According to the diffraction pattern of the ZnO with the PDF Card No: 01-070-8072 and the peak intensities, the presence of a higher amount of zinc oxide in the ZC313 compared to ZC213 could
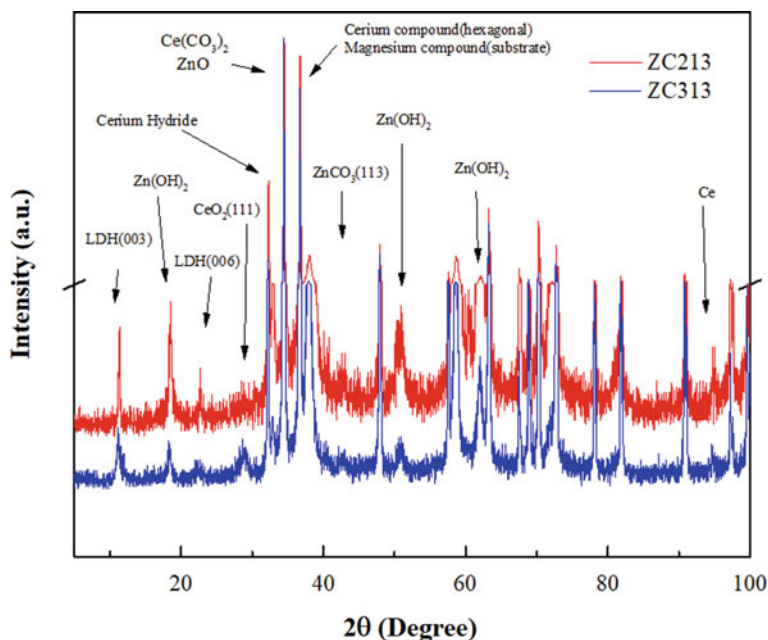
Fig. 1 XRD results of ZC213 and ZC313 samples. (Color figure online)

be confirmed. Also, the higher ratio of the Zn/Ce cation in the ZC313 could prove the hypothesis related to the synthesizing process. Additionally, the reflected peaks at around 50° and 62° are related to the zinc hydroxides which could confirm the formation of the LDHs structures in higher amounts due to the higher intensities of the peaks for ZC213. The cerium cations have two states of the valences (Ce^{3+} and Ce^{4+}), where the ionic size of the Ce^{3+} is bigger than the Ce^{4+} and thus, intercalation of the Ce^{4+} into LDH structures would be more convenient [18, 21]. As well, the intercalation of the tetravalent cerium into the LDH structure would be possible. However, increasing the pH value leads to oxidation of the Ce^{3+} to Ce^{4+} which could be deduced from the following equations:

$$4Ce^{3+} + 4OH^- + O_2 + 2H_2O \rightarrow 4Ce(OH)_2^{2+} \tag{1}$$

$$Ce(OH)_2^{2+} + 2H_2O \leftrightarrow Ce(OH)_4 + 2H^+ \tag{2}$$
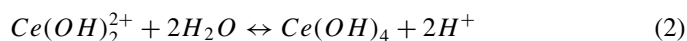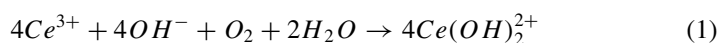
Consequently, intercalation of the cerium cations into the LDH structures would be in the combination of the Ce (III) and Ce (III) hydroxides in high pH values. Furthermore, because of the high pH values of the solution, the Al ions could be released from the substrate and incorporate into the LDHs formation and leads to the deposition of the ZnCeAl LDHs which has inhibition properties [22]. Also, according to the Pourbaix diagram, at high pH values of the precursor solution, the cations (zinc

and cerium) could be converted into the oxide form via the following equations [9, 21, 23]:

$$2Ce(OH)_2^{2+}(aq) + 2OH^-(aq) \rightarrow CeO_2.H_2O(s) + H_2O \tag{3}$$

$$2Ce(OH)_2^{2+}(aq) + 2OH^-(aq) \rightarrow CeO_2(s) + 2H_2O \tag{4}$$
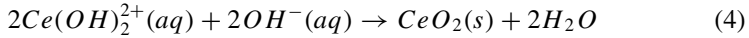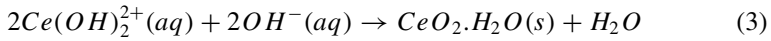
Consequently, a one-step in situ deposition of the oxide/LDHs composite coatings would be possible when the pH of the precursor solution consisting of Zn and Ce cations is approximately 13.

Microstructural morphologies and related EDS results of the different areas of the ZC213, ZC313 coating are shown in Fig. 2. Accordingly, two kinds of microstructure can be seen in the coatings. Also, by changing the ratios of the Zn/Ce cations, the microstructures can be changed significantly. As seen in Fig. 2a, the common flower-like morphology of the LDH sheet that is previously reported are in area 2. Also, in area 2 of Fig. 2d, the same morphologies are seen [6, 24]. However, the amounts of the perpendicular curved plate-like LDH microcrystals for ZC313 are less than the ZC213 sample which is in good agreement with the XRD results. The cluster-shaped structures in the ZC213 sample could be the results of the oxide form of the zinc and cerium elements in agreement with the EDS results (Fig. 2b, e). ZC213 sample containing a higher amount of the cerium compound (about 27wt.%) would have the potential to enhance the inhibition properties and anti-corrosion performance of the coating [25, 26]. The coating of the ZC213 sample containing a uniform scaffold-like structure can be suitable for increasing the protective properties as well as the wear resistance of the coating [27, 28]. However, the higher amount of the Zn compound due to the higher ratios of the Zn cations in the precursor solution (Zn: Ce: 3) means that the free Zn which could not incorporate with the cerium cations in the LDH structures prevents the formation of the uniform scaffold-like clusters. Also, the higher Zn caused the formation of cracks on the coating which would deteriorate corrosion resistance.

Corrosion Properties

The corrosion rate of the AZ31 magnesium alloy, ZC213 sample, and ZC313 sample were comparatively investigated via the potentiodynamic polarization (PDP) technique. Generally, lower corrosion currents and higher corrosion potentials reveal the lower corrosion dynamic rate and a lower corrosion thermodynamic tendency of the related coating. In this regard, the weak polarization zone (between $\pm$ 10 and $\pm$ 70 mV vs. E_{corr}) was chosen to investigate the PDP results with the EC-Lab software [29]. According to Fig. 3, the bare AZ31 magnesium alloy showed the highest corrosion current density and the lowest corrosion potential ($i_{corr} = 1.2 \times 10^{-5}$ A cm^{-2}, and $E_{corr} = $ -1.57 V versus SCE). Meanwhile, the anti-corrosion properties of the
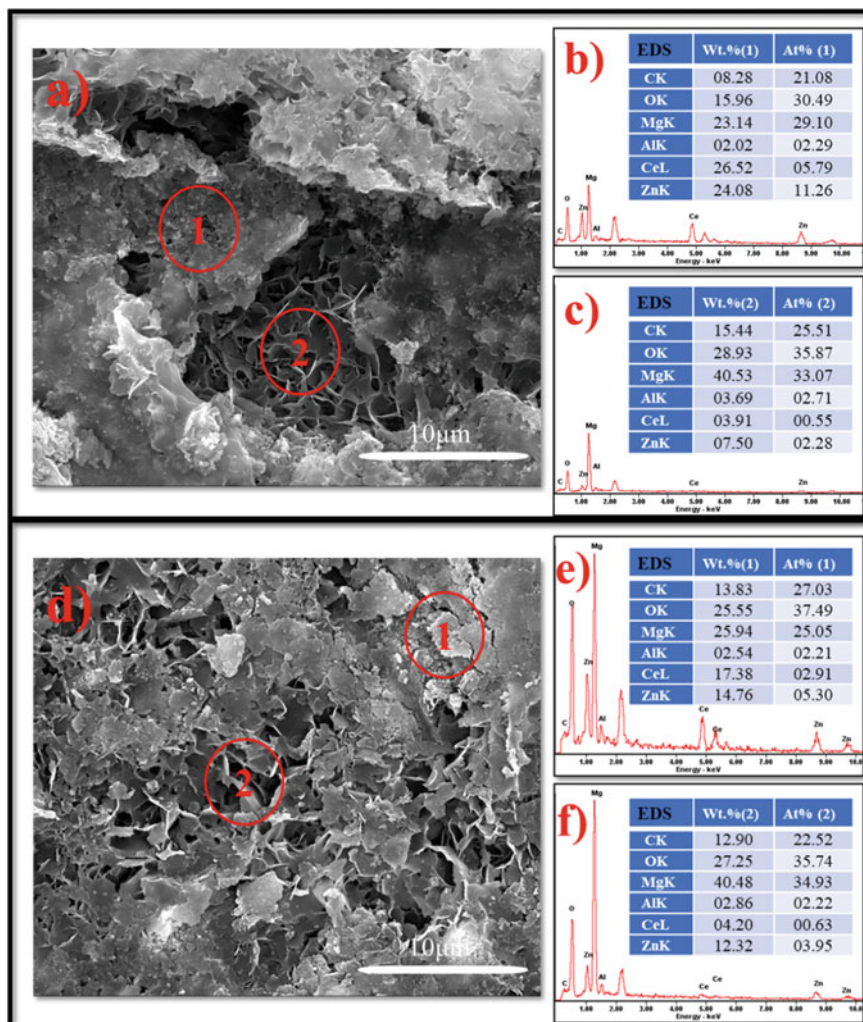
Fig. 2 SEM of the **a** ZC213 sampled) ZC313 sample and corresponding EDS results of **b** area 1 of ZC213 **c** area 2 of ZC213 **e** area 1 of ZC313 **f** area 2 of ZC313 sample. (Color figure online)

AZ31 were enhanced approximately by two orders of magnitude via applying the composite coating on it. The i_{corr} and E_{corr} values for ZC213 and ZC313 samples are 9.7×10^{-8} A cm^{-2}, 4.5×10^{-7} A cm^{-2}, and -1.26 V versus SCE, -1.31 V versus SCE, respectively. The highest anti-corrosion properties are related to the ZC213 sample due to the uniform scaffold-like structure which is in good agreement with the microstructures in Fig. 2. A reasonable explanation for the above results is that the composite coating consists of the oxide clusters and LDH plates that prevent the aggressive ions the reaching the substrate. Also, in the ZC213 coating, the uniform
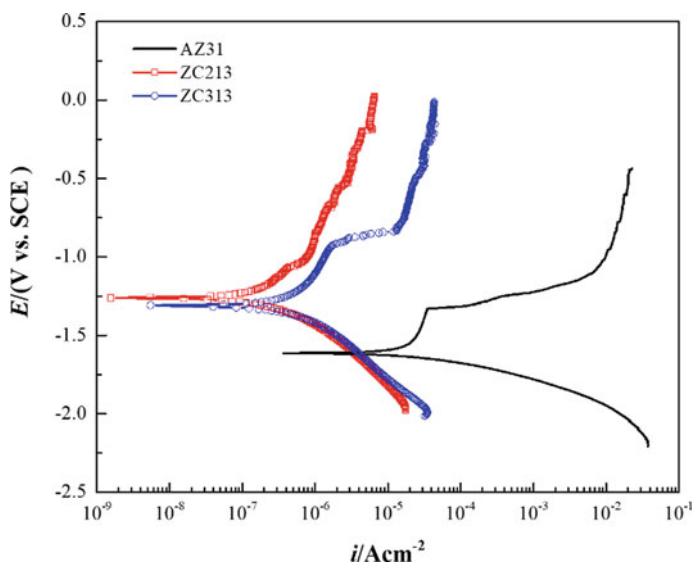
Fig. 3 Potentiodynamic polarization curves of bare AZ31 magnesium alloy with and without the coating of ZC213 and ZC313 coatings that were immersed in 3.5 wt % NaCl solution. (Color figure online)

oxide clusters could make the coating more stable and block the penetration sites of the aggressive solution through the coating. In the anodic branches around −0.8 V, some breaks have happened and the corrosion current increased sharply which could be due to the breaking of the protective layers, especially for the ZC313 sample. However, after the breaks occurred and the corrosion current in the ZC213 sample increased, the currents rapidly pulled back and decreased which is attributed to the healing effect of the LDHs and cerium containing oxide clusters properties. Thus, the deposition of the cerium hydroxides (low water solubility) on the surface exactly in the corroded areas could be the main reason for this event.

Figure 4 illustrates the Nyquist plots, corresponding equivalent circuit, and typical bode diagrams as well as the fitted curves of the ZC213 and ZC313 samples. Generally, a bigger loop of the Nyquist plots represents the higher resistance of the coating. Also, the impedance modulus in the lower frequencies reveals the corrosion resistance [30]. In this regard, the values of the impedance in the 10 mHz indicate that the ZC213 sample had better protective properties, which are consistent with the result of the Tafel polarization.

The equivalent circuit of the fitted curves is listed in Table 1. To fit the results of the EC, the ZSimpWin 3.5 software was conducted, and the results were accepted when the χ^2 parameter was lower than 5×10^{-3} [29]. The R_s value represents the resistance of the solution. Regarding the inherent inhomogeneity of the coating and the metal surface, the capacitors in the equivalent circuit have been represented by the constant phase elements (CPEs). The R_{out} and Q_{out} values are related to the outer
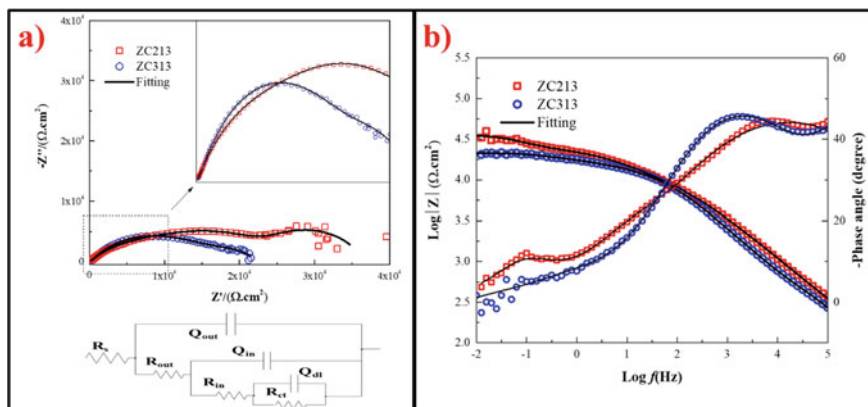
Fig. 4 **a** Nyquist plots and corresponding equivalent circuit and **b** Bode diagrams for different coatings on the AZ31 magnesium alloy that were immersed in 3.5 wt. % NaCl solution. (Color figure online)

porous part of the composite coatings. The R_{out} value of the ZC213 is higher than the ZC313 which indicates the higher stability of the outer part of the coating. The R_{in} and Q_{in} values reveal the resistance and capacitance of the inner dense layer of the composite coatings which the results of this part are approximately equal in both coatings. The R_{ct} and Q_{dl} value denote the charge-transfer resistance and the electric double layer capacity at the interface. The ZC313 sample has shown a lower amount of R_{ct} which could be due to the higher amount of the pores or capillary channels compared to the ZC213 coating.

Long-term Immersion

Generally, the LDH plates as the smart structures which have the ion-exchange ability could heal the defected areas of the coatings [31]. On the other hand, the LDH-based film is the storage and release inhibitor on demand as a result of ion exchange between anions and corrosion-relevant anions such as chloride and/or hydroxyl anions. Besides, environmentally friendly cerium compounds, which have healing abilities due to the deposition of the hydroxide form in the defected areas, could be one of the appropriate alternatives for the chromium compounds [11]. Thus, the combination of the cerium compounds and the LDH structures would be the conventional method to fabricate a smart anti-corrosion coating. In order to investigate the healing efficiencies of the composite coating the scratched coated sample has been placed in the 3.5wt.% NaCl solution for different times (Fig. 5). After 2 days of immersion, some black parts have been observed on the scratched areas of the ZC213 surface, which could be the effect of the corrosion products. Also, after 7 days of immersion, growth of the black areas nearly stopped which could indicate

Table 1 EIS results of the ZC213 and ZC313 coatings

Samples	$R_s/$ Ωcm^{-2}	$Q_{out}/10^{-06}$ S s^{α} cm^{-2}		$R_{out}/$ $k\Omega cm^{-2}$	$C_{out}/$ $(\mu F \cdot cm^{-2})$	$Q_{in}/10^{-06}$ S s^{α} cm^{-2}		$R_{in}/$ $k\Omega cm^{-2}$	$C_{in}/$ $(\mu F \cdot cm^{-2})$	$Q_{dl}/10^{-06}$ S s^{α} cm^{-2}		$C_{dl}/$ $(\mu F \cdot cm^{-2})$	$R_{ct}/$ $k\Omega cm^{-2}$
		Y_1	α_1			Y_2	α_2			Y_3	α_3		
ZC213	45.95	2.26	0.54	15.19	1.27	8.23	0.61	10.78	1.74	162	0.82	182.9	10.75
ZC313	29.76	0.6	0.63	0.74	0.006	0.97	0.62	14.4	0.07	68.42	0.48	33.78	7.62
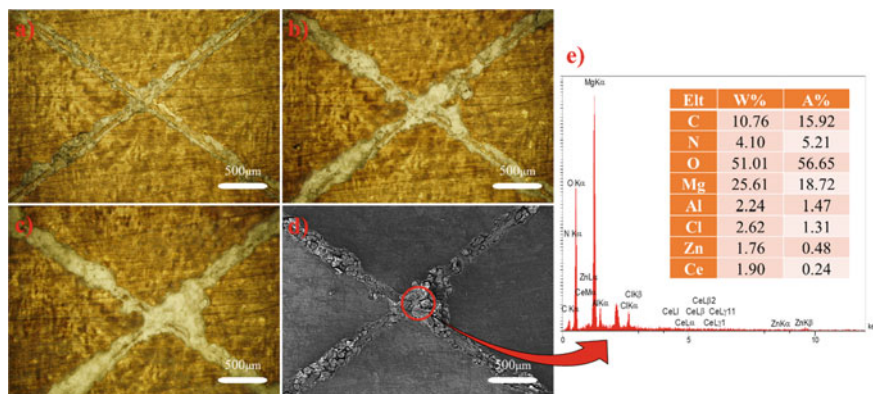
Fig. 5 The scratched part of the ZC213 sample that was immersed for **a** 2 days, **b** 7 days, **c** 21 days, in the 3.5%wt NaCl solution. Also, **d**, **e** illustrate the SEM and EDS of the 21 days of immersion sample, respectively. (Color figure online)

the inhibition properties. Consequently, even after 21 days, corrosion products did not grow further on the surface and no sign of the pitting was detected on the surface and the scratched areas as deduced via the SEM picture and EDS results (Fig. 5d, e). On the other hand, the presence of Zn, Ce, C, O, and Cl in the scratched area could prove the migration of the zinc and cerium from the host layers into the solution and formation of the hydroxide films on the substrate.

Conclusion

In the current study, the one-step in situ synthesis of the composite coating containing oxides and LDHs via the hydrothermal process was investigated for the first time. It is found that the hydrothermal method in the high pH values ($\approx$13) of the precursor solution containing only cerium and zinc cations in the ratios of 2, and the carbonates, would be an appropriate method to fabricate a smart composite coating with high efficiency. The synthesized LDH structures were composed of the Zn^{2+} and the complex of the Ce^{3+} and Ce^{4+}. The oxide/LDHs composite coating consists of a high amount of cerium compounds ($\approx$27wt.%) with the incorporation of the LDH structures were successfully applied on the magnesium alloy (ZC213), which have shown an appropriate self-healing property and anti-corrosion performance (9.7 $\times$ 10^{-8} A cm^{-2}).

References

1. Rives V (2001) Layered double hydroxides: present and future, Nova Publishers
2. Ishizaki T, Kamiyama N, Watanabe K, Serizawa A (2015) Corrosion resistance of Mg(OH)2/Mg-Al layered double hydroxide composite film formed directly on combustion-resistant magnesium alloy AMCa602 by steam coating. Corros Sci 92:76–84. https://doi.org/10.1016/j.corsci.2014.11.031
3. Guo L, Wu W, Zhou Y, Zhang F, Zeng R, Zeng J (2018) Layered double hydroxide coatings on magnesium alloys: a review. J Mater Sci Technol 34:1455–1466. https://doi.org/10.1016/j.jmst.2018.03.003
4. Zhou M, Pang X, Wei L, Gao K (2015) Insitu grown superhydrophobic Zn-Al layered double hydroxides films on magnesium alloy to improve corrosion properties. Appl Surf Sci 337:172–177. https://doi.org/10.1016/j.apsusc.2015.02.086
5. Cao Y, Zheng D, Li X, Lin J, Wang C, Dong S, Lin C (2018) Enhanced corrosion resistance of superhydrophobic layered double hydroxide films with long-term stability on Al substrate. ACS Appl Mater Interfaces 10:15150–15162. https://doi.org/10.1021/acsami.8b02280
6. Tang Y, Wu F, Fang L, Guan T, Hu J, Zhang SF (2019) A comparative study and optimization of corrosion resistance of ZnAl layered double hydroxides films intercalated with different anions on AZ31 Mg alloys. Surf Coatings Technol 358:594–603. https://doi.org/10.1016/j.surfcoat.2018.11.070
7. Anjum MJ, Zhao J, Zahedi Asl V, Yasin G, Wang W, Wei S, Zhao Z, Qamar Khan W (2019) In-situ intercalation of 8-hydroxyquinoline in Mg-Al LDH coating to improve the corrosion resistance of AZ31, Corros Sci 157:1–10. https://doi.org/10.1016/j.corsci.2019.05.022
8. Wu L, Pan F, Liu Y, Zhang G, Tang A (2018) Influence of pH on the growth behaviour of Mg–Al LDH films, Surf Eng 0844. https://doi.org/10.1080/02670844.2017.1382062
9. Hoshino K, Furuya S, Buchheit RG (2019) Effect of Solution pH on Layered Double Hydroxide Formation on Electrogalvanized Steel Sheets. J Mater Eng Perform 28:2237–2244. https://doi.org/10.1007/s11665-019-03963-x
10. Wu L, Yang D, Zhang G, Zhang Z, Zhang S, Tang A, Pan F (2017) Fabrication and characterization of Mg-M layered double hydroxide films on anodized magnesium alloy AZ31. Appl Surf Sci https://doi.org/10.1016/j.apsusc.2017.06.244
11. Zahedi Asl V, Zhao J, Anjum MJ, Wei S, Wang W, Zhao Z (2019) The effect of cerium cation on the microstructure and anti-corrosion performance of LDH conversion coatings on AZ31 magnesium alloy, J Alloys Compd 153248. https://doi.org/10.1016/j.jallcom.2019.153248
12. Song J, Cui X, Jin G, Cai Z, Liu E, Li X, Chen Y, Lu B (2018) Self-healing conversion coating with gelatin–chitosan microcapsules containing inhibitor on AZ91D alloy. Surf Eng 34:79–84. https://doi.org/10.1080/02670844.2017.1327187
13. Calado LM, Taryba MG, Carmezim MJ, Montemor MF (2018) Self-healing ceria-modified coating for corrosion protection of AZ31 magnesium alloy. Corros Sci 142:12–21. https://doi.org/10.1016/j.corsci.2018.06.013
14. Yan H, Wang J, Zhang Y, Hu W (2016) Preparation and inhibition properties of molybdate intercalated ZnAlCe layered double hydroxide, 678 https://doi.org/10.1016/j.jallcom.2016.03.281
15. Smalenskaite A, Vieira DEL, Salak AN, Ferreira MGS, Katelnikovas A, Kareiva A (2017) A comparative study of co-precipitation and sol-gel synthetic approaches to fabricate cerium-substituted MgAl layered double hydroxides with luminescence properties. Appl Clay Sci 143:175–183. https://doi.org/10.1016/j.clay.2017.03.036
16. Zhang Y, Liu J, Li Y, Yu M, Yin X, Li S (2017) Enhancement of active anticorrosion via Ce-doped Zn-Al layered double hydroxides embedded in sol-gel coatings on aluminum alloy. J Wuhan Univ Technol Mater Sci Ed 32:1199–1204. https://doi.org/10.1007/s11595-017-1731-6
17. Wang Y, Peng W, Liu L, Gao F, Li M (2012) The electrochemical determination of l-cysteine at a Ce-doped Mg–Al layered double hydroxide modified glassy carbon electrode. Electrochim Acta 70:193–198. https://doi.org/10.1016/j.electacta.2012.03.106

18. Silva CG, Bouizi Y, Fornés V, García H (2009) Layered double hydroxides as highly efficient photocatalysts for visible light oxygen generation from water. J Am Chem Soc 131:13833–13839. https://doi.org/10.1021/ja905467v
19. Diniz EM, Diniz EM (2019) The Cerium peculiar valence charge in CeN. Curr Appl Phys https://doi.org/10.1016/j.cap.2019.11.015
20. Bouchaud B, Balmain J, Bonnet G, Pedraza F (2012) PH-distribution of cerium species in aqueous systems. J Rare Earths 30:559–562. https://doi.org/10.1016/S1002-0721(12)60091-X
21. Pourbaix M (n.d.) Atlas of Electrochemical Equilibria in Aqueous Solutions
22. Yao Q, Zhang F, Song L, Zeng R, Cui L (2018) Corrosion resistance of a ceria/polymethyltrimethoxysilane modified Mg-Al-layered double hydroxide on AZ31 magnesium alloy, J Alloys Compd 764:913–928. https://doi.org/10.1016/j.jallcom.2018.06.152
23. Zhang G, Wu L, Tang A, Ma Y, Song GL, Zheng D, Jiang B, Atrens A, Pan F (2018) Active corrosion protection by a smart coating based on a MgAl-layered double hydroxide on a cerium-modified plasma electrolytic oxidation coating on Mg alloy AZ31. Corros Sci 139:370–382. https://doi.org/10.1016/j.corsci.2018.05.010
24. Zeng RC, Li XT, Liu ZG, Zhang F, Li SQ, Cui HZ (2015) Corrosion resistance of Zn–Al layered double hydroxide/poly (lactic acid) composite coating on magnesium alloy AZ31. Front. Mater. Sci. 9:355–365. https://doi.org/10.1007/s11706-015-0307-7
25. Gobara M, Baraka A, Akid R, Zorainy M (2020) Corrosion protection mechanism of Ce4+/organic inhibitor for AA2024 in 3.5% NaCl, RSC Adv. 10:2227–2240. https://doi.org/10.1039/c9ra09552g
26. Paula Loperena A, Leticia Lehr I, Beatriz Saidman S (2019) Cerium oxides for corrosion protection of AZ91D Mg Alloy, Cerium Oxide Appl Attrib. https://doi.org/10.5772/intechopen.79329
27. Aliofkhazraei M, Gharabagh RS, Teimouri M, Ahmadzadeh M, Darband GB, Hasannejad H (2016) Ceria embedded nanocomposite coating fabricated by plasma electrolytic oxidation on titanium. J Alloys Compd 685:376–383. https://doi.org/10.1016/j.jallcom.2016.05.315
28. Yang J, Cui F, Lee IS (2011) Surface modifications of magnesium alloys for biomedical applications. Ann Biomed Eng 39:1857–1871. https://doi.org/10.1007/s10439-011-0300-y
29. Zhang C, Zahedi Asl V, Lu Y, Zhao J (2020) Investigation of the corrosion inhibition performances of various inhibitors for carbon steel in CO2 and CO2/H2S environments, Corros Eng Sci Technol 1–8. https://doi.org/10.1080/1478422X.2020.1753929
30. Anjum MJ, Zhao JM, Zahedi Asl V, Malik MU, Yasin G, Khan WQ (2020) Green corrosion inhibitors intercalated Mg:Al layered double hydroxide coatings to protect Mg alloy, Rare Met https://doi.org/10.1007/s12598-020-01538-7
31. Chen J, Fang L, Wu F, Xie J, Hu J, Jiang B, Luo H (2019) Progress in Organic Coatings Corrosion resistance of a self-healing rose-like MgAl-LDH coating intercalated with aspartic acid on AZ31 Mg alloy. Prog Org Coatings 136:105234. https://doi.org/10.1016/j.porgcoat.2019.105234

Improvement of Corrosion Resistance by Zn Addition to Mg Alloy Containing Impurity Ni

Koki Ezumi, Taiki Morishige, Tetsuo Kikuchi, Ryuichi Yoshida, and Toshihide Takenaka

Abstract There is the deleterious influence of corrosion resistance of Mg alloy by contaminant of impurity element Ni during Mg recycling. Mg_2Ni precipitates trigger the galvanic corrosion with Mg matrix phase. Zn addition into Mg alloy may reduce the detrimental impact of impurities because a small amount of Ni element is dissolved into Mg-Zn intermetallic phase. Therefore, the microstructure and corrosion behavior were investigated by changing the amount of Zn in Mg alloy with a trace amount of Ni. From the results of the microstructural observation, Ni element existed in $MgZn_2$ intermetallic phase when the Zn content exceeded 6 mass%, to change the existing state of Ni whereas Mg_2Ni phase was dispersed in Mg-Zn alloy with a few percent of Zn.

Keywords Mg · Corrosion · Zinc

Introduction

Mg alloy has the characteristics of being the lightest and high specific strength among practical metal materials, and in recent years, the demand has been expanding in the transportation equipment field and the like. Along with this, the amount of Mg scrap increases, so recycling of Mg is drawing attention. However, impurities such as Cu, Fe, and Ni are mixed in the recycling process. Since these impurity elements have a small solid solution limit, they form a cathode portion with a low hydrogen overvoltage and elute Mg violently. At the same concentration, it has been clarified that it acts as an active cathode in the order of Ni> Fe> Cu and promotes the corrosion of Mg. Fe impurity can be easily separated by Mn addition, but no effective removal

K. Ezumi (✉)
Graduate School of Science and Engineering, Kansai University, Suita, Japan
e-mail: k450980@kansai-u.ac.jp

T. Morishige · T. Takenaka
Department of Chemistry and Materials Engineering, Kansai University, Suita, Japan

T. Kikuchi · R. Yoshida
CHUO-KOSAN, LTD, Tokyo, Japan

method has been established for Cu and Ni. From past reports, it is clear that by addition of Zn, which has a high affinity for Mg-0.2mass% Cu, the intermetallic compound phase of Mg(Zn, Cu)$_2$ can be formed and the effect of Cu on corrosion can be suppressed.

Therefore, in this study, since Cu, Zn, and Ni are transition elements with consecutive atomic numbers, the suppression of the influence of Ni was investigated by addition of Zn in the similar way as neutralizing Cu on corrosion.

Experimental

The experimental apparatus is illustrated in Fig. 1. A furnace tube was placed in the center of the electric furnace, and a thermocouple for temperature measurement was inserted into the electric furnace so as to touch the furnace tube. A gap between the furnace core tube and the upper part of the electric furnace was filled with a heat insulating material, and pure Ti rod (made by Nilaco Co., Ltd.) as a stirring rod was inserted into the rubber stopper above the furnace core tube. The inside of the furnace core tube was once evacuated by a vacuum pump (ULVAC G-10DA), argon gas was filled so that the inside of the furnace core tube became atmosphere pressure,

Fig. 1 Schematic diagram of experimental apparatus. (Color figure online)
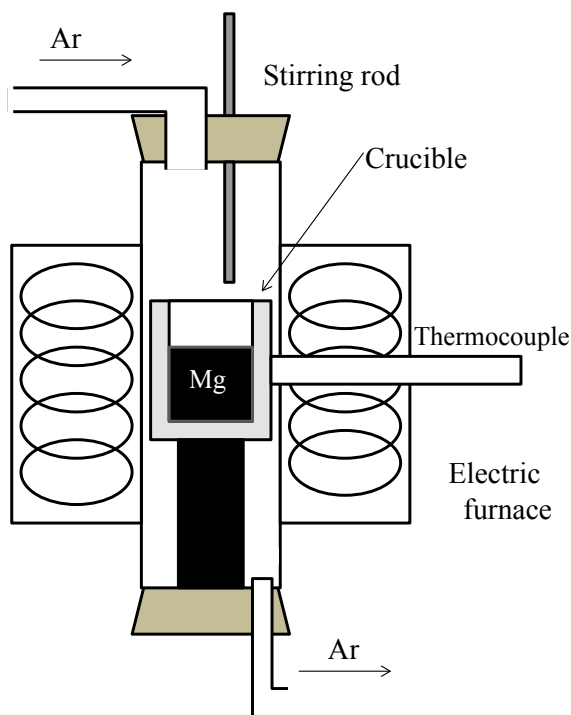
and heating was started using an electric furnace. In order to prevent damage to the furnace core tube due to a rapid temperature change, after reaching 550 °C, the temperature was raised again after holding for 40 min. After reaching 750 °C, the sample was taken out of the electric furnace after being held for 3 h while stirring every 30 min and then naturally cooled.

The composition of the produced sample was analyzed by an X-ray fluorescence analyzer (JEOL JSX-1000) with a collimator of $\varphi2.0$ mm. At that time, in each sample, an average value of three measurements was taken as each composition.

Immersion test was performed to observe the corrosion form and measure the corrosion depth of each sample. It was adjusted to 5 mass% NaCl aqueous solution using distilled water and NaCl (>99.5% special grade made by Kishida Chemical). The sample was placed upright in a beaker with a volume of 500 mL, and a graduated cylinder with a rubber stopper having a volume of 200 ml was placed on the top of the beaker. 500 mL of 5 mass% NaCl aqueous solution was put into a graduated cylinder and a beaker, and the sample was completely immersed in the 5 mass% NaCl aqueous solution. Since the corrosion weight loss volume can be calculated from the bubbles generated in the aqueous solution during the immersion test, the corrosion rate was determined by calculating the corrosion weight loss volume from the amount of hydrogen gas generated after immersing the test piece for 4 h and dividing by the surface area and time of the test piece.

Figure 2 shows a schematic diagram of the experimental setup for measurement of hydrogen gas evolution.

The reaction formula in the immersion test and the corrosion calculation formula are shown below.

(Reaction formula):

$$\text{(anode reaction)} \qquad Mg \rightarrow Mg^{2+} + 2e^-$$
$$\text{(cathode reaction)} \qquad 2H^+ + 2e^- \rightarrow H2 \uparrow$$

(Calculation formula):

$$\text{Corrosion rate}(g\ cm^{-2}\ day^{-1}) = \frac{\text{hydrogen generation(L)}}{22.4\left(\frac{L}{mol}\right)} \times 24.3(g/mol)$$
$$\times \frac{1}{\text{corrosion area}(cm^2)} \times \frac{24(h)}{4(h)}$$

For the purpose of observing the presence or absence of precipitates on the measurement surface and the microstructure for each Zn content after the immersion test, measurement with an optical microscope (made by Nikon ECLIPSE MA 100) was performed. In addition, using a digital microscope (made by KEYENCE VHX-2000), surface observation, macrostructure observation, and depth measurements were made.

A tabletop scanning electron microscope (made by JEOL JCM-6000 acceleration voltage 15 kV) was used to observe the surface of the sample. In addition,
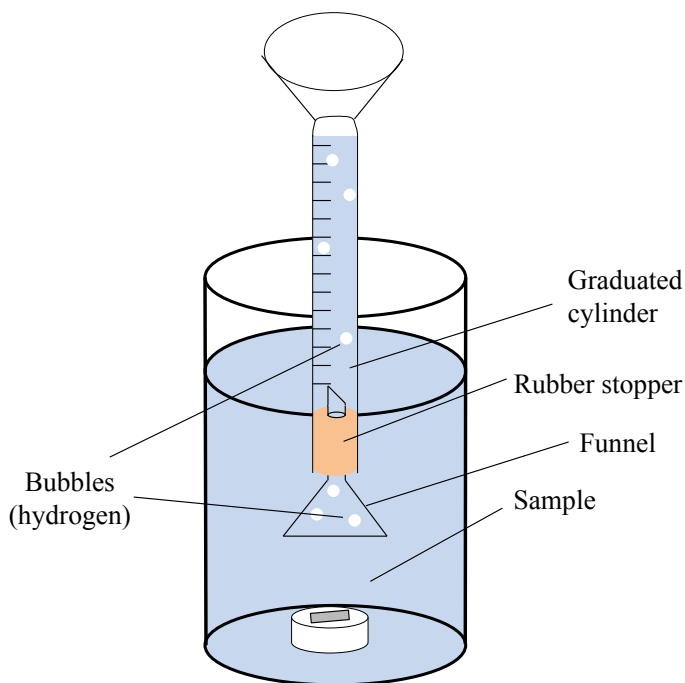
Fig. 2 Schematic diagram of hydrogen generation amount measuring device. (Color figure online)

elemental mapping was also performed by energy dispersive X-ray analysis (made by JEOL MP-00040EDAP). The state of existence of elements in the precipitate was investigated by EDX element mapping.

XRD analysis (made by Rigaku RINT-2550 V acceleration 40 kV diffraction angle from 10 to 90° wave source Cu Kα with wavelength 1.5406 Å scan speed 40.00°/min number of steps 0.02°) was performed to identify the constituent phases of the sample. Identification of constituent phases for the measured peaks was performed using the inorganic chemistry database.

Results and Discussion

Figure 3 shows the SEM image of each sample. White precipitates appeared as the Zn content increased. From Fig. 3, the area ratio of the precipitates starts to increase when the Zn content exceeds 4 mass%, and the precipitates are remarkably present in a network form at the Zn content of 6 mass% and more. Therefore, it is suggested that the precipitation phase changes with increasing Zn content.

Figure 4 shows the XRD pattern of Mg-Xmass%Zn-0.1mass%Ni (X = 2, 4, 5, 6, 9). From Fig. 4, the peaks in all regions were clearly seen. A peak of Mg_2Ni
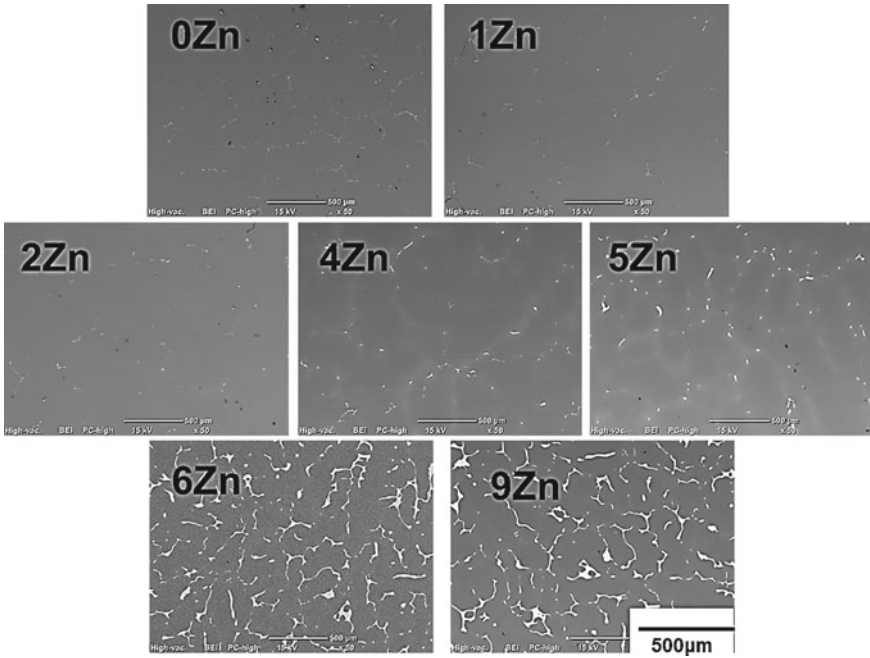
Fig. 3 SEM image of each organization before immersion
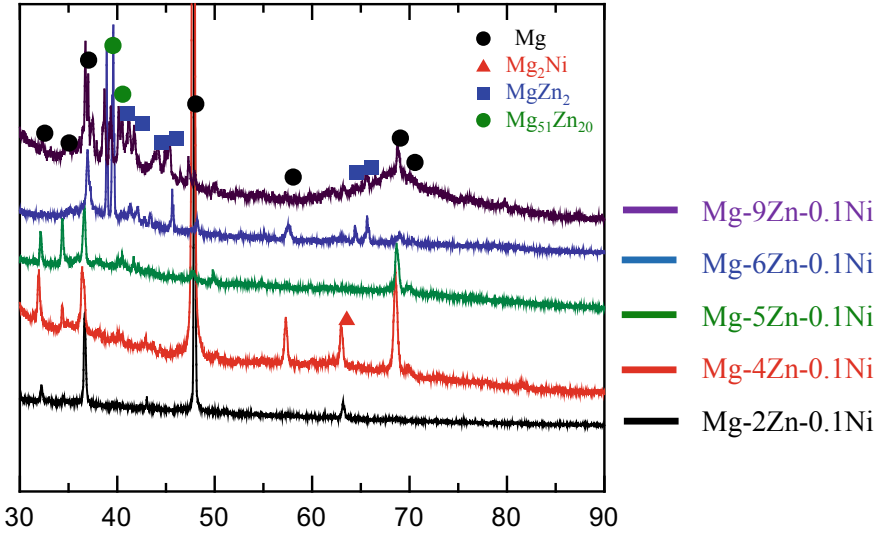
Fig. 4 XRD pattern of Mg-Xmass%Zn-0.1mass%Ni (X = 2, 4, 5, 6, 9). (Color figure online)

was observed up to a Zn content of 4 mass%. $Mg_{51}Zn_{20}$ and $MgZn_2$ phases were remarkably observed as the Zn content increased. From this, it indicates that the constituent phase changes with the increase of the Zn content. Further, only the Mg matrix and Mg_2Ni were observed even when the Zn content is 2 mass% or less.

Next, we focused on the existence state of Ni. Figure 5 shows the results of EDX mapping of Mg-6mass% Zn-0.1mass% Ni. Table 1 shows the results of the point analysis at that time. Two distinct white phases were observed. There are two types of white, dark white, and light white. From the results of SEM–EDX and XRD patterns, the dark white precipitate was $MgZn_2$ and the light white precipitate was $Mg_{51}Zn_{20}$. In addition, since Ni was not concentrated in the light white part and was present only in the dark white part, it is considered that Ni was concentrated in $MgZn_2$.
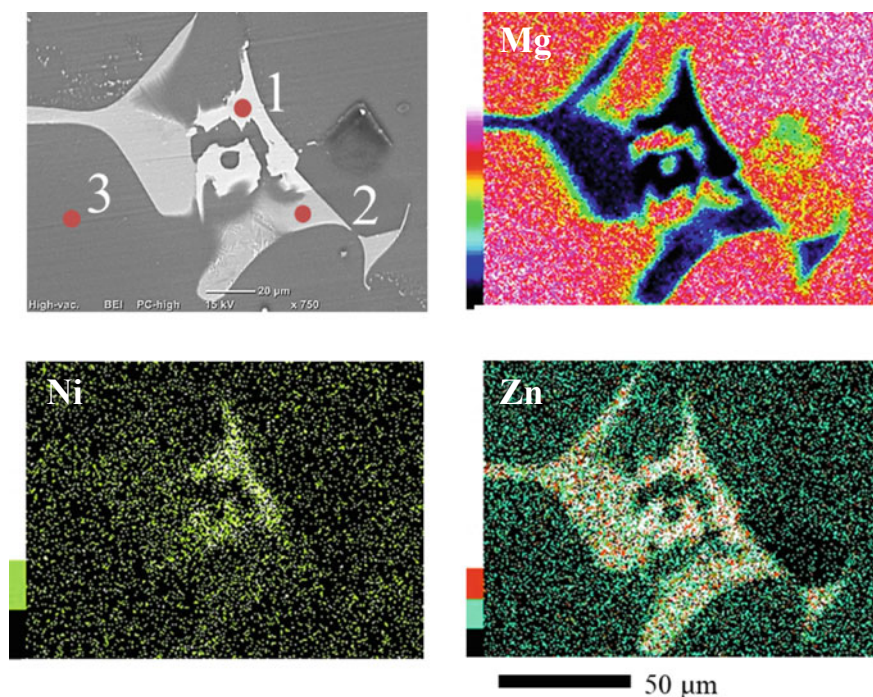
Fig. 5 Mapping image of Mg-6mass% Zn−0.1mass% Ni. (Color figure online)

Table 1 Point analysis result

Element	Concentration (at.%)		
	Point1	Point2	Point3
Mg	27.78	63.05	97.59
Ni	12.68	0.04	0.02
Zn	59.54	36.90	2.41

Let the atomic radius of the main component metal r_0 and the atomic radius of the alloy component elements be r_A. The value of $| r_0 - r_A | / r_0$ is within 15%, the solid solubility is generally large, so the Hume-Rothery rule that a substituted solid solution is likely to form is mentioned. The rule is considered as the reason why Zn was used for detoxifying Cu. When the values of r_0 is Zn atom and r_A is Cu atom sizes were substituted and calculated, the value was 4.48%, which was smaller than 15%, so it was considered that substitutional solid solution is possible. This time, assuming that Ni is a substitutional solid solution in the Zn part of $MgZn_2$, the values of $r_0 = Zn$, $r_A = Ni$ were substituted and calculated, the value was 7.46%, which was smaller than 15%. Therefore, it is considered that Ni was substituted and solid-dissolved at the position of Zn as in the case of detoxifying Cu. Since Mg forms a eutectic compound with Zn in the case of containing Zn of 6 mass% and more in the Mg-Zn binary phase diagram, the addition of 6 mass% and more of Zn, Ni element does not form a compound with Mg, but Ni present at the position of Zn with a closer atomic radius, which is considered to form $Mg(Zn,Ni)_2$. In addition, unlike the previous case, since Ni is concentrated on the entire surface of $MgZn_2$, it is suggested that Ni is completely concentrated on $MgZn_2$ and the existing state of Ni was changed.

Figure 6 shows the relationship between the Zn content of Mg-Xmass%Zn-0.1mass%Ni (X = 0, 1, 2, 4, 5, 6, 9) and the corrosion rate. In a structure with a low Zn content, Ni acts as a cathode because it forms a compound as Mg_2Ni, and the micro-galvanic corrosion that promotes anodic dissolution of the matrix phase is progressing, so it is suggested that the corrosion resistance is not so much improved. It can be seen that when the Zn content is 4 to 6 mass%, the corrosion rate gradually decreases. This is because $MgZn_2$ is gradually formed and Ni is taken into the $MgZn_2$, whereby the existing state of Ni is gradually changed, and the compound containing Ni does not act as a cathode and suppresses the influence of Ni on corrosion. It is considered that the corrosion resistance has improved. Then, by adding 6 mass% or more of Zn, Ni does not form a compound with Mg but forms a compound with $MgZn_2$ which is a Mg-Zn eutectic compound. Therefore, the existing state of

Fig. 6 Relationship of Zn content and corrosion rate. (Color figure online)
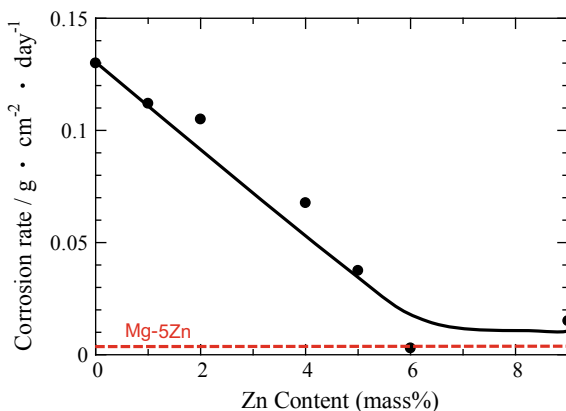
Ni changes, and Ni is incorporated into $MgZn_2$ to form $Mg(Zn,Ni)_2$. It is considered that the absence of Ni as Mg_2Ni acting as a cathode significantly suppressed the influence on corrosion and improved the corrosion resistance of the Mg alloy to the same extent as the Mg-5Zn compound containing no Ni. Therefore, it is considered preferable to add 6 mass% or more of Zn when Mg contains 0.1 mass% of Ni.

Conclusion

Even if the composition contains Ni, the presence of $MgZn_2$ is expected to improve corrosion resistance by incorporating Ni into the precipitate. By adding 6% by mass or more of Zn, the corrosion resistance was equivalent to that of the Ni-free Mg-5Zn alloy. It is believed that the presence of $MgZn_2$ can change the presence of Ni and reduce the effect of Ni on corrosion resistance. Therefore, it was clarified that the corrosion resistance can be improved to a practical level by adding Zn of 6% by mass or more.

The Role of Native Oxides on the Corrosion Mechanism of Laves Phases in Mg–Al–Ca Composites

Markus Felten, Jakub Nowak, Patrick Grünewald, Florian Schäfer, Christian Motz, and Daniela Zander

Abstract Magnesium–aluminum–calcium composites are characterized by thermally stable Laves phases, which enable high-temperature material applications. Nevertheless, immersing the material into an electrolyte causes an increased corrosion rate as a consequence of micro-galvanic effects among the Laves phases and the matrix. The Volta-potential difference determined under atmospheric conditions on a freshly polished surface using Scanning Kelvin Probe Force Microscopy (SKPFM) is a valid measure for the micro-galvanic coupling and the dynamic growth kinetics of a native oxide film. In the present study, the time-dependent native oxide film formation of magnesium–aluminum–calcium alloys is analyzed via in situ SKPFM measurements. An inhomogeneous evolution of the Volta-potential on the Laves phases compared to the matrix indicates heterogeneous native oxide formation.

Introduction

The mechanical strength of magnesium (Mg) increases with aluminum (Al) as an alloying element by precipitation hardening through the intermetallic β-phase [1]. However, reduced stability of the β-phase at operating temperatures above 150 °C inhibits high-temperature applications of the material [2]. With calcium (Ca) as an additional alloying element, thermally stable Laves phases with increased creep resistance are formed as a function of the Ca/Al ratio [3, 4]. These secondary phases further enhance the micro-galvanic effect of Mg alloys as a consequence of the relatively low standard potential of Mg. Under immersion conditions, an increasing free corrosion potential occurs resulting from an evolving oxide-/hydroxide layer

M. Felten · J. Nowak · D. Zander (✉)
Chair of Corrosion and Corrosion Protection, Division of Materials Science and Engineering, Foundry Institute Aachen, RWTH Aachen University, Aachen, Germany
e-mail: D.Zander@gi.rwth-aachen.de

P. Grünewald · F. Schäfer · C. Motz
Department of Material Science and Technology, Saarland University, Bldg. D2.2, 66123 Saarbrücken, Germany

[5]. The chemical composition and stability of this oxide-/hydroxide layer depend on the native oxide layer formed under atmospheric conditions [6, 7]. The contact of metallic magnesium with oxygen forms an initial MgO layer according to (1) [8].

$$Mg + O^{2-} \rightarrow MgO + 2e\text{-} \qquad (1)$$
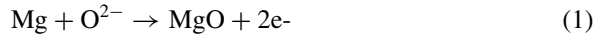
The formation of this layer is characterized by an inverse-logarithmic kinetics based on the Mott–Cabrera model [8–10]. In a second step, a relatively thin $Mg(OH)_2$ layer is obtained on the surface of the native oxide as a result of the MgO hydration with adsorbed water molecules according to (2) [6]. Therefore, the native oxide layer can be described by the duplex structure shown in Fig. 1a [6, 11].

$$MgO + H_2O \rightarrow Mg(OH)_2 \qquad (2)$$
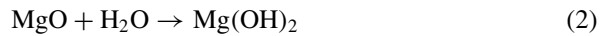
The structure of the native oxide is further altered by the alloying elements. Nordlien et al. [7] revealed an Al accumulation in the native oxide layer resulting in an
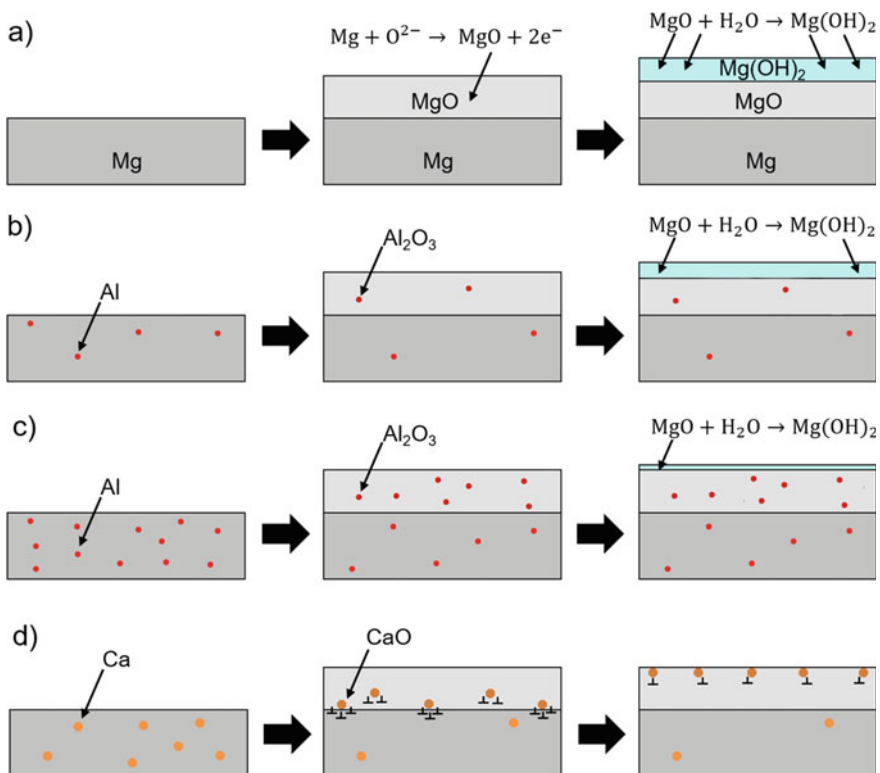
Fig. 1 Schematic representation of the native oxides on **a** pure Mg, **b** Mg with Al in solid solution **c** Mg with more Al in solid solution and **d** the effect of Ca in solid solution. (Color figure online)

increased oxide stability, which lead to a reduced hydration tendency (see Fig. 1a–c). Up to an Al content of 5 wt.% in solid solution they observed a saturation of 35% Al in the MgO layer. Feliu et al. [12] and Souda et al. [13] additionally showed CaO components in the native oxide layer as a consequence of Ca impurities in the Mg alloys. CaO components cause a larger lattice strain at the metal/oxide interface, due to the 1.36 times larger atomic radius of Ca^{2+} ions compared to Mg^{2+} ions. By segregating Ca^{2+} ions to the oxide/atmosphere interface, the lattice distortion decreases, resulting in a time-dependent accumulation of Ca^{2+} ions in the outer oxide layer (see Fig. 1d) [13]. While Scanning Kelvin Probe Force Microscopy (SKPFM) studies have been used predominantly to determine Volta-potential differences between the secondary phases and the matrix to assess micro-galvanic effects under immersion conditions, Revilla et al. [14] showed that in situ SKPFM measurement is furthermore capable of representing the growth kinetics of the native oxide. They observed two phases of the Volta-potential after imprinting a scratch on an Al surface. The first phase consists of a rapid increase of the Volta-potential while the second phase comprises a reduced time depending change of the Volta-potential. The first phase was associated with a rapid reaction-controlled phase of nucleation, while the second phase was described by an inverse-logarithmic oxide growth according to the Mott–Cabrera model.

Materials and Methods

In the present study, the alloys listed in Table 1 were ground up to a #4000 SiC grid and subsequently polished with a diamond suspension with a 0.25 μm grain size. Directly after the application of a SiO final polishing, in situ SKPFM measurements were performed using a Dimension Icon AFM from Bruker Corporation. The frequency-modulated peak force mode and a working distance of 100 nm with a scan velocity of 0.5 Hz were used. A constant bias voltage of $U_b = 6$ V and the alternating voltage of $U_{AC} = 4$ V were applied to the silicon nitride tip (PFQNE) from Bruker Corporation. The measurements were performed under atmospheric conditions at room temperature and a humidity of approx. 35%. Prior to each measurement, an additional calibration was performed on a gold/aluminum-coated silicon reference sample, enabling the indication of the Volta-potential with respect to gold (Au). An EDX analysis was subsequently performed on the same location using the Sigma VP SEM from Carl Zeiss AG and the Oxford-X-Max EDX detector from Oxford

Table 1 Nominal chemical composition of Mg and Mg–Al–Ca composites

Alloy	Al [wt.−%]	Ca [wt.−%]	Ca/Al [−]	Mg [wt.−%]	Condition [−]
1	–	–	–	99.999	as cast
2	3.68	3.80	1.03	Bal	as cast
3	5.44	1.73	0.32	Bal	as cast

Instruments. Additionally, several EDX line scans were performed on the Mg–Al–Ca composites within the interdendritic domain to evaluate the content of Al and Ca in the matrix.

Results and Discussion

Microstructure

Figure 2 shows two representative evaluations of the EDX line scans conducted on the interdendritic domain of the alloys 2 and 3. At a distance of a few μm from the secondary phases, the concentration of Al and Ca in the solid solution is nearly constant. Table 2 shows the averaged concentrations of four different line scans.
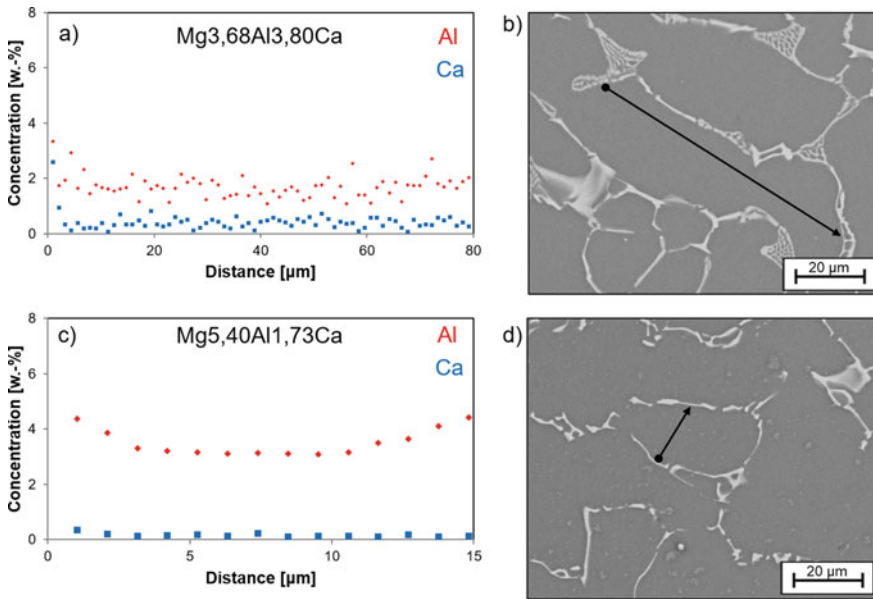
Fig. 2 Representative illustration of the performed EDX line scan analysis for **a**, **b** alloy 2 and **c**, **d** alloy 3. (Color figure online)

Table 2 Averaged concentration of the Al and Ca concentration in the matrix

Alloy	Matrix Al content [wt.−%]	Matrix Ca content [wt.−%]
1	–	–
2	1.7 ± 0.3	0.4 ± 0.2
3	3.2 ± 0.4	0.1 ± 0.05

Alloy 3 with the highest nominal Al content exhibits also quantitatively the highest Al content in the matrix. The Ca contents of 0.1 and 0.4, respectively, are under the detection limit of the EDX analysis and are therefore only considered as a qualitative feature of a higher Ca concentration in the solid solution of alloy 3.

Pure Mg

Figure 3a–d shows the time-dependent evolution of the Volta-potential of alloy 1 after the polishing process. The development of the Volta-potential is divided into three phases. In the first phase (0–2 h), the Volta-potential increases rapidly around approximately $\Delta V = 150$ mV. However, during the subsequent second phase (2–13 h), the Volta-potential exhibits a reduced time depending change of $\Delta V = 50$ mV and remains nearly constant at a potential of approximately $V = -1150$ mV$_{Au}$ throughout the third phase. This variation of the Volta-potential thus corresponds to the inverse-logarithmic oxidation kinetics observed by Revilla et al. [14] and may therefore correspond to the growth of a MgO layer according to the Mott–Cabrera model.
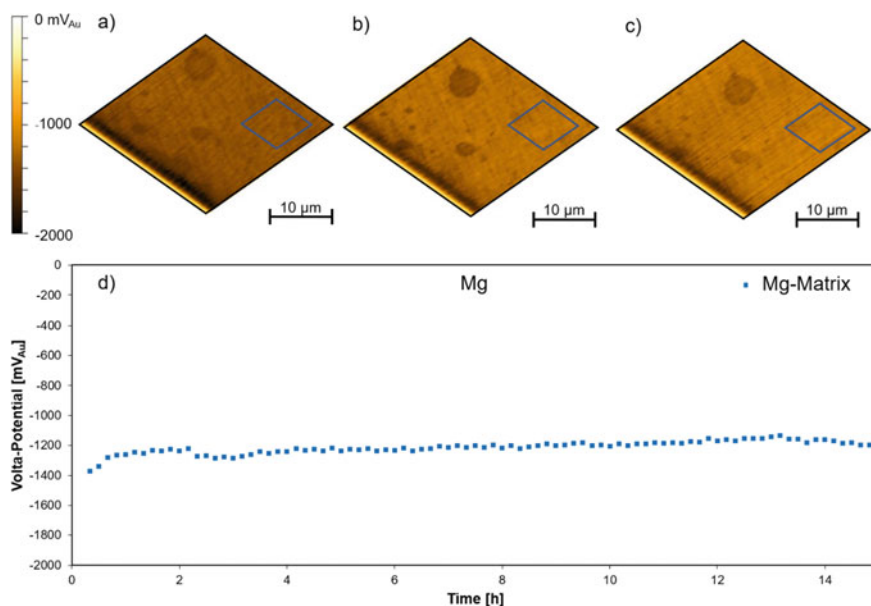
Fig. 3 In situ SKPFM measurements of alloy 1 after **a**, 0 h **b** 6 h, **c** 15 h with the corresponding average Volta-potential of the selected region as a function of time after the polishing process. (Color figure online)

Mg3.68Al3.80Ca

Figure 4a–d displays the evolution of the Volta-potential of alloy 2 as a function of time after the polishing process. The initial evolution of the Volta-potential measured on the matrix is comparable with pure Mg up to 6 h after the polishing process. In this phase, the evolution of the Volta-potential may also be described by inverse-logarithmic oxidation kinetics and is thus related to the oxide growth. However, the maximum Volta-potential in this phase is approximately $V = -750$ mV$_{Au}$. The higher maximum Volta-potential of alloy 2 might result from the higher Al content in the matrix. Thereby, the nobler Al accumulates progressively in the MgO layer and causes the higher Volta-potential. In contrast, the period of 9–15 h after the polishing process shows a reduction of the Volta-potential of approximately $\Delta V = 500$ mV. This variation has not been described in the literature under atmospheric conditions. The hydration of the MgO layer might cause such a reduction of the Volta-potential [15]. Nevertheless, Al in the MgO layer causes a reduced tendency to hydration compared to pure magnesium [7]. Since the evolution of the Volta-potential of pure Mg in Fig. 3 reveals no reduction of the Volta-potential, hydration seems to be an unlikely explanation for the reduction of the Volta-potential. Whereas the migration of the less noble Ca^{2+} ions into the top layer of the MgO film may cause the observed reduction of the Volta-potential. The development of the Volta-potential
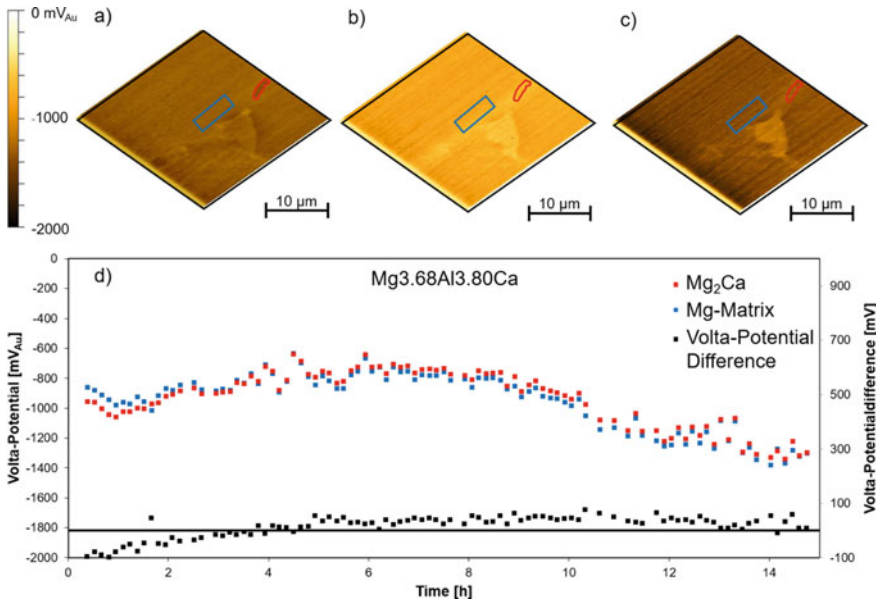
Fig. 4 In situ SKPFM measurements of alloy 2 after **a**, 0 h **b** 6 h, **c** 15 h with the corresponding average Volta-potential of the selected region, as well as the Volta-potential difference of the phases, as a function of time after the polishing process. (Color figure online)

of the Mg_2Ca Laves phase shows a qualitatively similar behavior in comparison to the more noble matrix. However, the Volta-potential increases more rapidly in the growth phase of the MgO layer, resulting in an inversion of polarity from $\Delta V = -100$ mV to $\Delta V = +100$ mV with respect to the matrix. This accelerated increase of the potential suggests a different structure of the oxide-hydroxide layers. Although there is no knowledge about the structure of an oxide layer on the Laves phases so far, a higher Al content could cause such a variation. Based on the inversion of the polarity, one can clearly conclude that for the assessment of micro-galvanic effects between two phases, the Volta-potential difference in the freshly polished state should be used, since a growth of the native oxide layer can distort the real difference of the work function. The reduction of the Volta-potential associated with Ca migration, on the other hand, is quantitatively the same compared with the matrix, leading to a constant Volta-potential difference.

Mg5.44Al1.73Ca

Figure 5a–d shows the evolution of the Volta-potential of alloy 3 as a function of the time after the polishing process. The development of the Volta-potential is qualitatively comparable with alloy 2. After the increase of the Volta-potential, associated
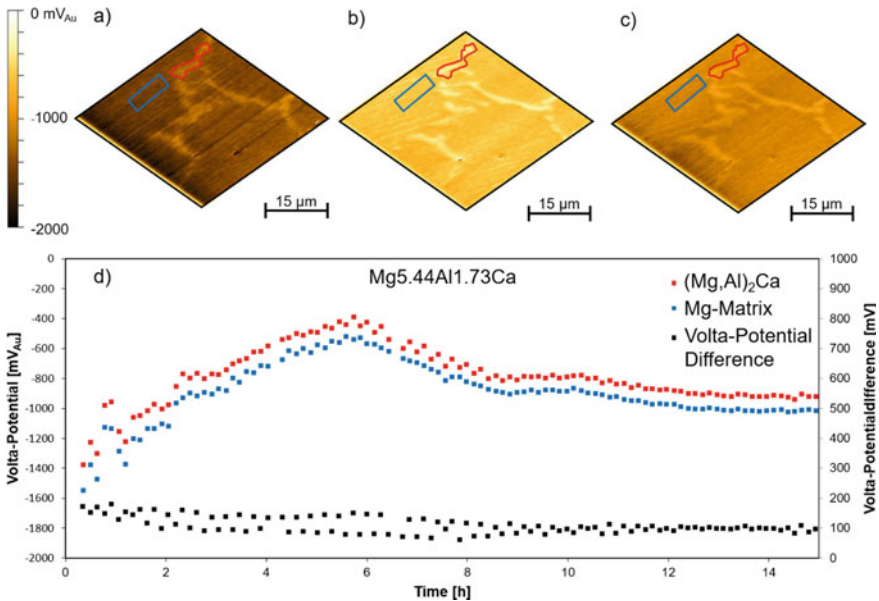
Fig. 5 In situ SKPFM measurements of alloy 3 after **a**, 0 h **b** 6 h, **c** 15 h with the corresponding average Volta-potential of the selected regions, as well as the Volta-potential difference of the phases, as a function of time after the polishing process. (Color figure online)

Table 3 Maximum Volta-potential measured during in situ SKPFM analysis

Alloy	Matrix Al content [wt.−%]	Matrix Ca content [wt.−%]	Max. Volta-potential [mV$_{Au}$]
1	–	–	−1150
2	1.7 ± 0.3	0.4 ± 0.2	−720
3	3.2 ± 0.4	0.1 ± 0.05	−540

with the oxide growth and the incorporation of Al into the native oxide layer, a peak occurs after 6 h at V = −540 mV$_{Au}$. Subsequently, the Volta-potential decreases about $\Delta V = -400$ mV before reaching an approximately constant plateau after 13 h. The decrease in the Volta-potential is comparable in magnitude to that shown in Fig. 4, suggesting that this effect is caused by the alloying elements Ca or Al in the Mg–Al–Ca composites and thereby illustrates that migration of Ca^{2+} ions in the native oxide layer is the potential underlying mechanism.

Based on the results of the maximum achieved Volta-potential shown in Table 3, it is evident that with increasing Al content a higher maximum Volta-potential occurs in the investigated time period. The Al content of the matrix is lower than 5 wt.%, hence the maximum saturation of Al in the native oxide layer as described by Nordlien et al. [7] has not been reached. Therefore, a higher maximum Volta-potential as a result of a higher concentration of Al in the native oxide layer appears to be a reasonable mechanism for this effect.

Both the thickness and the chemical composition of the native oxide layer are known to influence the electrochemical corrosion properties of Mg and Mg alloys. The growth of the layer observed by in situ SKPFM measurements suggests that an almost terminated growth of the native oxide layer is reached after approximately 15 h. In order to determine comparable electrochemical properties of Mg alloys, this period should subsequently elapse before performing the electrochemical measurements. However, the observed Volta-potential curves need to be statistically validated and the effect of different native film thickness on the electrochemical properties of Mg needs to be further experimentally investigated.

Conclusion

In situ SKPFM studies on Mg–Al–Ca composites under atmospheric conditions revealed a time-varying development of the Volta-potential immediately after the polishing process. Based on the comparison with the Volta-potential evolution of pure Mg, the growth kinetics and the composition of the native oxide layer were derived. The following conclusions are obtained:

- In situ SKPFM measurements show an inverse-logarithmic growth of the native oxide on Mg and Mg–Al–Ca composites according to the Mott–Cabrera model.

- With increasing Al content of the alloys, a higher maximum Volta-potential is observed throughout the studied time period.
- The in situ SKPFM measurements of the Mg–Al–Ca composites show a reduction of the Volta-potential of about $\Delta V = 500$ mV after a global maximum. This effect was associated with the migration of Ca^{2+} ions in the native oxide layer.
- A nearly constant Volta-potential is achieved in the investigated alloys after about 15 h. This plateau is associated with a reduced oxide growth.
- A varying oxide layer growth on the secondary Mg_2Ca Laves phase and the matrix causes an inversion of the polarity.

References

1. Fatmi M, Djemli A, Ouali A, Chihi T, Ghebouli MA, Belhouchet H (2018) Heat treatment and kinetics of Precipitation of β-$Mg_{17}Al_{12}$ phase in AZ91 Alloy. Results Phys.
2. Mathur HN, Maier-Kiener V, Korte-Kerzel S (2016) Deformation in the γ-$Mg_{17}Al_{12}$ phase at 25–278 °C. Acta Mater.
3. Suzuki A, Saddock ND, Jones JW, Pollock TM (2005) Solidification paths and eutectic intermetallic phases in Mg-Al-Ca ternary alloys. Acta Mater. 53:2823–2834
4. Zhang L, Deng K, Nie K, Xu F, Su K, Liang W (2015) Microstructures and mechanical properties of Mg-Al-Ca alloys affected by Ca/Al ratio. Mater. Sci. Eng. A 636:279–288
5. Tiwari S, Balasubramaniam R, Gupta M (2007) Corrosion behavior of SiC reinforced magnesium composites. Corros, Sci
6. Nordlien JH (1995) Morphology and Structure of Oxide Films Formed on Magnesium by Exposure to Air and Water. J. Electrochem. Soc. 142:3320
7. Nordlien JH (1996) Morphology and Structure of Oxide Films Formed on MgAl Alloys by Exposure to Air and Water. J. Electrochem. Soc. 143:2564
8. Esmaily M, Svensson JE, Fajardo S, Birbilis N, Frankel GS, Virtanen S, Arrabal R, Thomas S, Johansson LG (2017) Fundamentals and advances in magnesium alloy corrosion. Prog. Mater, Sci
9. Cabrera N, Mott NF (1949) Theory of the oxidation of metals. Rep. Prog. Phys. 12:163–184
10. Do T, Splinter SJ, Chen C, Mcintyre NS (1997) The oxidation kinetics of Mg and Al surfaces studied by AES and XPS. Surf Sci 387:192–198
11. Santamaria M, Di Quarto F, Zanna S, Marcus P (2007) Initial surface film on magnesium metal: A characterization by X-ray photoelectron spectroscopy (XPS) and photocurrent spectroscopy (PCS). Electrochim. Acta 53:1314–1324
12. Feliu S, Galván JC, Pardo A, Merino MC (2010) Native air-formed oxide film and its effect on magnesium alloys corrosion. Tocorrj. 3:80–90
13. Souda R, Hwang Y, Aizawa T, Hayami W, Oyoshi K, Hishita S (1997) Ca segregation at the MgO(001) surface studied by ion scattering spectroscopy. Surf Sci. 387:136–141
14. Revilla RI, Terryn H, Graeve I (2018) On the use of SKPFM for in situ studies of the repassivation of the native oxide film on aluminium in air. Electrochem. Commun. 93:162–165
15. Örnek C, Leygraf C, Pan J (2020) Real-time corrosion monitoring of aluminum alloy using scanning kelvin probe force microscopy. J. Electrochem. Soc. 167:81502

Part VI
Modeling and Simulation

Numerical Modeling of the Forging Response of a Magnesium Alloy Control Arm

Bruce W. Williams, Tharindu Abesin Kodippili, Jonathan McKinley, Stephan Lambert, and Hamid Jahed

Abstract The pronounced temperature and strain-rate sensitivity of magnesium alloys were apparent during full-scale forging of control arm components. To achieve the required fatigue resistance of ZK60 and AZ80 control arms, it was necessary to forge at a low temperature of 300 °C. At this temperature, a slow strain rate was used to ensure the force required for forging was within the available load capacity of the equipment. The final forging sequence required to achieve complete material fill of the component was determined through a combination of experimental forging and numerical simulations. The temperature and rate sensitivity of the alloys and the material model utilized in the simulations will be detailed. Differences between Adaptive Remeshing (AR), Arbitrary Lagrangian–Eulerian (ALE), and Combined Eulerian–Lagrangian (CEL) finite element methods for predicting large deformation under isothermal conditions will be discussed. The challenges of forging a complex-shaped magnesium alloy component are highlighted.

Keywords Magnesium forging · Euler–Lagrange · Strain rate · Temperature

Introduction

The high levels of strain induced during forging decrease porosity and refine grain structure compared to the cast structure leading to an increase in strength, ductility, and fatigue resistance. The Hexagonal Close-Packed (HCP) crystal structure leads to poor (bending) ductility at room temperature but excellent formability at elevated temperature. The formability of Mg alloys is significantly influenced by temperature and strain rate, which can vary during the forging process. The use of Finite Element (FE) simulations can reduce design cost and time and has been employed by various researchers [1–7] in the forging response of Mg alloys. It is necessary to use a FE

B. W. Williams (✉) · J. McKinley
CanmetMATERIALS, Natural Resources Canada, Hamilton, ON, Canada
e-mail: bruce.williams@canada.ca

T. A. Kodippili · S. Lambert · H. Jahed
University of Waterloo, Waterloo, ON, Canada

229

method capable of capturing the high levels of strain induced during forging. Also, a well-calibrated material model, one that captures the softening response of Mg alloys due to dynamic recrystallization as a function of temperature and strain rate, is required.

The goal of the current work was to produce a prototype Mg alloy control arm that achieves weight reduction yet with a stiffness and fatigue resistance comparable to an aluminum alloy control arm. This required both experiment and simulation throughout the development process. Three simulation methods to capture high deformation were used in this study including Adaptive Remeshing (AR), Arbitrary Lagrangian–Eulerian (ALE), and Combined Eulerian–Lagrangian (CEL) which are solution techniques available in the commercial software DEFORM3D and ABAQUS. AR and ALE are meshing techniques with a mainly Lagrangian framework where the mesh moves, whereas the CEL technique is based on material moving through the mesh as with an Eulerian framework.

Several small- and intermediate-scale forgings were conducted to aid in the development of the forging process for the control arm but were also used to validate the FE model. The microstructure, texture, strength, ductility, and fatigue response analysis of these specimens are detailed in literature including, but not limited to, [8, 9] and will not be addressed in the paper. It is of note that the specimens forged at 250 °C showed the highest strength and fatigue resistance.

Forging Experiments

Commercial ZK60 and AZ60 alloys were considered in this work. Initially, small uniaxial compression tests were performed using a Gleeble to characterize the stress–strain response of the two alloys at temperature ranging from 300 °C to 450 °C with strain rates ranging from near quasi-static (0.001 s^{-1}) to 1 s^{-1}. The test details and results for ZK60 are summarized by Hadadzadeh et al. [10] and by Prakash et al. [11] for AZ80. The stress versus strain response from the Gleeble tests is shown in Fig. 1 at 300 °C and 450 °C for various strain rates. It is of note that the strain at which the softening occurs is much less than that induced during forging of the control arm such that it would be expected that the full control arm experienced dynamic recrystallization. Additionally, the response between AZ80 and ZK60 is similar for the same temperature and strain rate, with AZ80 displaying slightly higher strength.

Several laboratory-scale forgings were carried out to aid in the development process for the control arm, as shown in Fig. 2. The Gleeble specimens were 10 mm in diameter by 15 mm length. The "pancake" forgings were 88.9 mm diameter with 133 mm length and the "flatbread" forgings were 63.5 mm diameter by 65 mm. The "coin" forgings were 20 mm diameter by 45 mm length and the T-shape design was selected to produce material flow in two directions. The I-beam was 63.5 mm diameter with 65 mm length and was used to assess underfill, forging defects, and flash formation. All these experiments with tests performed between temperature of
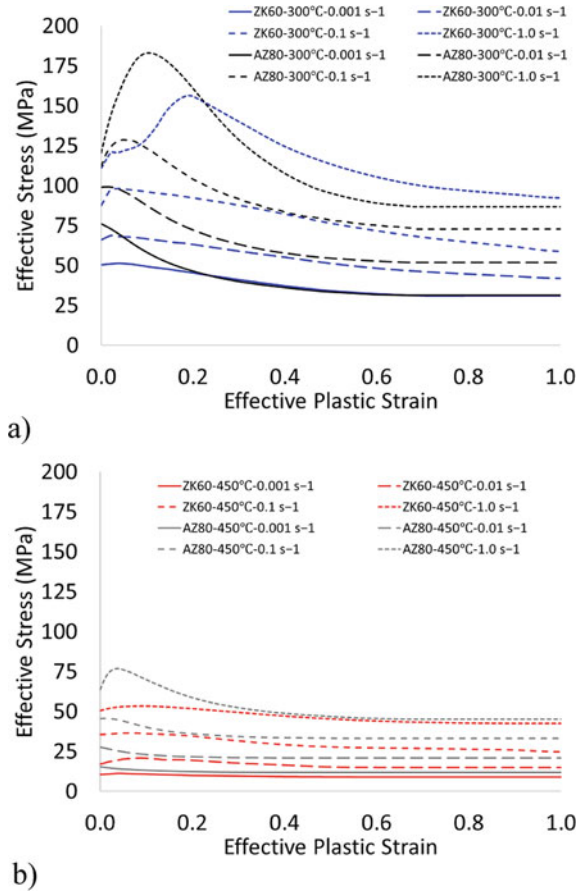
Fig. 1 Stress versus strain response of AZ80 and ZK60 at **a** 300 °C and **b** 450 °C for various strain rates reproduced from data in [10, 11]. (Color figure online)
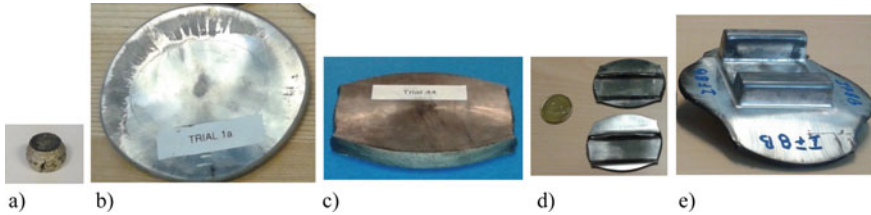
Fig. 2 Laboratory-scale forgings of Mg alloys **a** Gleeble, **b** pancake, **c** flatbread, **d** coin, and **e** I-beam specimens. (Color figure online)
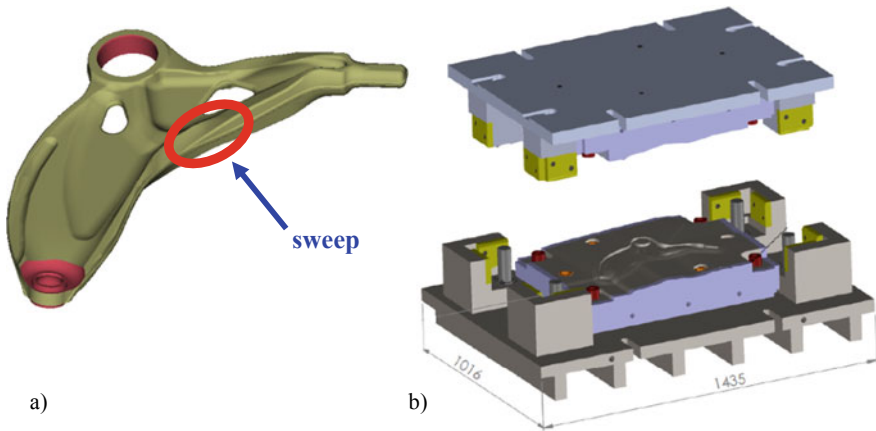
Fig. 3 a Mg control arm geometry and **b** forging die. (Color figure online)

300 °C and 450 °C with strain rates varying from 0.001 s^{-1} to 1 s^{-1} were used to validate the FE models. Details of the experiments are given in [12, 13].

The first step in the design of the control arm was to perform load optimization simulations to ensure that the required stiffness could be achieved. Having produced a preliminary shape of the control arm, the forging die was then designed. Consideration was given to the parting line, die side thrust, corner radii, fillet radii, ribs, draft angles, and flash geometry. Full details of the design are given in [14]. Once the geometry was designed, another structural analysis was performed to estimate the fatigue performance indicating a fatigue critical area in the sweep of the control arm. The geometry of the Mg control arm and the forging die is shown Fig. 3.

The control arms were forged from extruded bar stock 63.5 mm in diameter and about 700 mm in length. The three steps in the forging process involved bending, flattening, and forging as shown in Fig. 4. The operations were all performed at the same temperature and involved pre-soaking the billet to temperature for at least 2 hours prior to each operation. The tooling was at room temperature for the bending and flattening operations, but the rate was sufficient to prevent heat loss during forming. The final forging operation was conducted in a heated die which ensured isothermal forging conditions.

Initially, ZK60 and AZ80 forgings were conducted at 450 °C but it was realized that the control arm would not have the required fatigue resistance. Laboratory-scale testing indicated a significant improvement in fatigue performance when forging was conducted at 250 °C compared to 450 °C, as there was a remarkable strength improvement while still achieving a dynamically recrystallized grain structure. Forging could not be conducted at this temperature for the control arm due to tearing in the bending and flattening operations and over-loading of the hydraulic press in the final forging stage. Forging would need to be conducted at 300 °C to ensure the required fatigue resistance of the control arm was achieved. Figure 5 shows the difference between a ZK60 control arm forged at 450 °C and 300 °C. There is significantly more flash
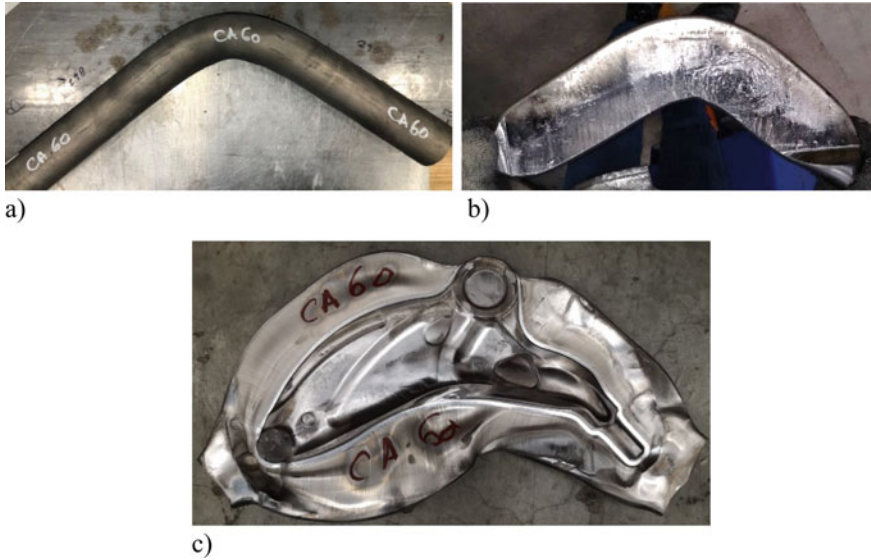
Fig. 4 Operations for forging control arm **a** bending, **b** flattening, and **c** forging. (Color figure online)

Fig. 5 ZK60 control arm forgings at **a** 450 °C and **b** 300 °C. (Color figure online)

formation in the sweep area for the 450 °C forging, in an area where fatigue is critical. The flattening operation was important to ensure that a defect (Fig. 6a) would not present itself in the sweep area during forging and simulation was used to help optimize the flattening operation.

To forge the control arm at 300 °C within a realistic load (that is, the 1500-ton limit of the hydraulic press), it was necessary to greatly reduce the strain rate during forging, as shown in the displacement versus time response seen in Fig. 7. Whereas the ZK60 forgings conducted at 450 °C took 30 s (to achieve final displacement with an additional 30 s hold at 1500-ton), it was approximately 1000 s to forge at 300 °C.
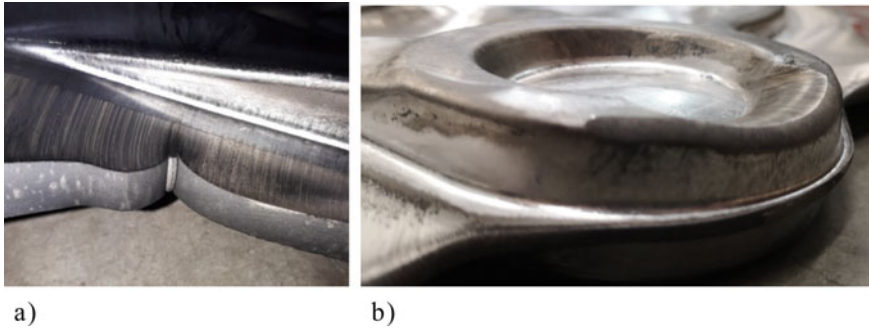
Fig. 6 Defects in forging on control arm **a** defect in flash in a fatigue critical area and **b** underfill of the top bushing. (Color figure online)

Fig. 7 Displacement versus time response during forging of ZK60. (Color figure online)
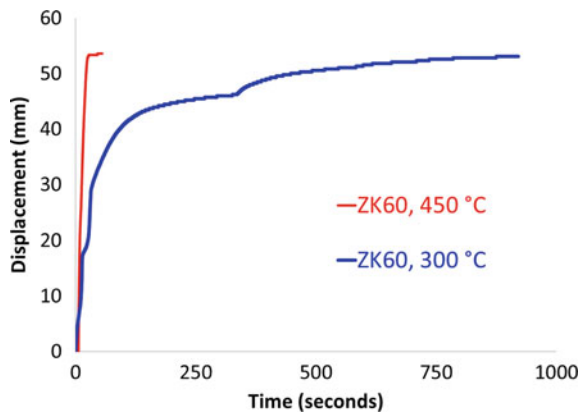
Simulation Models

The models performed with DEFORM3D used a Lagrangian framework with Adaptive Remeshing (AR). The step increment was set to 0.1 mm/step, yielding 635 steps for 63.5 mm displacement which was sufficient to prevent convergence issues and mesh distortion. A simulation of the bending operation (Fig. 4a) was not performed. In other words, the stress and strain state from the bending operation was not carried forward to the flattening simulation. Rather, the starting geometry was the bent bar which was meshed with about 150,000 tetrahedron elements with a mesh size of about 2 mm. The forging die surfaces were considered rigid. Mesh sensitivity studies confirmed that this level of mesh size produced accurate forging results within a reasonable computational time.

The Arbitrary Lagrangian–Eulerian (ALE) simulations were performed in ABAQUS. This technique is mainly a Lagrangian framework in which the mesh moves with the Eulerian framework to allow nodes to move easily along boundaries,
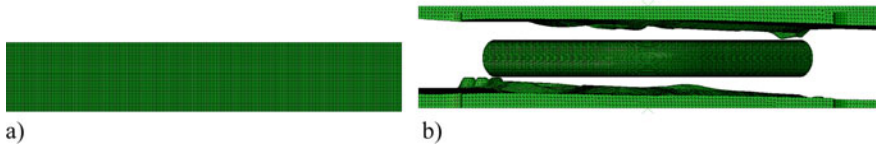
Fig. 8 Combined Eulerian–Lagrangian mesh **a** Eulerian block mesh and **b** solid meshes of upper and lower dies (Lagrangian) and portion of Eulerian mesh with material indicating the initial position of the bar. (Color figure online)

with remeshing between a defined number of steps. The bent bar was modeled with about 57,000 hexahedral elements and about a 2 mm mesh size. The die surfaces were each modeled using about 20,000 four-noded shell elements. Remeshing was specified to occur every 5,000 steps with 10 mesh sweeps in the explicit solver.

The Combined Eulerian–Lagrangian (CEL) technique within ABAQUS was also used for the forging simulations. In this method, a stationary block mesh was used in which the material could flow. The Eulerian block mesh is shown in Fig. 8 and comprised of about 5,000,000 hexahedral elements of 2 mm size. The simplicity of the block mesh was counter-acted by the large number of elements required, and a more optimized mesh could be considered for future work. Unlike the AR and ALE models where rigid and deformable shell elements were satisfactory for the die surfaces, it was necessary to use solid elements, as seen in Fig. 8b, for the forging dies to prevent material escape during contact between the dies and bar. Also shown is the initial bar based on elements in the block mesh for which material is defined. Material only flows within the mesh when it comes into contact with the dies. Only isotropic (von Mises) deformation was used for the CEL simulation but anisotropic material flow should be considered in future work.

All simulations were performed under isothermal conditions. The dies and preform temperature were kept the same and constant during the entire forging process.

The flow stress curves shown in Fig. 1 were used to describe the stress–strain response of ZK60 and AZ80 in the Adaptive Remeshing (AR) simulations performed in DEFORM3D. For wrought magnesium alloys, the intensity of asymmetry and anisotropy decreases with increasing temperature. The Hill48 anisotropic yield function was used in the DEFORM3D models to capture the anisotropic response of the materials. Yield tension/compression symmetry was assumed between the temperatures of 300 °C and 450 °C, though this would not be the case for wrought magnesium alloys deformed at room temperature. Future work should consider comparing the tension and compression responses at elevated temperature to confirm yield symmetry/asymmetry.

The Hill48 yield function is given by

$$f(\sigma) = \sqrt{F(\sigma_{22} - \sigma_{33})^2 + G(\sigma_{33} - \sigma_{11})^2 + H(\sigma_{11} - \sigma_{22})^2 + 2L\sigma_{23}^2 + 2M\sigma_{31}^2 + 2N\sigma_{12}^2} \qquad (1)$$

where the anisotropy is described by the six coefficients, F, G, H, L, M, and N with $11-$, $22-$, and $33-$ being the extrusion, transverse, and radial directions, respectively. This model has been used to model the anisotropic response of wrought AZ80 by Kobold et al. [6]. In the current work, the uniaxial compression tests were used to define F, G, and H. Shear hat tests [15] were performed to generate data for the shear coefficients L, M, and N. Shear hat tests were performed on the Gleeble at strain rates of 0.1 s^{-1} and 1 s^{-1} at multiple temperatures for AZ80 and ZK60 alloys. The shear hat geometry and force versus displacement response of an AZ80 specimen performed at 300 °C at 1 s^{-1} are shown in Fig. 9 [13].

The resulting coefficients for AZ80 at 300 °C at 1 s^{-1} were $F = 0.413$, $G = 0.413$, $H = 0.705$, $L = 1.45$, $M = 1.45$, and $N = 1.82$ [13]. The resulting anisotropic yield function is compared to the isotropic (von Mises) yield response in Fig. 10.
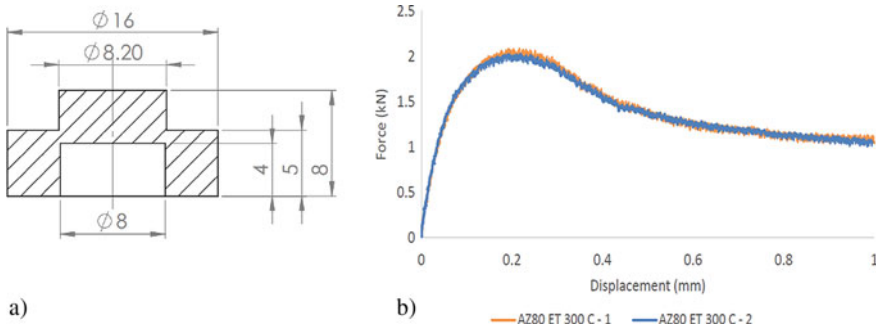
Fig. 9 **a** Shear hat test geometry and **b** force versus displacement response of AZ80 at an Extrusion Temperature (ET) of 300 °C and a strain rate of 1 s^{-1} [13]. (Color figure online)

Fig. 10 Comparison of isotropic and anisotropic yield surfaces for AZ80 at 300 °C ($\sigma_{33} = 0$, $\sigma_{12} = 0$, $\sigma_{23} = 0$, $\sigma_{31} = 0$). (Color figure online)
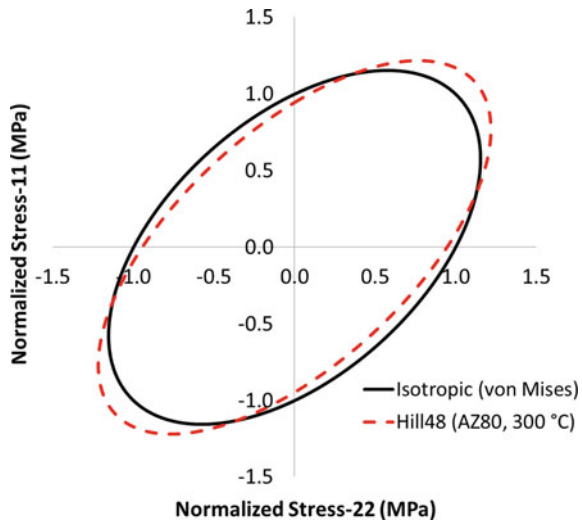
As mentioned above, yield symmetry (the same response in tension and compression) was assumed. Under planar loading conditions, there is only a small difference between the isotropic and anisotropic responses. There were slight differences in the anisotropic flow response for AZ80 and ZK60 between 300 °C and 450 °C and strain rates between 0.1 s^{-1} and 1 s^{-1}. Consequently, the coefficients for AZ80 at 300 °C and 1 s^{-1} were deemed sufficient for all temperature and strain-rate ranges considered in the study.

Models for predicting damage during forging simulations are detailed in [16–18]. Rao et al. [16] studied several damage models and concluded that the normalized Cockroft and Latham criterion was among the most reliable models to predict damage. In the DEFORM3D models, failure was modeled using the Cockroft and Latham criterion which is given by

$$\int\limits_{0}^{\bar{\varepsilon}} \frac{\sigma_{\max}}{\tilde{\sigma}} d\bar{\varepsilon} \geq C \tag{2}$$

where σ_{max} is the maximum principal stress, $\tilde{\sigma}$ is the effective stress, and $\bar{\varepsilon}$ is the effective strain. The material has failed when the integral exceeds the critical damage value, C. Xue et al. [18] indicated critical values between 0.26 and 0.46 at 400 ºC for strain rates ranging from 0.001 s^{-1} to 0.1 s^{-1} for AZ80. In the current, it was found that specifying a critical damage value of 0.3 [19] allowed good agreement with experiment for all cases. Although it would be expected that this value would vary slightly for each material with temperature and strain rate, it was the intent to ensure that no damage occurred in the main body of the component during forging and any damage would be limited to the flash region.

Friction plays a role during forging as it can resist flash formation, leading to reduced underfill, but a larger coefficient of friction increases the load required for forging. Reducing the friction coefficient too much may lead to too much flash and underfill. The forgings conducted at 450 °C were conducted with graphite lubricant whereas a graphite/polymer lubricant was used at 300 °C. Ring compression tests [12, 13] were carried out to determine that the coefficients of friction for the graphite and graphite/polymer lubricants were 0.2 and 0.05, respectively.

Forging Simulations

The simulations were validated using the laboratory-scale experiments (Fig. 2). Figure 11 shows the predicted response from an ALE coin forging simulation performed with isotropic deformation and a constant flow stress of 30 MPa. The predicted shape was in reasonable agreement with the experimental for the coin forging. ALE could predict the deformation to high levels of plastic strain (>100%). However, there were convergent issues when simulating the I-beam and control arm
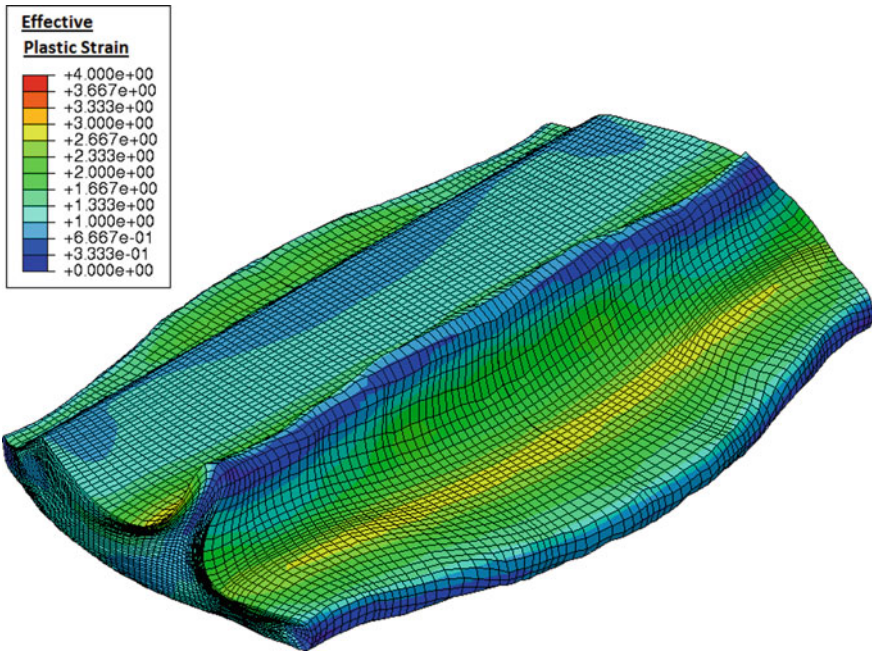
Fig. 11 ALE coin forging with isotropic deformation and flow stress of 30 MPa. (Color figure online)

(with ~60,000 hexahedral elements) forgings with ALE, such that it was not pursued further in this work. An advantage of the ALE technique is that the deformation can be easily tracked using tracer particles by following the movement of the mesh. The complex stress and strain state along a certain particle path can then be used to predict texture, as was the case in [20] for Mg alloy extrusions, and ALE should be considered further in future work.

Figure 12 presents overlays of the predicted (yellow) and experimental shape of a coin forging of ZK60 forged at 450 °C and 0.4 mm/s and an I-beam forged from ZK60 at 450 °C and 0.06 mm/s [12]. The simulations were conducted using the AR technique in DEFORM3D and show good agreement with the measured shape.

The load versus displacement responses predicted from AR simulations considering isotropic (von Mises) and anisotropic (Hill48) deformation for ZK60 coin forgings at 450 °C and 0.4 mm/s are compared with the measured response in Fig. 13 [12]. The final load predicted for the anisotropic simulation is in better agreement with the final load measured, whereas during forging the isotropic response is in better agreement with the measured response. This suggests that using anisotropic material behavior will result in slightly improved predictions of the forging load required.

To assess the influence of temperature on forging of the control arm, AR simulations were performed with AZ80 material properties in the isotropic condition, using a friction coefficient of 0.2 and a temperature of either 350 °C or 400 °C at $1\ s^{-1}$.
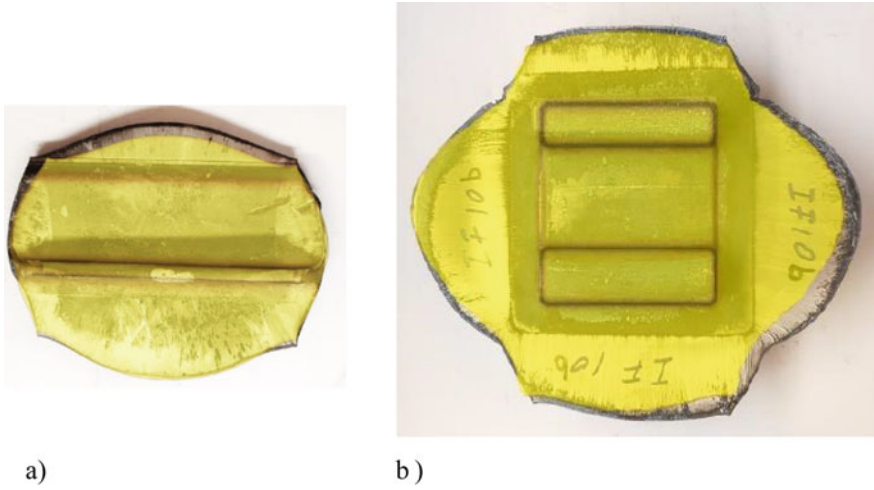
Fig. 12 Overlap of measured and predicted shapes (yellow) for **a** coin forging of ZK60 at 450 °C and 0.4 mm/s and **b** I-beam of ZK60, 0.06 mm/s, 450 °C [12]. (Color figure online)
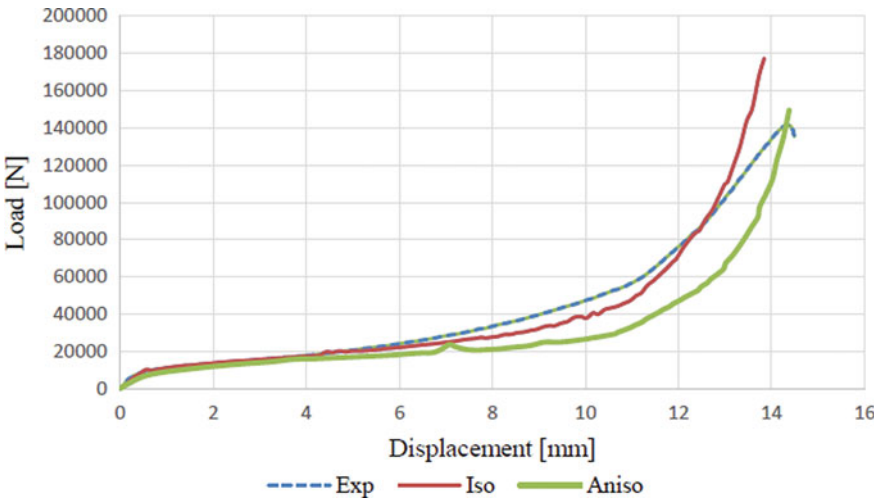
Fig. 13 Comparison of load versus displacement response between experiment, isotropic (von Mises) and anisotropic behavior [12]; ZK60 coin forging conducted at 450 °C and 0.4 mm/s. (Color figure online)

The flow stress responses at each temperature and the corresponding load prediction for forging the control arm are shown in Fig. 14 [13]. The results show that even a small temperature difference of 50 °C can significantly influence the load required for forging, with 2,270 tons predicted at the higher temperature and 4,820 tons required
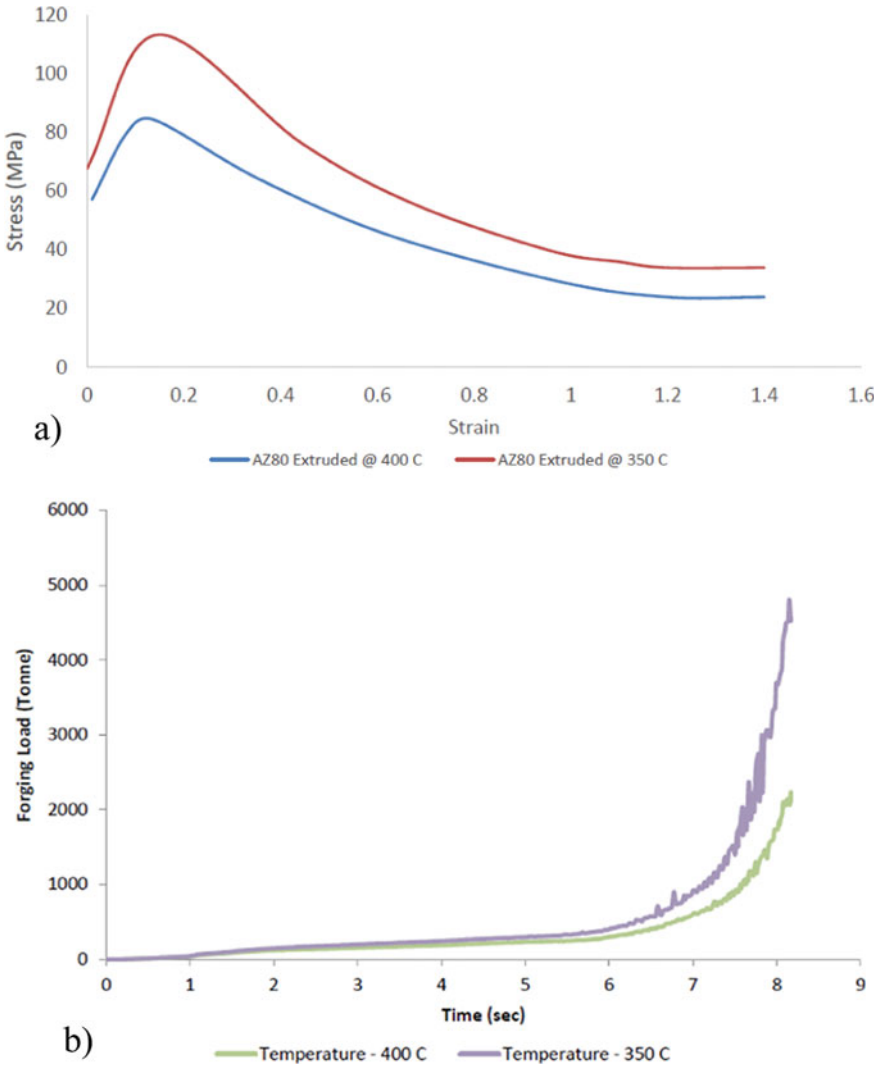
Fig. 14 **a** Flow response of AZ80 at 350 °C and 400 °C at 1 s^{-1} and **b** corresponding forging load response [13]. (Color figure online)

at the lower temperature. To reduce the load required at 300 °C to realistic values, it was necessary to reduce strain rate.

Another way to reduce the forging load is to reduce the coefficient of friction, but if friction is reduced too much there could be increased flash formation and underfill. Figure 15 shows the forging pattern predicted from CEL simulations performed with a friction coefficient of either 0.2 or 0.05, with the corresponding load response shown in Fig. 16. The simulations were performed based on the flow response of
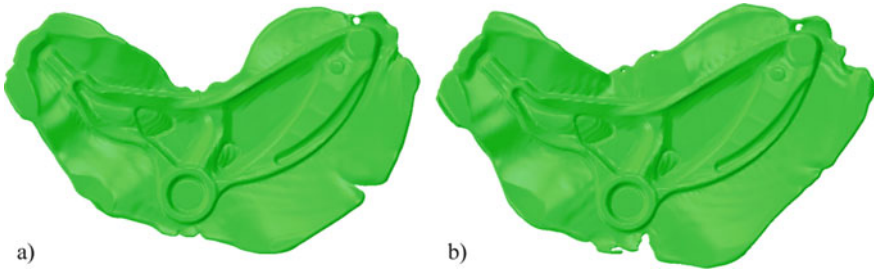
Fig. 15 Predicted influence from CEL forging simulations of friction for coefficient of friction of **a** 0.2 and **b** 0.05. (Color figure online)

Fig. 16 Predicted influence of friction on forging load response of control arm. (Color figure online)
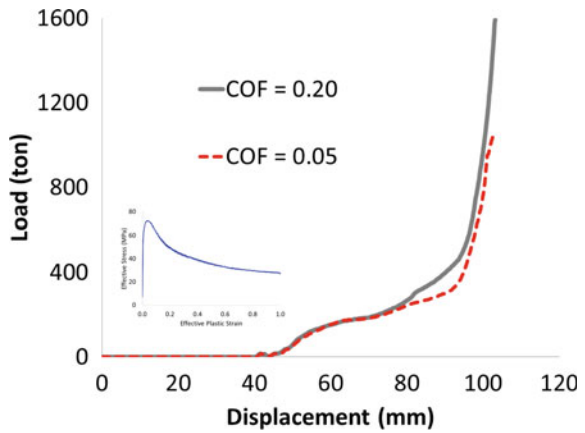
AZ80 at 400 °C and 0.1 s^{-1} which is also shown in the figure. The higher coefficient of friction leads to less flash formation in the sweep, a fatigue critical area, of the control arm. Though the effect of friction is seen in the load response only near the end of the forging process, the forging load required is significantly reduced for the lower friction coefficient with a value of 1,050 tons compared to 1,590 tons for the larger value. A friction coefficient of 0.05 was achieved using a graphite/polymer lubricant compared to only graphite lubricant with a value of 0.2. The forging die was designed using simulations with a friction coefficient of 0.2.

In addition to reducing the strain rate and coefficient of friction, it is needed to be ensured that there was minimal underfill and no damage in the control arm. This was accomplished by performing several AR simulations with the most accurate material description (strain rate and anisotropy) to optimize the preform shape (Fig. 4a and b) to ensure the final control arm was defect free. An advantage of DEFORM3D was the ability to track the fold line formation during forging which occurred when two separate material surfaces came together. This was a fatigue critical region and it needed to be ensured that the fold line was pushed out of the sweep (Fig. 3a). The progression of the fold is indicated in Fig. 17.
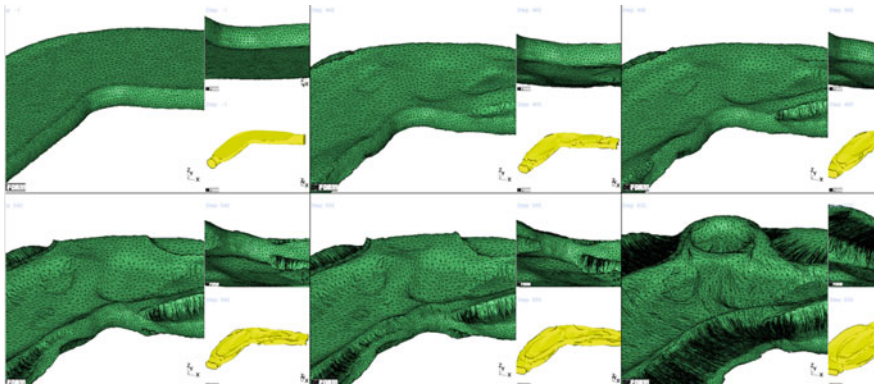
Fig. 17 Predicted progression of fold line in the sweep region of the control arm. (Color figure online)

A contour plot of the damage is shown in Fig. 18 indicating that there was no damage in the main body of the control arm (damage level < 0.15) and that the most likely locations of damage were in the flash.

The final simulation of the ZK60 control arm forged at 300 °C with a displacement versus time profile given in Fig. 7 is shown in Fig. 19a. The corresponding ZK60 forging is shown in Fig. 19b (also shown in Fig. 5b and Fig. 6b). It can be seen that the flash geometry was captured pretty well, except with an over prediction of flash at the top bushing.
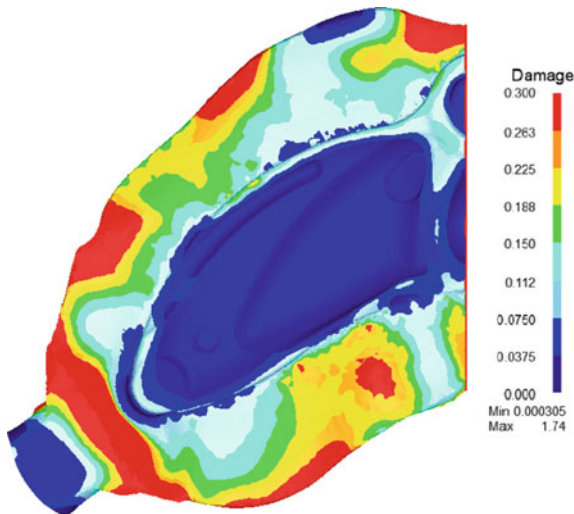
Fig. 18 Predicted influence of friction on forging load response of control arm. (Color figure online)
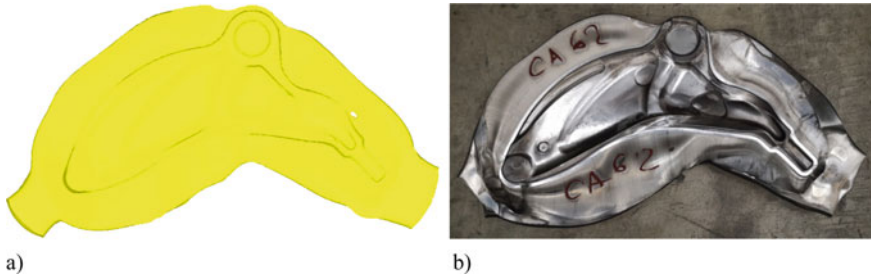
Fig. 19 Predicted influence of friction on forging load response of control arm. (Color figure online)

There are a few factors that might explain the differences between simulation and experiment. During experimental forging there were small temperature differences (± 10 °C) that were not captured in the isothermal simulations. As shown above, even small temperature difference can influence the forging response of magnesium alloys. The simulations also assumed a constant friction coefficient, while in forging trials this could vary based on the amount of graphite/polymer lubricant applied, sliding distance, and pressure. Additionally, the assumption of one set of parameters for anisotropic deformation at all strain rates might have a slight influence on the results.

Conclusions

Three finite element simulation methods were studied to capture the large level of strain induced during warm forging of magnesium alloys, including Adaptive Remeshing (AR), Arbitrary Lagrangian–Eulerian (ALE), and Combined Eulerian–Lagrangian (CEL). All three methods accurately captured the response of simple forging geometries. The pronounced influence of temperature and strain rate for magnesium alloys became apparent during the simulations. As the complexity of the forging geometry increased, the AR and CEL techniques were shown to produce more accurate predictions. The most advanced simulations incorporating temperature, strain rate, and anisotropic plastic deformation dependence were carried out using the AR technique. To forge a control arm with the required fatigue resistance, it was necessary to forge at 300 °C. A slow strain rate is needed to be used to prevent unrealistically large forging loads. The AR and CEL simulation techniques aided in the design of the final forging process. The AR technique proved reliable for capturing defects and ensures the prototype control arm was defect free. The combined use of simulation and experiment reduced the development time and cost of the prototype control arm. The material models presented for magnesium alloys can also be used for simulation of manufacturing processes of other components.

References

1. Skubisz P, Sinczak J, Bednarek S (2006) Forgeability of Mg-Al-Zn magnesium alloys in hot and warm closed die forging. J Mater Process Technol 177:210–213
2. Kim WJ, Lee HW, Park JP, Kim MG, Yoon US (2009) Forging of Mg-3Al-1Zn-1Ca alloy prepared by high-frequency electromagnetic casting. Mater Des 30:4120–4125
3. Pepelnjak T, Werkhoven R, Kobold D, Kuzman K (2010) Analysis of warm magnesium forging in digital environment. J Technol Plasticity. 35:13–23
4. Rap KP, Prasad YVRK, Suresh K (2011) Materials modeling and simulation of isothermal forging of rolled AZ31B magnesium alloy: anisotropy of flow. Mater Des 32:2545–2553
5. Shan D, Xu W, Han X, Huang X (2012) Study on isothermal precision forging process of rare earth intensifying magnesium alloy. Mater Sci Eng, B 177:1698–1702
6. Kobold D, Gantar G, Pepelnjak T (2012) Finite element analysis of magnesium AZ80 wrought alloy anisotropic behavior during warm forging. Mechanika 18:251–258
7. Yoon J, Lee S (2015) Warm forging of magnesium AZ80 alloy for the control arm in an automobile. J Automobile Eng. 229:1732–1738
8. Karparvarfard SMH, Shaha SK, Behravesh SB, Jahed H, Williams BW (2016) Microstructure, texture and mechanical behavior characterization of hot forged cast ZK60 magnesium alloy. J Mater Sci Technol 33:907–918
9. Gryguc A, Shaha SK, Behravesh SB, Jahed H, Wells M, Williams B, Su X (2017) Monotonic and cyclic behaviour of cast and cast-forged AZ80 Mg. Int J Fatigue 104:136–149
10. Hadadzadeh A, Wells MA, Shaha SK, Jahed H, Williams BW (2017) Role of compression direction on recrystallization behavior and texture evolution during hot deformation of extruded ZK60 magnesium alloy. J Alloy Compd 702:274–289
11. Prakash P, Toscano D, Shaha SK, Wells MA, Jahed H, Williams BW (2020) Effect of temperature on the hot deformation behavior of AZ80 magnesium alloy. Mater Sci Eng, a. https://doi.org/10.1016/j.msea.2020.139923
12. Yu G (2016) Forging specimen design for magnesium alloys. M.A.Sc. thesis, University of Waterloo
13. Paracha T (2018) Modelling of the forging process for a magnesium alloy automotive control Arm. M.A.Sc. thesis, University of Waterloo
14. Kodippili TA (2018) Hot forging tool design for a magnesium alloy front lower control Arm. M.A.Sc. thesis, University of Waterloo
15. Peirs J, Verleysen P, Degrieck J, Coghe F (2010) The use of hat-shaped specimens to study the high strain rate shear behavior of Ti-6Al-4V. Int J Impact Eng 37:703–714
16. Rao AV, Ramakrishnan N, Kumar RK (2003) A comparative evaluation of the theoretical failure criteria for workability in cold forging. J Mater Process Technol 142:29–42
17. Kim SW, Lee YS (2014) Comparative study on failure prediction in warm forming processes of Mg alloys sheet by the FEM and ductile fracture criteria. Metall and Mater Trans B 45:445–453
18. Xue Y, Zhang ZM, Wu YJ (2013) Study on critical damage factor and the constitutive model including dynamic recrystallization softening of AZ80 magnesium alloy. Sci Sinter 45:199–208
19. Xia YF, Quan GZ, Zhou J (2010) Effects of temperature and strain rate on critical damage value of AZ80 magnesium alloy Transactions of Nonferrous Metals Society of China, 20:580–583.
20. Williams, BW, Agnew SR, Klein RW, McKinley J (2015) Development of thin-walled magnesium alloy extrusions for improved crash performance based upon texture control. In: Magnesium technology 2015, The minerals, metals & materials society pp 203–208

Part VII
Structural, Functional, Biomedical, and Energy Applications

Kink Deformation Dynamics of LPSO Alloy from the Experimental Viewpoint of Multilayer Structure Deformation

Kazuya Aizawa, Wu Gong, Stefanus Harjo, and Takuro Kawasaki

Abstract The kink deformation dynamics of a unidirectionally solidified 18R LPSO alloy, which is a typical stacking material of hard and soft layers, was investigated via hybrid in situ pulsed-neutron diffraction combined with acoustic emission (AE) measurement at room temperature under the condition of mainly activating a kink deformation mode. It was found that distinctive kink formation starts after the macroscopic yield point from the evolution of neutron diffraction peaks of several lattice planes, whereas the angles between the formed kink planes and the initial undeformed planes have a broad range from the basal plane distribution after kink deformation. Additionally, the size of the formed is widely distributed from the interpretation of the absolute energy distribution of the detected AE signal. The study revealed that kink formation does not occur randomly but follows a specific statistical distribution expressed by the waiting time of the AE signal event. We propose that one possible kink formation mechanism is the incremental deformation theory that considers the effect of initial internal stress. This theory is based on the rheological treatment of stacking hard and soft layers of arbitrary mutual fractions. It may account for the experimental characteristics of the formation of ridge-type or wedge-type kinks and sinusoidal kinks of various sizes.

Keywords LPSO · Neutron diffraction · Acoustic emission

Introduction

When Mg-based LPSO alloy, which is a stacking material of hard and soft layers, is introduced into the kink structure by hot extrusion, it exhibits both high strength and good ductility compared with common commercial Mg alloys [1]. Thus, it is expected to serve as a novel lightweight structural material. However, the reason for its strength

K. Aizawa (✉) · S. Harjo · T. Kawasaki
J-PARC Center, Japan Atomic Energy Agency, Tokai, Ibaraki, Japan
e-mail: aizawa.kazuya@jaea.go.jp

W. Gong
Elements Strategy Initiative for Structural Materials, Kyoto University, Kyoto, Japan

and its mechanism is not fully understood despite numerous studies [2, 3]. Various kinks have been observed in different materials, including metals [4], minerals [5], ceramics [6], and polymers [7]. These include ortho-type (kink band), wedge-type (conjugated kink band), ridge-type, and wavy (sinusoidal) kinks. Particularly, ridge-type and wavy kinks are dominant in Mg-based LPSO alloys. To determine the cause of the high strength in Mg-based LPSO alloys with kink structures, it is important to determine the kink formation mechanism by introducing effective kinks. Therefore, evaluating the dynamics of kink formation is indispensable. Kink formation dynamics in a unidirectionally solidified 18R single-phase Mg-based LPSO alloy [8], which is a typical and simple LPSO structure system, and has been observed to be intermittent rather than continuous [9]. Hence, it is useful to use acoustic emission (AE) measurements to detect the dynamic changes in microscopic structures inside bulk samples by identifying elastic waves generated by microscopic deformation, combined with crystal structural monitoring techniques, such as diffraction of the bulk sample. In this paper, we mainly report the statistical characteristics of kink formation dynamics based on the analysis of AE signal data obtained by hybrid in situ neutron diffraction measurements under compressive stress loading.

Experimental

Hybrid in situ pulsed-neutron diffraction measurements under compressive loading at room temperature were performed by TAKUMI, BL19 [10] in MLF, J-PARC. Here, "Hybrid" implies that neutron diffraction measurements and AE signal detection are performed simultaneously. An AE system (1283 USB AE Node, Micro 30) by Physical Acoustics Corporation, USA was used. A unidirectional solidified 18R LPSO alloy, $Mg_{85}Zn_6Y_9$, [8] was used as a sample. Here, "unidirectional solidified" means that the c-axis of crystal plates is aligned perpendicular to a growth direction. The obtained alloy was machined into a cylindrical shape of 8 mm diameter and 16 mm length, with the cylindrical axis perpendicular to the crystallographic *c*-axis of the LPSO structure. The sample was mounted, with the cylindrical axis of 45° to the incident neutron beam direction, into a loading machine at room temperature. Pulsed-neutron diffractions of several planes in the axial and radial directions of the sample were collected simultaneously using a pair of neutron detector banks. The AE sensor was attached to a sample attachment of the loading machine several centimeters apart from the sample end. Compressive stress was loaded up to approximately 250 MPa with a strain rate of approximately 4.2×10^{-5}/s and a strain of up to -0.2 along the cylindrical axis. A strain gage attached to the sample surface was used for macroscopic strain monitoring. Neutron diffraction data were obtained by the event record technique and converted to a diffraction pattern ranging from 0.7 to 3.2 nm. The AE signal was measured using a threshold technique that collected various data, such as the waveform of the elastic wave, detection time for event occurrence, and absolute energy of elastic wave. In this study, we primarily used the detection time and absolute energy to perform analysis.

Results

It is known that the experimental condition primarily causes kink deformation as a deformation mode [8]. This study confirmed its behavior by neutron diffraction evolution, as shown in Fig. 1. The left vertical axes correspond to the d-spacing of the lattice, whereas the right vertical axes correspond to the macroscopic stress for both Fig. 1a, b. The horizontal axes correspond to the macroscopic strain for both Fig. 1a, b. The lattice planes were indexed using the crystal structure of $P3_212$, $a = 1.11$ nm, $c = 4.7$ nm [11]. Figure 1a shows the evolution in which the $(60\bar{6}0)$ diffraction peak disappeared and the $(60\bar{6}18)$ peak appeared in the axial direction after the yield point. In contrast, (0 0 0 18), $(4\bar{2}\bar{2}8)$, and $(4\bar{2}\bar{2}10)$ diffraction peaks disappeared in the radial direction (Fig. 1b). These observations indicate that crystal rotation occurred after the yield point, which corresponded to the beginning of the distinct kink formation mode. Figure 2 shows the pole figure of the (0 0 0 18) plane in both the initial and fully deformed states. The (0 0 0 18) plane is aligned to the radial direction before loading. After full loading and formation of the kink structure,
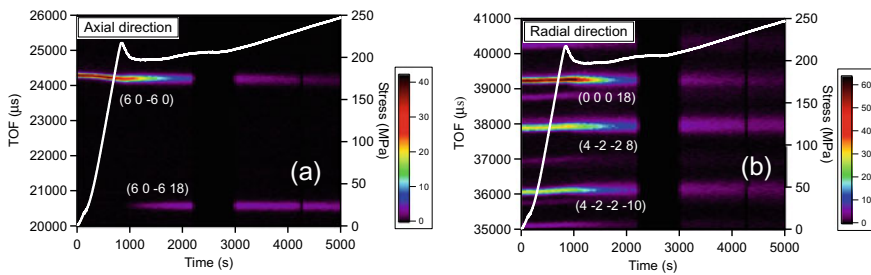
Fig. 1 Evolutions of neutron diffraction peaks **a** axial direction, **b** radial direction. (Color figure online)
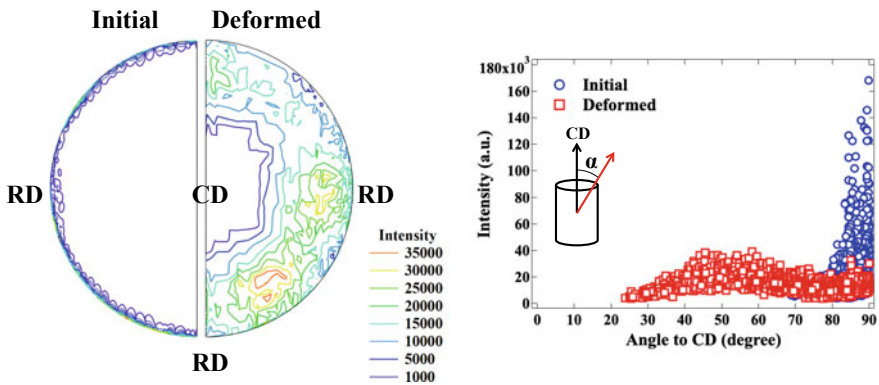
Fig. 2 Pole figure of (0 0 0 18) plane. (Color figure online)

the direction of the (0 0 0 18) plane ranged broadly from approximately 30° to 90° with a weak peak. These features indicate that the formed kinks have various angles between the formed kink planes and the initial undeformed planes.

Figure 3 shows the frequency distribution for the absolute energy of the detected AE signals after the yield point, indicating that the distribution varies widely over eight digits and ranging from six digits in the energy scale. Because the absolute energy is related to the deformation size, this distribution implies that the kink formation mechanism allows for various kink sizes. Another characteristic is power law-like behavior over eight digits in the high-energy region. This implies that kink size is scale free; more precisely, there is no characteristic scale for kink size.

Therefore, the main process of the formation mechanism may not include the characteristic size. This feature justifies a continuum deformation treatment, which we will discuss later. Furthermore, there is a flat part in the lower energy region, which corresponds to smaller deformation. This implies that kink deformation of the small scale does not obey the abovementioned continuum treatment. Figure 4 shows the frequency distribution of intervals of two adjacent AE signal detection times, namely, the waiting time associated with kink deformation in the uniaxial compressive loading of the sample. The vertical scale in Fig. 4a is linear, whereas that of Fig. 4b is logarithmic. If kink formation occurs randomly following the Poisson process, the frequency distribution of the waiting time becomes an exponential distribution. However, the distribution shape in Fig. 3 is significantly different from that of the exponential distribution. This implies that kink deformation does not occur randomly for the experimental loading condition. In contrast, this frequency distribution has the following remarkable features:

Fig. 3 Absolute energy distribution of the detected AE signal. (Color figure online)
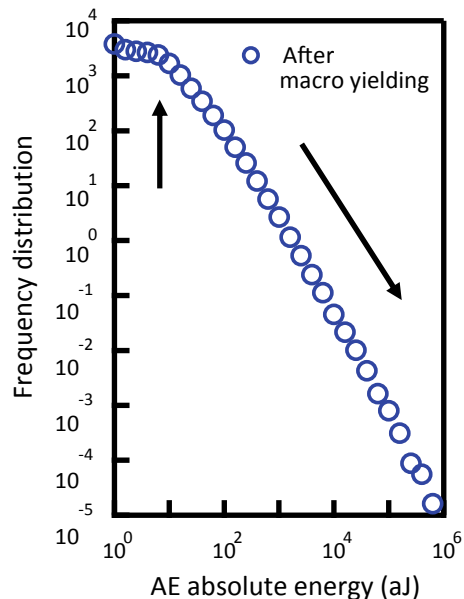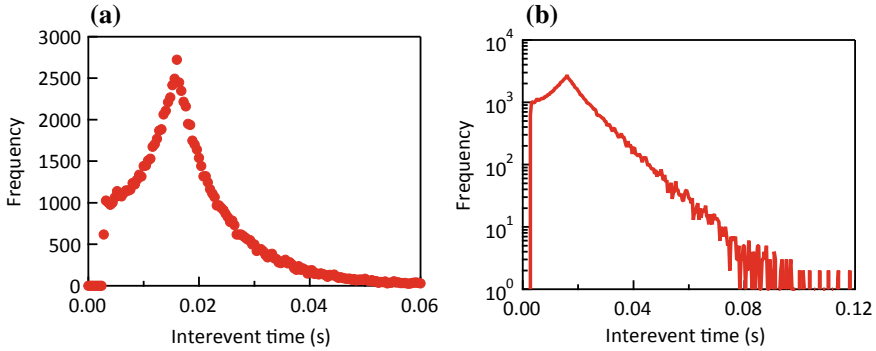
Fig. 4 Frequency distribution of waiting time of the AE signal **a** linear scale, **b** log scale. (Color figure online)

- The distribution has a sharp peak.
- The distribution is skewed (asymmetrical).
- The distribution has a heavy tail (long tail).

These are characteristics of a stable distribution (α Lévy stable distribution). If we adopt this distribution as a frequency distribution of waiting time, we can interpret it as a unified distribution, namely, the same dynamics for all kink formations. The stable distribution is defined as follows: assume x_1 and x_2 are independent copies of random variable x. Random variable x is stable when random variable $ax_1 + bx_2$ (a and b are constants) has the same distribution as $cx + d$ (c and d are constants). There is no analytical expression of the probability density function of a stable distribution, and it is expressed by the Fourier transform of the characteristic function as follows:

$$f(x) = \frac{1}{2\pi} \int_{-\infty}^{\infty} \varphi(t) e^{-ixt} dt \tag{1}$$

The characteristic function is expressed using four parameters $\alpha, \beta, \chi, \delta$ as follows:

$$\varphi(z) = exp\left[i\delta z - \gamma |z|^{\alpha} \{1 + \beta sgn(z)\omega(z, \alpha)\}\right] \tag{2}$$

$$\omega(z, \alpha) = tan\frac{\pi\alpha}{2}(\alpha \neq 1) \tag{3}$$

$$\omega(z, \alpha) = \frac{2}{\pi}log|z|(\alpha = 1) \tag{4}$$

$$0 < \alpha \leq 2, -1 \leq \beta \leq 1, \gamma > 1 \tag{5}$$

However, to obtain a probability density function by determining four parameters of the characteristic function of a stable distribution is difficult, and we did not obtain it. We propose that the frequency distribution of the kink formation statistics is expressed by a stable distribution.

Discussion

There are several theories about the kink formation mechanism in metallurgy, including the Hess and Barrett theory [12]. This theory is based on dislocation movement and offers a microscopic explanation of the formation mechanism of a macroscopic kink. Starting from the Euler buckling of an elongated rod, an ortho-type kink is formed by the generation of vertically aligned positive and negative edge dislocation pairs and dislocation multiplication. In the case of ridge-type kink formation, opposite ortho-type kinks of the same size are formed almost simultaneously and coalesce. However, when the theory is applied to the kink deformation in the LPSO alloy, its validity becomes unclear because the kink of the LPSO alloy observes at arbitrary positions rather than special one which is theoretical expectations. There is ambiguity in the special formation account of ridge-type kinks, and, by experiment, the formed kink size has a wide distribution. Another theory, proposed by Frank and Stroh [13], does not consider initiation of kink formation. First, this theory initially assumes the presence of an elliptic kink region and considers its growth to form a kink band. The elliptical shape is attributed to the effect of the attractive force between both ends of the parallel positive and negative dislocation pair. Similar to the theory by Hess and Barrett, the basis for the initial kink as applied to the kink formation in the LPSO alloy is unclear. These theories are based on dislocation theory. In contrast, continuum deformation in the mesoscale obtained from AE data interpretation is useful from the viewpoint of general deformation features.

Furthermore, incremental deformation theory [14, 15] introduces a type of continuum mechanics applied in geology. This theory focuses on the instability of the averaged rheological properties of a homogeneous anisotropic material stacking of hard and soft layers in the presence of internal stress. In this theory, the deformation behavior is described as follows [14, 15]:

$$(L - P)\frac{\partial^4 \Phi}{\partial x^4} + 2(2M - L)\frac{\partial^4 \Phi}{\partial x^2 \partial y^2} + L\frac{\partial^4 \Phi}{\partial y^4} = 0 \tag{6}$$

$$M = N + P/4 \tag{7}$$

$$L = Q + P/2 \tag{8}$$

$$P = (S_{22} - S_{11}) \tag{9}$$

where Φ is the displacement function, N is the compressive modulus, Q is the shear modulus, and S_{11} and S_{22} are the initial stresses. The general solutions of Eq. (6) can be expressed as follows:

$$\Phi = f_1(x + \xi_1 y) + f_2(x - \xi_1 y) + f_3(x + \xi_2 y) + f_4(x - \xi_2 y) \qquad (10)$$

where ξ is arbitrary constant and f_1, f_2, f_3, and f_4 are arbitrary functions.

The most remarkable feature is that instabilities are dependent on L, M, and P for real ξ via the following equation:

$$L\xi^4 + 2(2M - L)\xi^2 + (L - P) = 0. \qquad (11)$$

Two instabilities—type 1 and type 2—are under the conditions given below:

$$M/L > \frac{1}{2};\ P/L > 1 \text{type 1} \qquad (12)$$

$$M/L < \frac{1}{2};\ 1 > P/L > 4M/L(1 - M/L)\text{type 2} \qquad (13)$$

In the case of type 1 instability, sinusoidal fluctuations occurs. In contrast, the kink band structure is produced in type 2 instability. Moreover, if layer fluctuation exists in some layered regions, it may form wedge-type kinks via similar mechanisms of type 2 instability. Intermittency and size dependence for the formation of wedge-type kinks are ensured by numerous fluctuation regions and sample sizes. Our results support these findings.

Conclusion

We performed hybrid in situ pulsed-neutron diffraction for a unidirectional solidificated 18R LPSO alloy. We determined the start of the distinct kink formation and the dependence of the angle between the kink plane and the initial undeformed direction from neutron diffraction. The distribution of absolute energy and waiting time of AE signal events were also determined. One possible kink deformation mechanism in the 18R LPSO alloy is a mechanism explained by the incremental deformation theory with initial internal stress as proposed by Biot.

References

1. Kawamura Y, Hayashi K, Inoue A, Masumoto T (2001) Rapidly solidified powder metallurgy $Mg_{97}Zn_1Y_2$ alloys with excellent tensile yield strength above 600 MPa. Mater Trans 42:1172–1176
2. Hagihara K, Yamasaki M, Honnami M, Izuno H, Tane M, Nakano T, Kawamura Y (2015) Crystallographic nature of deformation bands shown in Zn and Mg-based long-period stacking ordered (LPSO) phase. Philos Mag 95:132–157
3. Hagihara K, Li Z, Yamasaki M, Kawamura Y, Nakano T (2019) Strengthening mechanisms acting in extruded Mg-based long-period stacking ordered (LPSO)-phase alloys. Acta Mater 163:226–239
4. Orowan E (1942) A type of plastic deformation new in metals. Nature 149:643–644
5. Mügge O (1898) Über Translationen und verwandte Erscheinungen in Krystallen. Neues Jahrb Mineral Geol Palaeontol 1:71–158
6. Barsoum MW, Farber L, El-Raghy T (1999) Dislocations, kink bands, and room-temperature plasticity of Ti_3SiC_2. Metall Mater Trans A 30:1727–1738
7. Robertson RE (1969) Formation of kink bands in oriented polymers. J Polym Sci A-2 Polym Phys 7:1315–1328
8. Hagihara K, Yokotani N, Umakoshi Y (2010) Plastic deformation behavior of Mg12YZn with 18R long-period stacking ordered structure. Intermetallics 18:267–276
9. Drozdenko D, Máthis K, Harjo S, Gong W, Aizawa K, Yamasaki M (2019). Investigation of the evolution of the microstructure in the directionally solidified long-period stacking-ordered (LPSO) magnesium alloy as a function of the temperature. In: Joshi V, Jordon J, Orlov D, Neelameggham N (eds) Magnesium technology 2019. Springer, Cham
10. Harjo S, Ito T, Aizawa K, Arima H, Abe J, Moriai A, Iwahashi T, Kamiyama T (2011) Current status of engineering materials diffractometer at J-PARC. Mater Sci Forum 681:443–448
11. Egusa D, Abe E (2012) The structure of long period stacking/order Mg–Zn–RE phases with extended non-stoichiometry ranges. Acta Mater 60:166–178
12. Hess JB, Barrett CS (1949) Structure and nature of kink bands in zinc. Trans AIME 185:599–605
13. Frank FC, Stroh AN (1952) On the theory of kinking. Phys Soc B 65:811–821
14. Biot MA (1965) Mechanics of incremental deformations. Wiley, New York
15. Cobbold PR, Cosgrove JW, Summers JM (1971) Development of internal structures in deformed anisotropic rocks. Tectonophysics 12:23–53

Part VIII
Advanced Characterization and Fundamental Theories

The Influence of Recrystallization on the Temperature Dependence of Twinning in Magnesium Alloys

Abhijit Brahme, Kaan Inal, Raja K. Mishra, Amir Farzadfar, and Etienne Martin

Abstract The nucleation of twin formation, an important mechanism in the deformation of magnesium alloys, is still an active topic of discussion. The twin formation is generally tied to the amount of shear stress resolved on the twin system. This work sheds light on the formation of twins by studying the deformation in three different Mg alloys. The alloys are deformed at 350C. The flow curves show the signature of dynamic recrystallization in all the alloys. The resultant microstructures are studied optically and using electron backscatter diffraction maps. The results clearly show the formation of dynamic recrystallized (DRX) grains is primarily located inside the twins. The volume fraction of DRX and twins is calculated using ASTM E562-02 standard from the optical micrographs. The volume fraction of DRX and twins thus calculated shows inverse correlation. Thus, indicating that the increase in the DRX leads to decrease in the amount of twinning by reduction in the conditions conducive for twin formation.

Keywords Magnesium · Twinning and recrystallization

Introduction

Mechanical twinning plays an important role in the deformation of magnesium alloys [1]. It facilitates accommodation of deformation along the c-axis, especially when the pyramidal slip is inactive [2], since all of the easy slip directions, $< 11\bar{2}0 >$, are perpendicular to the c-axis. Twinning in Mg alloys has been studied by various

A. Brahme · K. Inal · R. K. Mishra
Department of Mechanical Engineering, University of Waterloo, 200 University Avenue West, Waterloo, ON N2L 3G1, Canada

A. Farzadfar
Corning Incorporated, One Riverfront Plaza, Corning, NY 14831, USA

E. Martin (✉)
Department of Mechanical Engineering, Chemin de Polytechnique, École Polytechnique, Montreal, QC T3 1J4, Canada
e-mail: etienne.martin@polymtl.ca

257

researchers over the past few decades, yet there is no clear consensus on the exact criterion for the inception/nucleation of twins. There has been much debate on what yield criterion is appropriate for twinning. Most analytical treatments assume a critical shear stress criterion similar to Schmid's law for slip [2–4]. These look at the resolved shear stress on the twinning direction and based on a threshold decides if the particular twin system will be activated or not. Several authors have demonstrated a weak relationship if any between the Schmid factor and twinning [5–8]. Mu et al. [5] showed that the primary twin variant was not the one with the highest Schmid factor rather the one with the most accommodation by the neighboring grains. Lind et al. [8] confirmed this observation on 3D in situ neutron diffraction. Similar conclusions were reported by Pei et al. 2012 and Mishra et al. 2019 on almost no correlation on the volume fraction of twin and the Schmid factor measured from microstructural observations [6, 7]. Moreover, the amount of twinning as reported in multiple studies [9, 10] is strongly temperature dependent while CRSS is usually reported to be temperature independent [11, 12]. Despite the impressive number of publications in this area the CRSS for twinning remains to be established for Mg alloys.

There are several possible mechanisms for twin formation [13, 14]. For all cases, twin nucleation is inhomogeneous and requires stress concentration. One major source of stress concentration arises from dislocation piles-up along the grain boundaries (GB) [15–17]. These sources of stresses can be relaxed by the formation of low-energy dislocation configurations (LEDS) [18]. The formation of LEDS is favored by diffusion and thus temperature. In Mg alloys, the formation of LEDS is important since it leads to continuous dynamic recrystallization (cDRX) [19]. This work discusses the possibility of a new yield criterion for twinning based on the analyses of dynamic recovery and recrystallization. In the proposed research, the temperature dependence of twinning in three different magnesium alloys is linked to their recrystallization behavior.

Experimental Procedure

Three different Mg alloys, Mg-2.Y, Mg-5Zn-2Y, and Mg-2.9Zn, were produced by induction melting. The exact composition of the three alloys can be found here [20]. The as-cast texture of the three alloys was evaluated by XRD using a Bruker D8 diffractometer. Figure 1 shows the typical as-cast random texture obtained from the cast materials. Compression samples were machined with an aspect ratio (h/d) of 1.5, the height, h, of the sample is parallel to the longitudinal direction of the cast rod. Compression tests were performed at 350 °C and at a true strain rate of 1 s^{-1}. The samples were compressed to three strains, half of the peak strain, peak strain, and strain of 1, and they were then water quenched to room temperature. Microstructure analysis of compressed samples was performed by optical microscopy and EBSD using a Hitachi S-3000 FE-SEM. The polished samples were electropolished in 10% Nital solution at 20 V. For optical microscopy, the samples were etched with acetic picral solution.
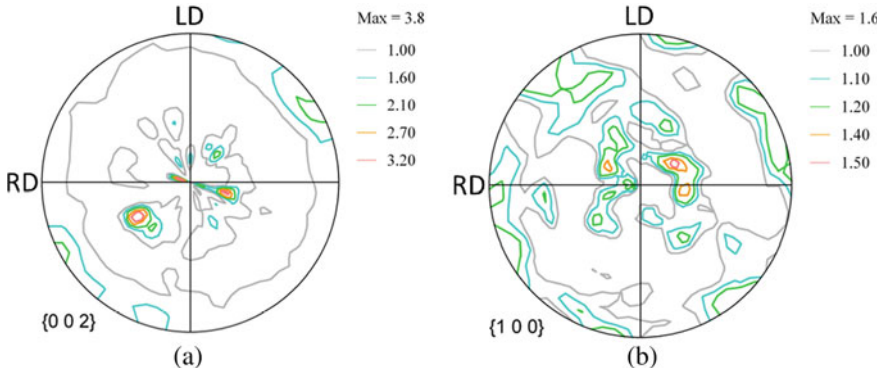
Fig. 1 X-ray {00.2} pole figures representing the initial (as-cast) texture of Mg-2.9Zn alloys. The longitudinal (LD) and radial directions of the cast rod are used as reference frames. (Color figure online)

The volume fractions of twins and recrystallized material were determined using a simple point counting technique (ASTM E562-02). Three to six digital micrographs were taken of each sample at magnifications ranging from 100x to 200X. Next, 31 points by 18 points grid was superimposed on the images. The volume fraction of twin and recrystallized grains was determined by calculating the ratio of the number of points located within such features to the total number of points.

Results and Discussion

The true stress–true strain (σ—ε) curves determined under the present conditions are illustrated in Fig. 2. The three materials show evidence of DRX. The flow stress rises rapidly to a peak stress at a relatively low strain; strain softening then occurs leading to a steady state at high strains. The addition of Yttrium increases the hardening rate significantly leading to higher peak stress. The lower peak stresses in Mg-5Zn-2Y and Mg-2.9Zn alloys are also associated with higher softening prior and after the peak stress.

In order to evaluate the appearance of DRX grains and twinning, samples were deformed to half of the peak strain, peak strain, and strain of 1. A typical series of such microstructures taken at half of the peak strain is displayed in Fig. 3. At the peak strain, DRX did not start in the two alloys containing Y while fine DRX grains can be observed in Mg-2.9Zn alloy in Fig. 3c. The DRX mechanism in Mg alloys has been studied previously by [19]. The authors shown that new DRX grains first begin by the formation of LEDS and the continuous integration of new dislocations leads to the formation of new grains with high angle boundaries.

The formation of DRX grains is favored along grain and twin boundaries [21]. Similar observations have been reported in other Mg alloys [22, 23]. The formation
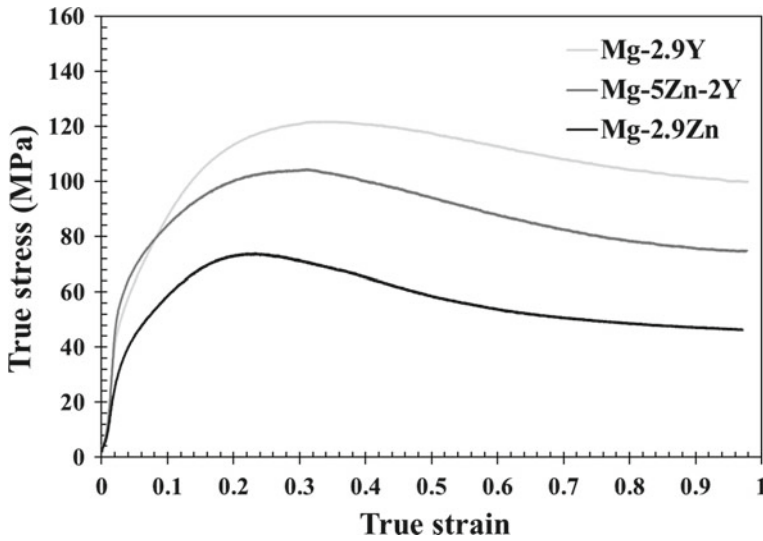
Fig. 2 Stress–strain curves obtained after uniaxial compression at 350 °C and true strain rate of 1 s-1

of twins along twin boundaries and in the twin lamella is shown in Fig. 4. Figure 4a shows an EBSD-IPF map of the Mg-5Zn-2Y taken at peak strain. In Mg-2.9Y, only few DRX grains can be observed after a strain of 1. Figure 4b shows DRX grains forming inside a contraction twin. The evolution of DRX grains with strain is shown in Fig. 5a for the three alloys. After half of the peak strain, approximately 15% of the microstructure undergoes DRX in Mg-2.9Zn and reaches 100% at a strain of 1. When Y is added, DRX is retarded. The effect of Y on recrystallization kinetic has been investigated previously. It is shown that Y in solid solution decreases the mobility of GBs [24] and the formation of LEDs [25]. In Mg-5Zn-2Y alloy, DRX begins above half of the peak strain. At the peak strain, approximately 10% of the Mg-5Zn-2Y microstructure is made of DRX grains. The formation DRX increases sharply above this point and the microstructure is almost fully recrystallized (~85%) after a strain of 1. In the Mg-2.9Y alloy, DRX begins after the peak strain and only 25% of the microstructure recrystallizes after a strain of 1.

The rapid initiation of DRX in Mg-Zn also coincides with an important reduction in the twin volume fraction when compared with the Mg-2.9Y alloy (see Fig. 3). This can be partially explained by the fact that DRX begins first inside twins and thus decreases the number of visible twins in the microstructure. For this reason, the DRX twins that can be obviously identified (like in Fig. 4b) were counted as a twin in Fig. 5b. The measurements were not performed at half of the peak and peak strains in some alloys since the amount of DRX is important and the twins with DRX cannot be distinguished properly at those strains in the Mg-5Zn-2Y and the Mg-2.9Y alloys.

By comparing the volume fraction of DRX and twins in Fig. 5, one can observe that twin volume fraction is higher in alloys that have a lower DRX volume fraction. The
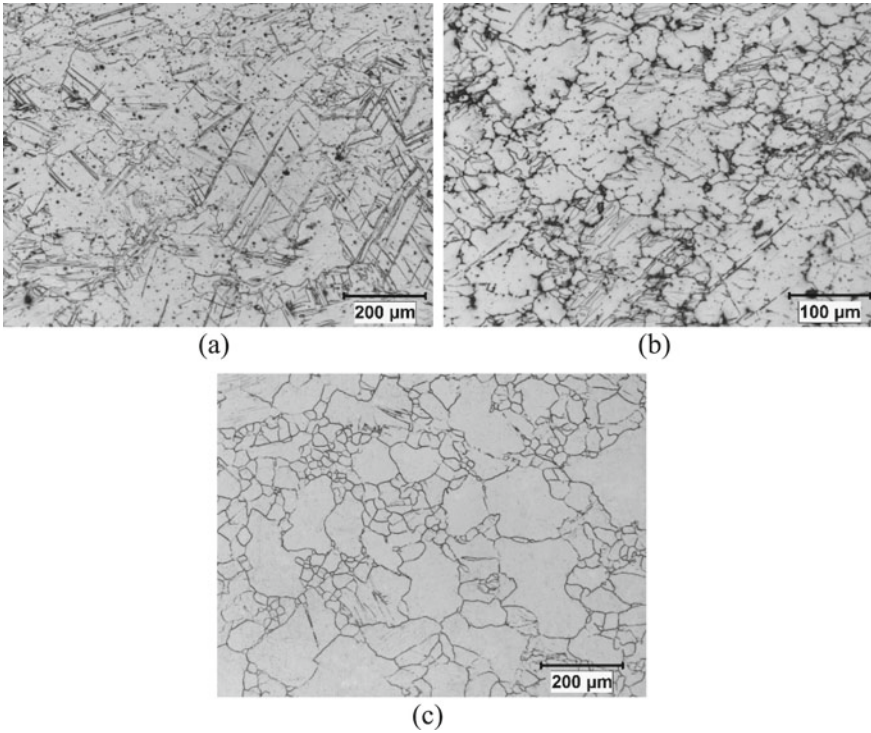
Fig. 3 Optical images showing the microstructure evolution immediately after compression to the half of the peak strain in **a** Mg-2.9Y, **b** Mg-5Zn-2Y, and **c** Mg-2.9Zn
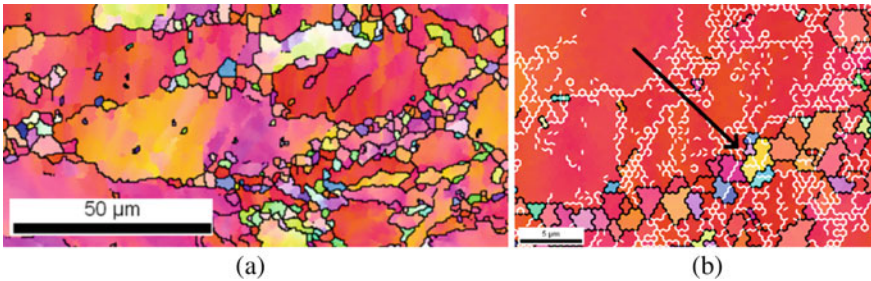
Fig. 4 OIM images showing dynamic recrystallization in **a** Mg-5Zn-2Y at peak strain and **b** Mg-2.9Y after a strain of 1. The HABs (>15°) are shown in black and the LABs (<15°) are shown in white in **b** only. (Color figure online)
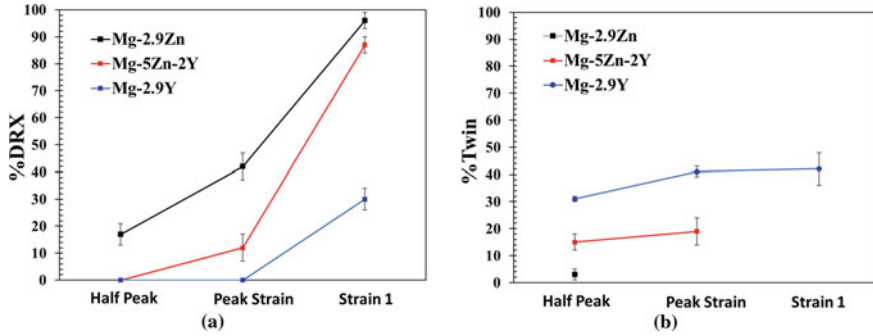
Fig. 5 Volume fraction of **a** DRX and **b** twinning as a function of strain level for the three alloy compositions. The error bars correspond to the standard deviation associated with the measurement taken on different optical images. (Color figure online)

highest volume fraction of twin is observed in Mg-2.9Y followed by Mg-5Zn-2Y and Mg-2.9Zn. DRX in Mg alloys is preceded by the formation of LEDS, suppressing the dislocation piles along GBs. This results in lower stress concentration at the boundaries that are likely to result in sites for twin nucleation. Accordingly, less twins form in Mg-5Zn-2Y compared with Mg-2.9 Y as can been be seen in Fig. 3. At the half peak strain, no DRX grain can be observed in the Y containing alloys, but since DRX kinetic is higher in Mg-5Zn-2Y more LEDS are likely to form reducing the amount of stress concentration in form of piles-ups at grain boundaries. In this case, the suppression of twinning when temperature increase seems to be correlated to the formation of LEDs rather than the activation of non-basal slip systems.

Conclusions

This work analyzes the amount of twinning and the DRX for three Mg alloys deformed at 350 °C. Microstructural observations clearly show the presence of twins in the Yttrium-containing alloys. For investigation using electron backscatter diffraction maps show that in those alloys the DRX grains are primarily located along the twin boundaries and in the twins. The Yttrium-containing alloys show lower volume fraction of DRX when compared to the Mg-2.9Z alloy. This work clearly shows that the amount of DRX and the occurrence of twins are inversely correlated. This gives credence to the hypothesis that the presence of DRX substructure leads to reduction in the conditions favorable for twin formation through a reduction in the stress concentration.

References

1. Sadeghi A, Martin É, Pekguleryuz M (2014) Texture evolution and twinning during the expansion of hot extruded AZ31 + Sr Seamless tubes, Metall Mater Trans A 45:6304–6316. https://doi.org/10.1007/s11661-014-2546-0

2. Jiang L, Jonas JJ, Mishra RK, Luo AA, Sachdev AK, Godet S (2007) Twinning and texture development in two Mg alloys subjected to loading along three different strain paths, Acta Mater 55:3899–3910. https://doi.org/10.1016/j.actamat.2007.03.006

3. Godet S, Jiang L, Luo AA, Jonas JJ (2006) Use of schmid factors to select extension twin variants in extruded magnesium alloy tubes. https://doi.org/10.1016/j.scriptamat.2006.07.059

4. Choi SH, Song YS, Kim JK, Jung BJ, Park YB (2007) Implementation of twin reorientation and softening schemes in a polycrystal plasticity model for Mg alloys, In: Recryst. Grain Growth III, Trans Tech Publications, pp 1063–1068. https://doi.org/10.4028/www.scientific.net/MSF.558-559.1063

5. Mu S, Jonas JJ, Gottstein G (2012) Variant selection of primary, secondary and tertiary twins in a deformed Mg alloy. https://doi.org/10.1016/j.actamat.2012.01.014

6. Pei Y, Godfrey A, Jiang J, Zhang YB, Liu W, Liu Q (2012) Extension twin variant selection during uniaxial compression of a magnesium alloy. Mater Sci Eng A 550:138–145. https://doi.org/10.1016/j.msea.2012.04.046

7. Mishra RK, Brahme A, Sabat RK, Jin L, Inal K (2019) Twinning and texture randomization in Mg and Mg-Ce alloys. Int J Plast 117:157–172. https://doi.org/10.1016/j.ijplas.2019.03.001

8. Lind J, Li SF, Pokharel R, Lienert U, Rollett AD, Suter RM (2014). Tensile twin nucleation events coupled to neighboring slip observed in three dimensions. https://doi.org/10.1016/j.actamat.2014.04.050

9. Jain A, Agnew SR (2007) Modeling the temperature dependent effect of twinning on the behavior of magnesium alloy AZ31B sheet. Mater Sci Eng A 462:29–36. https://doi.org/10.1016/j.msea.2006.03.160

10. Molodov KD, Al- T, Molodov DA, Gottstein G (2015) on the role of Anomalous Twinning in the Plasticity of Magnesium. https://doi.org/10.1016/j.actamat.2015.10.043

11. Barnett MR (2003) A Taylor model based description of the proof stress of magnesium AZ31 during hot working, Metall Mater Trans A 34 A: 1799–1806. https://doi.org/10.1007/s11661-003-0146-5

12. Chapuis A, Driver JH (2010) Temperature dependency of slip and twinning in plane strain compressed magnesium single crystals. https://doi.org/10.1016/j.actamat.2010.11.064

13. Anderson PM, Hirth JP, Lothe J (2017) Theory of dislocations, Cambridge University Press

14. Christian JW, Mahajan S (1995) Deformation twinning. Prog Mater Sci 39:1–157. https://doi.org/10.1016/0079-6425(94)00007-7

15. Martin É, Capolungo L, Jiang L, Jonas JJ, Woodruff GW (2010) Variant selection during secondary twinning in Mg–3%Al. Acta Mater. 58:3970–3983. https://doi.org/10.1016/j.actamat.2010.03.027

16. Wang J, Hoagland RG, Hirth JP, Capolungo L, Beyerlein IJ, Tomé CN (2009) Nucleation of a (1̄012) twin in hexagonal close-packed crystals. Scr Mater 61:903–906. https://doi.org/10.1016/j.scriptamat.2009.07.028

17. Beyerlein IJ, Capolungo L, Marshall PE, McCabe RJ, Tome CN (2010) Statistical analyses of deformation twinning in magnesium. Philos Mag 90:2161–2190. https://doi.org/10.1080/14786431003630835

18. Kuhlmann-Wilsdorf D (1999) The theory of dislocation-based crystal plasticity, Philos Mag A Phys Condens Matter Struct Defects Mech Prop 79 :955–1008. https://doi.org/10.1080/01418619908210342.

19. Martin É, Jonas JJ (2010) Evolution of microstructure and microtexture during the hot deformation of Mg-3% Al. Acta Mater 58:4253–4266. https://doi.org/10.1016/j.actamat.2010.04.017

20. Farzadfar SA, Sanjari M, Jung I-H, Essadiqi E, Yue S (2011) Role of yttrium in the microstructure and texture evolution of Mg. Mater Sci Eng A 528:6742–6753. https://doi.org/10.1016/j.msea.2011.05.064

21. Martin E, Mishra RK, Jonas JJ (2011) Deformation structures and recrystallization in magnesium alloys. In: Czerwinski F (ed), Magnesium alloys—design, processing and properties

22. Al- T, Gottstein G (2008) Dynamic recrystallization during high temperature deformation of magnesium. Mater Sci Eng A 490:411–420. https://doi.org/10.1016/j.msea.2008.02.004

23. Ma Q, Li B, Marin EB, Horstemeyer SJ (2011) Twinning-induced dynamic recrystallization in a magnesium alloy extruded at 450 °C, Scr Mater 65: 823–826. https://doi.org/10.1016/j.scriptamat.2011.07.046

24. Farzadfar SA, Martin E, Sanjari M, Essadiqi E, Yue S (2012) Texture weakening and static recrystallization in rolled Mg-2.9Y and Mg-2.9Zn solid solution alloys, J Mater Sci 47:5488–5500. https://doi.org/10.1007/s10853-012-6440-0

25. Farzadfar SA, Martin É, Sanjari M, Essadiqi E, Wells MA, Yue S (2012) On the deformation, recrystallization and texture of hot-rolled Mg-2.9Y and Mg-2.9Zn solid solution alloys—A comparative study, Mater Sci Eng A 534:209–219. https://doi.org/10.1016/j.msea.2011.11.061

Part IX
Recycling and Environmental Issues

Effects of MgCl$_2$ and NaCl on Si-Thermic Reduction of MgO in Recycle of Mg-air Battery

Check for updates

Atsushi Hayashida, Toshihide Takenaka, and Taiki Morishige

Abstract The effects of the chlorine content used as electrolyte should be controlled in the recycle process of Mg-air battery. The influence of MgCl$_2$ and NaCl in Si-thermic reduction of MgO has been studied in this study. The mixture of MgO with MgCl$_2$ or NaCl was reduced by metallic Si at 1150 °C for 3 h, and the reduction rate was estimated. The reduction rate without MgCl$_2$ or NaCl addition was about 55% under our reduction condition, and 1 mol% addition of MgCl$_2$ rarely affected the reduction rate. However, the reduction rate decreased with added amount of MgCl$_2$, and became about 15% in 10 mol% addition. Even 1 mol% addition of NaCl worsened the reduction rate, and the reduction rate decreased with the addition amount. It is confirmed that the chlorine should be removed before Si-thermic reduction in the recycle of Mg-air battery.

Keywords Si-thermic reduction · Recycle of Mg-air battery · Effects of chloride · Mg metal production

Introduction

Mg-air battery is paid attention as an energy storage and conversion device, [1–4] and its recycling should be required in the near future. [5] The recycle of Mg metal is particularly important in Japan from the view of Mg supply. In the recycle of used Mg-air battery, the reduction of oxidized Mg electrode which mainly consists of

A. Hayashida (✉)
Graduate School of Science and Engineering, Kansai-University, 3-3-35 Yamate-cho, Suita-city, Osaka 564-8680, Japan
e-mail: k016431@kansai-u.ac.jp

T. Takenaka · T. Morishige
Department of Chemistry and Material Engineering, Kansai-University, 3-3-35 Yamate-cho, Suita-city, Osaka 564-8680, Japan
e-mail: ttakenak@kansai-u.ac.jp

T. Morishige
e-mail: tmorishi@kansai-u.ac.jp

267

$Mg(OH)_2$ is necessary. Some other elements which are contained in $Mg(OH)_2$ from used Mg-air battery must be controlled.

Si-thermic reduction is widely applied to Mg metal production from dolomite, $MgCa(CO_3)_2$, and Pidgeon process is well known. [6] The total reaction of Si-thermic reduction of dolomite is shown as follows:

$$MgCa(CO_3)_2(s) + 1/2Si(s) \rightarrow Mg(g) + 1/2Ca_2SiO_4(s) + 2CO_2(g) \qquad (1)$$
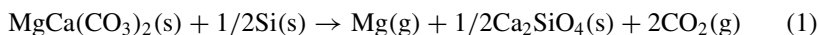
In the recycle of used Mg-air battery, $Mg(OH)_2$ is calcined to MgO, CaO, and Si or Fe-Si is mixed and the reduction is carried out around 1500 K under vacuum, and the reduction (1) occurs. The elements contained in $Mg(OH)_2$ from used Mg-air battery can be influenced; it is especially considered that the chlorine content strongly affects the reduction because the reduction occurs at the interface of solid MgO and Si.

The influence of a small amount of $MgCl_2$ or NaCl added to MgO and CaO mixture was studied in this study. $MgCl_2$ or NaCl was added to $Mg(OH)_2$ and $Ca(OH)_2$ mixture, and the mixture was calcined. Metallic Si was added to the calcine mixture, and the reduction was carried out at 1150 °C. The product and residue were analyzed after the reduction, and the influence of $MgCl_2$ and NaCl was discussed.

Experimental Method

The compounds used in this study were anhydrous $Mg(OH)_2$ (>95%), $Ca(OH)_2$ (>96.0%), $MgCl_2$ (>99.5%), NaCl (>99.5%), and Si (99%, 75 µm). $MgCl_2$ or NaCl was mixed with $Mg(OH)_2$ and $Ca(OH)_2$ in water as the composition was $Mg(OH)_2$:$Ca(OH)_2$:$MgCl_2$ or NaCl = 1:1:x (x = 0.01, 0.05, 0,1, and 0.15) in molar ratio. The solution was dried longer than 24 h, and then calcined at 800 °C for 3 h, where $Mg(OH)_2$ and $Ca(OH)_2$ were decomposed to MgO and CaO. Si was added to the calcined mixture as MgO:Si = 2:1 in molar ratio, and pressed to be a green compact.

The schematic diagram of thermic reduction equipment is shown in Fig. 1. The green compact (just "specimen" herein after) was set on a BN boat and heated at 1150 °C for 3 h under vacuum, where the Si-thermic reduction of MgO occurred. After Si-thermic reduction, the residual material on the BN boat and the product condensed near cooling part were collected. The residual material and the product were observed by SEM–EDX and analyzed by XRD.
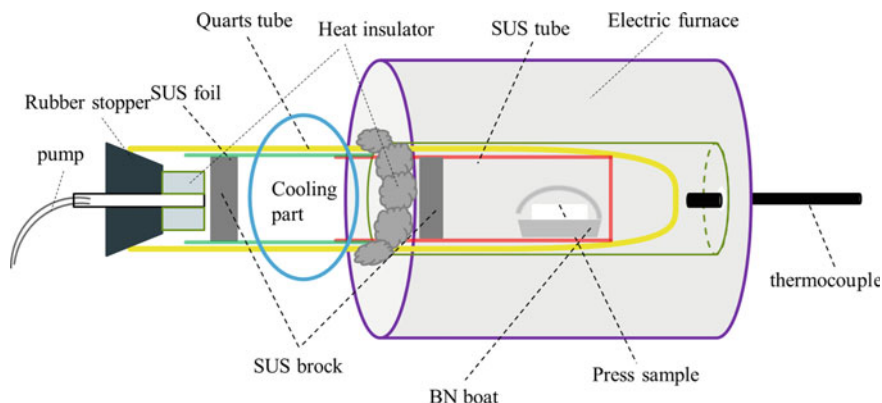
Fig. 1 Schematic diagram of thermic reduction equipment. (Color figure online)

Results

Reduction Products Condensed on Cooling Part

A small amount of materials was condensed on the inside surface of cooling part outside the furnace. The SEM images of the condensed materials for the specimens with 10 mol%-MgCl₂ or 10 mol%-NaCl are shown in Fig. 2 with their element distributions. The condensed materials seemed very fine particles, and mainly consist of Mg and O. It is considered that Mg vapor was formed by the reduction in the high-temperature part, condensed in the cooling part, and oxidized when it was taken out after the experiment. Cl was also detected in the condensed materials for the specimen with MgCl₂ and NaCl, and Na was also detected in the condensed materials for the
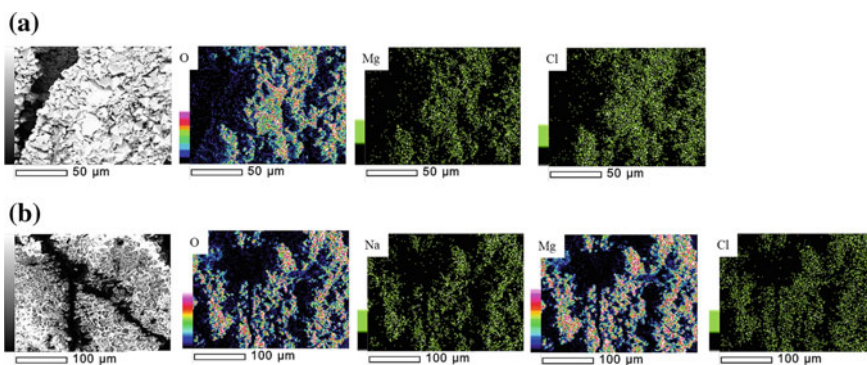
Fig. 2 The SEM images and elements distributions of the products with **a** 10mol%-MgCl2 and **b** 10mol%-NaCl. (Color figure online)

specimen with NaCl. It is indicated that the added $MgCl_2$ and NaCl were partially vaporized and condensed in the cooling part.

The amount of the condensed materials was very little, so XRD analysis and the weight measurement could not be performed.

Residual Specimens After Si-thermic Reduction

The SEM images and element distributions of residual specimen with 5 mol%-NaCl are shown in Fig. 3. Si particles seemed to decrease in residual specimens than original specimens regardless of addition amounts of $MgCl_2$ or NaCl, and it is considered that Si reacted in thermic reduction. Concentrated area of Ca, Si, and O (in red circle in Fig. 3) was seen. XRD analysis of residual specimen with 5 mol%-NaCl is shown in Fig. 4, and this particle can be identified as Ca_2SiO_4, which is not seen in the original specimens, and seen only in residual specimens despite the additional amounts of $MgCl_2$ or NaCl. Ca_2SiO_4 is a by-product of reduction of MgO from (2), so it is considered that MgO was reduced regardless of adding $MgCl_2$ and NaCl.

$$2MgO(s) + 2CaO(s) + Si(s) \rightarrow 2Mg(g) + Ca_2SiO_4(s) \tag{2}$$

$CaCl_2$ was also detected in the residual specimens with $MgCl_2$ and NaCl, and Na_2SiO_3 was also detected in residual specimens with NaCl from XRD analysis. These substances show that other reactions except reduction of MgO can occur. Therefore, it is considered that these reactions or substances influence reduction of MgO. These reaction formulas are shown in (3)–(5).

$$MgCl_2(g) + CaO(s) \rightarrow CaCl_2(l) + MgO(s) \tag{3}$$
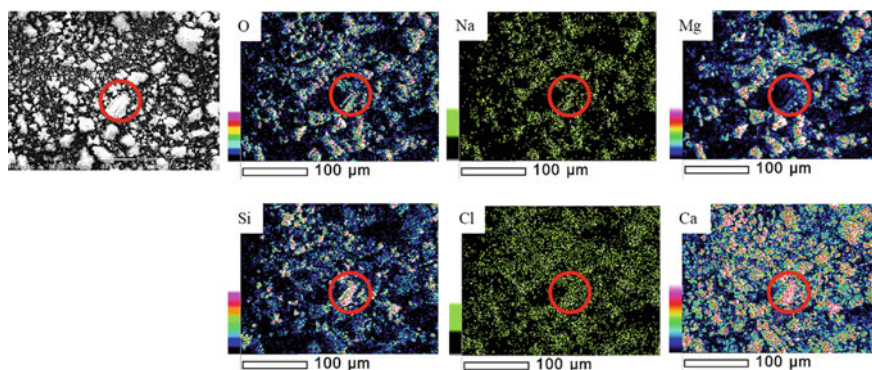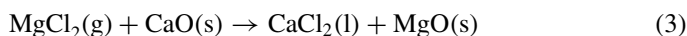
Fig. 3 The SEM images and elements distributions of residual specimens with 5 mol%-NaCl. (Color figure online)

Fig. 4 XRD analysis of residual specimen with 5mol%-NaCl. (Color figure online)

$$2NaCl(g) + CaO(s) \rightarrow CaCl_2(l) + Na_2O(s) \tag{4}$$

$$Na_2O(s) + Ca_2SiO_4(s) \rightarrow Na_2SiO_3(l) + 2CaO(S) \tag{5}$$
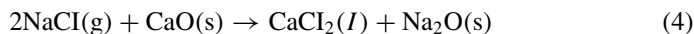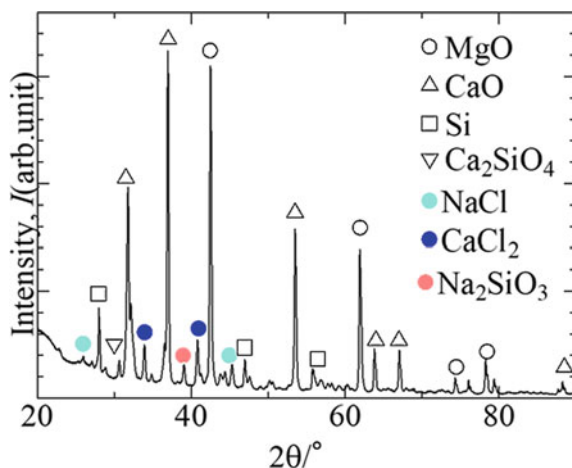
Reduction Rate

The weight of residual specimens decreased regardless of addition amount of MgCl₂ and NaCl. The weight of products condensed on cooling part could not be measured due to being very little, so the reduction rate was calculated with the decreasing amount of weight by (6).

$$Reduction\ rate(\%) = (W_s - W_r)/W_{Mg} \times 100\% \tag{6}$$

where W_s, W_r, and W_{Mg} are the weight of specimens, residual specimens, and Mg from MgO in the specimens, respectively. Volatilization of MgCl₂ and NaCl during thermic reduction was considered against calculation of reduction rates. Reduction rates of addition of MgCl₂ or NaCl and no addition are shown in Fig. 5. Reduction rates improved slightly than that of no addition when 1 mol% and 15 mol%-MgCl₂ were added. Reduction rates decreased obviously when 5 mol% and 10 mol%-MgCl₂, and 1~ 0 mol%-NaCl were added. Therefore, it is considered that very little amount of MgCl₂ can improve reduction rate, and NaCl needs to be removed because NaCl largely impedes reduction of MgO.
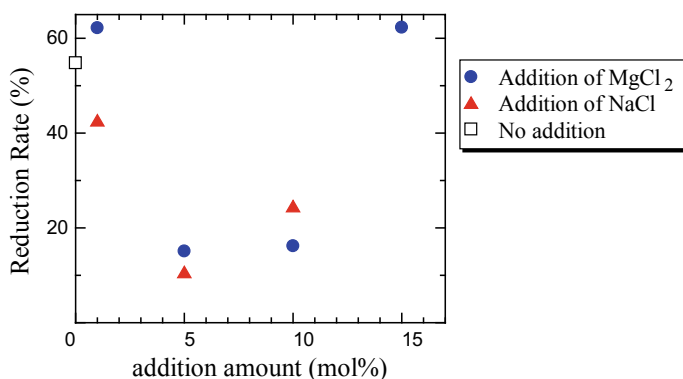
Fig. 5 Reduction rates of addition of MgCl$_2$ or NaCl and no addition. (Color figure online)

Discussion

Effects on reduction rates can strongly depend on the contact condition of particles in specimens. Reduction of MgO is a solid phase reaction and contact of MgO, CaO, and Si is needed for reduction. Good factor can be molten CaCl$_2$. Molten CaCl$_2$ coating on these particles can make the contact condition better and improve reaction rate of reduction of MgO. Bad factor can be volatilization of MgCl$_2$ and NaCl. Volatilization of MgCl$_2$ and NaCl can increase the pores in specimens, and worsen contact condition to make lower reaction rate of reduction of MgO. Molten CaCl$_2$ coating as good factor can affect more strongly when 1 mol% or 15 mol%-MgCl$_2$ was added. Volatilization of MgCl$_2$ and NaCl as bad factor can affect more strongly when 5 mol% or 10 mol%-MgCl$_2$ or 1~10 mol%-NaCl was added.

If reduction time is long enough for complete reduction of MgO, it would be possible to obtain more Mg metal. However, it could not be good from both ecological and environmental side as it needs more time than no addition of MgCl$_2$ and NaCl. To decrease CaO which works to promote reduction of MgO can make it impossible to reduce all amount of MgO to Mg metal.

It is found that both MgCl$_2$ and NaCl volatilized during thermic reduction and were condensed in reduction products. Therefore, volatilization of MgCl$_2$ or NaCl can badly effect on purity of Mg metal. It is considered that MgCl$_2$ or NaCl needs to be removed from the point of view of high-purity Mg production.

Conclusions

In this study, the influence of MgCl$_2$ and NaCl on the recycling of Mg from waste Mg-air battery was investigated. In particular, their effects and permission ranges were examined experimentally. MgO was reduced to Mg metal in the Si-thermic process

even with the addition of MgCl$_2$ or NaCl. The reduction rates improved slightly when 1 mol% and 15mil%-MgCl$_2$ were added. However, it decreased when 5 mol% and 10mo%-MgCl$_2$ and 1~10 mol%-NaCl were added. The positive effect of chloride addition is the formation of molten CaCl$_2$ which improves the contact condition of particle, but the volatilization of MgCl$_2$ and NaCl during the Si-thermic process can worsen the reduction process. Permission range of MgCl$_2$ is about 1 mol%, but NaCl needs to be removed as much as possible for the efficient Mg recycling process.

References

1. Mordike B, Ebert T (2001) Magnesium properties–application–potential. Mater Sci Eng A 302:37–45
2. Zhao H, Bian P (2009) Electrochemical performance of magnesium alloy and its application on the sea water battery. J Environ Sci 21:S88–S91
3. Zhang T, Zhanliang T, Jun C (2014) Magnesium-air batteries: from principle to application, Mater Horiz 196–206
4. Khoo T, Howlett PC, Tsagouria M, MacFarlane DR, Forsyth M (2011) The potential for ionic liquid electrolytes to stabilise the magnesium interface for magnesium/air batteries, Electrochimica Acta 583–588
5. Mahmoud MS, Yabe T (2017) Silicothermic reduction of MgO using diode laser: Experimental and kinetic study. J Magnesium Alloys 5:430–438
6. Wang Y, Jing Y, Jianping P, Yuezhong D (2016) Production of magnesium by vacuum aluminothermic reduction with magnesium aluminate spinel as a by-product, JOM 68: 1728–1736

Correction to: Understanding Deformation Behavior of AM50 and AZ31 Magnesium Extrusions with Various Heat Treatments in Comparison with AA6063 and AA6082 Aluminum Extrusions

Baris Kara, Enes Kurtulus, Asım Zeybek, Meryem Altay, and Hakan Aydın

Correction to:
Chapter "Understanding Deformation Behavior of AM50 and AZ31 Magnesium Extrusions with Various Heat Treatments in Comparison with AA6063 and AA6082 Aluminum Extrusions" in: A. Luo et al. (eds.), *Magnesium 2021*, The Minerals, Metals & Materials Series, https://doi.org/10.1007/978-3-030-72432-0_16
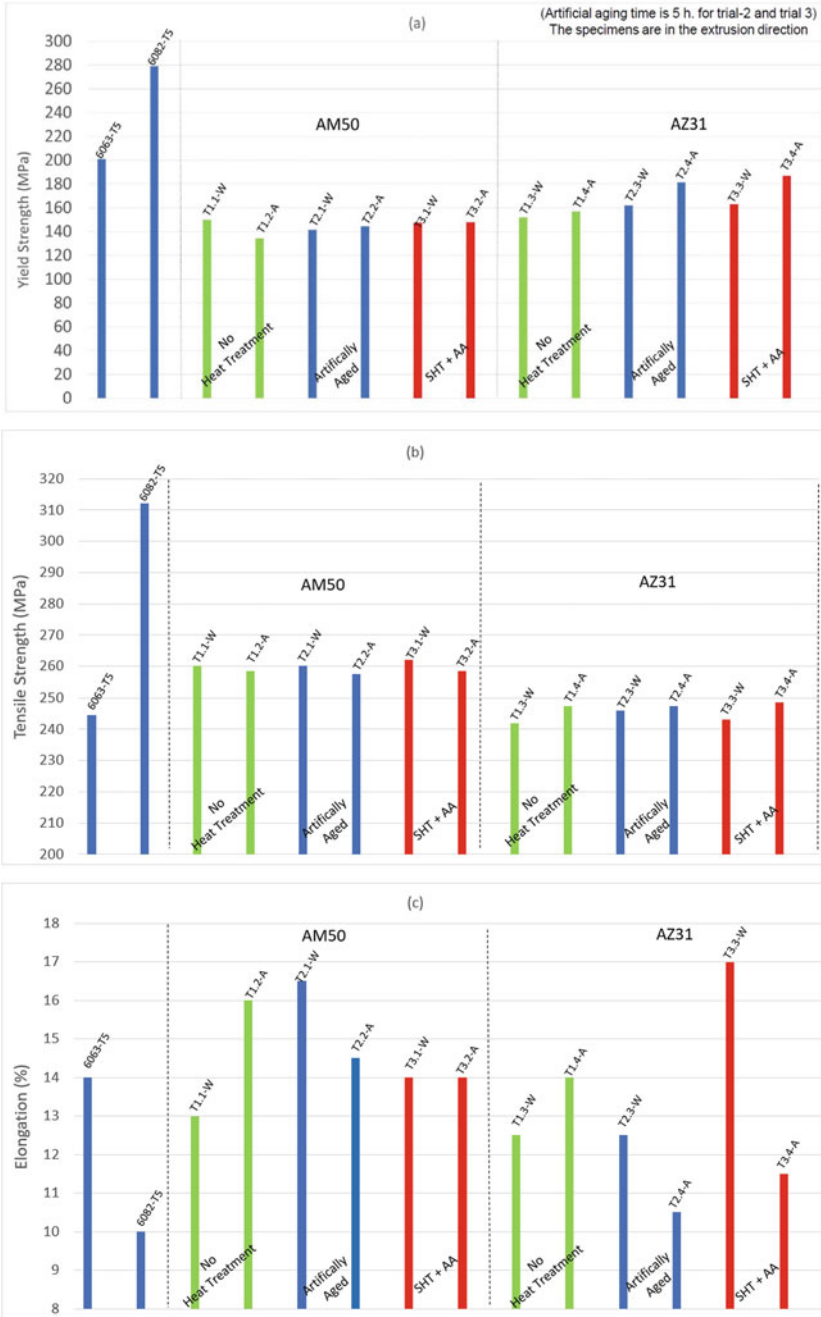
The original version of this chapter was revised: Author provided figure 5 correction and changes in Abstract have been incorporated.

The chapter and book have been updated with the changes.

Incorporated Figure 5 given as in below:

Fig. 5 Heat treatment effect on mechanical properties on **a** Yield strength **b** Tensile strength **c** Elongation **d** Fracture energy (Note: Artificial aging time is 5 h. for trial 2 and trial 3). (Color figure online)
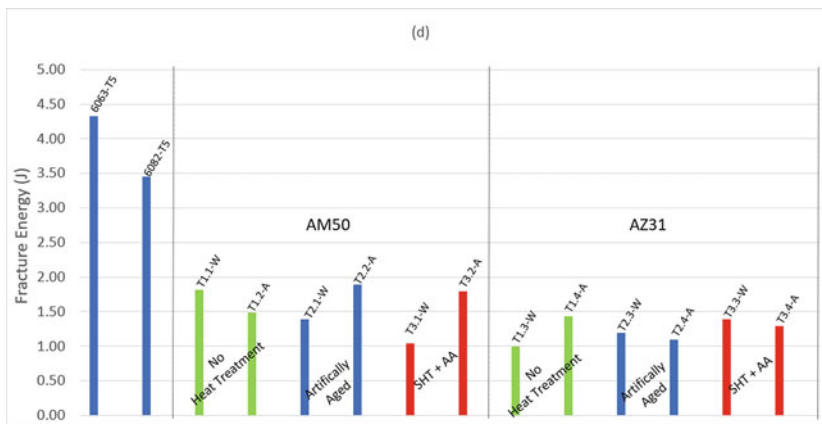
Fig. 5 (continued)

Author Index

Subject Index